Published in final edited form as:
Phys Rep. 2014 October 10; 543(2): 61–162. doi:10.1016/j.physrep.2014.05.002.

Nonlinear and Stochastic Dynamics in the Heart

Zhilin Qu[1,*], **Gang Hu**[2], **Alan Garfinkel**[1,3], and **James N. Weiss**[1,4]

[1]Department of Medicine (Cardiology), David Geffen School of Medicine, University of California, Los Angeles, California 90095, USA

[2]Department of Physics, Beijing Normal University, Beijing 100875, China

[3]Department of Integrative Biology and Physiology, University of California, Los Angeles, California 90095, USA

[4]Department of Physiology, David Geffen School of Medicine, University of California, Los Angeles, California 90095, USA

Abstract

In a normal human life span, the heart beats about 2 to 3 billion times. Under diseased conditions, a heart may lose its normal rhythm and degenerate suddenly into much faster and irregular rhythms, called arrhythmias, which may lead to sudden death. The transition from a normal rhythm to an arrhythmia is a transition from regular electrical wave conduction to irregular or turbulent wave conduction in the heart, and thus this medical problem is also a problem of physics and mathematics. In the last century, clinical, experimental, and theoretical studies have shown that dynamical theories play fundamental roles in understanding the mechanisms of the genesis of the normal heart rhythm as well as lethal arrhythmias. In this article, we summarize in detail the nonlinear and stochastic dynamics occurring in the heart and their links to normal cardiac functions and arrhythmias, providing a holistic view through integrating dynamics from the molecular (microscopic) scale, to the organelle (mesoscopic) scale, to the cellular, tissue, and organ (macroscopic) scales. We discuss what existing problems and challenges are waiting to be solved and how multi-scale mathematical modeling and nonlinear dynamics may be helpful for solving these problems.

Keywords

excitable medium; heart rhythm; arrhythmias; electrical turbulence; dynamics; control

---

[*]Correspondence to: Zhilin Qu, PhD, Department of Medicine, Division of Cardiology, David Geffen School of Medicine at UCLA, A2-237 CHS, 650 Charles E. Young Drive South, Los Angeles, CA 90095, Tel: 310-794-6050, Fax: 310-206-9133, zqu@mednet.ucla.edu.

> "…,*we should recognize that such roads [between the sciences], while the quickest shortcut to another part of our own science, are not visible from the viewpoint of one science alone*."
>
> P.W. Anderson

1. Introduction

The human heart beats every second or so, totaling 2 to 3 billion heartbeats in a normal life span. The contractions of the heart are triggered by electrical excitations which originate from a region in the right atrium, called the sino-atrial node (SAN). The SAN works relentlessly as an oscillator to generate heart rhythms, while its rate of oscillation is adaptive to changes in energy demand of the body and environmental factors. However, the heart may suddenly lose its ability to pump blood effectively due to SAN malfunction or to an occurrence of electrical turbulence in the ventricles, leading to sudden cardiac death (SCD). SCD is a leading cause of death in industrialized countries, accounting for 300,000–400,000 deaths annually in the United States of America [1, 2].

"*Sudden cardiac death: a problem in topology*", the title of a Scientific American article by Arthur Winfree 30 years ago [3], highlights that SCD is not only a problem of biology and medicine, but also a problem of physics and mathematics. This is because the heart is not only a biological organ but also an electrical conductor and a mechanical pump. The nonlinear dynamics of both mechanical and electrical properties of the heart have been an intensively studied research topic for more than a century, and have greatly improved our understanding of the mechanisms of normal excitation and contraction of the heart, as well as lethal arrhythmias and cardiac diseases. However, due to the highly interdisciplinary nature of this research, it is nontrivial for physicists and mathematicians to understand the complex biology and physiology of the heart, and, conversely, for biologists and cardiologists to grasp the nonlinear electrical and mechanical dynamics. The short reviews by Glass [4] and by Karma and Gilmour [5] are excellent introductory articles for physicists and mathematicians, as well as other more detailed recent reviews [6–8] that cover aspects of nonlinear dynamics in the heart.

In this article, our goal is to provide a comprehensive review of the current understanding of the nonlinear and stochastic dynamics in the heart, based on clinical observations, experimental studies, and mathematical modeling and theoretical analyses. The objectives are: 1) to provide a basic level introduction of cardiac excitation and conduction, the corresponding nonlinear and stochastic dynamics, and the methods used, geared towards graduate students in physics, mathematics, and engineering and the researchers who are interested in entering into this field; and 2) to provide a detailed, systematic, and holistic overview for current researchers in this field on what is known about the nonlinear and stochastic dynamics in the heart, what problems remain unsolved, and how nonlinear dynamics can be used for understanding the mechanisms of normal heart rhythms, lethal arrhythmias, and how they can be controlled therapeutically.

The article is organized as follows. Sections 2 and 3 are introductory sections on the normal heart rhythm, arrhythmias, and their multi-scale regulations, the nonlinear dynamics at different scales in the heart and their clinical features. Section 4 introduces the basic biophysics of excitable cells and mathematical modeling of the heart. Section 5 presents nonlinear dynamics occurring at the molecular and sub-cellular scales. Section 6 summarizes the nonlinear dynamics observed and modeled in single cells, such as period-doubling bifurcation and chaos induced by periodic pacing. Section 7 summarizes the electrical wave dynamics in cardiac tissue, and the manifestation of cellular dynamics at tissue and organ scales. Section 8 is a short summary of the dynamics of the pacemaker cells and heart rate variability. Section 9 reviews nonlinear dynamics applied to control and termination of arrhythmias. Finally, in Section 10, we discuss, in perspective, the remaining challenges and the role of nonlinear dynamics and complex systems theory in solving these problems.

2. The normal heart rhythm and arrhythmias

2.1. The heart and its normal rhythm

The heart consists of four chambers (Fig.1a): left atrium, right atrium, left ventricle, and right ventricle. The electrical impulses are generated repetitively in the SAN, which propagate to both the right atrium and left atrium. The atrium and the ventricle are electrically insulated from each other. The electrical impulses propagate from the atria to the ventricles via a special junction, called atrial-ventricular node (AVN), then to the Purkinje fiber network and the ventricles. The conduction velocity (CV) of the electrical impulse in atrial and ventricular tissue is about 0.5 m/s. The conduction in Purkinje fibers is much faster (2–3 m/s) than in the atrium or the ventricles [9]. The fast conduction in Purkinje fiber is important to allow an impulse to excite the whole ventricles in a short period of time, resulting in a synchronous contraction for effective pumping.

Cardiac tissue is mainly composed of rod-shaped cells called myocytes (Fig.1b). Cardiac myocytes are either excitable or oscillatory. Other types of cells also exist in the heart, such as fibroblasts which are small non-excitable cells. The size of an adult ventricular myocyte is about 100–200μm in length, 20–30μm in width, and 10–20μm in depth, which are roughly conserved from species to species [10, 11]. The contraction of the heart depends on the synchronous contraction (shortening) of its myocytes. Myocyte shortening is induced by a rise in intracellular calcium ion (Ca^{2+}) concentration triggered by the electrical impulse [12].

The behaviors of myocytes differ in different regions of the heart and heart wall (Fig.1c). The SAN cells and the cells in the AVN are oscillatory. During oscillations, the voltage varies between −60 mV and 40 mV. The cells in the AVN have a slower oscillation frequency than the SAN cells, and are entrained by the SAN oscillations during the normal heart rhythm. The atrial and ventricular myocytes are excitable cells, but can become oscillatory under diseased or experimental conditions. The atrial and ventricular myocytes have resting membrane potentials around −80 mV. A short-pulse stimulus above a threshold strength triggers a rapid reversal of membrane voltage to the positive range which then falls back to the resting potential after several hundred milliseconds. The event of membrane voltage rise and fall (in both excitable and oscillatory cells) is called an action potential. During an action potential, intracellular Ca^{2+} concentration also rises and falls, which then signals the contraction and relaxation of myocytes. This process is called excitation-contraction coupling. In addition to distinct difference in dynamical behaviors of cells from different regions of the heart, the action potential characteristics also vary regionally within the same cardiac chamber, such as the action potential morphology and duration differences between epicardial, mid-myocardial, and endocardial cells in the ventricles (Fig.1c).

In clinical settings, the electrical activity of the heart is detected with body surface electrodes, called an electrocardiogram (ECG). An ECG is a weighted measure of the electrical activity in the whole heart. Figure 1d shows a schematic plot of a normal ECG which exhibits distinct features of excitation of the heart. The small peak before the sharp spike is called the P-wave which is caused by the excitation of the atria. The subsequent large sharp spike is called the QRS complex, which measures the conduction of the electrical signal through the Purkinje fiber network and the ventricles. Since the electrical conduction in the Purkinje fibers is much faster, the width of the QRS complex is a rough measure of the conduction time from the endocardium to epicardium of the ventricles. The ECG signal then returns to the baseline after the full ventricular wall thickness has been depolarized, called the ST segment. As the regions of the ventricular tissue begin to repolarize, the ECG signal rises again more slowly to a peak and then falls again, called the T-wave. The time interval from the beginning of the QRS complex to the end of the T-wave is called the QT interval which is used clinically for diagnosis of long QT and short QT syndromes. The QT interval is a rough measure of action potential duration (APD) of the myocytes in the ventricles. The time interval between two consecutive QRS complexes is called the RR interval, which normally corresponds to the oscillation period of the SAN. Note that the polarities of the QRS complex and the T-wave, and their magnitudes, depend on the location of the ECG electrode relative to the heart. Since ECG measures the electrical activity in the heart, different ECG patterns indicate different electrical states of the heart, which is the firsthand information used in diagnosis of cardiac arrhythmias and other cardiac diseases.

2.2. Arrhythmias and anti-arrhythmic therapies

Under diseased conditions, heart rhythms can become abnormal, called arrhythmias. During arrhythmias, the heart beats either too fast (called tachycardia) or too slowly (called bradycardia), and/or irregularly. There are many types of arrhythmias, some are harmless, while some cause serious health problems. Ventricular arrhythmias, in particular ventricular fibrillation (VF) are life-threatening. When VF occurs, the heart loses its pumping ability and brain damage may occur within several minutes due to lack of blood supply. Atrial arrhythmias are less fatal, but atrial fibrillation increases the risk of stroke, and affects a large portion of the aging population, which is becoming a major healthcare issue [13, 14].

Ventricular arrhythmias usually occur suddenly and unexpectedly, in which the electrical activity in the ventricles becomes fast and frenzied, and the coordinated contraction of the heart is either weakened or lost. When arrhythmias occur, distinct changes occur in ECG. Figure 2 shows the ECG from a patient who suffered a life-threatening cardiac arrhythmia [15], which underwent three distinct transitions. At the first transition, the sinus rhythm suddenly changed to a fast abnormal rhythm, called ventricular tachycardia (VT). After several beats, the abnormal but relatively regular ECG became faster, attenuated, and more irregular, which is the transition from VT to VF. Fortunately, several seconds later, VF terminated spontaneously to resume sinus rhythm, which saved the patient's life. In many cases, VT either terminates spontaneously or is sustained without degenerating into VF. VF may spontaneously terminate without leading to SCD as does the one shown in Fig.2, but the majority of VF episodes are lethal unless promptly terminated via electrical defibrillation. Defibrillation is a treatment which delivers a high energy electrical shock to reset the electrical activities in the heart, converting the heart beat back to normal sinus rhythm.

The current treatment of ventricular arrhythmias and SCD has limited effectiveness. Clinical trials have shown that the anti-arrhythmic drugs presently available are not effective in preventing ventricular arrhythmias, and may even cause more deaths than placebo [16, 17]. Implantable cardioverter-defibrillators (ICDs) are so far the most effective therapy in preventing SCD, but they are expensive and limited in availability worldwide. They also can have severe side effects, such as pain, infection risk and inappropriate shocks [18]. Moreover, due to the limited efficacy of risk stratification and the unpredictability of the occurrence of arrhythmias, it is a challenge for clinicians to select patients who may benefit from the ICD therapy. Based on clinical trials [18, 19], 80% of the patients do not benefit from their devices within 5 years after implantation; i.e., only one out of five implanted ICDs actually delivers a life-saving shock.

There are several potential targets for treatment based on arrhythmia dynamics. As shown in Fig.2, arrhythmias occur suddenly and are unpredictable. The ideal strategy is to develop therapeutics that can prevent the occurrence of arrhythmias in high risk patients. An alternative is to prevent the degeneration from VT to VF, since VT is generally less lethal than VF and can give the patient more time to get to the hospital for treatment. The third choice is to develop therapeutics, either drugs or electrical devices such as ICDs, to promptly terminate arrhythmias once they occur. Therefore, understanding the mechanisms of *initiation*, *maintenance*, *transitions*, and *termination* of arrhythmias is of great importance for developing effective therapeutics of SCD.

2.3. Multi-scale regulation of the heart

The limited effectiveness of anti-arrhythmic therapies is largely due to the complexity of the heart and our inability of pinpointing the underlying mechanisms and the right therapeutic targets. The heart, like other organs, is regulated by factors at different scales of time and space. Time spans from milliseconds to years and length scales from nanometers to centimeters, ranging from gene, protein, to cellular and tissue structures (Fig.3). At the molecular scale, genes and proteins form regulatory and signaling networks to regulate ion channel functions, subcellular, cellular, and tissue structures. An ion channel is a complex protein inserted into a biological membrane, and form a pore allowing ions to pass through. A cardiac myocyte contains hundreds of thousands of ion channels, which interact to give rise to the action potential for excitation and intracellular Ca^{2+} signal for contraction. The ion channels open and close stochastically following thermodynamic rules, and thus at the molecular level, the dynamics is dominated by *microscopic* random thermal fluctuations.

The level immediately above single molecules is the organelle scale, such as the sarcoplasmic reticulum (SR), the internal Ca^{2+} stores of the cell, and the mitochondria, the energy factories of the cell. The spatial scale of these organelles ranges from a few hundred nanometers to several micrometers, containing tens to hundreds of ion channels. The dynamics at this scale is *mesoscopic*, characterized by collective behaviors of many random ion channels. For example, a Ca^{2+} spark [20, 21] is a collective behavior arising from a cluster of ion channels in the membrane of SR, called a Ca^{2+} release unit (CRU). Although a Ca^{2+} spark exhibits certain random features, it represents an emergent property of the CRU which behaves very differently from the random openings and closings of a single ion channel. A ventricular myocyte contains thousands of CRUs which form a network coupled by Ca^{2+} diffusion in both the SR and the cytosol. Ca^{2+} waves and oscillations occur due to CRU coupling in this network. At the whole-cell level, complex action potential and Ca^{2+} dynamics emerge via bifurcations and dynamical instabilities, such as APD alternans, limit cycle oscillations, chaos, etc. At the tissue and organ scales, different electrical wave dynamics emerge, which are responsible for normal heart rhythms as well as lethal arrhythmias. At the cellular and tissue scales, the dynamics is dominated by *macroscopic* deterministic behaviors. However, under certain condition, the microscopic thermal fluctuations at the molecular scale may result in macroscopic random fluctuations at the cellular and tissue scales, which may contribute to the unpredictability of arrhythmias and SCD.

Although the normal heart rhythm and arrhythmias are regulated by genes, proteins, subcellular, cellular and tissue scale properties, these factors are also affected by the rhythms of the heart. For example, the contraction of the heart may activate mechanosensitive channels; fast heart rates cause Ca^{2+} accumulation which then affect the excitation and Ca^{2+} cycling dynamics; and long term arrhythmias or fast heart rates cause remodeling in proteins, organelles, cellular and tissue scale properties, such as cardiac hypertrophy. In addition, the heart also interacts with other organs, especially the brain. For example, heart rate and the risk of arrhythmias are affected by circadian rhythms and also by the central nervous system.

3. Nonlinear and stochastic dynamics in the heart

Nonlinear and stochastic dynamics are important research topics in cardiac electrophysiology, which have been widely studied both theoretically and experimentally, as well as in clinical settings. These dynamics include limit cycle oscillations for SAN cells, bifurcations in cellular excitations, symmetry breaking to induce reentry and spiral waves, and pattern formation in excitation propagation in tissue, criticality in Ca^{2+} cycling, fractal variability in heart rates, etc. In this section, we briefly summarize some of these dynamics and their clinical manifestations. We then review in later sections the detailed nonlinear dynamics at different scales of the heart.

3.1. Nonlinear dynamics of heart rhythms and heart rate variability

In normal heart rhythm, the electrical impulses regularly originate from the SAN, resulting in a regular ECG pattern (Fig.4a). van der Pol first proposed to describe the heart as a relaxation oscillator using a model he developed for oscillations observed in electrical vacuum tube circuits [22, 23]. The SAN has since then been modeled as a limit cycle oscillator of voltage, and more recently as coupled voltage and Ca^{2+} oscillators [24]. The SAN may oscillate too slowly (called bradycardia) or too fast (called tachycardia), may pause, or fail to exit the SAN region, clinically known as sinus node dysfunction or sick sinus syndrome. Bifurcation analyses using mathematical models revealed very complex nonlinear dynamics [25–28], some of them can be used to explain the mechanisms of sinus node dysfunction. The nonlinear dynamical responses of a pacemaker cell to periodic stimulations have been extensively investigated by Guevara, Glass, Shrier, and colleagues [29–36] and by others [37–39] in both experimental and theoretical studies.

However, the RR interval in a normal heart is not truly periodic, but shows variation called heart rate variability (HRV). HRV is a normal behavior of the heart, and in certain diseased hearts, such as heart failure, the variability may be diminished (the RR interval becomes more periodic) and the patients have higher risk of SCD. It is shown that the HRV in the normal heart is fractal, and the fractal exponents of the normal heart may differ from those of the diseased hearts [40–42], which may be a better predictor of SCD risk as shown in clinical studies [43, 44]. The dynamical causes of the fractal behaviors are still unknown [45], and future investigations are needed to understand the underlying mechanisms and their links to SCD.

3.2. Alternans

One of the earliest nonlinear dynamical phenomena observed in the human heart dates to 140 years ago when Traube first reported pulsus alternans in a patient in 1872 [46]. Pulsus alternans is a state of a heart in which a strong contraction is followed by a weak contraction, which repeats to form a periodically alternating pattern, i.e. a period-2 behavior. Pulsus alternans is also referred to as mechanical alternans. A half century later, alternans was identified in the electrical system as electrical alternans [47–49]. Electrical alternans can occur as either alternating QRS amplitude, or alternating T-wave amplitude (Fig.4b) which is called as T-wave alternans (TWA). TWA is a widely observed clinical phenomenon and used clinically for risk stratification of cardiac arrhythmias [50, 51]. Since T-wave is a measure of the repolarization in the ventricles, TWA reflects the ECG manifestation of APD alternans. The dynamical mechanism of APD alternans was first investigated by Nolasco and Dahlen [52] in 1968, who used a rigorous analysis method of mathematics to show that when the slope of the APD restitution curve (see Section 6.1.1 for definition) is greater than one, a bifurcation from regular beating (period-1) to alternans (period-2) occurs. Many later experimental and theoretical studies [53–63] have expanded upon and extended this theory to explain more complex action potential dynamics, such as chaos, using the iterated map approach and bifurcation theory of nonlinear dynamics.

As a nonlinear dynamical phenomenon in the heart, alternans ranges from the subcellular, to cellular, and to tissue and organ scales. Theoretical, computational, experimental, and clinical studies have been carried out to investigate the underlying dynamical mechanisms, biological causes, and mechanistic links to arrhythmias and SCD. Alternans can be caused not only by instabilities driven by voltage (e.g., steep APD restitution curve) but also by instabilities from Ca^{2+} cycling. APD alternans and Ca^{2+} alternans can alternate in-phase, or out-of-phase, which can be explained by an instability caused by bi-directional coupling of voltage and Ca^{2+}. Ca^{2+} alternans inside a myocyte can be spatially uniform (in-phase) or out-of-phase, forming spatial patterns at the sub-cellular scale. At the tissue and organ scales, APD alternans and Ca^{2+} alternans can be in-phase or out-of-phase in space, forming spatial patterns in the heart. These patterns have been widely observed in experiments and investigated in theoretical and computational studies, and are considered to mechanistically link TWA to arrhythmogenesis [64, 65]. Moreover, the experimental and modeling studies have shown that the spatial patterns of alternans are formed via spatial mode instabilities, such as the Turing instability, as well as spatial inhomogeneities.

There has been great interest in cardiac alternans because of its role as a precursor of arrhythmias and SCD, such that the occurrence of alternans can be used as a risk stratifier. In addition to its diagnostic potential, preventing alternans has therapeutic potential to prevent arrhythmias, since alternans might be a direct cause of arrhythmias. One of the prevention methods is controlling alternans using control methods of nonlinear dynamics, which has been widely investigated both theoretically and experimentally.

3.3. Regular and irregular premature excitations

In either normal or diseased hearts, extra excitations can occur called premature atrial contractions in the atrium or premature ventricular contractions (PVCs) in the ventricles. A PVC (arrows in Figs.4 c and d) is a beat that occurs earlier than the next coming sinus beat, and therefore, the sinus beat is blocked by the PVC. Many different PVC patterns have been observed clinically. Figure 4c shows an ECG recording in which one PVC follows every two sinus beats, resulting in a periodic temporal pattern called trigeminy by cardiologists. There can be one PVC following every sinus beat (bigeminy), or every three beats (quadrigeminy), and so on. PVCs may occur in an irregular manner (Fig.4d), or in pairs (one sinus beat followed by two PVCs, called couplets), triplets, and so on. PVCs may occur in normal healthy hearts, but their frequency of occurrence increases in diseased hearts. Most of the PVCs are harmless, but some may initiate fatal ventricular arrhythmias, especially in diseased hearts.

The exact causes of PVCs and their complex patterns in the human heart are still poorly understood. Three cellular dynamics have been thought to be responsible: automaticity, early afterdepolarizations (EADs), and delayed afterdepolarizations (DADs). Automaticity means that a cardiac myocyte can beat by itself, just like a SAN cell. EADs are depolarizations in the repolarizing phase of an action potential, while DADs are depolarizations after the myocyte has repolarized from an action potential. EADs and DADs do not occur spontaneously but following a stimulated action potential, and are also called triggered activities. The nonlinear dynamics and bifurcations that lead to EADs and DADs are reviewed in detail later in this article.

3.4. Ventricular arrhythmias and electrical wave dynamics

During ventricular arrhythmias, the electrical activity originates locally in the ventricles. Since the rate of excitation is typically much faster than that of the sinus rhythm, the impulses from the SAN are overdriven by the faster electrical signals from ventricles, altering the QRS complex and ECG morphology (Fig.5). There are many types of ventricular arrhythmias which exhibit distinct ECG patterns. When the ECG pattern is regular and periodic (Fig.5a), it is called monomorphic ventricular tachycardia (VT). When the ECG pattern becomes non-periodic, it is called polymorphic VT or VF. In a widely observed type of polymorphic VT, called Torsade de Pointes, the ECG shows a quasi-periodic behavior (Fig.5b). In other types of polymorphic VT, the ECG patterns are more irregular (Fig.5c), which could be dynamical chaos. During VF (Fig.5d), the heart rate is even faster and the ECG pattern becomes attenuated, irregular, and most likely chaotic. VF is lethal, during which the ventricles quiver and are not able to pump owing to the frenziedly chaotic electrical activities.

An ECG recording is a reflection of the electrical wave dynamics in the heart. There are three types of characteristic waves that can occur in the heart. The first one is called target wave (Fig.6a), in which the electrical impulses generating from a focal source propagate in all directions. The normal excitations of the heart are target waves originating from the SAN. Focal sources can also form locally in atrial or ventricular tissue, which may cause atrial or ventricular arrhythmias in diseased hearts. For example, a PVC is a focal excitation from the Purkinje fiber or the ventricles.

The second type of wave is an electrical wave circulating repetitively around an obstacle (Fig.6b) or along a special pathway. This type of wave is called reentry, or more specifically, anatomical reentry. The concept of reentry as a mechanism of arrhythmias was first hypothesized in 1887 by McWilliam [66], and was demonstrated experimentally by Mines in dog hearts 100 years ago [67, 68]. Wiener and Rosenbluth [69] in 1946 developed the first cellular automation model to show that reentry could occur around an obstacle in an excitable medium, which is applicable to reentry in cardiac tissue. In the normal heart, especially in the atrium, there are many such types of structures and pathways. For example, the tricuspid valve in the atrium gives rise to such a structure in atrium and facilitates atrial arrhythmias. In the ventricles, the most relevant structures are regions of ischemia and infarction, where myocytes die due to lack of blood supply, and scars form in the ventricles. The scars are obstacles that can facilitate reentry in ischemic heart diseases.

The third type of wave is spiral wave (Fig.6c), also called functional reentry. Spiral waves are a generic behavior of excitable media [70], which can form in a completely homogeneous system. Spiral waves were demonstrated by Suzuki et al [71] in 1963 and by Zhabotinsky [72] in the well-known Belousov-Zhabotinsky reaction in 1970, published in English in 1973. Winfree [70] also demonstrated spiral waves in experiments of the Belousov-Zhabotinsky reaction published in 1972. Winfree [3, 73–75] was the first to introduce spiral wave dynamics to the western scientific community, which he applied to the genesis and termination of cardiac arrhythmias. He also put forth the concept of phase singularity, which is the rotation center of a spiral wave. Phase singularity analysis is now routinely used in optical mapping experiments as an identification of spiral waves in the heart [76–78]. Reentry without the presence of an obstacle was first demonstrated in the heart in 1977 by Allessie et al [79] in rabbit atrial muscle. Reentry without an obstacle was also demonstrated in other studies a decade later [80, 81]. With the advances in optical mapping, Davidenko et al [82–84] showed direct evidence of spiral waves in the heart in early 1990's, and now spiral wave as a mechanism of arrhythmias is widely accepted. Figure 7 shows a spiral wave recorded from a cultured neonatal rat ventricular myocyte monolayer and one from the epicardial surface of a rabbit heart [85]. Note that the heart is a three-dimensional (3D) object, spiral waves seen in experiments are scroll waves as seen in 3D excitable media, and more complex vortex structures can occur in 3D excitable media [86, 87].

The basic properties of spiral waves in two-dimensional (2D) media and their 3D counterparts, scroll waves, were widely investigated in early studies by Winfree, Keener, and many others [86–91]. A spiral wave can be either stable or unstable, and instabilities that lead to spiral wave meandering and drifting [92–94] and spiral and scroll wave breakup [95–97] have been shown in FitzHugh-Nagumo (FHN) type models. The same dynamics have also been demonstrated in cardiac tissue models [98–104], which are linked to different types of cardiac arrhythmias [105–107]. For example, a stable spiral wave gives rise to monomorphic VT (Fig.5a) when it occurs in the ventricles, and atrial flutter when it occurs in the atrium. A quasi-periodically meandering spiral wave gives rise to the quasi-periodic ECG morphology of Torsade de Pointes (Fig.3b). A chaotically meandering spiral wave gives rise to an irregular ECG pattern for polymorphic VT (Fig.3c). Spiral wave breakup, in which spiral waves continuously disappear and are reborn in a chaotic manner, is one of the mechanisms of VF.

3.5. Nonlinear dynamics at sub-cellular scales

Besides electrical excitation and wave conduction dynamics at the cellular and tissue scales, dynamics at the sub-cellular scale has also been widely studied, particularly intracellular Ca^{2+} cycling dynamics, such as Ca^{2+} sparks and Ca^{2+} waves. During normal excitation in ventricular myocytes, Ca^{2+} elevates synchronously inside the myocytes during depolarization (Fig.8a), which is trigged by Ca^{2+} entering the cell from the extracellular space. Under stressed or diseased conditions, spontaneous Ca^{2+} waves, either target or spiral waves (Figs.8 b and c), can occur, similar to the electrical waves in tissue. Since Ca^{2+} is coupled with voltage via Ca^{2+}-dependent ionic currents, these sub-cellular Ca^{2+} wave dynamics can cause action potential dynamics, such as EADs and DADs [108]. In SAN cells, spontaneous Ca^{2+} releases occur in normal heart rhythms. A key question is how Ca^{2+} sparks organize to form Ca^{2+} waves, which is a widely studied topic in cardiac myocytes as well as in other cell types [109, 110]. In a recent study, Nivala et al [111] showed that this transition is similar to a second-order phase transition in which criticality occurs. Criticality was also shown to occur in the mitochondrial network in the transition to mitochondrial oscillations in cardiac myocytes [112, 113]. Criticality may have important applications in normal heart rhythms and arrhythmias, which may link the microscopic molecular fluctuations at the sub-cellular scale to the macroscopic random appearance of excitations at the tissue scale, such as HRV, irregular PVCs, and unexpected occurrence of arrhythmias. However, future studies are needed to investigate such mechanistic links, which may provide the mechanism for the sudden occurrence and unpredictability of cardiac arrhythmias. A challenge in computer modeling is that it is computationally non-trivial to include the stochastic fluctuations of the single ion channels and the sub-cellular dynamics in tissue and organ scale models, multi-scale modeling approaches need to be developed to mechanistically link the microscopic molecular fluctuations to the macroscopic random cardiac events.

3.6. Transitions in the heart

As summarized above, the heart can exhibit many complex excitation and conduction dynamics, and the transitions between these dynamics are responsible for the transitions from normal heart rhythm to arrhythmias and between different types of arrhythmias, such as the transitions shown in Fig.2. The dynamical mechanisms for these transitions can be categorized as follows:

1. *Bifurcations via dynamical instabilities*. Bifurcations due to instabilities are responsible for many behaviors observed in the heart. For example, TWA can result from instabilities that cause APD alternans or Ca^{2+} alternans via period-doubling bifurcations. The transition from monomorphic VT to polymorphic VT can be caused by a Hopf bifurcation that causes the transition from a stable spiral wave to a meandering spiral wave. PVCs resulting from EADs can be caused by a dual Hopf-homoclinic bifurcation. Limit cycle oscillations originating via different bifurcations are responsible for oscillations of the SAN cells and automaticity in atrial and ventricular myocytes. Spatial mode instabilities have been shown to cause pattern formation in cardiac tissue, such as spatially discordant APD alternans, quasi-periodicity in reentry, and spiral wave breakup. Pattern formation via spatial mode instability can also occur inside a single cell, such as Turing instability-induced spatially discordant Ca^{2+} alternans.

2. *Thermodynamic phase transitions and criticality*. A myocyte contains thousands of ion channels which open and close randomly. The conformational motions of the ion channel proteins and ion flow through them follow thermodynamic laws (indeed the action potential dynamics in the heart is temperature sensitive) and thus thermodynamic phase transitions can occur. For example, a second-order phase transition and criticality may be responsible for the organization of random Ca^{2+} sparks into oscillations underlying the Ca^{2+} clock for the SAN cells and DADs in atrial and ventricular cells. Since DADs occur randomly in cells, the formation of a PVC from DADs in tissue can also be governed by similar dynamics of thermodynamic phase transitions.

3. *Transitions between multiple solutions*. Cardiac tissue can have multiple solutions and the transitions between these solutions underlie transitions of behaviors of the heart. For example, since both planar wave and spiral wave are solutions of an excitable medium, the transition from sinus rhythm (planar wave conduction) to VT/VF (spiral wave conduction) is a transition between the basins of attraction of the two different solutions. On the other hand, defibrillation is a reverse transition, i.e., it converts VT/VF into sinus rhythm by changing from one solution (arrhythmias) to the other (sinus rhythm) of the heart.

4. *Synchronization*. Synchronization of coupled oscillators is important as a dynamical process in the heart. For example, synchronization in SAN is key for the formation of electrical impulses for normal heart beating. Failure of

synchronization of chaotic cellular action potential dynamics in the ventricles can lead to complex spatiotemporal conduction patterns for initiation and maintenance of arrhythmias [6].

5. *Wave competition or entrainment*. Wave competition or entrainment is a generic dynamics of excitable media which is widely present in the heart. In an excitable medium with multiple origins of excitation waves (either target or spiral waves), waves with slower oscillation frequencies will always be taken over by the faster waves, and eventually, the whole medium will be entrained by the fastest wave frequency [114], as long as the medium is not so heterogeneous as to cause conduction block protecting the slower wave frequencies [115]. For example, the formation of the leading pacemaking site in the SAN region or pacemaker sites for Ca^{2+} waves and oscillations inside a cell is a consequence of wave entrainment. Under normal conditions, the heart beats are initiated from the SAN region, and the slower oscillations in the AVN are suppressed by the impulses from the SAN. But when SAN beats too slowly or stops, oscillations in the AVN will emerge and the AVN substitutes for the SAN as the pacemaker of the heart. Anti-tachycardia pacing [116], which is a clinically used therapy for treatment of slow VT, is a method that uses stimulated waves at faster frequencies than the frequencies of the electrical waves of the arrhythmia to entrain the heart. When the pacing is then terminated, the slow VT also often terminates.

6. *Dynamical transients*. Dynamical transients are also important in the heart. For example, a sudden change in heart rate can induce transient alternans, which may also be arrhythmogenic. Some arrhythmias, even VF on occasion (e.g. Fig.2), can terminate spontaneously. Spontaneous termination may be due to inherently transient dynamics, such as transient spatiotemporal chaos [117], and arrhythmias also induce systematic responses (e.g. autonomic tone) that directly change the parameter settings of the heart.

4. Biophysics of excitable cells and mathematical modeling of the heart

In this section, we review some of the basic biophysical properties of excitable cells and mathematical modeling of cardiac dynamics at different scales. The biophysical theories and the mathematical models have been essential for understanding the nonlinear and stochastic dynamics in the heart. Specifically, we first describe the electrical circuit theory of excitable cells, the development of the first action potential model by Hodgkin and Huxley, i.e., the Hodgkin-Huxley (HH) model, and its simplified version, the FHN model. We then introduce the cardiac action potential, excitation-contraction coupling, and action potential models, and summarize the mathematical and computational approaches used in modeling the dynamics in the heart at single ion channel, sub-cellular, cellular, tissue and organ scales.

4.1. Electrical circuit theory of excitable cells

4.1.1. The Nernst potential—Cell membranes are composed of lipid bilayers which are permeable to certain ions. If the ion concentrations are different inside (c_i) and outside (c_o) of a cell, an electrical potential will develop, called the Nernst potential. The Nernst potential can be derived using the Boltzman equation as follows. At thermodynamic equilibrium, the probability of finding a positively charged ion inside the cell is: $p_i=\frac{1}{Z}e^{-e\phi_i/kT}$, and outside the cell is $p_o=\frac{1}{Z}e^{-e\phi_o/kT}$, where k is the Boltzman constant, T is temperature, and φ_i and φ_o are the potentials inside and outside of the cell, respectively. On the other hand, the probability of finding an ion is proportional to its concentration, and thus

$$\frac{c_i}{c_o}=\frac{p_i}{p_o}=\frac{e^{-e\phi_i/kT}}{e^{-e\phi_o/kT}} \quad (1)$$

which leads to

$$E=\phi_i-\phi_o=-\frac{kT}{e}\ln\frac{c_i}{c_o}=-\frac{RT}{F}\ln\frac{c_i}{c_o} \quad (2)$$

Eq.2 is the Nernst equation and E is called the Nernst potential. For ions of charge z, the Nernst equation becomes:

$$E=-\frac{RT}{zF}\ln\frac{c_i}{c_o} \quad (3)$$

In cardiac myocytes (Fig.9), the intracellular potassium ion (K^+) concentration ($[K^+]_i$) is around 140 mM and the extracellular K^+ concentration ($[K^+]_o$) is around 4 mM, resulting in a Nernst potential of $E_K \approx -95$ mV at 37°C. During an action potential (the membrane voltage varies roughly from −80 mV to +50 mV), K^+ channels open, and the K^+ ions leave the cell due to a higher intracellular K^+ concentration, generating an *outward* current. For the sodium ion (Na^+), $[Na^+]_i \approx 10$ mM, $[Na^+]_o \approx 145$ mM, and, $E_{Na} \approx 70$ mV. When the Na^+ channels open, the higher extracellular Na^+ concentration causes Na^+ to enter into the cell, resulting in an *inward* current. For the calcium ion (Ca^{2+}), $[Ca^{2+}]_i \approx 0.1$ μ M, $[Ca^{2+}]_o \approx 1.5$ mM, and $E_{Ca} \approx 128$ mV. Like the Na^+ current, the Ca^{2+} current is also an inward current due to the high positive Nernst potential. The ion gradients are maintained in cardiac myocytes by ion pumps, such as Na^+-K^+ pump and Na^+-Ca^{2+} exchanger (NCX). The Na^+-K^+ pump transports two K^+ ions into the cell in exchange for three Na^+ ions out of the cell. The NCX pumps one Ca^{2+} ion out and three Na^+ ions in. The ionic gradients are required to maintain the cell electrically polarized and thus to make it to be excitable. For ventricular myocytes, the resting potential is around −80 mV. Since the Na^+ and Ca^{2+} channels are almost completely closed at very negative potentials, the resting potential is mainly determined by the Nernst potential of the K^+ channels, but is always more positive than E_K due to the limited permeability to other ions.

4.1.2. The Hodgkin-Huxley model—A mechanistic understanding of the action potential of excitable cells was not available until Hodgkin and Huxley developed the first action potential model of squid giant axon based on their experimental measurements, published in 1952 [118]. This work not only provides a fundamental understanding of action potentials in excitable cells, but also is key to the discovery of ion channels [119], and is the foundation of modern computational electrophysiology, for which Hodgkin and Huxley were awarded the Noble prize in Physiology and Medicine in 1963.

The basic approach in the HH model is to consider the excitation and propagation of action potentials using simple electrical circuits, in which the cell membrane is modeled as a capacitor and the ion channels as variable conductors (Fig.10a). Denoting the current through the capacitor as I_C and the current through the conductors as I_{ion}, and using the Kirchoff's current law, one has,

$$I_c+I_{ion}=0 \quad (4)$$

Using the relation between charge (Q), capacitance (C_m), and voltage (V), i.e., $Q = C_mV$, one obtains

$$I_c=\frac{dQ}{dt}=C_m\frac{dV}{dt} \quad (5)$$

Inserting Eq.5 into Eq.4, one has,

$$C_m\frac{dV}{dt}=-I_{ion} \quad (6)$$

In the presence of external stimulation, a stimulation current (I_{sti}), which can be a constant, a time-dependent function, or a single short pulse, is then added to the right side of Eq.6, which leads to

$$C_m\frac{dV}{dt}=-(I_{ion}+I_{sti}) \quad (7)$$

Eq.7 is the fundamental equation in electrophysiology. Hodgkin and Huxley, in a series of elegant experimental studies in the squid giant axon, identified a Na^+ current (I_{Na}), a K^+ current (I_K), and a "leak" current (I_L, now known to be chloride-mediated). The electrical circuit representation of the giant axon is shown in the right panel of Fig.10a. The ionic currents are mathematically formulated based on the Ohm's law, i.e., $I_{Na} = g_{Na}(V - E_{Na})$, $I_K = g_K(V - E_K)$, and $I_L = g_L(V - E_L)$. The total ionic current is:

$$I_{ion}=I_{Na}+I_K+I_L=g_{Na}(V-E_{Na})+g_K(V-E_K)+g_L(V-E_L), \quad (8)$$

in which g_{Na} and g_K are variable conductance depending on V, and g_L is a small constant.

The next step is to determine g_{Na} and g_K. Figure 10b shows the original voltage camp experimental data of g_K in which V was first depolarized by 25 mV from the resting potential and then repolarized back to the resting potential after a certain time period. Hodgkin and Huxley found that the decay of the conductance g_K after repolarization could be reasonably well fit by an exponential decay, i.e., $e^{-t/\tau}$, but the rise after depolarization could not be well fit by $1- e^{-t/\tau}$ as in a linear system, but could be reasonably well fit by $(1-e^{-t/\tau})^4$. This observation led them to formulate g_K as

$$g_K = \bar{g}_K n^4 \quad (9)$$

and n is described by

$$\frac{dn}{dt} = \alpha_n(1-n) - \beta_n n \quad (10)$$

where $\bar{g}_K$ is the maximum conductance, α_n and β_n are the rate constants which are functions of voltage. n is now called a gating variable. A widely used alternative form of Eq.10 is

$$\frac{dn}{dt} = (n_\infty - n)/\tau_n \quad (11)$$

where $n_\infty = \frac{\alpha_n}{\alpha_n+\beta_n}$ is the steady state of n at a constant V and $\tau_n = \frac{1}{\alpha_n+\beta_n}$ the corresponding time constant. Under a constant voltage V, the solution of Eq. 11 is

$$n(t) = n_\infty(V) - [n_\infty(V) - n_0]e^{-t/\tau_n(V)} \quad (12)$$

where n_0 is the value of n at t=0. Assuming that at the resting potential, the open probability of the channel is zero, i.e., $n_\infty(V_{rest}) = 0$, and at a holding potential higher than the resting potential, the open probability of the channel is non-zero, i.e., $n_\infty(V_{hold}) \neq 0$. When the voltage is switched from the resting potential to the holding potential, $n_0 = n_\infty(V_{rest}) = 0$, Eq.12 becomes $n(t) = n_\infty(V_{hold}) - n_\infty(V_{hold})e^{-t/\tau_n(V_{hold})}$, and thus $g_K = \bar{g}_K n^4 = \bar{g}_K[n_\infty(V_{hold})]^4[1-e^{-t/\tau_n(V_{hold})}]^4$. When the voltage is switched from the holding potential to the resting potential, $n_0 = n_\infty(V_{hold})$, Eq.12 becomes $n(t) = n_\infty(V_{hold})e^{-t/\tau_n(V_{rest})}$, and thus $g_K = [n_\infty(V_{hold})]^4 e^{-4t/\tau_n(V_{rest})}$ which decays exponentially. These solutions agree with Hodgkin and Huxley's observation of their experimental data.

n_∞ can be determined from experimental data using Eq.9 as $n_\infty = \left(\frac{g_{K\infty}}{\bar{g}_K}\right)^{1/4}$, where $g_{K\infty}$ is the steady-state conductance at the holding voltage. τ_n can be determined by inserting Eq.12 into Eq.9 and fit the g_K with the experimental data. After obtaining n_∞ and τ_n, one can then obtain α_n and β_n. By depolarizing the voltage to different values, one obtains the voltage dependence of α_n and β_n. Note that n_∞ is a sigmoidal function increasing with V (Fig.10c), indicating that more K^+ channels open at higher voltages.

The behavior of I_{Na} is more complicated. Depolarizing from the resting potential to another holding voltage, I_{Na} increases first but then decreases back to its initial value. To account for this behavior, Hodgkin and Huxley formulated g_{Na} as:

$$g_{Na} = \bar{g}_{Na} m^3 h \quad (13)$$

where $\bar{g}_{Na}$ is the maximum conductance. m is the activation gating variable and h is the inactivation gating variable, which are described by

$$\frac{dm}{dt}=(m_\infty - m)/\tau_m \quad (14)$$

and

$$\frac{dh}{dt}=(h_\infty - h)/\tau_h \quad (15)$$

where m_∞, τ_m, h_∞, and τ_h are functions of voltage (Fig.10c), and can be fit from experimental data [118]. m_∞ is an ascending sigmoidal function of V which causes the Na$^+$ channel to open, while h_∞ is a descending sigmoidal function of V which causes the Na$^+$ channel to close. Note that $\tau_m << \tau_h$, which allows the Na$^+$ channel to be sufficiently activated before it is inactivated.

The resting potential of the squid giant axon is around −70 mV (note that the resting potential in the original HH model was set around zero). If a stimulus elevates the voltage to about −60 mV, the Na$^+$ channels start to open (see the m_∞ curve in Fig.10c), which causes the voltage to depolarize since E_{Na} is around +50 mV. As voltage depolarizes, more Na$^+$ channels open, forming a positive feedback loop between Na$^+$ channel opening and voltage. This positive feedback finally shuts off due to inactivation of the channel (h_∞ decreases with voltage). On the other hand, as voltage elevates, more K$^+$ channels open (n_∞ increases with voltage), and opening of the K$^+$ channels tends to bring the voltage back to the resting potential since E_K is lower than −70 mV, forming a negative feedback loop between K$^+$ current and voltage. Since the K$^+$ channel activates much more slowly than the Na$^+$ channel, i.e., $\tau_n >> \tau_m$ (Fig.10c), the voltage quickly increases to above zero as the Na$^+$ channel activates, and then with a time delay, the K$^+$ channel activates, bringing the voltage back to the resting potential. The competition and time delay between the two types of ion channels give rise to an action potential. Figure 10d shows an action potential of the HH model, which agrees well with experimental recordings from squid giant axons [118]. Note that the presence of positive and negative feedback loops in this system is not only necessary for the genesis of an action potential, but also offers a rich spectrum of nonlinear dynamics, including excitable, oscillatory, and bistable behaviors.

Although the HH model was developed to describe the excitation and conduction in squid giant axons, its impact on electrophysiology, mathematical modeling in biology and nonlinear dynamics have been seminal. It represents the first quantitative description of action potential in nerve cells; has played a pivotal role in developing the concept of ion channels leading to the discovery of ion channels with the patch clamp technique (awarded a Nobel prize in 1991) and the molecular structure of the K$^+$ channel (award a Nobel prize in 2003); has opened a whole research field of quantitative electrophysiology; and has played a fundamental role in the theoretical and computational study of spiral wave and scroll wave dynamics. The HH model is still widely used in computational studies, not only for neural dynamics, but also for generic dynamics of excitable media.

4.1.3. The FitzHugh-Nagumo model—The HH model is strongly nonlinear and its solution can be only obtained by numerical simulations. Although not an issue for modern computers, it was nontrivial at the time of Hodgkin and Huxley (who used a mechanical calculator, Brunsviga, to numerically solve the differential equations to obtain the action potentials of the model [120]). Richard FitzHugh [121, 122] developed an analog computer to study impulse propagation, which led him to simplify the HH model to a simpler one by modifying the van der Pol model. This model turned out to be similar to the model used by Nagumo et al [123] to study nerve conduction, which became the now famous FHN model.

The van der Pol model is a second-order differnetial eqaution [22]:

$$\frac{d^2u}{dt^2}-\varepsilon(1-u^2)\frac{du}{dt}+u=0. \qquad (16)$$

Using a second variable, $v=u-\frac{1}{3}u^3-\frac{1}{\varepsilon}\frac{du}{dt}$, one can transform Eq.16 into two first-order differential equations as

$$\frac{du}{dt}=\varepsilon(u-\frac{1}{3}u^3-v)\ \frac{dv}{dt}=\frac{u}{\varepsilon} \qquad (17)$$

For $\varepsilon>0$, the fixed point ($u=v=0$) of the van der Pol model is always unstable and a limit cycle oscillator exists. To model the excitable system, which has one stable fixed point, FitzHugh [121] modified the second equation in Eq.16 and obtained the following equations:

$$\frac{du}{dt}=\varepsilon(u-\frac{1}{3}u^3-v)\ \frac{dv}{dt}=u-\beta v+a \qquad (18)$$

Eq.18 is the widely known FHN model. The nullclines of the FHN model (Fig.11) are similar to those of the HH model [124], and thus the FHN model can well capture the general dynamics of the HH model.

The steady states or fixed points of Eq.18 are determined by the intersections of the two nullclines (Fig.11). The stabilities of the fixed points are determined by the eigenvalues of the Jacobian:

$$J=\begin{pmatrix} \varepsilon f_u' & -\varepsilon \\ 1 & -\beta \end{pmatrix} \qquad (19)$$

The fixed point is stable when both the trace (τ) of matrix J is smaller than zero, i.e., $\tau = \varepsilon f_u'-\beta < 0$ and the determinant (Δ) is greater than zero, i.e., $\Delta = \varepsilon(1 - \beta f_u') > 0$, which occurs only when f_u' is small or negative. When there is only one stable fixed point, the system is excitable (Fig.11a), and when there are two stable fixed points, the system is bistable (Fig. 11c). The fixed point may become unstable when f_u' is positively large which can only occur in the middle segment of the N-shaped nullcline (Fig.11b). In this case, a limit cycle occurs, resulting in oscillations.

The FHN model played a key role in studying wave propagation dynamics in excitable media. It exhibits the generic dynamic features of an excitable cell and thus makes possible the dynamical understanding of excitable media; it allowed large-scale computer simulation possible at a time when the computer power was still limited; and it has made analytical treatment possible in many theoretical studies.

4.2. The cardiac action potential and modeling

4.2.1. The cardiac action potential and excitation-contraction coupling— Different from the action potentials in nerves, the duration of a cardiac action potential is much longer, typically lasting several hundred milliseconds. Figure 12a shows a typical action potential of a ventricular myocyte, which is traditionally divided into five phases, i.e., phase 0 to phase 4. Phase 0 is the upstroke of the action potential which is caused by the activation of voltage-dependent Na^+ channels. Phase 1 is the early repolarization phase in which the Na^+ channels rapidly inactivates, and the transient outward K^+ channels causes the voltage to decrease, after which they in turn inactivate. Phase 2 is the plateau phase, in which L-type of Ca^{2+} channels (LCCs) are activated to oppose the K^+ currents and maintain the action potential plateau. Phase 3 is the late repolarization phase in which the voltage quickly returns to the resting potential as inward rectifier K^+ channels reopen. Phase 4 is the resting potential, which is around −80 mV for ventricular myocytes. During a cardiac action potential, many different types (or sub-types) of ion channels are activated [125], which play different roles in action potential morphology and dynamics. Figure 12b shows a schematic diagram of ionic currents and intracellular Ca^{2+} cycling in a ventricular myocyte action potential model developed by Zeng et al [126].

The function of the heart is to pump blood to the whole body, which is achieved via the rhythmic contraction of the ventricles in response to elevated intracellular Ca^{2+}. During an action potential, the intracellular Ca^{2+} concentration increases and eventually decreases back to the resting state afterwards (Fig.12a). The increase of Ca^{2+} concentration is caused by opening of LCCs permitting Ca^{2+} entry from the extracellular space, which triggers additional Ca^{2+} release from internal Ca^{2+} stores located in the sarcoplasmic reticulum (SR). The SR Ca^{2+} release is the major component of Ca^{2+} elevation in mammalian cardiac myocytes. The Ca^{2+} brought in via LCCs is later pumped out by NCX, maintaining the balance of Ca^{2+} in the cells. The elevated Ca^{2+} increases the binding of Ca^{2+} to the contractile proteins and results in cell shortening, which generates the mechanical force for contraction of the heart. In addition to regulating contraction, Ca^{2+} is also a major signaling molecule which directly and indirectly regulates a number of ionic currents, and thus affects the properties of the action potential. Therefore, intracellular Ca^{2+} follows the change of voltage, but Ca^{2+} also affects voltage, forming feedback loops between voltage and Ca^{2+}. In other words, voltage and Ca^{2+} are bi-directionally coupled.

4.2.2. Action potential models—The action potentials of cardiac myocytes have been mathematically modeled following the same modeling strategy of the HH model. The governing equation for voltage is Eq.7 with the total ionic current, I_{ion}, being the summation of many different types of cardiac ionic currents (see Fig.12b), i.e.,

$$I_{ion}=I_{Na}+I_{Ca,L}+I_{Ks}+I_{Kr}+I_{K1}+I_{NCX}+I_{NaK}+\dots \quad (20)$$

In most of the action potential models, the ionic currents and gating variables are formulated following the same method as in the HH model.

The first cardiac action potential model was developed in 1962 by Denis Noble [127] who modified the HH model by adding the inward K^+ rectifier, I_{K1}, and slowing the time-dependent K^+ current (I_K) to simulate the action potential of Purkinje cells. Over the past 50 years, the cardiac action potential models have become much more detailed and quantitative, representing a variety of cell types (e.g., SAN cell [128], Purkinje fiber [127], atrial myocyte [129], and ventricular myocyte [130]) from different species (e.g., mouse [131], rat [132], guinea pig [133], rabbit [134], dog [135], and human [136]). There have been over 100 cardiac action potential models developed [137], most of them are available at CellML (http://models.cellml.org/cellml). The models can be classified by their generation. The first generation models only include a limited number of ionic currents, including Na^+ current, Ca^{2+} current, and K^+ current. The representative examples are the Beeler-Reuter model [130] and the phase I of Luo-Rudy (LR1) model [133]. The Na^+ and K^+ concentrations are fixed parameters in these models. Ca^{2+} concentration is simply regulated by Ca^{2+} current and intracellular Ca^{2+} cycling dynamics is not modeled. The models are typically described by less than 10 differential equations. The second generation models include the regulation of the intracellular Na^+ and K^+ concentrations as well as intracellular Ca^{2+} cycling dynamics. The 1994 Luo-Rudy model [138] can be considered as the prototype of this generation, even though earlier models from Noble’s group had taken into account intracellular Ca^{2+} cycling dynamics [139]. The ionic currents in the second generation models are much more detailed than those in the first generation models. These models usually contains 10 to 20 ionic currents, and are described by 20 to 40 ordinary differential equations with a large number of parameters and complex equations. Some models use Markov transitions to simulate single channel opening and closing and may contain hundreds or thousands of randomly simulated channels [140]. Models also have been developed to include biological signaling [141, 142]. The third generation models [143], which are still in the developmental stage, include spatiotemporal Ca^{2+} cycling dynamics as well as sarcolemma ion channel distributions (as described later). In this type of modeling, the myocyte is no longer considered as a point but a spatially extended entity, which can be used to simulate the spatiotemporal Ca^{2+} cycling dynamics and the corresponding excitation-contraction coupling dynamics of the myocytes. An intermediate phase of this generation of model was developed by Winslow’s group [144], the so-called common pool models, in which the Ca^{2+} cycling system includes thousands of CRUs and the RyRs and LCCs are described by Markov transitions and simulated stochastically.

Several precautions should be mentioned regarding action potential models. 1) In most cases, it is not possible to reproduce or code the model into a computer program from the original publication due to typographical errors in parameters values, units, and even equations. A request of the source code from the original authors is usually needed. CellML is a good resource for recovering a correct model. 2) Since most of the models were fit to one set of experimental data and/or at a certain pacing cycle length (PCL), the robustness and parameter sensitivity have not been well-tested. One needs to be cautious when extending these models to make predictions under different conditions other than those originally simulated, especially for quantitative predictions. For example, a study by Cooper et al [145] shows that the action potential models of the same species from different groups exhibit very different behaviors, such as very different APD restitution properties. 3) The first and second generation models are lowdimensional models developed phenomenologically based on whole-cell data. These models treat the cell as an entity with one or a few compartments. However, a cell is a spatially-extended entity with thousands of sub-compartments. How to, or under what conditions, one is justified in representing a spatially-extended system by a low-dimensional model does not have a clear answer. The mean-field method from statistical physics is a useful theoretical tool for treating systems composed of a large number of random elements, but can only be used when a system is away from criticality. For example, in a recent study [111], we show that the transition from Ca^{2+} sparks to Ca^{2+} wave is a second-order phase transition in which criticality occurs. How to represent the Ca^{2+} transient using a low-dimensional model when Ca^{2+} waves are present is an open question [146]. 4) Some of the models may be very sensitive to initial conditions and parameter changes, and some may require very small time steps for numerical integration to avoid numerical errors. 5) From a physiological perspective, a model with more physiological details is better at relating dynamical features to specific molecular properties. However, due to limited fitting processes in developing these models, a more detailed model is not necessarily better at illuminating the mechanisms underlying the dynamical features. Simple lower dimensional models which capture the essential physiological details phenomenologically are often superior for this purpose, and are computationally much less demanding. Therefore, depending on the purpose of research, one may choose to combine models with different levels of complexity to explore dynamical mechanisms and relate the dynamics to molecular entities which can be manipulated experimentally.

4.3. Modeling electrical wave conduction in tissue and organ

Cardiac cells are coupled via gap junctions (Fig.13a) so that the action potential can conduct from one cell to the next. Gap junctions are a type of ion channels which allow ions to pass from one cell to the other. When one cell's membrane potential is higher than its coupled neighbors, ions pass through the gap junctions according to Ohm's law to elevate the membrane potentials of the neighboring cells, and vice versa.

In computer modeling, one can couple the neighboring cells via gap junction conductance to form a tissue model. For example, for a one-dimensional (1D) chain of cells as in Fig.13b, the governing differential equation for voltage of the i^{th} cell in the chain is:

$$C_m(i)\frac{dV(i)}{dt}=-I_{ion}(i)+g_j[V(i-1)+V)(i+1)-2V(i)] \quad (21)$$

in which C_m is the capacitance of a single cell (around 100 pF for a ventricular myocyte), I_{ion} is the single cell current instead of the current density, and g_j is the gap junction conductance between two cells, which is about 600 nS for well coupled ventricular myocytes, either side-to-side or end-to-end [147]. Similarly, for a 2D array of coupled cells, the equation for the $(i,j)^{th}$ cell in the array is:

$$C_m(i,j)\frac{dV(i,j)}{dt}=-I_{ion}(i)+g_j[V(i-1,j)+V(i+1,j)-2V(i,j)]+g_j[V(i,j-1)+V(i,j+1)-2V(i,j)] \quad (22)$$

However, in normal ventricular tissue, a myocyte has on average 11 neighboring myocytes; this number is reduced to about 6 in ischemic tissue [148]. Therefore, a regular array in which a cell has 4 neighbors in 2D or 6 neighbors in 3D may not be an ideal model for cardiac conduction. As shown by Hubbard et al [149], different arrangements of cells in space can give rise to different conduction speeds. For an irregularly distributed cell network, the equation becomes

$$C_m(i)\frac{dV(i)}{dt}=-I_{ion}(i)+\sum_{k=1}^{N}g_j(k)[V(k)-V(i)] \quad (23)$$

where N is the total number of neighbors and $g_j(k)$ is the gap junction conductance between the i^{th} cell and its k^{th} neighbor, which can be the full gap junction conductance or a portion of it, depending on how the two cells are coupled. Equation 23 can also be used to simulate cardiac tissue composed of different types of cells, such as when myocytes are coupled to fibroblasts in diseased heart tissue [150, 151].

In most of the computer simulation studies, cardiac tissue are treated as a syncytium (i.e., continuous in space) with the voltage described by a partial differential equation, a standard reaction-diffusion equation. For example, for a 2D tissue model, the equation for voltage is

$$\frac{\partial V}{\partial t}=-I_{ion}/C_m+D_x\frac{\partial^2 V}{\partial x^2}+D_y\frac{\partial^2 V}{\partial y^2} \quad (24)$$

where D_x is the diffusion constant in the longitudinal direction and D_y is the diffusion constant in the transverse direction. The diffusion constants are related to the gap junction conductance or resistance as

$$D_x=\frac{1}{C_m\rho_x\chi}\text{and}D_y=\frac{1}{C_m\rho_y\chi} \quad (25)$$

where ρ_x and ρ_y are the resistivities in the longitudinal and transverse directions and χ is surface-to-volume ratio of the myocyte. In cardiac tissue, the membrane capacitance is C_m = 1 μF/cm^2, the longitudinal and transverse resistivities were experimentally [152] measured to be $\rho_x \approx 0.4$ kΩcm and $\rho_y \approx 3.6$ kΩcm, and the surface-to-volume ratio can be set as $\chi \approx$ 2500 cm^{-1} (for a 20 × 20 × 100μ m^3 cell, χ is close to 2000 cm^{-1}). Using these numbers, one obtains the longitudinal diffusion constant as D_x=0.001 cm^2/s and the transverse as D_y=D_x/9. Due to the difference in diffusion constants, CV in the x-direction (θ_x) is different from that in the y-direction (θ_y), which is called anisotropy. The anisotropic ratio, $\theta_x/\theta_y=\sqrt{D_x/D_y}$, varies in different regions of the heart and plays important roles in cardiac arrhythmias [153]. In many computer simulation studies, an isotropic medium has been used, formulated as

$$\frac{\partial V}{\partial t}=-I_{ion}/C_m+D(\frac{\partial^2 V}{\partial x^2}+\frac{\partial^2 V}{\partial y^2}) \quad (26)$$

which is obtained by the transformations $x'=x\sqrt{D_x/D}\text{and}y'=y\sqrt{D_y/D}$. Note that this type of scaling is only truly valid for continuous and electrically homogeneous media. Cardiac tissue is electrically heterogeneous (i.e. I_{ion} is a function of space) and non-continuous (due to finite cell sizes), one needs to be cautious when Eq.26 is used for simulations, especially when the cells are weakly and heterogeneously coupled and/or the tissue is electrically heterogeneous [149].

The real heart is a 3D object with a complex structure in which muscle bundles and sheet structures form and rotate in the ventricles (Fig.13c and d). Due to fiber direction change in space, the diffusion rate also changes in space, and the governing equation for voltage is then

$$\frac{\partial V}{\partial t}=-I_{ion}/C_m+\nabla\cdot\overrightarrow{D}\nabla V \quad (27)$$

where $\vec{D}$ is the diffusion tensor, which can be determined once the local fiber direction is known [103, 104, 154].

The models described above only consider conduction via gap junction, which are called monodomain models. In real cardiac tissue, electrical conduction occurs in both the intracellular and extracellular space in cardiac tissue, and the conductance and anisotropic ratios differ in the two spaces [155]. Due to this difference, under certain conditions, such as strong electrical stimulations (e.g., defibrillation shocks), the electrical behaviors may not be properly described by a monodomain model, such as the virtual electrode and dog-bone excitation patterns [156–158]. Under such conditions, a bidomain model is needed, which is given as [159–161],

$$\chi(C_m\frac{\partial V}{\partial t}+I_{ion})=\nabla\cdot(\overrightarrow{\sigma}_i\nabla V)+\nabla\cdot(\overrightarrow{\sigma}_i\nabla\phi_e)\ \ \nabla\cdot[(\overrightarrow{\sigma}_i+\overrightarrow{\sigma}_e)\nabla\phi_e]=-\nabla\cdot(\overrightarrow{\sigma}_i\nabla V) \quad (28)$$

where $V = \varphi_i - \varphi_e$ is the transmembrane voltage as used in the monodomain models, φ_i and φ_e are intracellular and extracellular potentials, $\vec{\sigma}_i$ and $\vec{\sigma}_e$ are the intracellular and extracellular conductivity tensors, respectively. When the intracellular and extracellular anisotropic ratios are the same, i.e., $\vec{\sigma}_i = \alpha\vec{\sigma}_e$, the bidomain equations can be reduced to a monodomain equation since φ_e is eliminated from Eq.28. Comparison of monodomain and bidomain models on cardiac conduction have shown that the differences are small in the absence of stimulation current [162, 163]. Therefore, a bidomain model is needed when one simulates the effects of strong stimulation, such as defibrillation, but a monodomain model is adequate for simulating cardiac excitation and conduction when no large external stimulations are present. The monodomain model is computationally much faster than the bidomain model.

The heart is an organ with complex fiber structure and boundaries, and thus the extension of tissue modeling to organ modeling is not straightforward even though the governing equations for voltage are still the same as Eqs. 27 or 28. Whole heart modeling was first carried out by Hunter and colleagues [154, 161] who developed a canine ventricle model with the geometry and fiber structure obtained via histology. This model has been widely used for simulations of the mechanics and excitations of the anatomical heart [164]. Whole heart models of other species, such as rabbit [165, 166] and human [167], have also been developed (see a recent review by Trayanova [168] for more details).

Due to the high computational requirements, especially organ scale simulations, advanced computational and numerical methods are needed. One widely used numerical algorithm was first implemented by Rush and Larsen [169] to effectively deal with the stiff change of the gating variables. For example, the gating variable *n* is updated in the computer program as

$$n(t+\Delta t)=n_{\infty}-[n_{\infty}-n(t)]e^{-\Delta t/\tau_n} \quad (29)$$

where Δt is the time step of integration. Another widely used numerical algorithm is operator splitting, which allows adaptive time steps in tissue scale simulations [170, 171]. Computational methods using graphic processer units have also been developed [172], and additional numerical methods of cardiac computation are reviewed by Plank et al [173].

4.4. Stochastic modeling

Stochastic modeling has been a very important component of electrophysiology, especially after the development of patch clamp technology that allows recording of random single channel openings and closings. An ion channel is a complex protein inserted into a biological membrane, and form a pore allowing ions to pass through, which opens and closes stochastically (Fig.14a). Ion channels are typically selective, allowing only specific ion(s) to pass through the pore, such that the ionic current is determined by both voltage gradient and ion concentration gradient across the membrane. The openings of ion channels are not completely random, since they are biased by voltage and other factors. For example, the K^+ channel has four voltage sensors controlling the open probability of the pore, which can open only when all four are in a certain configuration regulated by voltage (Fig.14b).

Stochastic ion channel openings and closings are modeled using Markov transitions. The simplest model is the random transition between an open state and a closed state (Fig.14c), with α and β being the transition rates which can be constants or functions of voltage. However, an ion channel can have many states. For example, the K^+ channel has four voltage sensors which sense the membrane voltage to regulate the channel. The channel opens when its four voltage sensors are in their vertical positions (Fig.14b), but it is closed when anyone of the sensors is in its tilted position. Therefore, there are four close states (C_1 to C_4) and one open state (O). C_1 is the close state in which one voltage sensor is in the tilted position and the other three are in their vertical positions, C_2 is the state in which two voltage sensors are in their tilted positions, and so on. Assuming that the sensors move independently of each other, then if α is the transition rate for a sensor changing from the tilted position to the vertical position and β is the reverse rate, one can then construct a five-state Markov model for the K^+ channel with the corresponding rate constants shown in Fig. 14d. Markov models for various ion channels have been developed for cardiac myocytes as well as other cell types based on patch clamp recordings. Fig.14e is a Markov model of Na^+ channel developed by Clancy and Rudy [140].

With a Markov model, one can carry out simulations to study the stochastic dynamics of a single channel or an ensemble of channels. Assuming that at time t, the channel is in the O state, and that at $t+\Delta t$ the probability that the channel changes from O to C is $\beta\Delta t$, then the probability that the channel remains in the O state is $(1-\beta\Delta t)$. One then randomly selects a number r between 0 and 1 from a uniform random number generator to decide whether the channel remains in the O state or transitions to the C state based on the two probabilities. Specifically, if r falls in $[0, \beta\Delta t]$, the channel changes its state to C, and if r falls in $(\beta\Delta t, 1]$, the channel remains at O. When the channel is in the C state, then the probability that the channel changes from C to O is $\alpha\Delta t$, and the probability that it remains in the C state is then $(1-\alpha\Delta t)$.

To simulate an ensemble of channels using the above method, the computation becomes more burdensome as the channel number N increases, since at each time step N random numbers need to be generated. Another way to simulate an ensemble of ion channels is to use a Markov chain that describes the number of channels in different states. For example, for N channels described by the simple two-state model, one can model the number of channels at the open state by a Markov chain as shown in Fig.14f, and use the same random simulation method to simulate the transitions. One can also write down the Master equation for the scheme in Fig.14f as

$$\frac{dp_n}{dt}=(N-n+1)\alpha p_{n-1}+(n+1)\beta p_{n+1}-[(N-n)\alpha+n\beta]p_n \quad (30)$$

The steady-state solution of Eq.30 is a binomial distribution

$$p_n^{\infty}=\frac{N!}{n!(N-n)!}p^n(1-p)^{N-n} \quad (31)$$

where $p = \alpha/(\alpha + \beta)$ which is the steady state open probability of a single channel.

The accuracy of the simulations in the two methods described above strongly depends on the time step Δt. An exact stochastic simulation method was developed by Gillespie for chemical reactions [174], which can be used to simulate stochastic ion channel openings and closings. For example, for the two-state model in Fig.14c, the simulation can be done as follows. Assume at time t, the channel switches from C to O, and the probability (p) that the channel remains in the O state obeys

$$\frac{dp}{dt}=-\beta p \quad (32)$$

whose solution is $p(t) = e^{-\beta t}$. This process can be exactly simulated by predicting the dwell time of the O state using the following equation:

$$\tau = -(\ln r)/\beta \quad (33)$$

where r is a random number uniformly distributed in (0, 1). Then at time $t+\tau$, the channel switches from the O state to the C state. Once the channel is switched to the C state, then another random number r is generated to determine the dwell time of the C state using $\tau = -(\ln r)/\alpha$, and so on. For an ensemble of ion channels, one can also use this method to perform stochastic simulations using the Markov chain in Fig.14f. Since α and β are usually functions of voltage, which changes with time during an action potential, the algorithm needs to be modified for variable transition rates [143, 175].

Using the Markov model and stochastic simulations, the total ionic current of an ensemble of ion channels is then formulated as

$$I_x = \bar{g}_x N_o (V - E_x) \quad (34)$$

where $\bar{g}_x$ is the single channel conductance, and N_o is the total number of open channels which fluctuates randomly with time.

In many action potential models, ion channels have been modeled using Markov models with deterministic simulations to generate the whole cell current. For example, for the two-state model, if the probability that the ion channel is in the open state is P_o and the probability that the ion channel is in the closed state is P_c, with $P_o + P_c = 1$, then the differential equation for P_o is

$$\frac{dP_o}{dt} = \alpha(1 - P_o) - \beta P_o \quad (35)$$

which is the same equation used by Hodgkin and Huxley to describe the gating variables in the HH model. Similarly, one can write down the Master equations for other states for a multiple-state Markov model and solve the equations jointly to obtain P_o. For an ensemble of N identical ion channels, the total ionic current is then given by

$$I_x = \bar{g}_x N P_o (V - E_x) \quad (36)$$

Since an individual myocyte contains hundreds of thousands of ion channels, stochastic simulation of the individual channels in the whole cell is computationally demanding, let alone tissue and organ scale simulations. Fox [176] developed a Langevin equation for the gating variables of the HH formulation to allow fast stochastic simulations. For example, for the gating variable n of the K$^+$ current, the corresponding Langevin equation is

$$\frac{dn}{dt} = \alpha_n(1 - n) - \beta_n n + \xi_n(t) \quad (37)$$

where $\xi_n(t)$ is a Gaussian noise with $<\xi_n(t)>=0$ and $<\xi_n(t)\xi_n(t')>=\Gamma_n\delta(t-t')$, and the noise strength Γ_n is described by

$$\Gamma_n=\frac{\alpha_n(1-n)+\beta_n n}{N} \quad (38)$$

where N is the total number of channels.

4.5. Sub-cellular modeling

The myocyte is a spatial entity with a complex sub-cellular structure. Figure 15a is a schematic plot illustrating the ultrastructure in a ventricular myocyte, which is composed of a spatially distributed network of organelles including the SR, mitochondria, and myofibrils, and a transverse tubular system to facilitate effective communication between the intracellular and extracellular space. SR is the major Ca^{2+} store inside the cell which exhibits a complex network structure surrounding the myofibrils, called network SR. The regulation of Ca^{2+} cycling in ventricular myocytes is shown schematically in Fig.15b. Ca^{2+} release from the SR is through RyR channels clustered in a distinct region called junctional SR. Normally, a RyR cluster is colocalized with a LCC cluster in the T-tubule membrane, forming a CRU or a couplon. A ventricular myocyte contains thousands of CRUs, estimated between 20,000 and 50,000. Ca^{2+} entry from the voltage gated LCCs activates the RyRs, causing them to open and release Ca^{2+} from the SR. This process is called Ca^{2+}-induced Ca^{2+} release (CICR), and constitutes a positive feedback loop. This collective process results in discretized Ca^{2+} release events called Ca^{2+} sparks [20, 21]. Ca^{2+} entry from the LCCs or from the SR is re-uptaken into the SR via a Ca^{2+} pump called sarcoplasmic/endoplasmic reticulum Ca^{2+} ATPase (SERCA) or extruded out of the cell by NCX. In human or large animals, 60–70% of the total Ca^{2+} activating the myofilaments is released from the SR, with only 30–40% entering through the LCCs. The high Ca^{2+} concentration caused by Ca^{2+} entry from the LCCs and release from the SR activates contraction of the myofilaments to initiate shortening of the cell. In the absence of LCC openings, the Ca^{2+} released from the SR via random opening of one or two RyRs may also activate other RyRs to open to result in a Ca^{2+} spark. Alternatively, Ca^{2+} diffusion from the neighboring CRUs may also be enough to trigger a spark, especially if the myocyte is Ca^{2+}-overloaded. CICR is a universal mechanism for Ca^{2+} release dynamics in biological cells [177], which is responsible for the complex Ca^{2+} signaling dynamics in many other organs as well as the heart [178–181].

Computational models of either a single CRU or a network of CRUs have been developed at different scales of spatial resolution and network sizes [143, 182–186]. The CRU models were developed based on the local regulation scenario depicted in Fig.15b. The governing equation for Ca^{2+} is a reaction-diffusion equation, e.g., for myoplasm:

$$\beta_m\frac{\partial c_m}{\partial t}=D_m\nabla^2 c_m+J_m \quad (39)$$

where $c_m(x,y,z,t)$ is the Ca^{2+} concentration, β_m is the Ca^{2+} buffering constants, which are instantaneous functions of the Ca^{2+} concentration in the corresponding spaces, following Wagner et al. [187], J_m is the net Ca^{2+} flux, and D_m is the Ca^{2+} diffusion constant. The myocyte model developed by Nivala et al [143] contains 100 × 20 x10 CRUs (Fig.15c). A shown in Fig.15d, each CRU contains a junctional SR which is diffusively connected to the network SR, and a dyadic space, which is diffusively connected to the myoplasmic space. Extracellular Ca^{2+} enters the dyadic space via a leak conductance or LCCs that are simulated stochastically. Ca^{2+} is released from the junctional SR through its associated cluster of RyRs to the dyadic space with the RyRs simulated stochastically. Each CRU contains 10 LCCs and 100 RyRs. Ca^{2+} is either extruded from the cell via the NCX or re-uptaken back up into the SR via the SERCA pump. The CRUs are coupled via Ca^{2+} diffusion in the SR and in the myoplasm, i.e., the SR spaces and the myoplasmic spaces of the CRUs are independently coupled in the 3D space as in Fig.15c via Ca^{2+} diffusion, forming a bidomain model.

4.6. Some notes on experimental technologies

The development of voltage clamp, patch clamp, and optical mapping technologies allows accurate measurement of the electrical and Ca^{2+} cycling properties, from random dynamics of single ion channels to the spatiotemporal voltage and Ca^{2+} wave dynamics in the whole heart. Voltage clamp is a technique in which a feedback electrical circuit is used to control the voltage across the cell membrane so that one can measure the time course of whole-cell ionic currents at a fixed voltage, as shown by Hodgkin and Huxley [118, 188]. This experimental technique allows detailed characterization of different types of ion currents in excitable cells, which has been instrumental for electrophysiology as well as quantitative computer modeling of excitable cells. Patch clamp [189, 190] is a special voltage clamp technique that can measure currents through single ion channels at a fixed voltage, which leads to the direct demonstration of the existence of ion channels and was awarded a Noble prize in 1991. This technique allows one to observe the microscopic behaviors of an ion channel, study the mechanisms of ion channel opening and closing, and link the microscopic ion channel dynamics to the macroscopic properties of the whole-cell ionic current. Optical mappings [191] are techniques using voltage-sensitive or Ca^{2+}-sensitive dyes and digital cameras to measure spatiotemporal dynamics of voltage and Ca^{2+} in cells and tissue. An advantage of the optical mapping is that it can have measurements of high spatial resolutions so that one can study both the temporal and spatial dynamics in the heart, such as the complex spiral wave dynamics. In addition to their importance for experimental biology, these technologies have made the quantitative modeling possible and are necessary to validate theoretical predictions by comparing computer simulation results with experimental measurements. In the past century, the integration of the experimental technologies with computational and theoretical methods have played a fundamental role in improving the mechanistic understanding of the biological mechanisms and the nonlinear dynamics of cardiac excitations and contractions.

5. Dynamics at the molecular and sub-cellular scales

At the molecular and sub-cellular scales, the dynamics are dominated by stochastic fluctuations, but they are not purely random, even for a single ion channel. There are hundreds of thousands of ion channels distributed in the membrane of a cell, which are assumed to act independently with respect to each other, but they are globally coupled via membrane voltage, forming a globally coupled system. Inside the cell, ion channels (namely, the SR Ca^{2+} release channels) form clusters and are locally coupled via Ca^{2+} diffusion. The SR Ca^{2+} release channels are also activated by Ca^{2+}, forming a positive feedback loop to regulate SR Ca^{2+} release. A rich spectrum of spatiotemporal dynamics of Ca^{2+} cycling at the sub-cellular scale has been demonstrated, which couples with the voltage dynamics to give rise to cellular excitation and contraction dynamics. Here we review some of the dynamics observed in the single channel and sub-cellular scales.

5.1. Power-law distribution of ion channel closed times

An interesting observation of ion channel behavior in experiments is that the closed time distribution (but not the open time distribution) exhibits a power-law with a unique −3/2 exponent [192–194]. Figure 16 shows a closed-time distribution of a delayed rectifier K^+ channel in neural cells [192], showing a power-law distribution across several order of time scales. Theories have been developed to understand the underlying mechanisms.

If one assumes the channel is governed by a two-state model as in Fig.14c, the dwell-time distribution of the closed state obeys the following equation:

$$\frac{dp_c(\tau)}{dt} = -\alpha p_c(\tau) \quad (40)$$

which gives rise to

$$p_c(\tau) \propto e^{-\alpha\tau} \quad (41)$$

Even one assumes that the channel follows the Markov scheme in Fig.14d, a power-law closed-time distribution cannot be obtained. In a study by Millhauser et al [195], the authors assumed that an ion channel can have many configurations and energy states, and added many closed states to the model. By solving the Master equation, they were able to obtain a closed-time distribution with a −3/2-power law, $p(\tau) \propto \tau^{-3/2}$, under the conditions that the number of closed states is very large ($N \to \infty$) and the rate constants are roughly equal. The fractal behavior was also studied in simulations by Lowen et al [196]. In another study by Goychuk and Hanggi [197], using a Fokker-Planck-Kramer model, the authors could also derive a −3/2-power law closed-time distribution under the limit of very slow diffusion.

Although theoretical studies of both groups can give rise to the power-law distribution under certain limited conditions, they are not unique. A much simple mechanism of a unique - 3/2-power distribution of the dwell-time has been shown in general nonlinear dynamical systems, the so-called on-off intermittency [198–200]. On-off intermittency is a noise or chaos induced bursting behavior in nonlinear systems. The simplest system exhibiting such a behavior is [199]:

$$\frac{dx}{dt} = [a + \xi(t)]x - x^3 \quad (42)$$

where $\xi(t)$ is a Gaussian white noise with $<\xi(t)>=0$ and $<\xi(t)\xi(t')>= D\delta(t-t')$. In the absence of noise, when $a<0$, the steady state $x=0$ is stable and when $a>0$, it is unstable. In the presence of noise and for a close to zero, a bursting behavior occurs in which the system lingers around x=0 for a certain period of time and then randomly exits and comes back to this state, exhibiting an intermittent behavior. The distribution of the dwell time τ around x=0 (the off state) can be analytically derived as [199],

$$p(\tau) \propto \tau^{-3/2} e^{-(a^2/4D)\tau} \quad (43)$$

which shows that a stronger noise (larger D) or a less deep energy well (smaller a) gives rise to a better −3/2-power law distribution. Whether this mechanism is applicable to the ion channel closed-time distribution needs further investigation using specific models that describe the ion channel opening and closing.

5.2. Dynamics of Ca^{2+} sparks

Intracellular Ca^{2+} signaling plays a ubiquitious role in biological functions, and the general principles and dynamics are universal even though the details of Ca^{2+} signaling pathways may vary in different cell types [12, 177, 201, 202]. Ca^{2+} sparks are considered as the elementary Ca^{2+} release events for Ca^{2+} signaling in heart cells [21], which are collective behaviors of the Ca^{2+} release channel clusters. In the heart, Ca^{2+} not only modulates many biological signaling processes [201], but also directly mediates contraction [12]. Under normal conditions, Ca^{2+} rises during the action potential and returns to the baseline after the action potential, oscillating in tune with the cardiac cycle (and thus the term Ca^{2+} *cycling* is used in cardiology).

A Ca^{2+} spark is a result of collective opening of RyRs in a CRU. When one or two RyRs open, a small Ca^{2+} release event occurs, which is not strong enough to elicit the positive feedback loop (i.e., CICR) to cause more RyR channels to open. This pure random event is called a Ca^{2+} quark. When several RyRs happen to randomly open at the same moment or the LCCs open, the amount of Ca^{2+} released into the dyadic space (see Fig.15) is large enough to initiate CICR and thus recruit more RyRs to open, resulting in a large release event which is called a Ca^{2+} spark. A spark is not a purely random event, but since the number of RyRs in a CRU is limited (~100 RyRs), stochasticity still has a very important influence on Ca^{2+} sparks. Ca^{2+} sparks have been widely studied and characterized in cardiac myocytes [21], and the underlying dynamical mechanisms responsible for their initiation and termination are still under debate [203, 204]. The duration of the Ca^{2+} spark in cardiac myocytes is about 50 ms (Fig.17a), but in an experimental study, Zima et al [205] showed that partially blocking the RyR open probability induced long sparks lasting up to 1 s (Fig. 17b). The mechanism of long-lasting sparks can be understood in terms of nonlinear dynamics as shown in modeling studies by Hinch [206] and by Stern et al [207]. Under the normal conditions, Ca^{2+} entry from the LCCs or from random opening of several RyRs activates the CICR process which causes most of the RyRs to open resulting in a large Ca^{2+} release. Depletion of the SR and/or inactivation of the RyRs terminate the release process, bringing the system back into the unique steady state (see Fig.17c). Under conditions relevant to long-lasting sparks, however, the system has three steady states, exhibiting bistability (Fig.17d). As CICR induces a large release state, the system transits from the lower steady state to the upper steady state. If the system were deterministic, it would remain at the upper steady state forever. However, due to the limited number of RyRs, random fluctuations will cause the exit of the system from the upper steady state to the lower steady state, terminating the spark.

Therefore, for the two cases, the mechanisms of spark termination are different. In the former case, spark termination is by SR depletion or RyR inactivation that shuts off the CICR. A spark is a transient process in a mono-stable system with random variations due to limited number of RyR channels, and the distribution of spark duration is expected to be a normal distribution around its average. In the latter case, the CICR remains active to facilitate the second stable steady state, but stochastic fluctuations cause the system to escape the stable steady state, terminating the spark. This is a typical Kramer escape problem in a bistable stochastic system and the duration of a spark is roughly the first-passage time crossing the potential barrier. Based on the Kramer theory [208], the mean first-passage time is $< \tau > \propto \exp(\Delta U / D)$ where ΔU is the height of the potential barrier and D is the noise strength. The probability density of the first-passage time τ follows an exponential distribution, i.e.,

$$p(\tau) = \frac{1}{<\tau>} \exp(-\tau / <\tau>) \quad (44)$$

A detailed analytical treatment specific to Ca^{2+} spark duration was carried out by Hinch [206], who obtained a spark duration distribution similar to Eq.44.

In the experiments by Zima et al [205], the spark distribution under the normal condition is close to a normal distribution (Fig.18a), but when the RyR open probability is partially blocked to result in long-lasting sparks, the spark distribution tends to exhibit an exponential tail (Fig.18b). Computer simulations by Hinch (Figs.18 c and d) [206] and by Stern et al [207] show similar spark duration distributions, i.e., for normal sparks, the distribution is close to a normal distribution, but for long-lasting sparks, the distribution tends to exhibit an exponential tail.

5.3. Criticality in the transition from Ca^{2+} sparks to waves and oscillations

Ca^{2+} waves and oscillations are ubiquitous phenomena in biology [209–213]. In cardiac cells, intracellular Ca^{2+} waves have been widely observed [214–217], including target waves and spiral waves (Fig.8). Ca^{2+} waves and oscillations play important roles in oscillations of the SAN cells that generate sinus rhythm [24], but are pathological when they occur in the ventricles [218] by causing DADs and EADs [108, 218].

A central question of Ca^{2+} signaling is how the Ca^{2+} sparks organize to give rise to Ca^{2+} waves and oscillations. Experimental studies [109, 212–215] have shown a hierarchy of Ca^{2+} signaling dynamics, including quarks, sparks, spark clusters, abortive and persistent Ca^{2+} waves. Using computer simulations of an IP_3R cluster array model [219], Falcke first showed that nucleation from Ca^{2+} sparks to large spark clusters triggering Ca^{2+} waves was responsible for intracellular Ca^{2+} oscillations. Later studies by Falcke and colleagues [220–222] have shown that the whole-cell Ca^{2+} oscillations are intrinsically stochastic, which is not an oscillatory behavior of a IP_3R cluster but rather an emergent behavior of the IP_3R cluster network of the whole cell. In a recent study, Nivala et al [111] combined computer simulation and experiments to address the question of how local random Ca^{2+} signaling events self-organize into global Ca^{2+} signaling events in cardiac myocytes. They showed that the transition from Ca^{2+} sparks to oscillations undergoes a critical transition, similar to the second-order phase transition in statistical physics or self-organized criticality in natural systems [223–225].

The Ca^{2+} signaling hierarchy has been observed by elevating Ca^{2+} (or IP_3 in many other cell types). When Ca^{2+} level is low, the system is dominated by random quarks and sparks, when Ca^{2+} is high, it is dominated by spark clusters and waves. In the transition from sparks to waves, all types of the behaviors in this hierarchy can be observed (Fig.19a) [143], i.e., quarks, sparks, spark clusters, and waves co-exist. A Ca^{2+} quark (labeled as “q” in Fig.19a) is a pure random and small release event caused by random opening of one or two RyRs. A Ca^{2+} spark (labeled as “s” in Fig.19a) is a discretized release event of a CRU via collective opening of many RyRs. The Ca^{2+} released in a spark may diffuse to cause its neighboring CRUs to fire, or neighboring CRUs may fire coincidentally together, forming spark clusters (labeled as “c” in Fig.19a). When a cluster becomes large enough, it may initiate a propagating Ca^{2+} wave (labeled as “w” in Fig.19a), depending on the status of the surrounding CRUs.

Statistical analyses of the clustering of Ca^{2+} sparks show that when Ca^{2+} in the cell is low or the CRU coupling is weak, the system is dominated by quarks and sparks, and the spark cluster size distribution is exponential (Fig.19b). As Ca^{2+} level increases, the distribution changes toward a power-law. This same clustering behavior is observed in permeabilized mouse ventricular myocytes (Fig.19c). The power-law clustering indicates that the system is in a critical state in which events of different spatial scales co-exist.

Since at low Ca^{2+} levels, the system is dominated by random quarks and sparks, the whole-cell Ca^{2+} remains at a low level with small fluctuations (Figs.20 a and b). Close to the critical state, Ca^{2+} waves occur occasionally which result in Ca^{2+} spikes at the whole-cell level and irregular Ca^{2+} oscillations. As the Ca^{2+} level becomes even higher, it passes the critical region, and the whole-cell Ca^{2+} oscillates more regularly. These Ca^{2+} oscillation behaviors can be seen in the inter-spike interval histograms obtained from long simulations of a smaller system size [226]. Close to criticality, the distribution of the inter-spike interval exhibits a fat-tail while at the high Ca^{2+}, the distribution becomes Gaussian (Fig.20c).

Criticality in Ca^{2+} cycling dynamics is also observed using a simplified model (Fig.21), in which the Ca^{2+} spark is represented by an agent model [111]. Specifically, a Ca^{2+} spark is modeled by a three-state cycle (Fig.21a): excitable→excited→recovery→excitable. The transition from the excitable state to excited state is random with a transition rate α. The CRUs are coupled in a 3D array with nearest-neighbor coupling and coupling strength γ. This model allows one to separate the effects of spark rate (α) and CRU coupling strength (γ). When the CRUs are uncoupled (γ=0), the cluster size distributions are exponential for small α values. As α increases to a critical value (α=0.008), the cluster-size distribution becomes a power-law (Fig.21b), which agrees with the traditional percolation theory [227, 228]. However, the value of α estimated from experimental data and simulations, as well as previous experiments [214], is much lower than that required for a power-law distribution in percolation theory. When the CRUs are coupled, a much lower spark rate is required to reach the critical state. For example, for α=0.0001 with a non-zero γ, the cluster size distribution changes from an exponential distribution to a power-law distribution at large γ values (Fig.21c). The strong coupling between CRUs is important for Ca^{2+} waves. Even though a power-law cluster distribution can occur via percolation, due to the high spark probability, the excitable space for propagation is much less than the one formed via strong CRU coupling (Fig.21d), and thus the latter case creates a much better environment for a wave to propagate in space.

However, the CRU network in the real cell is not homogeneous [229], and thus self-organization of spark clusters is also not uniform in space, such that waves tend to originate from preferred locations. Theoretically, when the distribution of CRUs is uniform inside a cell, the wave initiation sites should occur randomly and uniformly in space [111]. This type of wave pattern has been observed in many experiments [213–215, 217]. But in other experiments, waves have also been observed to originate repetitively from the same locations in a cell [230–233], indicating that heterogeneities in the CRU network is important. Moreover, both behaviors can occur in the same cell at different Ca^{2+} levels [111]. The question is how stable pacemaker sites self-organize in a cells as Ca^{2+} level increases. Nivala et al [226] have carried out computational and theoretical study to answer this question. The authors first showed in computer simulations of a heterogeneous CRU network model that at low Ca^{2+} levels, Ca^{2+} waves originate randomly in space and time, but as the Ca^{2+} level increases to high values, Ca^{2+} waves originate from the same location. They also developed a theory of random entrainment to explain the underlying mechanism. Due to the broad and fat-tail distribution of the inter-spike interval at low Ca^{2+} levels (Fig. 20c), a firing site of Ca^{2+} waves is difficult to be entrained by other firing sites since the difference in firing frequencies is smaller comparing to the broadness of the inter-spike interval distribution. At high Ca^{2+} levels, the inter-spike interval distribution is a narrow Gaussian distribution (Fig.20d), the difference in the firing frequencies of two different sites allows more effective entrainment. At this case, the fastest firing site effectively entrains the slower ones, acting as a pacemaker region to entrain the whole cell.

Criticality as a mechanism for the transition from Ca^{2+} sparks to Ca^{2+} waves may have several implications for the heart. For example, once a system is in a critical state, a tiny perturbation can grow into a macroscopic fluctuation due to the power-law behavior [223, 234]. This provides a general theoretical framework for how single channel fluctuations may lead to macroscopic large random fluctuations at the cellular scale as well as the tissue scale, such as the irregularly occurring DADs or PVCs. In the SAN cells, local Ca^{2+} release plays a vital role in pacemaking activity [235]. Local Ca^{2+} releases generating Ca^{2+} waves via criticality may provide a sub-cellular mechanism accounting for HRV and for its fractal properties [236, 237].

Besides target waves, spiral Ca^{2+} waves can also occur in cardiac myocytes, as shown in Fig.8c. The mechanisms of intracellular spiral Ca^{2+} wave formation and dynamics and their roles in excitation-contraction coupling have not been well studied, and need further investigation in both experiments and computational modeling.

6. Nonlinear dynamics in single myocytes

Both atrial and ventricular myocytes are excitable cells, which are subjected to external driving during sinus rhythm. Under normal conditions at normal rates of stimulation, these cells exhibit a regular response to the stimuli. At fast rates of stimulation and/or under diseased conditions, beat-to-beat dynamical changes can occur, which are the cellular dynamics underlying arrhythmias at the organ level. In the past several decades, many cellular dynamics have been identified and investigated in experiments and theoretical studies. In this section, we summarize most of these cellular dynamics and the underlying mechanisms. Specifically, we cover the following dynamics: APD alternans, chaos, hysteresis, and the effects of short-term cardiac memory; intracellular Ca^{2+} alternans, its coupling with voltage, and sub-cellular Ca^{2+} alternans; the bifurcations leading to EADs and the nonlinear dynamics of EADs under periodic pacing; and finally the mechanisms of the DADs.

6.1. APD alternans and chaos

TWA is a manifestation of APD alternans in the ECG. There are two origins of instabilities in cardiac myocytes that can lead to APD alternans: instabilities arisng from the voltage system and instabilities arising from the intracellular Ca^{2+} cycling system. In the voltage system, APD restitution curve is a nonlinear function useful for analyzing the dynamics, with its slope being a control parameter that causes the period-doubling bifurcation resulting in alternans. The steep slope and nonlinearity of APD restitution curve can cause other complex APD dynamics, such as chaos. Moreover, memory effects plays an important role in the nonlinear cellular APD dynamics.

6.1.1. APD restitution—The duration of the cardiac action potential depends on the heart rate, which is called APD restitution. In most cases, APD is shorter at faster heart rates, but under some conditions and species, APD can lengthen at faster rates. APD restitution is usually quantitatively measured using an S1S2 pacing protocol (Fig.22a): the cell is first paced periodically at a slow pacing rate for many (S1) beats to let the APD equilibrate, and then a premature S2 stimulus is applied to elicit an extra action potential. The time interval between two action potentials is called the diastolic interval (DI) (graphically defined in Fig. 22a). By varying the S1S2 interval, both DI and APD are varied, and by plotting APD of the S2 beat against the preceding DI, one obtains an APD restitution curve (Fig.22b). The S1S2 APD restitution curve can be denoted by a onevariable function:

$$a=f(d) \quad (45)$$

where *a* is the APD of the S2 beat and *d* is the DI preceding the S2 stimulation (see Fig.22a).

The APD restitution curve can be a monotonically increasing function of DI, but it can also be non-monotonic, in which APD does not always decrease as DI decreases. Figure 22c shows APD restitution curves measured from a human heart [238, 239], which increase first, then decrease, and increase again as the S1S2 coupling interval increases. This type of restitution gives rise to dynamics that are different from those of the monotonic relationships. Moreover, APD restitution curves are different for different S1 PCLs. This is because myocytes settle into different steady states for different S1 pacing rates, resulting in different S1S2 responses. This effect is called short-term cardiac memory.

6.1.2. APD alternans and chaos induced by steep APD restitution—

Assuming that the myocyte is periodically paced, and the APD depends only on its immediately preceding DI, one can then rewrite Eq.45 as

$$a_{n+1}=f(d_n)=f(T-a_n) \quad (46)$$

where a_n and a_{n+1} are the APDs of the nth beat and the (n+1)th beat, respectively, d_n is the DI of the nth beat, and T is the PCL. The relation $a_n+d_n=T$ is used in Eq.46 (see Fig.23a for a graphical definition). The steady-state APD and DI are denoted as a_s and d_s, and they also satisfy $a_s+d_s=T$. Equation 46 is simply an iterated map and can be used to study the nonlinear action potential dynamics under periodic stimulation. This method was first elucidated by Nolasco and Dahlen in 1968 [52]. The steady state becomes unstable when

$$slope=\frac{df}{dd_n}\Big|_{d=d_s}=-\frac{df}{da_n}\Big|_{a=a_s}>1 \quad (47)$$

i.e., when the slope of the APD restitution curve at the steady state is greater than one, the steady state is unstable. At slow pacing, the DI is long and thus the slope of the restitution curve is smaller than one, and the steady state is stable. As the heart rate becomes faster, the DI becomes shorter, such that the slope of the APD restitution curve at the steady state becomes greater than one, then the steady state becomes unstable. The growth of a small perturbation to the steady state follows the equation:

$$\delta a_{n+1}=\frac{df}{da_n}\delta a_n=(-slope)^{n+1}\delta a_0 \quad (48)$$

Therefore, δa_{n+1} is positive and negative on alternative beats, which makes $a_{n+1} = a_s + \delta a_{n+1}$ to be longer and shorter on alternative beats. Since the APD restitution curve is nonlinear, the growth rate of δa_{n+1} is attenuated by the shallow slope region of the curve, and eventually the system may asymptotically settle into a stable alternating state, resulting in a period-2 APD pattern, i.e., APD alternans.

Cardiac myocytes (and any excitable cells) have a property called refractoriness, i.e., a cardiac myocyte cannot be excited by an external stimulus during the duration of an action potential and subsequent recovery period. This unresponsive period is called the refractory period, which means that when the S1S2 interval is shorter than a certain value, no action potential can be elicited. In periodic pacing, when the PCL is shorter than the refractory period, not all the stimuli are able to elicit an action potential, but a portion can. The ones that elicit action potentials are called capture beats, and the ones that do not are called non-capture beats. For example, when every other stimulus results in an action potential, the pattern is denoted 2:1 capture (or block). In general, if for every n stimuli, m action potentials are elicited, the resulting state is labeled as n:m capture in the literature. By considering the property of refractoriness, the iterated map is then rewritten as,

$$a_{n+1}=\begin{cases} f(T-a_n), \mathit{if}\ T>a_n+d_0 \\ f(2T-a_n), \mathit{if}\ T<a_n+d_0<2T \\ f(3T-a_n), \mathit{if}\ 2T<a_n+d_0<3T \\ \vdots \end{cases} \quad (49)$$

where 0 $a_n + d_0$ is defined as the refractory period. Note that d_0 is the minimum DI at which an action potential can be elicited and if DI is shorter than d_0, stimulation fails.

Equation 49 is a form of a shift map which can generate chaos when the slope of the function *f* is greater than one. Differing from the standard shift map in which *f* is a linear function, *f* in Eq.49 is a nonlinear function, such that other complex dynamics can occur. Figure 23b shows a bifurcation diagram by plotting APD against PCL obtained by iterating Eq.49 with a steep APD restitution curve. As the PCL decreases, bifurcations from the stable steady state (1:1) to alternans (2:2) and from 2:2 alternans to 2:1 block are observed, and more complex action potential dynamics are seen at even faster pacing rates. Note that the bifurcation sequence from the iterated map: 1:1→2:2→2:1→4:2→ID→4:1→8:2→ID, is very similar to the one observed in an experiment by Chialvo *et al.* [58] (Fig.23c): 1:1→2:2→2:1→4:2→3:1→6:2→4:1→8:2→ID, where ID stands for irregular dynamics. This indicates that the nonlinear dynamics caused by steep APD restitution may be indeed responsible for the complex dynamics observed in real cardiac myocytes.

When the APD restitution curve is non-monotonic, different bifurcation sequences become possible. Alternans, chaos, and other complex responses caused by non-monotonic APD restitution curve are also observed in experiments [61], and the bifurcations can be simulated using iterated maps [61, 240] as well as action potential models [241, 242]. A key difference in bifurcation diagrams for the two different types of APD restitution curves is that chaos only occurs after 2:1 block for the monotonic APD restitution curve, but chaos can occur before 2:1 block for the non-monotonic APD restitution curve. This is because in the former case, chaos is a result of a shift map in which 2:1 block serves as the folding process, while in the latter case, chaos is a result of a unimodal map [240].

6.1.3. Effects of cardiac memory—During an action potential, voltage and the ionic currents can be directly measured, but many other quantities are hidden and cannot be directly measured, such as the slow recovery of ion channels from their previous openings or the rebalancing of the ion concentration after a change in heart rate. Therefore, the action potential depends on the pacing history, a property known as short-term cardiac memory [239]. As shown in Fig.22c, the S1S2 APD restitution curves are different for different S1 PCLs, and thus a family of S1S2 restitution curves can be obtained, which is called restitution portrait [243]. Due to this memory effect, the slope of the S1S2 APD restitution curve is only qualitatively, but not quantitatively, predictive for the onset of APD alternans [244–246]. In principle, one can construct, from experimental data, an APD restitution function which depends not only on the immediately preceding DI but also on earlier APDs and DIs as [247],

$$a_{n+1}=f(d_n,a_n,d_{n-1},\ldots) \quad (50)$$

and thus use this higher-dimensional iterated map to analyze the nonlinear dynamics.

In a study by Fox et al [63], a 2D iterated map model was developed to study the effects of memory on APD alternans as follows:

$$a_{n+1}=f(d_n,M_{n+1})=(1-\alpha M_{n+1})f_0(d_n)M_{n+1}=g(M_n,d_n,a_n)=e^{-d_n/\tau}[1+(M_n-1)e^{-a_n/\tau}]d_n=T-a_n \quad (51)$$

where M is the memory variable and $f_0(d_\mathrm{n})$ is the S1S2 restitution function. The relation between M, a and d is shown in Fig.24a. It can be easily shown via linear stability analysis that the memory in the model suppresses the instability; in other words, alternans might be expected to occur when the slope of the S1S2 restitution curve is greater than one, but it does not because of the presence of memory (Fig.24b). In Eq.51, α=0 is the case of no memory, and in the presence of memory (α>0), APD is shorter which effectively reduces the slope of APD restitution. This type of memory can also suppress spiral wave instability [248] for the same reasons.

However, memory can also promote APD instabilities. Figures 24 c and d show a case in which memory promotes APD alternans in an action potential model in the presence of a transient outward K^+ current (I_{to}) [249]. In the bifurcation diagram in Fig.24c, alternans occurs between PCLs of 490 ms and 930 ms, corresponding to DIs of 345 ms and 640 ms, respectively. The S1S2 APD restitution curves recorded from the same model exhibit a strong memory (Fig.24d), i.e., they strongly depend on the S1 PCL. The two restitution curves shown in Fig.24d exhibit slope>1 over much narrower DI ranges than the DI range exhibiting alternans in Fig.24c. This indicates that memory promotes alternans. The strong memory effect is not caused by a single current [63, 248], but results from interactions between multiple ionic currents [249]. More complex APD dynamics due to this type of memory effect were observed in simulation studies [250, 251], and both the alternans and complex APD dynamics were shown in experiments two decades ago [252].

The alternans shown in Fig.24c occurs at much slower pacing rates than alternans shown in many other studies, such as the alternans shown in Fig.23. APD alternans can also occur at slow pacing rates in the absence of I_{to}, and is due to steep APD restitution and memory effects [253], similar to the case shown in Figs.24 c and d. Even though APD restitution is important for APD alternans occurring at both fast and slow pacing rates, the ionic causes are different. For APD alternans induced by fast pacing, the steep slope of the APD restitution is mainly caused by the recovery of the LCCs [65, 254, 255]. For APD alternans during slow pacing, the steep slope is caused by the steady-state $I_{Ca,L}$ or I_{Na} [253], and the system exhibits large memory effects.

In the presence of memory or instabilities that do not originate from voltage, the APD restitution slope can no longer predict the onset of alternans. Using a stochastic pacing protocol and transfer function method [256, 257], de Lange and colleagues can predict the onset of alternans in cardiac cells in the presence of memory or instabilities originating from intracellular Ca^{2+} cycling.

6.1.4. Hysteresis—Hysteresis in action potential dynamics during periodic pacing is widely observed in cardiac cells and tissue [258–263]. Specifically, when a cardiac cell is first paced with a ramping-up protocol in which the pacing rate changes from slow to fast, and then with a ramping-down protocol in which the pacing rate changes from fast to slow, one observes an overlap region in which two action potential behaviors co-exist for the same PCL. For example, an overlap region almost always occurs between n:1 capture and n+1:1 capture; Walker et al [260] showed that the onset of alternans is different using the different pacing protocols; and coexistence of a steady state with alternans and other dynamics was also observed. There are two possible causes for these hysteresis behaviors: one is a result of cardiac memory and the other is caused by bistability.

In cardiac cell or tissue, the memory effect can last from seconds to minutes. When the system changes from one type of behavior to another, it can take many beats for the system to adjust to its new steady-state behavior. When one uses the ramping-up and ramping-down pacing protocol with a limited number of pacing beats for each PCL (which is usually the case in experiments), a hysteresis loop forms. This is likely a mechanism for the hysteresis observed by Walker et al [260] and in other experiments.

Most of the hysteresis observed in periodically-paced cardiac cells are bistable behaviors occuring with the transitions between n:1 capture and n+1:1 capture. This can be obtained by solving the iterated map equation for steady-state solutions, and a simple example is as follows. Assuming a linear APD restitution curve described by $a_{n+1} = a_0 + \alpha d_n$, and solving Eq.49 for the steady-state solutions of the 1:1 capture and the 2:1 capture, one obtains the overlap region as

$$a_0+(1+\alpha)d_0<T<\frac{a_0+(1+\alpha)d_0}{1-\alpha} \quad (52)$$

which shows that the overlap region is wider for a steeper APD restitution curve (larger α). Eq.52 also shows that there is always an overlap region between the 1:1 capture and the 2:1 capture as long as the slope of the APD restitution curve is positive, i.e., $\alpha>0$. Similarly, one can obtain the overlap region of T for the transitions between any n:1 and n+1:1 captures. Since the true APD restitution curve is usually nonlinear, the steady-state solution of 1:1 capture may be unstable in the overlap region, and thus APD alternans occurs, leading to the co-existence of 2:1 capture with APD alternans.

6.2. Intracellular Ca^{2+} alternans

Since Ca^{2+} and voltage are bi-directionally coupled, instabilities originating from the voltage system that cause APD alternans and other complex APD dynamics also cause alterans and complex dynamics in intracellular Ca^{2+} cycling. However, the regulation of Ca^{2+} cycling system is also very complex, and includes positive feedback loops (e.g., CICR) which can cause instabilities in Ca^{2+} cycling, such as Ca^{2+} alternans. Indeed, Ca^{2+} alternans can be observed experimentally when APD is fixed (i.e., under the condition of voltage or action potential clamp) [264–266], demonstrating that instabilities do occur in the Ca^{2+} subsystem. Moreover, spatially discordant Ca^{2+} alternans inside a myocyte has also been observed in many experimental studies [265, 267–271]. Dynamical mechanisms of Ca^{2+}

alternans and spatially discordant Ca^{2+} alternans have been developed, and some of them are supported by experimental evidence.

6.2.1. Steep fractional SR Ca^{2+} release as a mechanism of Ca^{2+} alternans—

The first mechanism of Ca^{2+} alternans, proposed by Eisner et al [272], postulated that Ca^{2+} alternans is due to a steep nonlinear dependence of SR Ca^{2+} release upon the diastolic SR Ca^{2+} load immediately preceding the release (i.e., a steep fractional release-load relationship). Fractional SR Ca^{2+} release is an experimental observation in which the fraction of Ca^{2+} released from the SR during a paced beat depends on how much Ca^{2+} that the SR contains right before the stimulation. This dependence is typically a steep nonlinear function (Fig.25a) [273]. An instability can occur leading to alternans due to the steep slope of this function. Based on the argument of Eisner et al, Shiferaw et al [274] developed a Ca^{2+} cycling model to simulate Ca^{2+} alternans and showed theoretically that the steep fractional SR Ca^{2+} release can indeed cause an instability to result in Ca^{2+} alternans. Qu et al [240] developed an iterated map model that can incorporate the fractional release function measured from experiment to study the bifurcations. The iterated map model is:

$$l_{n+1}=l_n-g(l_n)+h(c^p_{n+1}), \quad (53)$$

where l_n is the Ca^{2+} content in the SR right before the next beat, i.e., the SR Ca^{2+} load at beat n; g is the function describing the fractional release, which depends on the Ca^{2+} load in the previous beat; and h is the function describing the re-uptake of Ca^{2+} back into the SR via the SERCA pump, which is a fucntion of peak Ca^{2+} at the present beat (denoted as c^p_{n+1}). c^p_{n+1} is calculated as the total Ca^{2+} (b) in the cell less the Ca^{2+} loaded to the SR (l_n), plus the Ca^{2+} released from the SR [$g(l_n)$], i.e.,

$$c^p_{n+1}=b-l_n+g(l_n). \quad (54)$$

Linearizating Eq.53 around the steady state gives rise to

$$\delta l_{n+1}=(1-g')(1-h')\delta l_n=\lambda\delta l_n. \quad (55)$$

The steady state becomes unstable when

$$|(1-g')(1-h')|>1, \quad (56)$$

where $g'=\frac{dg}{dl_n}|_{l_n=l_s}$ and $h'=\frac{dh}{dc^p_{n+1}}|_{l_n=l_s}$ are the slopes of the fractional release and the uptake functions at the steady state (l_s). Ca^{2+} alternans occurs when $\lambda < -1$. Using a fractional SR Ca^{2+} release function fitted from experimental data (Fig.25a), a period-doubling bifurcation leading to Ca^{2+} alternans and chaos can be observed by iterating Eq.53 (Fig.25b).

Evidence supporting this mechanism has been shown in experiments [265, 266, 275] and in simulations using detailed action potential models [275–278].

6.2.2. A mean-field theory of Ca^{2+} alternans—The steep fractional Ca^{2+} release as a mechanism of Ca^{2+} alternans requires that diastolic SR Ca^{2+} load before each beat alternate concomitantly with Ca^{2+} release. This is challenged by experimental studies in rabbit ventricular myocytes by Picht et al [279] and in cat atrial myocytes by Hüser et al and others [280, 281], who showed that under some conditions, SR refills to the same level before each beat yet cytosolic Ca^{2+} alternans still occurs, which disagrees with the prediction of the above mechanism. Note that the theory of steep fractional SR Ca^{2+} release causing Ca^{2+} alternans was developed phenomenologically based on whole-cell measurements, ignoring the microscopic or mesoscopic features of Ca^{2+} sparks. It is widely accepted that Ca^{2+} sparks are the elementary events in Ca^{2+} cycling. A Ca^{2+} spark is a collective Ca^{2+} release event of a cluster of RyRs in a CRU via CICR, and a ventricular myocytes may contain more than 20,000 CRUs which are coupled via Ca^{2+} diffusion in the cytosol and SR. Using the properties of Ca^{2+} sparks and a mean-field approach, Cui et al [282] and Rovetti et al [283] developed another theory of Ca^{2+} alternans, which links the microscopic spark properties to the macroscopic Ca^{2+} alternans and provides a unified mechanistic interpretation to many experimental observations [284].

There are three critical properties of a CRU or a spark: *randomness* (of Ca^{2+} spark activation), *refractoriness* (of a CRU after a Ca^{2+} spark), and *recruitment* (Ca^{2+} sparks inducing Ca^{2+} sparks in adjacent CRUs). At any time, a CRU is in one of the three states (Fig.26a): recovered, firing, or refractory. A recovered CRU may fire spontaneously due to high SR Ca^{2+} load or be activated directly by the opening of the LCCs. These types of sparks are called primary sparks (Fig.26b). Ca^{2+} released from a primary spark may diffuse to its neighboring CRUs, which may recruit the recovered CRUs to fire [285]. This type of sparks is called secondary sparks. After firing, a CRU remains refractory for a finite period of time. Due to the random opening properties of LCCs and RyRs, sparks are probabilistic events. The probability of a primary spark is assumed to be α and the probability of a primary spark to recruit a neighboring CRU to fire is assumed to be γ. The recovery of the RyRs and SR refilling in a CRU may give rise to spark amplitude restitution [286, 287] and also random refractory periods [288, 289]. The probability of a CRU remaining in the refractory state after its previous release is assumed to be β. If there are a total of N_0 CRUs in the system, and at the kth beat, N_k sparks occur, then at the (k+1)th beat, there are βN_k unrecovered CRUs and (N_0-βN_k) recovered CRUs. The number of primary sparks in this beat is then $\alpha(N_0-\beta N_k)$, and thus $(1-\alpha)(N_0-\beta N_k)$ recovered CRUs are available for recruitment. If a fraction *f* of these CRUs are recruited to fire, then the total number of sparks at (k+1)th beat is

$$N_{k+1}=\alpha(N_0-\beta N_k)+(1-\alpha)(N_0-\beta N_k)f \quad (57)$$

As illustrated in Fig.26b, recruitment can only occur when a neighboring CRU is in its recovered state. Therefore, the fraction *f* of recruitment is not simply the recruitment probability γ, but a complex function that is determined by the distribution of CRUs in different states. In principle, an exact formulation of *f* cannot be obtained due to the complex spatial coupling between CRUs and spatial clustering. But under the assumption that the system is well mixed so that the firing probability of a CRU is uniform in space, a formulism for f can be derived as a function of α, β, γ, and N_k using a mean-field approach [282, 283], which is:

$$f(\alpha, \beta, \gamma, N_k)=1-[1-\alpha\gamma(1-\beta N_k/N_0)]^M \quad (58)$$

where M is the number of nearest neighbors of a CRU, which is 4 in a two-dimensional array and 6 in a three-dimensional array. Note that in a real myocyte, a CRU may be capable of recruiting not only its nearest neighbors, but also non-neighboring CRUs if the Ca^{2+} diffusion in the cytosolic space is fast, such that M can be larger than 6. Eq.57 is an iterated map and can be used to study the beat-to-beat spark dynamics, and thus predict the occurrence of Ca^{2+} alternans.

Based on Eqs.57 and 58, no alternans can occur in the following three cases: 1) If there is no recruitment (γ=0), then f=0, such that Eq.57 becomes a linear equation with the steady state being $N_s=\alpha N_0/(1+\alpha\beta)$; 2) If α=1, all sparks are primary, and no recruitment can occur (even if γ>0), such that Eq.57 also becomes a linear equation with the steady state of $N_s=N_0/(1+\beta)$; 3) If the CRUs fully recover from their previous firings (β=0), then the right side of Eq.57 becomes a constant and $N_s=N_0-(1-\alpha)N_0(1-\alpha\gamma)_M$. Therefore, for alternans to occur in Eq.57, refractoriness, recruitment, and a certain degree of randomness are required. We also call this theory of Ca^{2+} alternans as the “3R’ theory. Through performing a linear stability analysis or numerical simulation of Eq.57, one can predict that alternans occurs at large β (>0.9), large γ, and intermediate α (Fig.26c).

Several implications arise from predictions of this theory, which can be used to explain experimental observations and simulation results. Intermediate α means that there must be enough CRUs available for recruitment such that neighboring CRUs can fire in one beat and remain refractory in the next beat, which also requires strong coupling (large γ). If α=1, all recovered CRUs fire as primary sparks, and no recruitment can occur. This explains why asynchronous Ca^{2+} release and mini-waves were required for alternans to occur in experiments by Diaz et al [265, 266, 290]. Moreover, these experiments were carried out under voltage clamp conditions in which the open probability of the LCCs was reduced to allow asynchronous Ca^{2+} release. Large β means that the majority of CRUs are refractory after firing during the previous beat, which indicates that these CRUs will fire on every other beat due to refractoriness, causing alternans at the individual CRU scale. However, if there is no spark recruitment (no coupling between CRUs), then due to randomness, the individual CRU alternans are randomly out of phase, resulting in microscopic alternans without whole-cell Ca^{2+} alternans. Large γ allows for spark recruitment to synchronize alternating CRUs more or less together in the same phase so that there are more Ca^{2+} sparks in one beat than the next beat, resulting in macroscopic alternans. This agrees with simulations in detailed models showing that alternans is promoted by stronger Ca^{2+} diffusion [185] or closer CRU spacing [283]. Finally, unlike α, β , and γ, SR Ca^{2+} content is not an explicit parameter in the mean-field theory of alternans, which means that SR Ca^{2+} load alternans is not a requirement for Ca^{2+} alternans, in line with the observation that Ca^{2+} alternans can occur without diastolic SR Ca^{2+} load alternans [279–281] and under SR Ca^{2+} clamp conditions [283, 291]. However, SR Ca^{2+} content indirectly affect α, β , and γ, and thus it still plays a very important role in Ca^{2+} alternans [291].

In an experiment carried out by Tian et al [271], a transition from microscopic Ca^{2+} alternans to macroscopic Ca^{2+} alternans was observed (Fig.27). Specifically, at a slower pacing rate, alternans was observed at individual measurement sites while the whole-cell Ca^{2+} is regular from beat to beat. At a faster pacing rate, alternans occurred at both the individual sites and the whole-cell level. This observation can also be explained by this theory as follows. At the slower pacing rate, alternans occur at individual coupling sites due to refractoriness (or other mechanisms), but the coupling strength γ is not large enough for spark recruitment to result in macroscopic alternans. At the faster pacing rate, the overall Ca^{2+} accumulation at faster rates enhances CRU coupling and thus spark recruitment, causing macroscopic alternans to occur.

Therefore, the mean-field theory of Ca^{2+} alternans links the microscopic (spark) behaviors to the macroscopic (alternans) behaviors, explaining how order arises from disorder in the formation of Ca^{2+} alternans in a cardiac myocyte.

The mean-field theory of Ca^{2+} alternans links microscopic features to the macroscopic dynamics but does not exclude that a steep fractional SR Ca^{2+} release relation exists concomitantly with Ca^{2+} alternans [283]. In fact, simulations showed that Ca^{2+} alternans always occurs in the SR Ca^{2+} load range where steep fractional SR Ca^{2+} release occurs [283, 291, 292]. Since Ca^{2+} alternans still occurs when SR Ca^{2+} is fixed at a constant, the two have no causal relation. In the mean-field theory of Ca^{2+} alternans, SR Ca^{2+} load affects α, β , and γ indirectly to affect Ca^{2+} alternans [291]. The mean-field theory can provide a holistic interpretation to many experimental observations of Ca^{2+} alternans, some of them may even be seemingly contradictory, and to the roles of each individual Ca^{2+} cycling regulation factors in the genesis of Ca^{2+} alternans. This was discussed in a recent article by Qu et al [284].

Nevertheless, different mechanisms can be responsible under different conditions, and the two mechanisms of Ca^{2+} alternans are not necessarily exclusive to each other. Future studies are needed to identify the specific conditions for the existence of the two mechanisms and investigate their interactions, which is important for identifying potential therapeutic targets.

6.2.3. Alternans dynamics due to voltage and Ca^{2+} coupling—Since both the voltage system and the Ca^{2+} system can exhibit instabilities, their bidirectional coupling can either modulate the existing instabilities or promote new ones. In experimental studies, two different voltage-Ca^{2+} alternans behaviors have been observed. In the one case (Fig.28a), the large contraction (indicated by large Ca^{2+}) is associated with the long APD, and vice versa, i.e., APD and Ca^{2+} alternate in-phase, and this type of alternans is called electromechanically concordant alternans. In the other case (Fig.28b), the large contraction is associated with the short APD, and vice versa, i.e., APD and Ca^{2+} alternate out-of-phase, and this type of alternans is called electromechanically discordant alternans. These behaviors have been explained using computer simulations by Shiferaw et al [293] and coupled iterated maps by Qu et al [240]. Here we summarize the iterated map analysis.

Coupling the iterated map for APD (Eq.46) with the one for Ca^{2+} cycling (Eq.53), the two-variable iterated map for the coupled system is [240]

$$a_{n+1}=f(d_n)+\gamma c^p_{n+1}a_{n+1}\ l_{n+1}=l_n-q(d_n)g(l_n)+h(c^p_{n+1}) \quad (59)$$

where $\gamma c^p_{n+1}a_{n+1}$ is the term describing the effect of Ca^{2+} on APD, and $q(d_n)$ is a function describing the effect of restitution on Ca^{2+} release. The dynamics of Eq.59 depends on how Ca^{2+} and voltage are coupled. According to Eq.59, when γ is positive, a larger Ca^{2+} amplitude causes a longer APD, which is called positive Ca^{2+}-to-APD coupling (equivalent to concordant electromechanical coupling). When γ is negative, a larger Ca^{2+} amplitude causes a shorter APD, which is called negative Ca^{2+}-to-APD coupling (equivalent to discordant electromechanical coupling). Direct experimental evidence of positive and negative Ca^{2+}-to-APD coupling by altering $I_{Ca,L}$ and I_{NCX} was demonstrated recently [294].

Figure 28c shows the boundaries of instability of the steady state of Eq.59 under three conditions: no coupling (γ=0), positive coupling (γ>0) and negative coupling (γ<0). When γ=0, Ca^{2+} has no effect on APD, and the vertical and horizontal boundaries (dashed gray lines) are due to instabilities from voltage and Ca^{2+}, respectively. When γ>0, the boundary of instability is pulled in from the dashed gray lines in the phase diagram, indicating that the coupling of Ca^{2+} and APD promotes instability. In other words, both systems can be stable when they are uncoupled, but become unstable when they are coupled. Alternans via bifurcation from this boundary is electromechanically concordant, i.e., the long APD is associated with the large Ca^{2+} amplitude. When γ<0, the boundary of instability is pushed out from the dashed gray lines in the phase diagram, indicating that the coupling suppresses instability. However, new dynamical behaviors occur in this case. When the instability is dominated by the voltage system (boundary II in Fig.28c), the alternans is electromechanically concordant, i.e., the large Ca^{2+} amplitude is associated with the long APD, and vice versa. When the instability is dominated by the Ca^{2+} system (boundary I), the alternans is electromechanically discordant, i.e., the large Ca^{2+} amplitude is associated with the short APD, and vice versa. When the instabilities are strong in both systems (boundary III), the association between Ca^{2+} and APD is modulated by a new frequency, becoming quasi-periodic, i.e., the alternans changes between concordant and discordant alternans quasi-periodically. Quasi-periodic action potential behavior was indeed observed in periodic paced real myocytes [295, 296], and quasi-periodic dynamics due to Ca^{2+} and voltage coupling might be one of the mechanisms.

Since both voltage and Ca^{2+} cycling can cause instabilities to result in alternans, it is important to identify the origins of instabilities to develop strategies for therapeutic targets. In a computer model, one may be able to use linear stability analyses to dissect the origins or contributions [297], but in real cells, this is nontrivial due to the bi-directional coupling of voltage and Ca^{2+}. One of the important tasks of computational modeling is to identify characteristics of alternans that can be used to infer the origins of instabilities. In a study by Sato et al [298], characteristics was identified in computer simulation to differentiate the origins of instabilities for alternans.

6.2.4. Mechanisms of sub-cellular discordant Ca^{2+} alternans—A cardiac myocyte is a spatial entity, and spatiotemporal patterns can form within the cell. Fig.34 shows spatially discordant Ca^{2+} alternans observed in a cat atrial myocyte by Blatter et al [299], in which Ca^{2+} alternates out of phase at the two end of the cells. That is, at one end, the amplitude of the Ca^{2+} signal exhibit a pattern of *large, small, large*, …, while the other end exhibits a pattern of *small, large, small*, …. Similar patterns have been observed in ventricular mycoytes by other researchers [265, 268, 269, 271]. Different mechanisms have been proposed to explain the sub-cellular spatiotemporal pattern formation, which are summarized below.

6.2.4.1. Discordant Ca^{2+} alternans as pattern formation via Turing instability: In a theoretical study by Shiferaw and Karma [300], a mechanism of sub-cellular discordant Ca^{2+} alternans has been proposed, in which a Turing instability [301] is responsible for the pattern formation. Following their amplitude equation for APD alternans in tissue [302, 303], they have developed a set of equations composed of two amplitude equations: one for APD alternans and the other for Ca^{2+} alternans. The equations are

$$\frac{d\Delta a}{dt}=\alpha\Delta a+\frac{\beta}{l}\int_0^l\Delta c(x,t)dx \quad \frac{\partial\Delta c}{\partial t}=\delta\Delta c+\gamma a+\frac{\mu}{l}\int_0^l\Delta c(x,t)dx-\chi\Delta c+D_c\frac{\partial^2\Delta c}{\partial x^2} \quad (60)$$

where $\Delta a=a_{n+1}-a_n$ is the difference in APD between two consecutive beats, called APD alternans amplitude. Since the diffusion of voltage in a single cell is almost instantaneous, Δa does not depend on space. $\Delta c(x,t)=c_{n+1}-c_n$ is the amplitude of Ca^{2+} alternans which is a function of both time and space. Time $t=n\tau$ with τ as the period of pacing; D_c is proportional to the intracellular Ca^{2+} diffusion constant; l is the length of the cell; α, β, γ, δ, μ, and χ are parameters.

It can be shown [300] using Eq.60 that depending on the coupling conditions between Ca^{2+} and voltage, a Turing instability can occur in this system. The specific condition for this instability to occur is

$$\beta\gamma<0 \text{and} \delta+\mu-\alpha>0 \quad (61)$$

The signs of β and γ define the coupling conditions between Ca^{2+} and voltage. $\beta>0$ indicates positive Ca^{2+}-to-APD coupling, and $\beta<0$ indicates negative Ca^{2+}-to-APD coupling. $\gamma>0$ indicates positive APD-to-Ca^{2+} coupling, and $\gamma<0$ indicates negative APD-to-Ca^{2+} coupling. Therefore, based on Eq.61, a Turing instability can occur when Ca^{2+}-to-APD coupling is negative while APD-to-Ca^{2+} coupling is positive, or Ca^{2+}-to-APD coupling is positive while APD-to-Ca^{2+} is negative. Shiferaw and Karma [300] have demonstrated in a mathematical model with computer simulations that under conditions of positive Ca^{2+}-to-APD coupling ($\beta>0$), only concordant alternans can be observed while under conditions of negative Ca^{2+}-to-APD coupling ($\beta<0$) discordant alternans can develop (Fig.30a).

In most realistic conditions, both Ca^{2+}-to-APD and APD-to-Ca^{2+} couplings are positive, and thus the Turing instability may not occur naturally in real cells. In recent studies by Gaeta et al [270, 304], the authors used a feedback control protocol to change the APD-to-Ca^{2+} coupling from positive to negative while maintaining the Ca^{2+}-to-APD coupling positive to cause a Turing instability inducing discordant Ca^{2+} alternans. They first showed in simulation that sub-cellular discordant Ca^{2+} alternans could develop after they changed APD-to-Ca^{2+} coupling from positive to negative. They then applied the same feedback control mechanism to a real ventricular myocyte to show that this control algorithm indeed caused the transition from concordant alternans to discordant alternans (Fig.30b), demonstrating experimentally that the Turing instability induced spatially discordant alternans.

6.2.4.2. Other mechanisms of sub-cellular discordant Ca^{2+} alternans: Although the Turing instability demonstrated by Shiferaw and Karma [300] and by Gaeta et al [270, 304] is a beautiful application of nonlinear dynamics to cardiac systems, it is not the only mechanism for sub-cellular discordant Ca^{2+} alternans. In an experimental study by Diaz et al [265], discordant Ca^{2+} alternans was observed under voltage clamp conditions, in which the Ca^{2+} and voltage are uncoupled, indicating that other mechanisms are responsible. In a study by Aistrup et al [269], it was shown that heterogeneity in Ca^{2+} release properties can result in spatially discordant Ca^{2+} alternans due to phase mismatch in the neighboring regions. In a study by Xie and Weiss [268], it was shown that a Ca^{2+} wave occurring during pacing can reverse the phase in one region, causing phase mismatch in neighboring regions which results in spatially discordant alternans. Another mechanism involves a self-organization process in a random system with positive feedback (e.g., CICR), such that clusters of elements of the same dynamics can form in space [305]. In our spatially-extended Ca^{2+} cycling models [283, 291], we observed the same dynamical clustering phenomenon which results in patches of regions alternating out-of-phase. A similar process was seen in the study by Tian et al [271] in which multiple out-ofphase alternating regions exist. This might also be responsible for the discordant Ca^{2+} alternans seen by Diaz et al [265].

6.3. Early afterdepolarizations

6.3.1. Early afterdepolarizations and irregular dynamics—EADs are voltage oscillations occurring at the plateau phase of the action potential [306]. EADs are often associated with life-threatening arrhythmias such as Torsade de Pointes in the setting of cardiac diseases [307–309], including acquired and congenital long QT syndromes [310, 311] and heart failure [312, 313]. EADs were identified more than a half century ago [307, 314, 315] and have been the subject of many experimental and computational studies. It is known that EADs occur when outward currents are reduced and/or inward currents are increased, causing APD to be longer. However, drugs lengthening APD by increasing inward currents [316, 317] or reducing outward currents [318–320] do not always cause EADs. Conversely, some drugs cause EADs without significantly prolonging APD. Figure 31a shows EADs recorded from a single myocyte isolated from the ventricles of a transgenic long QT rabbit [311], illustrating the voltage oscillations during the plateau phase. These oscillations eventually cease, allowing the myocyte to repolarize. The amplitude of the oscillation varies with time, and, in many cases, the last EAD before full repolarization has the largest amplitude. Therefore, the key to understanding the mechanism of EADs is to understand the transient oscillations.

Another property of EADs is that the number of oscillations in the action potential varies from beat to beat in an irregular manner, which also causes large APD variations (Figs.31 b and c). One hypothesis is that this irregular behavior is caused by stochastic ion channel noise [321]. However, this type of irregular behavior does not occur in normal action potentials, only when EADs are present, raising the question of what is special about the action potential dynamics when EADs are present.

Recent studies [166, 253, 322–324] have developed a nonlinear dynamical theory for EADs and showed that EADs arise from a dual Hopf-homoclinic bifurcation, and that chaos is responsible for the irregular appearance of EADs. This theory is summarized in the following sections.

6.3.2. A bifurcation theory of EADs—A basic bifurcation theory of EADs was developed using a simple action potential model, the LR1 model, by Tran et al [322]. The model includes I_{Na}, $I_{Ca,L}$, I_K, and other time-independent K^+ currents. The equation for voltage is

$$C_m \frac{dV}{dt} = -[\overline{G}_{Na} m^3 hj(V-E_{na}) + \overline{G}_{Ca} df(V-E_{Ca}) + \overline{G}_K x x_1(V-E_K) + I_0(V)] \quad (62)$$

where *m, h, j, d, f*, and *x* are gating variables, and $I_0(V)$ is the summation of all other currents that change with voltage instantaneously. By altering the parameters (e.g., $\overline{G}_{Ca}$), EADs can occur in this model.

During an action potential of a myocyte, individual ionic currents activate and inactivate over different time scales, ranging from milliseconds to seconds. This type of system, called a fast-slow system, can exhibit complex dynamics [124, 325]. EADs have fast dynamics relative to the slow phase of action potential repolarization. The standard mathematical tool for analyzing fast-slow dynamics is to use the slow variable as a bifurcation parameter to study bifurcations in the fast subsystem. This approach has been widely adopted to study bursting dynamics in neurons and pancreatic β-cells [124, 325].

To perform a fast-slow dynamics analysis, one first needs to separate the fast and slow subsystems. In the LR1 model, all other currents except for I_K, can be considered to belong to the fast subsystem. Assuming that all of these currents reach their steady-state quickly in response to a voltage change, one can define a quasi-steady state current (I_{QSS}) as a function of voltage (i.e., quasi-steady state I-V curve, a frequently used classical technique in electrophysiology [317, 326]). This is calculated for the LR1 model as:

$$I_{QSS}(V,x) = \overline{G}_{Na} m_\infty^3 h_\infty j_\infty (V-E_{Na}) + \overline{G}_{Ca,L} d_\infty f_\infty (V-E_{Ca}) + I_0(V) + \overline{G}_K x x_1 (V-E_K) \quad (63)$$

in which the variables with the "∞" subscript are the steady state values at the corresponding voltage. *x* is the slow variable since the time constant of *x* is much longer than others. Since the steady state of I_{Na} in this model is almost zero at any voltage, its contribution to I_{QSS} is negligible. Figure 32a shows I_{QSS} versus *V* for different *x* values. When *x*=0, there are three voltages at which I_{QSS}=0, indicating that three fixed points exist, which we call quasi-steady states. As *x* increases, the fixed points at high voltages (the s- and p-states) disappear, leaving only one fixed point (the r-state) which is the resting potential. Therefore, if *x* grows slowly, the s- and p-states remain longer. If *x* grows slowly enough, the system will tend to approach the p-state. Depending on the stability of the p-state, different action potential behaviors can occur. When the p-sate is stable, the voltage will simply follow the change of the p-state as x grows until the p-state disappears, at which the voltage repolarizes to the resting potential. This process can result in ultralong action potentials [253], as have been observed in many experiments [316–318]. When the p-state is an unstable focus, the system will oscillate around the p-state, resulting in voltage oscillations at the plateau voltage, which are EADs. Note that transient oscillations can occur when the p-state is a stable focus, which can also result in EADs. If x grows fast or if the p-state does not exist (which occurs when the steady-state inward current is small or zero), the action potential repolarize normally.

A key question is whether such an instability can occur and, if so, what determines it. To analyze the stability of the p-state, Tran et al [322] used a reduced system in which I_{Na} was neglected since it is almost zero at the plateau voltage. The equation for voltage becomes

$$\frac{dV}{dt} = -[\overline{G}_{Ca} df(V-E_{Ca}) + \overline{G}_K x x_1 (V-E_K) + I_0(V)]/C_m = F(V,d,f) \quad (64)$$

The gating variables d and f are described by

$$\frac{dd}{dt} = [d_\infty - d]/\tau_d \quad (65)$$

and

$$\frac{df}{dt} = [f_\infty - f]/\tau_f \quad (66)$$

where d_∞ is the steady state activation curve of $I_{Ca,L}$ which is a sigmoidal function increasing with V, and f_∞ is the steady state inactivation curve, which is a sigmoidal function decreasing with V. x in Eq.64 is treated as a parameter in the stability analysis. As shown in Fig.32a, the steady state solutions of Eqs.64–66 depend on x. When x is large, there is only one solution, which is the resting potential. When x is small, there are three solutions. The stability of these solutions can be determined from the following Jacobian:

$$J = \begin{pmatrix} a & b & c \\ s_d/\tau_d & -1/\tau_d & 0 \\ -s_f/\tau_f & 0 & -1/\tau_f \end{pmatrix} \quad (67)$$

where $a=\partial F/\partial V$, $b=\partial F/\partial d$, $c=\partial F/\partial f$, $s_d=\partial d_\infty/\partial V$, and $s_f=-\partial f_\infty/\partial V$. $b>0$ and $c>0$ for $V<E_{Ca}$, and $s_d>0$ and $s_f>0$ for any V.

The condition of a Hopf bifurcation can be worked out analytically by solving the characteristic equation and obtaining the eigenvalues of J. However, at the Hopf bifurcation point, two of the three eigenvalues are $\lambda_{1,2}=\pm i\omega$. Inserting these values into the characteristic equation, one obtains the following conditions:

$$\omega^2 = \frac{1}{\tau_d \tau_f} - \frac{a}{\tau_d} - \frac{a}{\tau_f} - \frac{s_d b}{\tau_d} + \frac{s_f c}{\tau_f} > 0 \quad (68)$$

and

$$h=\frac{1}{\tau_f}(\frac{1}{\tau_f}-a)(\frac{1}{\tau_d}-a+s_fc)+\frac{1}{\tau_d}(\frac{1}{\tau_d}-a)(\frac{1}{\tau_f}-a-s_db)=0 \quad (69)$$

The p-state is unstable when $h<0$. Therefore, for a Hopf bifurcation to occur, h needs to change from positive to negative. Even though Eq.69 is complex, important information relevant to the biological properties required for the Hopf bifurcation can be extracted. Since all parameters in Eq.69 are positive except for a, and $a<0$ when $V>-30$ mV, then a large s_d is required for h to be negative. This can occur when the p-state is in the steep range of the activation curve of $I_{Ca,L}$. A slower inactivation process (larger τ_f) or a faster activation process (smaller τ_d) tends to make h negative, promoting the Hopf bifurcation.

Figure 32b shows the stability of the three quasi-steady states versus x, showing that the r-state is always stable and the s-state is always unstable (saddle point), while a Hopf bifurcation occurs for the p-state leading to oscillations. The amplitude of the oscillation increases as x increases until the orbit meets the saddle point (the s-state) at which a homoclinic bifurcation occurs. During an action potential with EADs, voltage oscillations manifesting as EADs occur due to the Hopf bifurcation and terminate via the homoclinic bifurcation (red trace in Fig.32b). One of the characteristic features of the dual Hopf-homoclinic bifurcation is that the oscillation amplitude increases while the oscillation frequency decreases. This feature can be clearly seen in Fig.32b. This behavior was also demonstrated in an experimental system in a recent study [324], which shows that the frequency decreases during the oscillations (Fig.32c).

However, the presence of quasi-steady states and a Hopf bifurcation in the fast subsystem is not sufficient to result in EADs [306, 322]. Whether EADs occur or not during an action potential also depends on the initial time course of the variables which bring the system into the basin of attraction of oscillations around the p-state. For example, in the two traces in Fig.32b, the only difference is that the blue one has a faster x gate, which misses the basin of attraction of the oscillations, resulting in no EADs, even though the bifurcations in the fast subsystem remain unchanged. On the other hand, adding a transient outward current (I_{to}) to accelerate voltage decay during phase 1, which exhibits almost no effect on the Hopf bifurcation, can bring the system into the basin of attraction of the oscillations, promoting EADs [306, 322].

The nonlinear dynamical analyses demonstrate that three conditions need to be satisfied to suffice the occurrence of EADs: 1) the formation of quasi-steady states in the plateau voltage range, which requires increased steady-state inward currents or decreased steady-state outward currents; 2) a Hopf-homoclinic bifurcation to cause and then terminate oscillations, which depends on both a steep activation curve and the p-state forming in the steeply sloped region; 3) a proper initial time course of the variables to bring the system into the basin of attraction of the oscillations arising from the Hopf bifurcation, which depends on the magnitudes and time constants of the transient components of the ionic currents. Using the dynamical theory of EADs, one can provide an integrative overview of the contributions of each ionic currents to the genesis of EADs and a unified interpretation of experimental observations, which has been reviewed by Qu et al in a recent article [306].

However, the mechanism summarized above may be only one of the mechanisms of EAD formation in cardiac myocytes, and other mechanisms may also exist [306]. For example, when Ca^{2+} oscillates in the cell, voltage will also oscillate in response, manifesting as EADs [108, 327]. Moreover, the coupling of voltage and Ca^{2+} may modulate the Hopf-homoclinic bifurcation to promote and suppress EADs, or to result in novel instabilities for EADs, which need to be further investigated using computer simulations and bifurcation analyses.

6.3.3. Nonlinear EAD dynamics—An important insight from the nonlinear dynamics of EADs is that the irregular beat-to-beat appearance of EADs observed in experiments is dynamical chaos. This has been shown in computer simulations and supported by experimental data [166, 322]. Figures 33 a and b show voltage recordings and a bifurcation diagram obtained from a computer simulation of an action potential model, illustrating that irregular action potential dynamics (chaos) occurs at the intermediate range of PCL. Figures 33 c and d show voltage recordings and a bifurcation diagram obtained from a ventricular rabbit myocyte treated with drugs, which also shows that the irregular behavior occurs in the intermediate range of PCLs. Although it is difficult to show that the irregular behavior shown in the experiments is frank chaos due to technical limitations including record length and noise, one can argue that if random noise is responsible for the irregular behavior, why does it not occur at long PCLs at which EADs also present? The similarity between the bifurcation diagrams of simulation and experimental data leads one to conclude that the irregular behavior seen in experiments is also chaos even though noise may contribute to the irregularity. Indeed, when random ion channel fluctuations were added to the computer model (Fig.33e), the bifurcation diagram remains similar [323]. Random noise causes the onset of irregular behavior at a shorter PCL but does not affect the inverse bifurcation point. It can be shown that the noise-induced irregularity is still chaotic [323], agreeing with the well-known mechanism of noise-induced chaos in nonlinear dynamical systems [328–331].

The mechanism of chaos in the presence of EADs can be analyzed following the same iterated map approach used in analyzing APD alternans. In the presence of EADs, the APD restitution curve exhibits a discontinuity. As shown in Fig.34a, following the same S1 beat, a 1 ms difference in DI can result in two very different action potentials, where one exhibits an EAD, while the other does not. The APD restitution curve is shown in Fig.34b, and is discontinuous and non-monotonic. By iterating the map using the same map equations as in Eq.46, one can obtain different dynamical behaviors, including alternans and chaos (Fig. 34c) [166, 323].

6.4. Delayed afterdepolarizations

Whereas EADs are secondary depolarizations during an action potential, DADs are depolarizations that follow repolarization after a stimulated action potential. DADs are easier to induce in diseased hearts than in normal hearts, and sometimes occur irregularly (Fig.35a) [332]. The dominant theory of DADs is that they are caused by spontaneous Ca^{2+} waves (Fig.35b) [333], which has been demonstrated in many experiments. During a Ca^{2+} wave, Ca^{2+} concentration is elevated, which increases I_{NCX} and other Ca^{2+}-sensitive currents. Since I_{NCX} is an inward current, it causes a voltage elevation. If the voltage elevation does not reach the threshold for I_{Na} activation, there is only a small voltage deflection (Fig.35b). Once it reaches the threshold of I_{Na} activation, an action potential is elicited (Fig.35a). As discussed in Section 5, the formation of Ca^{2+} waves is a self-organizing process, exhibiting large fluctuations. Thus, the occurrence of DADs is irregular, as can be seen in Fig.35a. DADs are a known cause of PVCs but how they induce arrhythmias at the tissue level still remains to be elucidated.

7. Electrical wave dynamics in tissue and organ

An excitable medium can support propagation of an undamped solitary wave or a train of solitary waves. In addition, spiral and scroll waves are also wave solutions of an excitable medium. Complex spiral wave and scroll dynamics have been widely investigated in generic excitable media. Cardiac tissue is an excitable medium and most of the wave conduction properties of generic excitable medium are also applicable to cardiac tissue. However, cardiac tissue also exhibits its own special dynamical properties because of the complex cellular dynamics and tissue structures. In this section, we summarize: 1) the basic properties of electrical wave conduction in cardiac tissue, including the effects of gap junction coupling and curvature; 2) the dynamical mechanisms for the formation of spatially discordant APD alternans and pattern formation due to failure of synchronization of cellular chaotic dynamics; 3) different mechanisms of reentry induction; 4) dynamical stability and bifurcations of anatomical reentry and spiral wave reentry; 5) the effects of tissue thickness, fiber rotation, and excitability on scroll wave stability; 6) reentry dynamics in real cardiac tissue observed in experiments; 7) bistable spiral wave and conduction; and 8) the mechanisms of formation of focal excitations in tissue. We discuss how cellular action potential dynamics manifest and how new spatiotemporal dynamics emerge at the tissue and organ scales to promote arrhythmias.

7.1. Basic properties of wave conduction in cardiac tissue

Waves in excitable medium can be planar (or rectilinear) or curved (Fig.36a). For a planar wave, the CV (θ) is proportional to the square root of *D*, i.e.,

$$\theta \propto \sqrt{D} \quad (70)$$

where *D* is the diffusion constant which is determined by the intracellular resistance and gap junction resistance in cardiac tissue (see Eq.25). This relation holds for continuous and homogeneous medium since the reaction-diffusion equation $\frac{\partial u}{\partial t}=f(u)+D\frac{\partial^2 u}{\partial x^2}$ is invariant under the rescaling relation $x'=x\sqrt{D}$, and thus $\theta=\frac{dx}{dt}=\sqrt{D}\frac{dx'}{dt}$. However, due to the finite size of cardiac myocytes, cardiac tissue is not a continuous excitable medium like a generic reaction-diffusion system, but rather a discretized medium. The scaling relation may still hold when the myocytes are well coupled (Fig.36b), but not when the gap junction resistance is large (diffusion constant is small). The discretized effects on conduction in cardiac tissue have been investigated in many modeling studies [149, 334–339]. Note that in a truly continuous medium, due to the scaling property, conduction never fails as *D* decreases. But in a discretized system, reduction of the gap junction conductance (thus *D*) can result in conduction failure. Therefore, cell decoupling alone, even if it is only partial, can result in conduction failure in real cardiac tissue.

CV also depends on excitability, which is strongly dependent on the magnitude of I_{Na} and the resting potential. Figure 36c plots θ versus the maximum conductance ($\bar{G}_{Na}$) of I_{Na}, showing that θ increases almost linearly with log$\bar{G}_{Na}$. There are many other factors affecting CV in cardiac tissue, such as cell size, anisotropy, heterogeneous cell-to-cell coupling, microscopic tissue structures, and myocyte-fibroblast coupling.

For a curved wave, the relation between CV and curvature obeys the so-called eikonal relation [88]:

$$\theta=\theta_0-D\kappa \quad (71)$$

where θ_0 is the planar wave velocity and κ is the wavefront curvature. A convex wave ($\kappa>0$) propagates more slowly than a planar wave while a concave wave ($\kappa<0$) propagates faster. Later studies showed that this relation needs to be modified [102, 340, 341], i.e.,

$$\theta=\theta_0-\gamma D\kappa \quad (72)$$

in which γ is a parameter dependent on other factors, such as PCL and the diffusion constant.

During a wave train, the conduction velocity also depends on the period T of the wave train, which is called the dispersion relation [90, 342], i.e.,

$$\theta=g(2\pi/\omega)=g(T) \quad (73)$$

In cardiac tissue, we call this the CV restitution curve, analogous to APD restitution curve [101], which is denoted as

$$\theta_{n+1}=g(d_n) \quad (74)$$

Figure 36d shows a CV restitution curve calculated from a numerical simulation of an action potential model. The action potential fails to conduct when the CV is reduced to a critical but finite velocity (θ_c).

The wave curvature affects not only CV but also APD [102, 343]. The relationship between APD and curvature can be approximated for small curvatures as

$$a=a_0+\beta\kappa \quad (75)$$

For large curvatures, this relationship becomes nonlinear [343].

The wavefront curvature and CV restitution are two properties that play important roles in cardiac conduction and dynamics, such as conduction block [338, 344], spiral wave formation [88], the onset of APD alternans [339], formation of spatially discordant APD alternans [65], and quasi-periodic dynamics [345].

7.2. Dynamical repolarization pattern formation in tissue

7.2.1. Spatially discordant alternans—APD and Ca^{2+} alternans observed in isolated myocytes also occur in tissue, but new spatiotemporal dynamics can arise via pattern formation. Under some conditions, all cells in the tissue may alternate in the same phase (in-phase), resulting in spatially concordant alternans. Under other conditions, cells in one region may alternate in the opposite phase (or antiphase) to the cells in neighboring regions, resulting in spatially discordant alternans. Figure 37a shows a transition from spatially concordant alternans to discordant alternans recorded in a guinea pig heart in experiments by Pastore et al [64]. At a slower pacing rate, APD in the entire tissue alternates in-phase, i.e., the APD in the entire tissue exhibits the same *long-short-long-short* … pattern, which is spatially concordant. As the pacing rate increases, APD alternates in opposite phases in neighboring regions, forming spatially discordant alternans with one region exhibiting a *long-short-long-short* … pattern while the adjacent region exhibiting a *short-long-short-long* … pattern. The border between the two regions forms a nodal line at which APD does not change from beat to beat. This same transition can be recapitulated in computer simulations (Fig.37b). In a large tissue, multiple nodal lines can form, as shown in a simulation in a 1D cable (Fig.37c). Discordant alternans was first observed by Konta [346] and later demonstrated in many experimental studies in intact hearts [64, 260, 347–354], monolayers of cultured myocytes [355], and clinical studies [356, 357]. TWA has been closely associated with cardiac arrhythmias and SCD, and a mechanistic link can be established by the studies [64, 65, 347] showing that spatially discordant APD alternans promotes reentry, in which the large spatial APD gradient caused by discordant APD alternans provides a substrate for reentry initiation.

Several mechanisms of spatially discordant alternans have been postulated. The prevailing one is the engagement of CV restitution, which was first shown in a study by Cao et al [347] and then in theoretical and simulation studies by others [65, 302, 303, 358]. Specifically, when there is no CV restitution engagement, i.e., CV is constant, alternans due to instabilities from either voltage or Ca^{2+} is spatially concordant. When CV restitution is engaged, discordant alternans will develop with the wavelength depending on the slope of the CV restitution curve. This mechanism predicts that as the PCL shortens, the nodal lines move toward the pacing site [359, 360], which was later shown experimentally [349, 350], supporting this mechanism.

The role of CV restitution in discordant alternans can be understood using a kinematic equation for conduction in a 1D cable, which was first analyzed by Qu et al [65]. Assuming that a 1D cable is periodically paced at one end (x=0) with a period T_0, the time interval between two consecutive beats at a location x, $T_n(x)$, can be calculated as,

$$T_n(x)+T_0+\int_0^x \frac{ds}{\theta_{n+1}(s)}-\int_0^x \frac{ds}{\theta_n(s)}=a_n(x)+d_n(x) \quad (76)$$

In other words, $T_n(x)$ equals to T_0 plus the difference between the times taken for the two consecutive waves to reach x. Note that the two waves conduct in different velocities so that $T_n(x)$ changes in space, otherwise $T_n(x)=T_0$. $T_n(x)$ also equals to APD plus DI (see definition in Fig.23a). The conduction velocity θ at location x is computed using the CV restitution function as

$$\theta_{n+1}(x)=g[d_n(x)]=g[T_n(x)-a_n(x)] \quad (77)$$

where the APD at location x, $a_n(x)$, is computed from the APD restitution function as

$$a_{n+1}(x)=f[d_n(x)]=f[T_n(x)-a_n(x)] \quad (78)$$

Discordant APD alternans can be easily simulated using Eq.76 with appropriate APD and CV restitution functions [361–363].

To gain insights into the role of CV restitution in the formation of discordant alternans [65], one rewrites Eq.76 as

$$T_n(x)=T_0-\int_0^x \frac{\theta_{n+1}-\theta_n}{\theta_{n+1}\theta_n}ds=T_0-\int_0^x \frac{\Delta\theta_n(s)}{\theta_{n+1}\theta_n}ds=T_0-\Delta T_n(x)=a_n(x)+d_n(x) \quad (79)$$

If there is no CV restitution, i.e., $\theta_{n+1}(x)=\theta_n(x)$=constant, then $\Delta\theta_n(x)=\theta_{n+1}(x)-\theta_n(x)=0$, and thus $\Delta T_n(x)=0$. Therefore, every cell sees the same PCL T_0 and must alternate uniformly in space. But if, for a PCL T_0, APD alternans occurs and CV restitution is engaged, then assuming that the system is in a stable in-phase alternating state and $a_{n+1}(x)>a_n(x)$ for any x, one can derive using Eq.79

$$T_0-\Delta T_n(x)-a_n(x)>T_0-\Delta T_{n+1}(x)-a_{n+1}(x) \quad (80)$$

Rearranging Eq.80, one obtains

$$\Delta a_n(x)=a_{n+1}(x)-a_n(x)>2\Delta T_n(x)=2\int_0^x \frac{\Delta\theta_n(s)}{\theta_{n+1}(s)\theta_n(s)}ds>0 \quad (81)$$

Uniform concordant alternans, in which $\Delta a_n(x)$ is constant over space, is impossible, since the integral in Eq.81 increases with x ($\Delta\theta_n(x)>0$ based on the concordant assumption). Non-uniform concordant alternans can exist when $\Delta\theta_n(x)$ and/or x, are small, for which Eq.81 can be satisfied. However, when either $\Delta\theta_n(x)$ or x is large, the integration in Eq.81 becomes larger and larger as x increases. However, $\Delta a_n(x)$ cannot increase with x indefinitely but must be finite. Therefore, the assumption that spatially concordant alternans exists in the presence of CV restitution cannot hold, and thus $\Delta\theta_n(x)$ must change its sign along x. This means that $\Delta a_n(x)$ must change sign along x, resulting in discordant alternans.

In the model above, APD and CV restitution are integrated, but the effects of diffusive coupling on APD are ignored. This effect can be taken into account by adding a coupling term into the equation, as shown in a study by Wang et al [363].

A more rigorous analysis of the instability leading to discordant APD alternans was performed by Echebarria and Karma [302, 303] who developed an amplitude equation starting with an equation similar to Eq.76 with diffusive APD coupling. The amplitude equation they obtained is:

$$\tau\frac{\partial\Delta a}{\partial t}=\sigma\Delta a-g\Delta a^3+\xi^2\frac{\partial^2\Delta a}{\partial x^2}-w\frac{\partial\Delta a}{\partial x}-\frac{1}{\Lambda}\int_0^x\Delta a(s,t)ds \quad (82)$$

where $\Delta a(x,t)=a_{n+1}(x)-a_n(x)$ is the amplitude of APD alternans (See Refs. [302, 303] for derivation of the equation and definitions of the parameters). Using a periodic boundary condition and linear stability analysis, one can obtain the eigenvalues for the steady state of Eq.82, from which it can be demonstrated that both standing patterns (the node is stationary) and traveling patterns (the node is moving) can exist. The wavelength of the two patterns can be estimated as

$$\lambda=\begin{cases}2\pi(w\Lambda)^{1/2}(\text{standing nodes})\\ 4\pi/\sqrt{3}(\xi^2\Lambda)^{1/3}(\text{traveling nodes})\end{cases} \quad (83)$$

The second mechanism of spatially discordant alternans is a spatial instability when Ca^{2+}-to-APD coupling is negative and alternans is Ca^{2+}-driven [364]. In this mechanism, CV restitution is not required. The negative Ca^{2+}-to-APD coupling can cause Ca^{2+} amplitude in two neighboring cells to alternate out-of-phase. Due to the electrotonic coupling, APD alternates out-of-phase over a much large spatial scale. Since Ca^{2+} and voltage are bidirectionally coupled, if one of the two systems forms spatially discordant alternans, then the other will also be spatially discordant. Certain distinct spatial properties of Ca^{2+} alernans amplitude in spatially discordant alternans have also been shown when alternans is driven by Ca^{2+} cycling instabilities [298, 365].

Spatially discordant APD alternans can be initiated by a premature stimulation [358] or by the pre-existing heterogeneities [349]. However, based on the current theories, if no CV restitution or no spatial instability is engaged, the induced nodal lines by a premature stimulation or heterogeneities cannot be stable. The nodal lines will eventually disappear and alternans becomes spatially concordant [349]. Therefore, premature stimulation or pre-existing heterogeneities help to induce discordant alternans, but CV restitution or dynamical spatial instability is needed to maintain discordant alternans. On the other hand, more complex spatial patterns of discordant APD alternans have been shown in experiments [353, 354], which remain to be elucidated by theories of nonlinear dynamics.

7.2.2. Chaos synchronization—Besides discordant APD alternans, dispersion of refractoriness develops in homogenous tissue when chaos is present in single myocytes. It is well studied in nonlinear dynamics that two chaotic systems desynchronize when they are weakly coupled [366]. This conclusion was extended to arrays of coupled chaotic oscillators [367]. As discussed earlier in this article, there are several mechanisms for cardiac cells to exhibit chaotic behaviors, which can desynchronize to induce large dispersion of refractoriness, forming a substrate for reentry [242]. Figure 38a shows voltage evolution in time in a 1D cable of coupled cells paced simultaneously, showing desynchronization of voltage and formation of chaotic spatial patterns. Synchronization depends on tissue size and the gap junction coupling. Synchronization fails when the tissue is greater than a critical size or the gap junction coupling strength becomes smaller than a critical value. Figure 38b shows the standard deviation of voltage over the cable versus the cable length L, demonstrating that synchronization fails after L exceeds a critical size (L_c). L_c can also be predicted by calculating the maximum Lyapunov exponent versus the wave number (Fig. 38c) using single cell simulations [242], i.e., $L_c = 2\pi / k_c$ for a periodic boundary condition. k_c is the wave number at which the Lyapunov exponent crosses zero. The same dynamics can be observed when chaos is caused by EADs [166]. Figure 38d shows APD distribution for three consecutive beats after a certain number of pacing beats in a 2D tissue model, in which chaos is caused by the presence of EADs. In this case, EAD islands form in tissue and the APD distribution changes from beat to beat chaotically.

Chaos synchronization in cardiac tissue can be further studied by coupled iterated maps. Coupled iterated maps were constructed in a theoretical study by Wang et al [363] to study chaos synchronization and discordant alternans in coupled cardiac cells. One of these coupled maps is:

$$a_{n+1}(i)=f[d_n(i)]+\varepsilon\sum_{j=1}^{\alpha}w_j\left\{f[d_n(i+j)]+f[d_n(i-j)]-2f[d_n(i)]\right\}, \quad (84)$$

where f is the APD restitution function, w_j is a Gaussian function, i.e., $w_j=\frac{e^{-j^2/2\sigma^2}}{\sqrt{2\pi}\sigma}$, which defines the range and the weight of coupling, α the maximum number of neighbors, and ε the coupling strength. The spatial stability of the uniform state can be analyzed by calculating the Lyapunov exponent as a function of wave number k, which can be analytically obtained for this model as

$$\lambda_k=\lambda_0+\ln\left|1-4\varepsilon\sum_{j=1}^{\alpha}w_j sin^2\frac{\pi jk}{L}\right| \quad (85)$$

where λ_0 is the Lyapunov exponent of the single cell, which depends on the APD restitution property and PCL. Once λ_0 is known, one can predict the characteristic wavelength or the critical size which is determined by the minimum k (k_c) that makes $\lambda_k \leq 0$, i.e., the critical size is $L_c=2\pi/k_c$. The iterated map predictions agree well with those from the ionic model [363].

7.3. Initiation of reentry

A clinically important issue is how arrhythmias are initiated in the heart, since understanding the underlying mechanisms may lead to the development of effective therapeutics to prevent arrhythmias. Both planar wave and spiral wave (or reentry) are solutions of an excitable medium. In other words, the heart, as an excitable medium, can always have two solutions: a planar wave solution (e.g., the sinus beat in the heart) and a spiral wave (or a reentry) solution, as long as the tissue size is large enough to accommodate a spiral wave. The transition from sinus rhythm to reentry requires that the system moves from the basin of attraction of the planar wave solution to the basin of attraction of a spiral wave solution (or reentry around an obstacle). The transition from a planar wave to a spiral wave also needs a symmetry break, which was first pointed out by Winfree, who noted that

SCD is a problem of topology [3]. In the normal heart, breaking the symmetry of a planar wave to initiate a spiral wave requires a very large perturbation, such as an electrical shock. In diseased heart, the basin of attraction of the planar solution is reduced while that of the spiral wave solution is increased, so that the threshold for the transition is much lower. Therefore, symmetry breaking and basins of attraction are two important dynamical behaviors that responsible for the initiation of arrhythmias. Here we summarize the different scenarios and the underlying dynamics with which arrhythmias can be initiated.

7.3.1. Reentry around an obstacle—Reentry was first demonstrated in an annulus of cardiac tissue [68], and the formation of reentry around an obstacle is well understood in cardiology. Figure 39 is a text-book schema of reentry formation around an obstacle. Consider a cardiac tissue with an obstacle (scar tissue or a vascular structure). A planar wave, a sinus rhythm or a PVC, can successful propagate both sides of the obstacle if the refractory period of the tissue is uniform (Fig.39a). However, if the tissue is heterogeneous and the refractory period in a region in the right pathway is longer than that of the remaining tissue, an appropriately timed premature impulse will not be able to propagate through the right pathway, but will successfully propagate through the left pathway and reenter the right pathway in the retrograde direction. If the impulse from the left pathway reaches the right pathway too early so that the right pathway is still in refractory, it cannot propagate through the right pathway (Fig.39b). If the delay is long enough for the right pathway to have recovered, the impulse can then reenter the left pathway and continue to circulate around the obstacle, forming a reentry (Fig.39c). In other words, a PVC entering into the pathways too early or too late cannot induce reentry, but a PVC in a certain time interval can induce reentry. This time interval is called vulnerable window.

7.3.2. Induction of reentry by a strong stimulus—Applying a strong stimulus to either a normal heart or a diseased heart, such as an electrical shock [80] or a mechanical impact [368, 369], can cause ventricular arrhythmias and SCD. It has been demonstrated in many experiments [80, 81, 370, 371] that reentrant arrhythmias can be induced by a properly-timed strong electrical stimulus delivered during the T-wave in the normal heart. A theory for the initiation of reentry by strong electrical stimulation from a point electrode was first proposed by Winfree [3, 73, 74] who called it the “pinwheel experiment” or “singular point hypothesis,” later called the “critical point hypothesis” by Frazier et al [81]. Figure 40a is a schematic plot illustrating the mechanism. At a critical time T_c, an electrical stimulus (S2) is applied from a point electrode, which occurs during the repolarization phase of a rectilinear (S1) wave, such as a sinus beat. This stimulus depolarizes a spatial domain of critical size A_c. The S2 excitation cannot propagate in the same direction of the S1 beat, since the tissue in this region has not recovered, but can propagate downwards where the tissue has recovered. At the boundary of propagation and non-propagation of the S2 beat, two singularities (wavebreaks) form, which subsequently turn inwards and attempt to form counter-rotating spiral waves. “Figure-of-eight” reentry results if the two spiral wave tips have enough room to form a central common conduction pathway. However, if the S2 depolarizes a spatial domain smaller (because of a weaker strength) than the critical area, or if the S2 is given too early or too late, the two spiral wave tips will collide and annihilate (annihilation occurs if the two dashed circles in Fig.40a intersect). This is demonstrated in

Fig.40b which shows once a large enough area is depolarized by S2, reentry forms. However, if the area is too small, the two tips collide and no reentry forms. If S2 depolarizes the whole recovered tissue, then no singularities can form and thus no reentry can form. Based on these arguments, reentry can only be induced in a certain time window and with a certain S2 strength range. Figure 40c shows the vulnerable window in a coupling interval and stimulation strength plot obtained from experiments of a dog ventricular tissue by Gotoh et al [371].

Cardiac tissue includes an intracellular space and an extracellular space which exhibit different conductivities and anisotropic ratios. Models that take into account the conductivities in both spaces are called bidomain models [159]. Novel electrical behaviors have been shown to occur in bidomain models responding to a strong stimulus. A strong point stimulus causes virtual electrodes, consisting of cathodal and anodal regions in a “dog bone” pattern [160]. This pattern was demonstrated in experiments of cardiac tissue [158]. Based on the new excitation properties of the bidomain model, Roth [372] extended the pinwheel experiment and showed that the bidoman effect would affect the size of the vulnerable period and number of rotors created. The effects of a bidomain model on rotor initiation have also been shown in real cardiac tissue [156]. In addition, APD and APD restitution can also affect the vulnerable window of arrhythmias caused by a strong stimulus, as indicated by computer simulations [373].

7.3.3. Unidirectional conduction block and reentry induced by premature excitations—In clinical settings, either electrical shocks or mechanical impacts are large extrinsic perturbations. But most arrhythmic events and SCDs occur spontaneously as a result of triggering events intrinsic to the heart. The prevailing theory is that a PVC (called a trigger) encounters proper tissue conditions (called a substrate) which results in reentry, leading to arrhythmias and SCD. A PVC is an early excitation in the heart, which is very different from the external strong stimulus. Unidirectional conduction block can occur when a PVC enters into a repolarizing region of a previous excitation and if the block is localized then reentry can form. Many simulation studies [65, 359, 361, 362, 374–385] and experimental studies [386–388] have carried out to investigate how a premature S2 beat induces unidirectional conduction block or reentry following the sinus rhythm (S1 beats) in heterogeneous tissue under various conditions.

The key to understanding how PVC induces reentry is unidirectional block, and the basic dynamics can be investigated using a 1D cable. An analytical treatment of the problem has been carried out by Qu et al [362, 381]. As illustrated in Fig.41a, assume that a premature S2 beat propagates in the same direction as the S1 beat. If the tissue is homogeneous, then the waveback velocity (Θ_1) of the S1 beat is the same as its wavefront velocity (θ_1). In this case, the wavefront velocity (θ_2) of the S2 beat is the same or slower than that of the S1 beat, and thus S2 can propagate safely. If there is an APD gradient (σ) in the tissue (Fig.41b), then Θ_1 of the S1 beat in the gradient region is slower than θ_1 due to the increasing refractory period, which can be slow enough so that the S2 beat collides with the waveback of the S1 beat and fails to propagate (Fig.41c). The relationship between Θ_1 and θ_1 can be derived as [65, 100, 381, 382]:

$$\Theta_1(x)=\frac{\theta_1(x)}{1+\theta_1(x)\sigma(x)} \quad (86)$$

where $\sigma(x) = \Delta a(x)/\Delta x$ is the spatial APD gradient of the S1 wave. The time interval (i.e., the DI) between the S2 wavefront and S1 waveback obeys the following differential equation:

$$\frac{d[d(x)]}{dx}=\frac{1}{\theta_2(x)}-\frac{1}{\Theta_1(x)} \quad (87)$$

where $d(x)$ is the DI preceding the S2 beat. If $\Theta_1<\theta_2$, $d(x)$ decreases with x, the S2 wavefront approaches the S1 waveback. If the difference is large, $d(x)$ will decrease to a critical value (see CV restitution in Fig.36d) at a certain location in the heterogeneous region, and thus the S2 beat fails to conduct through the heterogeneous region.

The time interval in which an S2 beat blocks somewhere in heterogeneous region is defined as the vulnerable window (w). w can then be analytically derived from Eq.87 using a piece-wise linear APD distribution as in Fig.41b and a CV restitution curve described by an exponential function as $\theta = \theta_0(1 - \delta e^{-(d-d_c)/\tau})$, which is [381]:

$$w=\Delta a-\frac{\tau}{1+\sigma\theta_0}\ln\frac{\sigma\theta_0^2}{\theta_c+\sigma\theta_c\theta_0-\theta_0} \quad (88)$$

where Δa is the refractory barrier, $\sigma=\Delta a/h$ is the APD gradient as defined in Fig.41b, and θ_c is the critical CV at which conduction fails as defined in Fig.36d. Equation 88 describes the roles of APD gradient and the properties of CV restitution in the vulnerable window for unidirectional block. Specifically, the vulnerable window for unidirectional conduction block is proportional to the refractory barrier for a fixed σ once σ exceeds a critical value (Fig.41d). The analytically derived vulnerable window also agrees well with the results from simulations using a detailed action potential model. Since a larger τ means a broader DI range over which CV changes, broadening CV restitution reduces the vulnerable window, i.e., CV restitution is protective under this condition. Note that CV restitution is also important in promoting spatially discordant APD alternans, which promotes large APD gradients and increase vulnerability. Therefore, the slope of the CV restitution has either suppressed or promoted vulnerability, depending on the specific conditions.

The critical APD gradient (σ_c) for conduction block can be obtained from Eqs.87 or 88 as [381]:

$$\sigma_c=\frac{1}{\theta_c}-\frac{1}{\theta_1} \quad (89)$$

Therefore, σ_c depends on the CV of the S1 wave and the critical CV for conduction failure. For faster S1 rates, θ_1 is smaller, and thus σ_c is also smaller. For normal conduction in the longitudinal direction, $\theta_1=\theta_0\sim0.5$ mm/ms and $\theta_c\sim0.2$ mm/ms, which gives rise to a minimum APD gradient of 3 ms/mm for unidirectional conductional block to occur. This agrees with observations by Laurita and Rosenbaum [389] from experiments in normal guinea pig hearts, which required a minimum APD gradient of 3.2 ms/mm for unidirectional conduction block to occur. An interesting implication of Eq.89 relates to the effects of decreased coupling strength between cells. It is well known that decreasing gap junction conductance increases the gradient of refractoriness, which was thought to promote unidirectional conduction block [390]. However, since CV scales to the square root of gap junction conductance, i.e., $\theta' \propto \sqrt{D}\theta$, then Eq.89 can be written as $\sigma > \frac{1}{\sqrt{D}}(\frac{1}{\theta_c} - \frac{1}{\theta_0})$, which indicates that a larger refractory gradient is needed for conduction block when gap junction conductance is reduced. This agrees with the following experimental observations: polymorphic VT could only be induced when the transmural APD gradient was greater than 10 ms/mm in failing dog hearts [386] in which gap junction conductance was reduced by heart failure. Also conduction block occurred at APD gradients from 10 ms/mm to 120 ms/mm in sub-acute myocardial infarction [387], in which cell coupling is likewise reduced.

Unidirectional conduction block in a 1D cable does not guarantee reentry in 2D or 3D tissue. Similar to the case shown in Fig.40, reentry formation requires that the two tips of the localized block are separated by a critical distance. For example, for a heterogeneous island in tissue [375], reentry cannot form for a small refractory barrier, but it also cannot form for a too large refractory barrier since the refractory period in the island is too long, the two tips will collide behind the island, preventing reentry to form. This type of tip collision has been observed in an experimental study of ischemia [391] in which high dose of lidocaine (a Na^+ channel blocking drug) prolonged the refractory period in the border zone much more than in the normal tissue, causing the tips to collide on the other side of the border zone. In addition to the height of the refractory barrier, the spatial scale of the heterogeneities is also an important factor as shown in simulation studies [375, 380].

In clinical settings, however, multiple PVCs often appear to be involved in the genesis of arrhythmias [392, 393]. For example, during clinical cardiac electrophysiological testing, programmed stimulation with multiple PVCs is often required to induce reentry. Relevant to this observation, experimental studies have shown that dispersion of refractoriness, which correlates inversely with the VF threshold [394], is modulated by PVCs [395] and rapid heart rates [386, 396]. Other experiments [397–402] have demonstrated that dispersion of refractoriness and inducibility of reentry are affected by the activation sequence of PVCs. Computer simulation studies [65, 358, 403] have shown that the ability of a PVC to modulate dispersion of refractoriness depends on APD restitution and CV restitution properties. Using a kinematic model, Fox et al [383] showed that the likelihood of conduction block by multiple PVCs depended on APD restitution and CV restitution. In addition, spatially discordant APD alternans induced by rapid pacing [64, 347] also dramatically increases the dispersion of refractoriness, creating a heterogeneous substrate favoring conduction block and initiation of reentry [65, 360, 361, 385]. Figure 42 shows an example of induction of reentry promoted by spatially discordant APD alternans in a computer simulation of a 2D tissue model.

7.3.4. EAD-induced reentry—An EAD can trigger a PVC which propagates in cardiac tissue. If the PVC encounters the proper tissue substrate, it may induce reentry by the mechanism described above. However, EADs may also induce reentry without requiring additional tissue substrate heterogeneity, if multiple regions susceptible to EADs are present in the tissue. This scenario is shown in Fig.43. In Fig.43a, a circular area of cells exhibit EADs is placed in the center of the tissue. The first three EADs fails to propagate while the 4^{th} EAD propagates successfully in all directions, forming a target wave and thus a PVC. In Fig.43b, an area composed of two circular regions is placed in the center of the tissue and all other parameters are the same as in Fig.43a. The first two EADs fail to propagate, while the 3_{rd} one propagates into the negatively curved region and then around the heterogeneous region, forming a reentry circuit. The negatively curved region enhances the source effect, helping the EADs to propagate.

7.3.5. Spatiotemporal instabilities and arrhythmia initiation—In the case of reentry induced by a strong stimulus, the symmetry is broken by the stimulation itself. In the cases of PVC or EAD induced reentry, the symmetry is broken due to strong tissue heterogeneities. Besides the mechanisms discussed above, reentry can be induced by symmetry breaking due to dynamical instabilities—the development of spatiotemporal chaos due to chaos desynchronization [166, 242]. Reentry can be induced under two cases. In the first case (Fig.44a), chaos occurs due to steep APD restitution and rapid pacing as shown in Fig.23. In a homogeneous 2D tissue, pacing from one side of the tissue generates planar waves propagating from left to right, which is initially synchronous in the y-direction. However, as pacing continues, the synchrony cannot be maintained because the underlying action potential dynamics of each cell is chaotic. Due to sensitivity to initial conditions, a characteristic of chaos, very small differences develop into large gradients, causing localized failure of conduction, initiation of reentry and complex wave dynamics. In the second case (Fig.44b), chaos is caused by EAD dynamics (Fig.33). The planar waves generated by pacing from one side of the 2D tissue desynchronize in the y-direction, forming islands of long APD. Differing from the first case (in which localized conduction failure occurs to the pacing beats to induce reentry), EADs generated from these long APD islands propagate in one direction but fail in the other direction, forming reentry and eventually developing complex spatiotemporal electrical wave dynamics.

7.4. Dynamics of reentry in cardiac tissue and organ

Reentry in cardiac tissue can be either stable or unstable, and the latter leading to complex wave dynamics. The stability of reentry has been widely investigated analytically and in computer simulation studies. These studies have shown that a Hopf bifurcation leading to quasi-periodicity is the first bifurcation followed by a transition to chaos. The quasi-periodicity and chaos are also observed in experimental recordings of arrhythmias [404, 405]. Moreover, the quasi-periodic behavior of reentry may be responsible for the quasi-periodic ECG dynamics of Torsade de Pointes, whereas the chaotic behavior of reentry may be responsible for the irregular ECG dynamics of polymorphic VT and VF. In this sub-section, we summarize: the bifurcation theory and nonlinear dynamics of reentry around an obstacle; the spiral wave and scroll wave stability and dynamics in generic excitable media and in cardiac tissue; spiral wave dynamics in cultured myocyte monolayers and in the real heart; and finally bi-stable spiral wave behavior in generic excitable media of the FHN model and in cardiac tissue.

7.4.1. Quasi-periodicity of reentry around an obstacle—Reentry around an obstacle was first demonstrated by Mines in 1914 in an annulus (Fig.45a) cut from a dog's right ventricle [68], which was first mathematically modeled and explained by Wiener and Rosenbluth [69]. In an experimental study, Frame and Simson [406] found that the reentry could be unstable with fluctuating circulating time and APD, exhibiting a quasi-periodic pattern (Fig.45b). This behavior can be readily recapitulated in computer simulations using a 1D ring [241, 345, 407–411], as shown in Fig.45c for comparison with the experimental data. The quasi-periodic behavior has been well-studied theoretically, first by Courtemanche et al [345, 408] who developed an integral-delay equation for a wave circulating in a ring, i.e.,

$$d(x)=\int_{x-L}^{x}\frac{ds}{\theta(s)}ds-a(x-L) \quad (90)$$

where $d(x)$ is the DI at location x, $a(x)$ is the APD at location x which is determined by the APD restitution function $a(x)=f[d(x)]$, $\theta(x)$ is the CV at location x which is determined by the CV restitution function $\theta(x)=g[d(x)]$, and L is the perimeter of the ring. The equation simply follows the conservation "DI=circulating time-APD." By taking derivatives with respect to x, the integral-delayed equation becomes

$$\frac{d}{dx}[d(x)+a(x-L)=\frac{1}{\theta(x)}-\frac{1}{\theta(x-L)} \quad (91)$$

which is called the neutral delayed-differential equation. By performing linear stability analysis of the steady-state solution of the neutral delayed-differential equation, they found that an infinite-dimensional Hopf bifurcation occurs when the slope of the APD restitution curve is equal to one, i.e., $f'=f_c^{'}=1$. The steady-state solution is unstable when $f'>f_c^{'}$. The wavelength at the bifurcation point can be approximately calculated from the linear stability analysis as

$$\lambda_k=\frac{2L}{2k+1}=\frac{2L^2\alpha}{(2k+1)^3\pi^2}, k=0,1,2,\ldots \quad (92)$$

where $\alpha = g' / \theta^2$ and g' is the slope of the CV restitution curve at the steady-state solution, indicating that the wavelength is determined by CV and CV restitution.

Note that the neutral delayed-differential equation does not take into account the effects of cell coupling on APD. This coupling effect was later considered by Vinet [410, 412] who introduced a coupling term in the neutral delayed-differential equation as

$$d(x)=\int_{x-L}^{x}\frac{ds}{\theta(s)}-\int_{-\alpha}^{\alpha}w(s)a(x-L+s)ds \quad (93)$$

where $w(s)$ is a Gaussian function describing the long-range coupling and $[-\alpha, \alpha]$ is the maximum coupling range. Following the same stability analysis, they found that the critical slope of the APD restitution curve for instability became [412],

$$f_c^{'}=e^{\eta q^2} \quad (94)$$

where η is a positive parameter depending on the coupling strength. When η=0, the APDs of the cells are uncoupled, which is the case studied by Courtemanche et al [345, 408]. Note that the steady-state solution becomes unstable, not at the slope of the APD restitution curve equals one, but at a critical slope that is greater than one, i.e., $f_c^{\prime}=e^{\pi q^2}>1$, indicating that the coupling between cells stabilizes the system. In addition, the Hopf bifurcation is no longer infinite-dimensional as in the model by Courtemanche et al [345].

A 1D ring is an idealized geometry to model reentry around an obstacle. Models of 2D annuli have been also used to investigate the dynamics of reentry around an obstacle and demonstrated how the size of the obstacle as well as wavefront curvature interacts with APD restitution to develop complex spatiotemporal wave dynamics [102, 413, 414]. For example, the cycle length of reentry is mainly determined by the size of the obstacle when the reentry is intact, but once wavebreaks occur due to a smaller obstacle size or a steeper APD restitution curve, the obstacle has little effects on the cycle length or the dynamics of the reentrant waves.

7.4.2. Dynamics of spiral waves in 2D tissue models

7.4.2.1. Spiral wave dynamics in generic excitable media: Spiral waves are a generic property of excitable media. A spiral wave in an excitable medium is called stable if its tip traces out a circle in a homogeneous space, but instabilities can occur leading to complex spiral wave behaviors. Meandering of the tip is a spiral wave behavior widely observed in computer models [92–94, 415] and experiments [416, 417]. Figure 46a shows spiral wave behaviors in a two-parameter space in the model by Barkley [415], showing stable spiral wave, meandering spiral wave, and drifting spiral wave regimes. The transition from a stable spiral wave to a meandering spiral wave occurs via a Hopf bifurcation [93]. The different meandering and drifting patterns of the tip of a spiral wave depend on the rotation frequency of the spiral wave (ω_1) and frequency arising from the Hopf bifurcation (ω_2). When $\omega_2<\omega_1$, the tip traces out an inward flower petal, and when $\omega_2>\omega_1$, the tip trances out an outward flower petal. When $\omega_2=\omega_1$, a resonant behavior occurs, which causes the spiral tip to drift along a straight line in space. Winfree [94] observed a more complex meandering pattern (Fig.46b), and called it hypermeander in which the spiral tip wanders irregularly in space. Even more complex spiral wave dynamics can occur, i.e., spiral wave breakup (Fig.46c), first shown in modified FHN models by Bar et al [95] and by Panfilov and Hogeweg [96]. During breakup, the spiral waves are unstable, and new spiral waves are continuously created via wave breaks, and at the same time, the existing spiral waves disappear by spiral tip colliding and meandering off the boundaries, producing a very complex spatiotemporal electrical wave pattern.

7.4.2.2. Spiral wave dynamics in homogeneous cardiac tissue models: The first computer simulation using a detailed cardiac action potential model to simulate spiral wave dynamics in cardiac tissue was carried out by Courtemanche and Winfree [418] with the ventricular action potential model by Beeler and Reuter [130] using a supercomputer at the San Diego

Supercomputer Center. Due to improvements in computer power and better numerical methods, simulations of spiral wave in 2D tissue using detailed cardiac action potential models is now routine, but still non-trivial. Although the action potential models have become more and more physiologically detailed, however, the basic spiral wave behaviors exhibit the same dynamics as in generic excitable models, i.e., stable spiral waves, quasi-periodic meandering spiral waves, chaotically meandering spiral waves, resonant spiral wave drift, and spiral wave breakup ("electrical turbulence") [98–102, 419–421].

To better understand the spiral wave dynamics in cardiac tissue, it is useful to first understand some of the basic properties of spiral waves. Following Zykov [88], certain characteristic points in a stable spiral wave can be defined (Fig.47a) [102]: the rotation center (labeled as 'O'); the 'q' point at which the wavefront meets the waveback; and the 'Q' point at which the CV is tangential to the circle it traces out. An arbitrary point in the spiral arm far away from the Q point is labeled as a 'P' point. Note that any point in a stable spiral wave traces out a circle, but only the CV of the Q point is tangential to its own trace. The Q point is the point in a spiral wave where conduction changes from regenerative (outside the circle) to decremental (inside the circle). The cycle length of a spiral wave (T), the radius of the spiral core (r_Q), and the CV (θ_Q) of the Q point satisfy: $T = 2\pi r_Q / \theta_Q$. Since the Q point is the location where regenerative conduction becomes decremental, one can define the excitable gap to be zero at this point. The excitable gap is the time interval between the end of the present wave and the next coming wave, during which a cell is in its excitable state. From the Q point to the P point, the wavefront curvature decreases. Based on the eikonal relation (Eq.71 or Eq.72), a larger wavefront curvature results in a slower conduction, and thus the conduction of the Q point is slower than that of the arbitrary P point. Also due to the curvature effect (Eq.74), APD at the Q point is also different from that of the P point. The properties of the Q and P points, such as CV and APD, can be directly measured from the 2D spiral waves. Alternatively, they can also be obtained from 1D cable simulations using different curvatures [102]. Figures 47 b and c show CV and APD restitution curves obtained from 1D cable simulations for two different curvatures, close to the curvatures of the P and Q points, respectively. The tilted dashed lines mark the smallest values of CL or DI at which the wave will propagate without failure at different curvatures. The solid vertical line in Fig. 47b marks the CL of the corresponding spiral wave in 2D tissue. This line intersects the conduction failure line at a point Q' and intersects the zero curvature CV restitution curve at another point P'. Comparison of the calculated quantities in the 1D simulation, such as APD, DI, CV, V, at Q' and P', to the same quantities at Q and P measured from the 2D spiral wave shows that they are virtually identical [102]. This has the following consequences for 2D spiral waves: 1. There is an excitable gap ahead of the wave front that can be quantitatively defined (patch regions in Figs.47 b and c), which decreases to zero at the Q point; 2) The CL is selected by the Q point at which the critical curvature for conduction failure is reached. In other words, the Q point is a location along the spiral arm of a stable spiral wave at which its CL equals its refractory period (and thus there is no excitable gap). The properties of q (spiral core), Q (spiral tip), and P (spiral arm) are also important for understanding spiral wave dynamics, as discussed below.

As opposed to the case of generic excitable media, in cardiac tissue, a physiological parameter determining spiral wave dynamics has been identified, namely the slope of the APD restitution curve is a critical parameter that regulates the stability of spiral wave reentry. The link of APD restitution to spiral wave stability and breakup were investigated in early simulation studies by Karma [99], Courtemanche [100], Qu et al [101, 102], and others. A detailed analysis of the mechanisms by which APD restitution influences different spiral wave dynamics was carried out by Qu et al [102], and is summarized below.

Figure 48a shows three spiral wave dynamics in homogeneous 2D tissue using a cardiac action potential model. APD and APD restitution are altered by changing the maximum conductance of the Ca^{2+} current. A stable spiral wave can also be generated with additional changes to the Na^+ channel [102]. When the APD restitution curve is flat, the spiral wave is either stable or meanders weakly. As the APD restitution curve becomes steeper, the spiral wave meanders more and more violently and becomes chaotic. As the slope of the APD restitution curve increases further, the spiral wave breaks up spontaneously into multiple small waves. In this case, spiral waves are constantly created and annihilated in a chaotic manner. As shown by the cycle length return maps, the transitions from a meandering spiral wave, to a chaotically meandering spiral wave, eventually to spiral wave breakup, are transitions from quasi-periodicity to spatiotemporal chaos. The transition to chaos is also verified by the calculated Lyapunov exponent (Fig.48b). This transition from quasi-periodicity to chaos may be consistent with the quasi-periodicity in arrhythmias observed in experiments [404, 405].

The nonlinear dynamical mechanisms of spiral wave breakup and chaos in cardiac tissue have not been rigorously investigated but can be generally understood in terms of the properties of the characteristic points of the spiral wave as follows [102].

Case 1: stable and quasi-periodic meander. When the slope of APD restitution curve is <1 for all DIs, no instability occurs in the spiral arm (from Q to P). Studies in generic excitable media [92, 93] show that the transition from a stable spiral wave to quasi-periodic meander is via a Hopf bifurcation which arises from an instability of the spiral core (q region). Therefore, when APD restitution curve is flat, the spiral wave is either stable or quasi-periodically meander via a Hopf bifurcation.

Case 2: breakup. When the slope of APD restitution curve is >1 over a wide range of DIs, an instability occurs in the spiral arm far away from the core. This instability is similar to the instability induced by rapid pacing with steep APD restitution, which result in alternans. If the magnitude of oscillation is large enough, conduction failure can occur and produce wavebreaks. However, for a spiral wave to break up, conduction block has to occur locally, but not everywhere, along the spiral wave arm, which requires the presence of a spatial mode instability to be present. Excitation of longitudinal spatial modes has been well characterized in 1D cables of coupled cardiac cells [302, 345, 363, 412]. In 2D tissue, however, not only the longitudinal modes but also the spatial modes transverse to the direction of propagation are excited if the tissue size is large enough [102]. The occurrence of both the longitudinal and transverse spatial modes causes the wavelength modulations in the spiral arm, leading to localized conduction failure. The nonlinear dynamical mechanisms of the spatial mode instability have not been rigorously analyzed and need further theoretical investigations. However, wavefront curvature is required, since this type of spatial mode instability cannot occur in planar wave conduction. As for any spatial mode instability, a certain tissue size is needed. Figure 48c shows the development of these spatial modes versus the tissue size. The size of the obstacle in each panels is the same so that the cycle length of reentry is the same. In a small tissue, no spatial mode instability occurs. But when the tissue is large enough, a spatial mode instability develops, which causes the occurrence of a bump of refractoriness in the back of the spiral arm (arrow in Fig.48c).

Case 3: chaotic meander. Between Cases 1 and 2 is the case in which the slope of APD restitution curve is smaller than 1 everywhere except for a narrow range of short DIs. As shown in Fig.47, the excitable gap is zero at the Q point but non-zero at the P point. Due to the curvature effect, the DI of the Q point is shorter than that of the P point. Therefore, it is possible that the slope of the APD restitution at the Q point is >1 but <1 at the P point, and thus oscillations occur at the Q point not at the P point. Since the excitable gap at Q is zero, any oscillations will result in conduction failure of the Q point, but since the excitable gap is much larger at the P point, conduction failure does not occur at this point. Thus, conduction block at the Q point cannot create new spiral waves, but rather affects the course of the spiral tip, resulting in a complex meandering pattern, i.e., chaotic meander.

The chaotic spiral wave dynamics in 2D tissue can be understood based on dynamics of the paced single cells. The chaotic dynamics in the paced cells is governed by a nonlinear shift map. The essential conditions are the slope of APD restitution curve >1 and loss of 1:1 capture. Slope>1 is necessary to create instability at a fixed point in a map, and the discontinuity caused by the lost of 1:1 capture makes the map non-invertible. Even though for the 2D spiral waves, this process is much more complex and it is not possible to use low-dimensional maps to study it, the mechanism of chaos in single cell is essentially still responsible, i.e., the same requirements for chaos to occur in 2D: an APD restitution slope >1, and conduction failure. When conduction failure begins to occur at the Q point, quasi-periodic meander becomes chaotic meander. Note that as indicated by the return map in Fig. 48a, the chaotic behavior is modulated by the quasi-periodicity due to instability from the core. As demonstrated in numerical simulations, chaos indeed occurs locally in the inner part of the spiral wave when it meanders chaotically [422]. When conduction failure occurs in the spiral arm far away from the Q point, spiral wave breakup occurs, and chaos becomes global and truly spatiotemporal [422].

Spiral wave breakup does not always lead to spatiotemporal chaos, and can produce multiple stable spiral waves, called spiral glass. In a simulation study by Karma [99] using the Noble model, spiral waves broke up due to APD alternans, but the final state consisted of many stable spirals. This can also be explained by the APD restitution theory described above [102]. Similarly, in the presence of cardiac memory, an induced spiral wave can undergo spiral wave breakup by the same mechanism as described above, but eventually evolve to multiple stable spiral waves in the tissue as the memory effect evolves [248]. It has also been shown that different spiral wave instabilities can be caused by non-monotonic APD restitution curves [423]. Other mechanisms of spiral wave breakup have also been shown in 2D cardiac tissue models [421].

7.4.2.3. Spiral wave dynamics in heterogeneous tissue models: Normal cardiac tissue is both structurally and electrically heterogeneous, and the degree of heterogeneity is increased in diseased hearts. Electrical heterogeneity is caused by heterogeneous ion channel density causing heterogeneous APD distribution and APD gradients in the heart. The effects of APD heterogeneities can be summarized into the following three cases. In the first case in which the APD gradient is mild, a spiral wave in this tissue drifts toward the long APD region at a certain angle to the direction of APD gradient (Fig.49a) [374, 424]. This drift property has also been shown in generic excitable medium, and the direction of drift depends on the excitability of the medium [425]. In addition, when multiple spiral waves are initially present in the tissue, the fastest one always drives the slower ones out towards a tissue border where they are extinguished, i.e., spiral waves with different cycle lengths cannot coexist in the same tissue [374, 426] so that the whole tissue is entrained into a single frequency by the fastest one. The time taken to entrainment is proportional to the difference in frequency [426], i.e.,

$$T \propto \frac{1}{|f_1 - f_2|} \quad (95)$$

In the second case [115, 374] in which the APD gradient exceeds a critical value, conduction blocks occur in the heterogeneous region via the same mechanism as described in Section 7.2.3. A spiral wave in the short APD region is fast, and the wavefronts emanating from it cannot propagate one-to-one through the large APD gradient region, such that conduction block occurs and forms new spiral waves (Fig.49b). The spiral waves rotate with different frequencies, and the frequency jumps suddenly from one to the other (see bottom panel in Fig.49b). The competition between spiral waves with different frequencies results in complex conduction patterns, including chaos [115]. In the third case, spiral wave breakup occurs via dynamical instabilities caused by a steep APD restitution curve. Even though the APD gradient is large, the distribution of the average frequency does not jump suddenly but varies nearly continuously in space, tracking the APD heterogeneity in space (Fig.49c). Note that in real cardiac tissue, the heterogeneities may exhibit different spatial scales and even vary from cell to cell. It has been shown that the spiral wave dynamics also depends on the spatial scale of the heterogeneity [427].

7.4.3. Dynamics of scroll waves in 3D tissue models—The heart is 3D and inhomogeneous, and the spiral waves seen on the epicardial surface of the heart are in fact scroll waves. The simplest case is a stack of 2D spiral waves to form a straight scroll wave in 3D (Fig.50a). The line that links the spiral tips in space is called the scroll filament (the red line in Fig.50a). If the tissue is heterogeneous and thus the spiral waves rotate at different periods in different layers, the filament can no longer remain straight, and twists to form a twisted scroll wave (Fig.50b). Twisted scroll waves can also result from fiber rotation in cardiac tissue, or due to dynamical instabilities of the filament itself in homogeneous tissue. In addition, more complex scroll behaviors can exist in excitable medium, such as scroll rings (Figs.50 c and d) and knotted scroll rings. Finally, fiber rotation and tissue thickness may cause instabilities resulting in scroll wave breakup. In this subsection, we summarize the roles of tissue thickness, excitability, and fiber rotation in scroll wave stability in 3D tissue models.

7.4.3.1. Thickness induced scroll wave instabilities: Winfree [428] argued that a certain tissue thickness (3–4 mm) is required for fibrillation (or electrical turbulence), based on his interpretation of experiments. Rotors (spiral and scroll waves) that are stable in thin tissue (e.g., the right ventricle) can become unstable in thick tissue (e.g., the left ventricle). Although we now know that fibrillation can occur in thin tissue, tissue thickness plays an important role in scroll wave dynamics. Thick tissue not only can allow reentry to occur in the third dimension, but also can generate instabilities that do not exist in 2D.

Since no analytical solutions can be obtained for spiral waves in excitable medium, the stability analysis becomes nontrivial. Stability analyses of a straight or a twisted scroll wave filament have been carried out by a number of authors [429–433], showing filament instability in thick homogeneous tissue. Here we summarize in detail one of the methods that has been used to study the scroll wave stability and the phenomena observed in numerical simulations by Qu et al [431].

Consider a FHN type model in a 3D medium using the following equations:

$$\frac{\partial u}{\partial t}=f(u,v)+D\nabla^2 u \;\; \frac{\partial v}{\partial t}=g(u,v) \quad (96)$$

Assume that a spiral wave solution [$u_0(x,y,t)$, $v_0(x,y,t)$] exists in a 2D tissue. Note that this solution is not limited to a stable spiral wave, but can be any type of spiral waves, including spiral wave turbulence. The corresponding 3D solutions are straight scroll waves. To analyze the stability of a straight scroll wave solution, one gives a small perturbation to this solution, i.e., $u(x, y, z, t)=u_0(x, y, t) + \delta u(x, y, t)\exp(ikz)$ and $v(x, y, z, t)=v_0(x, y, t) + \delta v(x, y, t)\exp(ikz)$. Inserting this perturbation into Eq.96, one obtains a linearized equation around the scroll wave solution as

$$\partial \mathrm{w}/\partial t=(\mathrm{M}-Dk^2\Gamma)\mathrm{w} \quad (97)$$

where $\mathrm{w}=\begin{pmatrix}\delta u(x,y,t)\\ \delta v(x,y,t)\end{pmatrix}, \mathrm{M}=\begin{pmatrix}f'_u+D\nabla_{xy} & f'_v\\ g'_u & g'_v\end{pmatrix}, \Gamma=(\Gamma_{xy}), \mathrm{and}\Gamma_{xy}=\begin{pmatrix}1 & 0\\ 0 & 0\end{pmatrix}$. w is a vector and M, and Γ are matrices in the *x*-*y* coordinate system. By numerically simulating Eqs.96 and 97, one can obtain the maximum Lyapunov exponent as a function of wave number *k* using

$$\lambda_k=\lim_{t\to\infty}\frac{1}{t}\ln\frac{\|w(t)\|}{\|w(0)\|} \quad (98)$$

The scroll wave is unstable when $\lambda_k>0$ for any *k*. The critical tissue thickness can be determined by the critical wave number k_c at which λ_k changes from positive to negative.

Figures 51 a and b show two filaments and their trajectories on the bottom surface of a thick homogeneous 3D medium from simulations of Eq.96. The corresponding spiral waves meander in a 2D medium. The filaments are no longer straight but become twisted. However, if the thickness is smaller than the critical value, the filaments remain straight, i.e., no filament instability can occur. Figure 51c shows λ_k versus *k* for the parameters used in

Fig.51b showing that λ_k first increases and then decreases with k, demonstrating that unstable spatial modes develop due to tissue thickness. The critical thickness for instability is predicted by the calculated λ_k [431]. Another type of tissue thickness related instability is in the regime of spiral wave breakup. Since in this regime, the spiral wave dynamics is chaotic, the filament stability becomes a problem of chaos synchronization in a 3D medium. Similar to the meandering cases, the filaments are stable when the tissue thickness is less than the critical value, but become unstable when it exceeds the critical value (Fig.51d), which can also be predicted from the calculated λ_k (Fig.51e). Note that in this case, λ_k decreases monotonically with k, indicating that no new instability is induced by the tissue thickness.

The tissue thickness induced instability shown in Figs.51 a–c was not found in simulations using a cardiac action potential in 3D tissue [104], at least in tissue models as thick as 15 mm which is roughly the thickness of the left ventricle of large animals. But filament instability due to chaos was observed in the same model, which occurred at tissue thickness less than 9 mm [104].

Filament instability has been demonstrated experimentally in a 3D Belousov-Zhabotinsky reaction by Luengviriya et al [434].

7.4.3.2. Fiber rotation induced scroll wave instabilities:

In cardiac tissue, the tip of a stable spiral wave is an ellipse, rather than a circle, due to anisotropic conduction in cardiac tissue. In the presence of fiber rotation from epicardium to endocardium, the ellipsoid trajectory also rotates as one goes down the filament axis, forming a twisted filament (Fig. 52a). The effects of fiber rotation on scroll wave stability was first investigated in 3D tissue slabs by Panfilov and Keener [435] using a FHN type model, and then by Fenton and Karma [103, 436] using the Beeler-Reuter model, Qu et al [104] using the LR1 model, and in a dog anatomic ventricular model by Xie et al [164]. These simulation studies have shown that fiber rotation causes an instability which further destabilizes scroll waves in 3D tissue compared to their 2D spiral wave counterparts.

When a spiral wave is stable in 2D tissue, the twisted filament in 3D tissue is also stable [103, 104]. But when the spiral wave meanders violently in 2D tissue, the filament in 3D tissue becomes unstable, causing it to bend, which then encounters tissue boundaries, breaking into two filaments (Fig.52b). The filament bending may also lead to formation of scroll rings. As these processes continue and more twisted filaments are created, a turbulent scroll wave pattern forms in the 3D tissue (Fig.52c), resulting in a spatiotemporally chaotic pattern. The mechanism of the filament bending can be understand as follows. During hypermeander, the spiral wave movement is violent, which leads to a large area of excitable tissue in the core region of the spiral wave (see the blue region in the chaotic meander in Fig.48a). In a 2D tissue, this area cannot be readily reexcited since no wavefront can enter into this region. However, in a 3D tissue, fiber rotation results in out-of-phase movements of the wavefronts in different layers (and thus filament twist). This out-of-phase excitation gives an opportunity for the excitable area in the core region to be re-excited by a wavefront from the z-direction, which results in the filament bending seen in Fig.52b. If the spiral wave is stable or meanders mildly, no large excitable regions near the core exist, precluding re-excitation from the z-direction, such that filament twist caused by fiber rotation cannot induce large scale filament bending.

The fiber rotation induced scroll wave instability depends not only on spiral wave stability (mainly controlled by APD restitution), but also on the tissue thickness and the rate of fiber rotation. Figure 52d shows simulation results using the LR1 model, summarizing how these factors interact to affect this instability. In the three panels shown, one of the three parameters is fixed and the other two are varied to show the boundary for filament breakup. The results are straightforward: filament breakup occurs more easily when the spiral wave is more unstable (meanders more violently), the tissue is thicker, and the fiber rotation rate is larger. It is noting that in the chaotic meander region ($\bar{G}_{si}$ from 0.045 to 0.06), the tissue thickness for breakup is around 5 mm and the fiber rotation is about 10 deg/mm, which is roughly comparable to the left ventricle of large mammals. The thickness for scroll wave breakup agrees with Winfree's observation that 3–4 mm thick tissue is needed for fibrillation to occur [428]. Moreover, the frequency of excitations in 3D tissue is much faster than the corresponding 2D spiral waves due to re-excitation of the recovered excitable region by reentry from the z-direction (Fig.52e). The effects of fiber rotation induced wavebreaks have also been demonstrated in an anatomically detailed ventricle model (Fig. 53) [164].

7.4.3.3. Negative filament tension: A scroll ring is usually not a stable solution in an excitable medium. For normal excitability, the scroll ring shrinks and drifts. The drift direction depends on the chirality of the spirals (Fig.54a). It has been shown theoretically that the velocities of the scroll ring shrinking and drifting obey the following equations [437]:

$$\frac{dr}{dt} = -\frac{\alpha}{r} \quad (99)$$

and

$$\frac{dz}{dt} = \frac{\beta}{r} \quad (100)$$

which were demonstrated in experiments [438, 439].

However, in a simulation study, Panfilov and Rudenko [440] showed that the scroll ring can also expand under certain parameters (Fig.54b). This expanding behavior was later called negative filament tension [441], since α in Eq.99 becomes negative. It is clear now that negative filament tension occurs under conditions of low excitability. Filament tension can also be studied using spiral waves subjected to an electrical field in a 2D medium [442–444]. Electrical field induced spiral wave drift has been observed in chemical reactions and in simulation studies [442, 445, 446]. In a 2D medium (*x*-*y* system) with an electrical field in the *x*-direction, the first equation of Eq.96 becomes:

$$\frac{\partial u}{\partial t} = f(u,v) + D\nabla_{xy}^2 u + E\frac{\partial u}{\partial x} \quad (101)$$

where *E* is a constant proportional to the electrical field strength. In a 3D medium with a scroll ring solution, if the (*x*,*y*,*z*)-coordinates are replaced by polar (*r*,θ,*z*)-coordinates (see Fig.54a), due to the rotational invariance of the scroll ring, the first equation of Eq.96 in a 3D medium can be transformed to the one in a 2D medium as:

$$\frac{\partial u}{\partial t}=f(u,v)+D\nabla_{rz}^{2}u+\frac{D}{r}\frac{\partial u}{\partial r} \quad (102)$$

Therefore, in the *r*-*z* plane, the spiral waves experience an additional force due to the curvature (κ = 1 / *r*) of the scroll ring, which is equivalent to the force generated by the electrical field in 2D. Therefore, understanding how a spiral wave responds to an electrical field in a 2D medium can give information relevant to the filament tension in a 3D medium. The observations and theories in 2D systems show that dense (normally excitable) spiral waves and sparse (low or weakly excitable) spiral waves drift in opposite directions under the same electrical field, indicating that the filament tension for the two types of waves are opposite. The tension is positive under normal excitability conditions but negative under low excitability conditions. It should be pointed out that negative tension can also occur in high excitability conditions as shown in simulations by Alonso and Panfilov [447].

Negative filament tension has been demonstrated in simulation studies of generic excitable medium [441, 448, 449] as well as in cardiac action potential models (Figs.54 c and d) [447, 450, 451]. The development of this instability from an initially straight scroll wave also depends on tissue thickness. When the tissue is thin (Fig.54c), the filament is stable. When the tissue exceeds a critical thickness (Fig.54d), however, filament instability develops, causing filament twist and bending. This results in a complex scroll wave pattern in tissue. Note that the critical thickness for instability in the presence of negative filament tension can be predicted using the linear stability analysis as shown in the study by Qu et al [431]. Note that filament instability can occur in the case of normal excitability but does not lead to complex spatiotemporal patterns because the filament tension is positive. Whether negative filament tension is responsible for complex wave dynamics in real cardiac tissue has not been demonstrated.

7.4.4. Spiral wave dynamics in real cardiac tissue—Since the heart is a 3D object, reentry in the heart occurs in the form of scroll waves. However, optical imaging can only be performed on the surface of the heart, such that only 2D projections on the surface of the scroll waves can be imaged. Genuine 2D cardiac spiral waves have been observed, however, in cultured cardiac monolayers which are true 2D tissue. Here we review the scroll/spiral wave dynamics observed in both native 3D cardiac tissue as well as in 2D cultured cardiac monolayers.

In cardiac monolayers, almost all spiral wave behaviors shown in generic excitable medium or chemical reactions have been observed. In a series of studies, Hwang et al observed stable and meandering spiral waves [452], period-1,2,3 and irregular spiral wave behaviors [453], and spiral wave with lines of defect [454]. Bursac et al [455] observed multi-armed spiral waves, as has been shown in generic excitable media [456, 457].

In the real heart, various spiral wave dynamics (as surface projections of scroll waves) have been observed including stable spiral waves, meandering spiral wave, and spiral wave breakup. Different spiral wave behaviors have been linked to different ECG morphologies and arrhythmias [458]. In the normal ventricles, spiral waves are unstable and break up into electrical turbulence, manifesting as cardiac fibrillation. In a number of experimental studies [459–462], pharmacological agents that reduce the slope of APD restitution curve convert irregular fibrillation dynamics into more periodic tachycardia, supporting the theory developed through computer modeling studies. An example of such observations by Wu et al [461] is shown in Fig.55, in which a Ca^{2+} channel blocker D600 was used to alter the APD restitution properties. The drug, which reduces the steepness of the APD restitution curve, converts multiple reentrant wavelets (fibrillation) with an irregular ECG behavior to a pair of stable spiral waves (tachycardia) with an almost periodic ECG signal. These studies have demonstrated the importance of dynamical instabilities, more specifically the importance of the steepness of the APD restitution curve in cardiac arrhythmias.

However, cardiac tissue is heterogeneous, and the role of heterogeneity in arrhythmia formation and maintenance has always been considered to be very important. As shown in computer simulations (Fig.49), when the spiral wave is intact and the heterogeneity is mild, only a single wave exists and the whole tissue is entrained by a single frequency. But when the heterogeneity is large, wavebreaks can occur in regions of steep APD gradient, resulting in multiple waves and sudden transitions in frequency. This scenario agrees with the case of mother rotor fibrillation in which a fast stable rotor causes fibrillatory conduction block [15, 463–465], resulting in discretized regions of frequency distribution in space (Fig.56a). In the spiral wave breakup regime, a discretized frequency distribution no longer exists but correlates regionally with the heterogeneity. This behavior likewise agrees with experimental observations under other conditions (Fig.56b) [466–468], supporting the multiple wavelets hypothesis [469, 470] in which dynamical instabilities, rather than tissue heterogeneities, play the dominant role.

7.4.5. Bistable spiral wave conduction—In a computer simulation of a 2D excitable medium with the FHN model, Winfree [342] has observed that over a certain parameter range, the medium can have two different stable spiral wave solutions, with one rotating faster than the other. As shown in Fig.57a, starting from a small ε, the period of the spiral wave increases slightly with ε until ε reaches a critical value, at which point the period suddenly shift to a longer one. If one starts with a large ε, the period of the spiral wave decreases until another critical value at which point the period jumps suddenly to the short one, forming a hysteresis loop. Therefore, for a range of ε, the fast rotating spiral wave and the slow one co-exist, exhibiting a bistable behavior. Figure 57b is a simulation of Winfree showing the co-existence of the two types of spiral wave in the same medium, where the faster one finally entrains the whole system.

The exact mechanism of the bistable behavior is not well understood, but Winfree showed that this may be related to the non-monotonic dispersion relation in which CV oscillates with wave length (Fig.58a). The non-monotonic behavior in conduction can also occur in cardiac tissue, which is called supernormal excitability or supernormal conduction [471], a well-known phenomenon in cardiac system. Figure 58b shows recordings from a Purkinje fiber, showing that the conduction time has a minimum at the end of the action potential. Supernormal excitability has been shown by Chialvo et al [59] to be a cause of chaotic action potential dynamics in cardiac myocytes. Whether the supernormal excitability can cause bistable spiral wave behavior has not been demonstrated in cardiac tissue. However, supernormal conduction has been shown to cause novel conduction and spiral wave dynamics in computer simulations and experiments [472–476].

Another type of bistable spiral wave conduction has been described in computer models and in experiments by Chang et al [477, 478]. In both the atrial and ventricular tissue, the wave conduction is mainly facilitated by I_{Na} which mediates the steep upstroke of the action potential. It is also known that when the resting potential is high so that I_{Na} is inactivated, $I_{Ca,L}$ becomes the major current facilitating conduction. Chang et al [477] have shown that bistable spiral wave behavior can occur in cardiac tissue in which two distinct types of spiral waves can be induced in the same tissue (Fig.59). In the first type of spiral wave, voltage recovers close to the resting potential (−80 mV) and both I_{Na} and $I_{Ca,L}$ are activated. In the second type of spiral wave, however, voltage only recovers to around −50 mV, so that I_{Na} is inactivated, and only $I_{Ca,L}$ is activating, resulting in a slower spiral wave. Differing from the bistable spiral wave behavior observed by Winfree [342], in this case, the system exhibits two distinct excitable states, and therefore is referred to as bi-excitability. Experimental evidence of bi-excitability has been shown in experiments of cultured neonatal rat ventricular myocyte monolayers [477, 478], by demonstrating that one type of conduction can be blocked by a Ca^{2+} channel blocker but not by a Na^{+} channel blocker, while the other type cannot be blocked by a Ca^{2+} channel blocker but can be blocked by a Na^{+} channel blocker.

Bi-excitability is a novel dynamics in cardiac tissue which gives rise to insights into the mechanisms of arrhythmias. As shown by Chang et al [477, 478], bi-excitability may provide a mechanism for Torsade de Pointes and explanation for why Torsade de Pointes often spontaneously terminates but sometimes degenerates into VF. Bi-excitability may also occur in other excitable systems; however, its generality and nonlinear dynamics require further elucidation in future studies.

7.5. Formation of focal excitations in cardiac tissue

Focal excitations are spontaneous activities occurring locally in the heart, which not only play the role of arrhythmia triggers, i.e., PVCs, but also can perpetuate arrhythmias. Therefore, it is important to understand the mechanisms by which focal excitations are generated in cardiac tissue. In this sub-section, we summarize different dynamical mechanisms of focal excitations in cardiac tissue.

7.5.1. Focal excitation formation in heterogeneous tissue—Since cardiac tissue is heterogeneous, a straightforward question is: if a group of cells in a cardiac tissue are capable of oscillating like the pacemaker cells, or exhibit EADs or DADs, under what conditions can they emerge and propagate? The question arises from a well-known property of excitable medium, the source-sink effect. That is, in a cardiac tissue, if only one cell is oscillatory while its neighbors are only excitable, this oscillation will not cause excitable waves; on the contrary, the cell itself may stop oscillating due to the source current being small compared to the sink arising from neighboring cells. Only when a region has enough cells in the oscillatory state to generate a current sufficient to overcome the sink from the surrounding cells can a pacemaker site form to drive focal excitations (Figs.60 a and b) [479]. Although the source-sink effect is well known, a rigorous mathematical analysis on this issue has only been performed recently by Tveito and Lines [480]. These authors used nonlinear stability analysis to show that the critical cell coupling strength for a certain size (a) of the oscillatory region is

$$D_c=\eta a^2 \quad (103)$$

where $\eta=0.0458$ for 1D cable and $\eta=0.0229$ for 2D tissue, which agree with numerical simulations using the LR1 model (Figs.60 c and d). Specifically, when $2D > D_c = \eta a^2$, no focal excitation can occur since the resting state is stable. In other words, the oscillatory cells in the oscillatory region are stabilized by the surrounding cells. When $D < D_c = \eta a^2$, the resting state in the oscillatory region becomes unstable and oscillations emerge to drive focal excitations. Although the parameter η may depend on many factors, the scaling relation between the coupling strength and the size of the oscillatory region should hold true universally. The same phenomenon has been demonstrated in simulations in which the oscillatory region of cells generate EADs or DADs triggering focal excitations [479].

7.5.2. Coupling of excitable cells with non-excitable cells promotes oscillations—Cardiac tissue is composed of not only myocytes but also other types of cells, such as fibroblasts or myofibroblasts [481]. Fibroblasts are small and non-excitable cells which play an important role in cardiac mechanics and wound repair. Recent studies have shown that fibroblasts may also develop gap junction coupling with myocytes [481, 482], which may affect cardiac electrophysiology. Fibroblasts have a more depolarized resting potential than myocytes, ranging from −50 mV to 0 mV. Therefore, the coupling of myocytes with fibroblasts causes myocyte depolarization, which can promote a Hopf bifurcation leading to oscillatory behaviors [483]. The oscillatory activity induced by myocyte-fibroblast coupling was demonstrated in cultured monolayers [483], in which the density of fibroblasts can be experimentally controlled and thus their effects on oscillations can be directly studied (Fig.61a). Theoretical and simulation studies have also been carried by other authors [484–486] on oscillatory activity, focal excitations, and complex self-organized patterns induced by coupling excitable cells to non-excitable cells.

Another scenario is when the coronary artery of a heart is occluded during a heart attack. The blood and oxygen supply to the myocytes in the corresponding region by the artery is substantially reduced, causing the myocytes to become depolarized and non-excitable even while they are still coupled to the normal oxygenated myocytes. The higher resting potential of the ischemic cells can thereby generate current flow to the normal cells which have a lower resting potential, called a “current of injury” in cardiology [487], which may induce PVCs or oscillatory activity leading to arrhythmias. This has been investigated theoretically by Keener [488] and by Peercy and Keener [489]. In their studies, the authors have shown that when a normal excitable cell is coupled to an ischemic non-excitable cell, even though the resting states of both cells are stable, an instability occurs in the coupled system via a Hopf bifurcation leading to oscillations (Fig.61b).

7.5.3. Focal excitation in homogeneous tissue via pattern formation—In the previous two mechanisms, heterogeneity is key for localized oscillations to occur. Focal excitations can also occur in homogeneous tissue via pattern formation. In a study by Yochelis et al [490], localized pacemaker sites can form in a homogeneous excitable medium via an instability similar to the Turing instability, in which the inhibitor diffuses much faster than the activator. However, this condition is not feasible in cardiac tissue in which only voltage diffuses. On the other hand, in the presence of EADs, the action potential dynamics can be chaotic, such that chaos desynchronization results in islands of long APD with EADs bordering with islands of normal APD without EADs, forming a complex spatiotemporal pattern (see Fig.38d). When the EADs can propagate out of the EAD islands into the regions without EADs, focal excitations occur. Figure 62a shows a simulation of a 1D homogeneous cable which is initially paced at one end six times. After the pacing stops, focal excitations form in the cable which maintain the activity transiently before self-terminating. Similarly, one can induce multifocal excitations in 2D tissue (Fig. 62b) and in the whole-heart model [166]. Note that the focal excitations formed via this mechanism are not stable (unlike the above two mechanisms), but vary dynamically in space and time. This feature agrees with the experimental observations of focal arrhythmias in drug induced long QT syndrome [491, 492], in which multiple shifting foci occur (Fig.62c).

8. Nonlinear dynamics of the pacemaking system

The SAN is a specialized area in the right atrium of the heart [493], in which the myocytes are oscillatory. The oscillation frequency of a SAN cell is determined intrinsically by the oscillation dynamics of voltage and intracellular Ca^{2+} cycling which are regulated by many signaling pathways. The cells in the SAN area are not identical but exhibit a heterogeneous distribution [493], and the gap junction coupling of the cells synchronizes them to result in electrical impulses for pacemaking. The SAN is surrounded by atrial tissue and the electrical impulses exit the SAN area to excite the atrial tissue to generate the heart rhythms. Moreover, the heart rate is extrinsically regulated by the central nervous system, i.e., the parasympathetic nerves tend to decelerate the heart rate and the sympathetic nerves tend to accelerate the heart rate. More specifically, the parasympathetic nerve (or vagal) activity is elevated at rest to decrease the heart rate and sympathetic nerve activity is elevated during excise to increase the heart rate. The regulation of heart rate by the central nervous system is called autonomic control. A proper autonomic control is needed for the heart to be efficiently adaptive to different energy demands of the body and other environmental changes. When the SAN functions improperly, it causes a disease called sinus node dysfunction or sick sinus syndrome, such as sinus tachycardia, bradycardia, and sinus arrhythmias. Sinus node dysfunction can be asymptomatic or symptomatic, and the only effective treatment of the bradycardic symptoms is pacemaker implantation. Since the implanted pacemaker is not autonomically responsive, developing an autonomically responsive biological pacemaker is a very attractive alternative therapy [494]. Another clinically important property of the SAN is HRV, a normal behavior of the heart. However, numerous clinical studies have shown that certain properties of HRV may link to the risk of ventricular arrhythmias and SCD. HRV has been not only clinically attractive but also an important research topic of nonlinear dynamics, yet the underlying mechanisms are not well understood. In this section, we review the nonlinear dynamics that may be responsible for normal SAN function, sick sinus syndrome, and HRV.

8.1. Oscillatory mechanisms of pacemaker cells

Ever since the first model was developed by van der Pol in 1928 [23], the concept that the SAN oscillates as a limit cycle has been well accepted. Many mathematical models of SAN cells have been developed to study the oscillatory dynamics and the physiological features [25, 28, 128, 495–498]. These models, combined with experimental observations, have provided a detailed understanding of the roles of each ionic current in generating the oscillatory behavior and regulating the heart rate. Bifurcation analyses of these models have shown very complex bifurcations for the SAN cells entering into or exiting limit cycle oscillations. These bifurcations include Hopf bifurcations, homoclinic bifurcations, saddle-node bifurcations of periodic orbits, and saddle-node on an invariant cycle, etc. Figure 63 show three ways that a SAN cell can exit limit cycle oscillations obtained from the Irisawa-Noma model [128] studied by Guevara and Jongsma [25]. The first one is via Hopf bifurcation (Fig.63a): as a parameter (such as the magnitude of a current) gradually changes, the magnitude of the oscillations decreases and eventually the oscillation disappears. This same behavior was observed in experiments by blocking the Ca^{2+} current with a drug [499]. The second way that a SAN cell exits limit cycle oscillation is via skipped beats (Fig.63b): as a parameter gradually changes, the amplitude has little change, but the frequency decreases by skipping beats between two beats until the oscillation stops. This behavior is a consequence of homoclinic bifurcation. This skipped-beats behavior has been observed in many experiments (see cited references in [25]). The third way of exiting the limit cycle is via a perturbation, such as a stimulus (Fig.63c), which brings the system to another stable solution. In this case, a limit cycle co-exists with a stable equilibrium point. Conversely, a stimulus can also cause the transition from the stable equilibrium point to the limit cycle. Evidence of this type of behavior has also been shown in experiments in SAN cells and other types of cardiac cells (see cited references in [25]).

The view that the oscillation of the SAN is a single limit cycle oscillator of voltage has been challenged in recent studies [24, 500, 501], which show that SAN oscillation is regulated by two coupled voltage and Ca^{2+} oscillators. For a limit cycle of pure voltage, the major ionic currents that are necessary for the oscillator are: the funny current (I_f), $I_{Ca,L}$, and different K^+ currents. I_f causes the phase-4 depolarization (the slowly depolarizing phase) which elevates voltage to a level at which $I_{Ca,L}$ is activated, causing the fast depolarization. The activation of the K^+ currents causes repolarization. This process repeats to result in oscillations. However, studies show that NCX also plays an important role in pacemaker activity [502, 503], indicating that intracellular Ca^{2+} cycling may play an important role in pacemaker activity, which has been demonstrated in many later experimental studies. Figure 64a is a plot of voltage and Ca^{2+} from a SAN cell, showing that spontaneous Ca^{2+} release occurs before the fast depolarization. These spontaneous Ca^{2+} release events are called local Ca^{2+} releases, which are collective events of the CRU network in the SAN cells (Fig.64b) [504]. It has also been shown that the cycle length of the voltage oscillation correlates well with the local Ca^{2+} release period (Fig.64c), providing further evidence for the importance of Ca^{2+} cycling in pacemaking activity. Since Ca^{2+} can oscillate independent of voltage, and voltage can oscillate independent of Ca^{2+}, the view of coupled oscillators is now the dominant hypothesis in which two oscillators entrain each other to control the heart rate. However, intracellular Ca^{2+} regulation is governed by a complex network of coupled CRUs, in which complex spatiotemporal and stochastic dynamics occur. The interactions between these dynamics in rhythm control of the heart await further investigation, and detailed Ca^{2+} cycling models are being developed for this purpose [111, 226, 504, 505].

8.2. Phase locking and chaos in periodically paced pacemaker cells

In a series of studies by Guevara, Glass, Shrier and colleagues [29–36] as well as by other authors [37–39], the nonlinear dynamics of periodic stimulated pacemaker cells has been studied both experimentally and theoretically. These cells exhibit phase-locking behavior at different locking ratios, exhibiting the devil's staircase (Figs. 65 a and b). Irregular responses have also been observed (Fig.65c). The nonlinear dynamics can be generally studied by a circle map of the following form [32]:

$$\phi_{i+1}=g(\phi_i)+\tau(\mathrm{mod}1) \quad (104)$$

where φ_i is defined as the phase right before the ith stimulus and τ is the normalized period between stimuli. Figure 65d shows an example of using a circle map to model the irregular response. The left panel Fig.65d is a plot of the relation between φ_{i+1} and φ_i, i.e., the first return map of phase φ, obtained from the experimental data. The middle panel shows that the first return map was fitted to a function as Eq.104. The right panel shows the simulation results by iterating the obtained map equation with noise, which recapitulates the experimental data.

8.3. Spatiotemporal dynamics in the SAN

Even though the SAN is an anatomically small region in the right atrium, complex spatiotemporal dynamics can still occur. The SAN is a heterogeneous area in which the cells in the central region exhibit different behavior from the cells in the periphery, with cells isolated from the central region have a slower oscillation frequency, a shorter action potential duration, and a less negative phase-4 maximum diastolic potential [493, 497]. However, even though the peripheral cells beat faster than the central cells, the leading pacemaking site in the intact SAN is still located in the central region, indicating that pacemaking is an emergent phenomenon caused by the interactions between the coupled SAN cells. Computer modeling studies have been carried out to investigate the dynamics of pacemaker formation and impulse propagation in heterogeneous tissue structures [497, 506]. Recent optical mapping studies have shown complex shifting patterns of the leading pacemaking site and dynamics of impulse propagation under varying autonomic conditions [507, 508], and the underlying mechanisms are still in debate [509].

8.4. Fractal heart rate variability

The heart rate of a normal heart is not fixed but varies over time (Fig.66a), while in certain diseased hearts, such as in hearts with severe congestive heart failure, the heart rate loses its variability (Fig.66b). The Fourier transform power spectrum of the normal heart rate shows a power-law distribution (Fig.66c). This fractal behavior has been widely observed in many studies [40–42, 236, 510–513], for both normal and diseased hearts. HRV is an important parameter for risk stratification of arrhythmias and SCD, and the fractal exponents have been demonstrated to be a useful predictor [43, 44]. However, despite the widely observed phenomenon and clinical association, both the biological and dynamical mechanisms of HRV are still not well understood.

The heart rate is affected by many external factors, such as respiration, circadian rhythm, sympathetic and vagal activity, as well as intrinsic factors, such as ion channel fluctuations and other molecular fluctuations. HRV can be abolished by blocking both parasympathetic and sympathetic activity [514], but why autonomic regulation causes fractal HRV is unknown. One hypothesis is that the autonomic control of SAN activity may give rise to chaotic heart rates and thus fractal HRV. Chaos was shown in a mathematical model of a vagally driven SAN cell [37]. However, whether HRV is chaotic remains under debate [45, 515–517]. On the other hand, recent studies [237, 518, 519] have shown that power-law HRV exists in cultured monolayers or cell aggregates lacking autonomic control (Fig.67), indicating that the autonomic control is not necessary for fractal HRV, and intrinsic mechanisms can be responsible. Computer modeling studies exclude random ion channel fluctuations as a cause of the power-law behavior [237].

So far, the fractal nature of HRV is largely an observation from analyses of experimental and clinical data [514, 520], the underlying biological origins and dynamical mechanisms are unclear. Even though autonomic control plays an important role in HRV based on experimental and clinical observations, whether it is the primary cause is still unknown. The HRV and its fractal nature can be originated from different sources or a combination of them. At the cellular scale, even though the random membrane ion channel fluctuations are shown not likely to be a cause, the self-organization of random Ca^{2+} sparks into more deterministic Ca^{2+} waves and oscillations for the Ca^{2+} clock of the SAN cell can be a source of fractal HRV. As summarized in Section 5, the transition from Ca^{2+} sparks to waves underlies criticality in which power-law behavior is observed [111, 226]. At the tissue scale, power-law cluster firing has been shown in cultured monolayers of cardiac cells [521] and in cultured networks of glial cells [522]. Since the SAN is a spatially extended tissue composed of coupled pacemaker cells, the tissue-scale selforganization phenomena may also be a contributor to the fractal properties of HRV. The fractal HRV can also be directly stemmed from the neural bursting since power-law neural bursting is widely observed [523]. Besides these individual sources, fractal HRV is most likely a result of the complex interactions of the whole system. Nevertheless, to better understand how the fractal behavior occurs and why it has the potential to be predictive for risk of arrhythmias, future multiscale modeling with nonlinear dynamics at the systems level may eventually provide an answer

9. Control and termination of arrhythmias

Therapeutically, preventing the occurrence of arrhythmias is the ideal strategy. However, once life-threatening arrhythmias occur, prompt termination is the only choice. Clinically, defibrillation is the most reliable way to terminate an arrhythmia, by delivering a strong electrical shock to the heart to “reset” the system. Since the transition from sinus rhythm to an arrhythmia is a type of dynamic instability in the heart, suppressing instabilities to prevent arrhythmias or utilizing the instabilities to promote arrhythmia termination is of great interest among dynamicists, which may provide mechanistic insights leading to the development of effective therapies for arrhythmias. In this section, we summarize the recent developments of arrhythmias control based on nonlinear dynamics, including controlling alternans and chaos using nonlinear dynamical control methods; self-termination or drug-induced termination of arrhythmias due to transient spatiotemporal chaos; wave competition due to entrainment in excitable medium; and control of electrical turbulence via low-energy electrical stimulations.

9.1. Dynamical control of cardiac chaos and alternans

Experiments have shown that single cardiac cells can exhibit chaotic dynamics [29, 58, 524], and that irregular arrhythmias in heart tissue can be dynamical chaos. Dynamical chaos has been shown to be controllable by small perturbations [525], validated experimentally [526]. A control method was applied by Garfinkel et al [524] to convert chaotic rhythms to periodic rhythms in cardiac tissue experiments (Fig.68). Following the same idea, controlling cardiac alternans is also a topic of interest, which has been studied theoretically and experimentally by many authors [527–537]. Since alternans is a precursor of arrhythmias, control of alternans might prevent arrhythmias. In cardiac cells or tissue, the accessible parameters are limited, and most control algorithms vary the PCL. A typical control algorithm of this type is [532, 535]:

$$T_n = \begin{cases} T_0 + \Delta T_n, \mathit{if}\, \Delta T_n < 0 \\ T_0, \mathit{if}\, \Delta T_n \geq 0 \end{cases} \qquad (105)$$

where $\Delta T_n = \gamma(a_n - a_{n-1})/2$, T_0 is the intrinsic period of the heart rhythm (e.g., sinus rhythm), γ is the feedback control strength, and a_n and a_{n-1} are APDs of two consecutive beats. One is restricted to delivering premature stimulations which advance the intrinsic heartbeat, since there is no general method to delay the intrinsic beats. Therefore, in the control algorithm, only negative ΔT_n can be used. This algorithm is effective in controlling alternans in single cells, but has limited effectiveness at controlling alternans in tissue. Figure 69 shows experimental results of controlling alternans in a canine Purkinje fiber by Christini et al [535]. The pacing and the controlling stimuli are given at the left end of the fiber. As shown in this experiment, when alternans is weak, it can be controlled along the 2 cm long fiber, but when its amplitude is large or discordant alternans develops, control is lost. Moreover, the control may convert spatially concordant alternans into spatially discordant alternans [532], which is undesirable since it amplifies APD gradients. The failure can be analytically shown to be due to the inability of a local pacing algorithm to stabilize the unstable spatial mode along the fiber [532, 534].

Whether these control methods are applicable in the real heat is still unclear [538]. First, arrhythmias and discordant alternans are spatiotemporal phenomena. As shown in a theoretical study by Hu and Qu [539], multiple control sites are needed to control a spatiotemporal system. How to safely implement pacing at multiple control sites in the heart is a challenging issue. Second, alternans may not necessarily be causal to ventricular arrhythmias, and clinical VT/VF episodes are not always preceded by alternans. Therefore, whether control of alternans can reliably prevent clinical arrhythmias is an open question.

9.2. Transient spatiotemporal chaos and spontaneous termination of arrhythmias

Arrhythmias occur spontaneously but can also terminate spontaneously. For example, Torsade de Pointes is a type of arrhythmia that usually terminates after a variable number of beats from several to several hundred [540, 541]. VF is generally lethal but episodes of spontaneous termination have also been observed clinically [15, 542–545] (e.g., the case shown in Fig.2), and in experiments [405, 546]. Spontaneous termination of atrial fibrillation is widely observed [547, 548]. In almost 100 years ago, Garrey [546] observed that persistence of fibrillation depends on tissue mass and form, leading to the well-known “critical mass hypothesis.” The rationale for many drug therapies is based on this concept, which is designed to increase the wavelength and thus effectively reduce the tissue size. This hypothesis has been validated by recent theoretical studies using nonlinear dynamics and chaos theory [117, 549].

Figure 70 shows a computer simulation of spiral wave breakup in a finite size 2D tissue [117]. The turbulent electrical activity lasts for a certain period and eventually self-terminates. Termination is facilitated by two processes: spiral waves can collide to annihilate each other, and they also can drift to a tissue border. Since the spiral wave breakup process continuously generates new spiral waves, the competition between the birth and death of spiral waves can finally lead to a quiescent tissue. The nonlinear dynamics of spontaneous termination of spiral wave turbulence in an excitable medium has been first analyzed by Strain and Greenside [549], who have shown that spiral wave breakup in a finite size tissue is transient spatiotemporal chaos whose duration depends on tissue size. They show that the Lyapunov dimension is proportional to the area of the medium (Fig.71a). In a simulation study using the same generic excitable medium model, Qu [117] has shown that the duration of the turbulent behavior is inversely proportional to the maximum Lyapunov exponent (Fig. 71b). In cardiac tissue, the stability of spiral waves is mainly determined by the steepness of the APD restitution curve, and Qu [117] has also shown that the duration of the electrical turbulence is shorter if the slope of APD restitution curve is steeper. Due to the chaotic behavior of the spiral waves, the duration of the turbulent behavior is irregular. The likelihood of spontaneous termination decreases exponentially as tissue size increases but also depends on the geometry of the medium. Spiral wave turbulence terminates faster in the rectangular tissue than in the square tissue of the same area. This is because in both generic excitable media and cardiac tissue, the average duration of electrical turbulence is exponentially proportional to the area-to-perimeter ratio (Fig.71 c and d) [117].

Chaos may also play an important role in the spontaneous termination of multi-focal polymorphic VT. As shown in Fig.65a, the pace-induced foci terminate spontaneously due to their chaotic appearance and disappearance. The number of foci occurring in the tissue depends on the tissue size, with a larger size tissue accommodating more foci. Thus, the duration of the focal activity (i.e., the inverse of the probability that all foci will self-terminate) is size-dependent. This same mechanism may be responsible for the frequently observed spontaneous termination of polymorphic VT or Torsade de Pointes in clinical settings [540, 541].

Real cardiac tissue is a 3D object of complex geometry with fiber rotation and electrical heterogeneities. These factors affect the transient behavior of the electrical turbulence in the heart. In addition, arrhythmias themselves can affect the cellular and tissue properties, such as causing ischemia of the heart due to ineffective pumping of blood. There is a well-known phenomenon in cardiology that “atrial fibrillation begets atrial fibrillation” [547]: with sustained rapid heart rates, atrial fibrillation becomes permanent rather than transient. But the general influences of dynamical stability and tissue size on arrhythmia duration still apply when the key nonlinear dynamics involves transient spatiotemporal chaos.

9.3. Drug-induced spiral wave instability and termination of arrhythmias

Anti-arrhythmic drugs can sometimes terminate ventricular fibrillation and are more effective at terminating atrial fibrillation [542, 550, 551]. To some extent, their antifibrillatory actions have been rationalized according to Garrey’s “critical mass hypothesis” [546] and Moe’s “multiple wavelet hypothesis” [469, 470]. For example, Class IA (Na^+ channel blocker) and class III (K^+ channel blocker) anti-arrhythmic drugs prolong wavelength, so that the same size tissue can support fewer reentrant circuits, which may cause fibrillation to self-terminate. However, this mechanism has been challenged by experimental studies [552, 553] which show that these drugs have limited effects on wavelength and refractory period. Therefore, the rationale for these drugs to terminate arrhythmias may not be simply lengthening the wavelength. In a simulation study, Qu and Weiss [374] have shown that blocking the Na^+ channel does increase the refractory period and the core size of spiral wave reentry, but also promotes meandering, such that the drift in heterogeneous tissue is much faster, increasing the likelihood of self-termination at a tissue border. These two actions may contribute to the effect of Na^+ channel blockers at terminating arrhythmias. K^+ channel blockers prolong APD at slow rates, but much less at fast rates, making APD restitution steeper. This steepening causes the reentrant waves to become more unstable and drift, enhancing the probability of colliding with other waves or tissue borders and self-terminating. Promoting spiral wave instabilities by drug-induced steepening of APD restitution to terminate arrhythmias has been demonstrated in experimental studies [554–556], in agreement with the theoretical predictions.

9.4. Fast pacing induced termination of arrhythmias

Certain arrhythmias can also be terminated by pacing, such as anti-tachycardia pacing that is used clinically [116, 557]. The basic rationale is that in excitable media, high frequency excitations always entrain low frequency excitations. If low frequency waves originate from reentry, they will be eventually terminated by the faster paced beats [342, 426]. In a series of computer simulation studies, Zhang and colleagues [114, 449, 558–560] showed that spiral wave turbulence can be driven out of the medium by rapid pacing (Fig.72a), but only over a narrow frequency range (Fig.72b) and in homogeneous tissue. Due to the narrow frequency window requirement, and because the controlling frequency is close to the frequency of spiral turbulence, the time that it takes to drive all waves off the tissue may be too long to be practical, and thus its application to real cardiac tissue is limited. In the real heart, anti-tachycardia pacing is effective only for slow VT, but not for faster arrhythmias [561], such as VF, because the heart is heterogeneous and the arrhythmias, in particular VF, exhibit a wide range of frequencies.

9.5. Termination of arrhythmias by low-energy electrical stimulations

Defibrillation is currently the only reliable therapy to prevent SCD. The basic idea of defibrillation is that a high energy electrical shock depolarizes the whole tissue and thus eliminates excitable tissue required for wavefronts to continue to propagate. The success of defibrillation is probabilistic due to the irregular dynamics of fibrillation. The probability of defibrillation success increases with energy, exhibiting a sigmoid relation and across roughly a 10-fold increase in energy from no success to 100% success [562]. The lowest energy needed for defibrillation is comparable to the highest energy that induces reentry and VF (see Fig.40c for vulnerability window versus energy), called the upper limit of vulnerability [563]. In other words, when the energy delivered is lower than the upper limit of vulnerability, it not only fails to eliminate the existing reentrant waves but can also induce new reentrant waves. Therefore, to ensure successful defibrillation, an electrical shock with an energy higher than the upper limit of vulnerability is necessary. Shocks of this energy level are quite painful if the patient is awake, which limits the usefulness of defibrillators in patients with slow VT or atrial fibrillation. Recent theoretical and experimental studies, however, are shedding light on how to lower the energy requirements. For example, a theoretical study carried out by Takaji et al [564] showed that lowenergy field stimulation can cause depolarization at an obstacle in cardiac tissue (Fig.73a). If reentry is pinned around the obstacle during slow VT, for example, a low energy shock could cause the spiral wave, depending on the relative phase of the reentry, to become unpinned so that it would drift and terminate. This mechanism has been demonstrated in experiments by Ripplinger et al [565], and shown to be more effective than anti-tachycardia pacing. However, this method is only suitable for terminating reentry around an obstacle, and there is also a chance that the low energy shock will induce VF.

In a more recent study, Pumir et al [566] proposed another theory on how low-energy field stimulation can control complex spatiotemporal electrical turbulence which capitalizes on structural heterogeneities of the heart. The basic idea is as follows:

First, field stimulation causes depolarization at obstacles (Fig.73a), which can be described by the following equation [567]:

$$\nabla^2 e-\frac{e}{\lambda^2}=0 \quad (106)$$

where $e = V - V_{rest}$ with V being the membrane potential and V_{rest} the resting potential, and λ is the space constant on the order of mm. The solution of Eq.106 in a polar coordinate system is

$$e(r,\theta)=-\frac{K_1(r/\lambda)}{K_1^{'}(R/\lambda)}E\lambda\cos\theta \quad (107)$$

where K_1 is the modified Bessel function of the second kind, monotonically decaying with *r*, and K_1' is its derivative. For a fixed electrical field *E*, the maximum depolarization occurs at the boundary of the obstacle in the direction of electrical field (θ=0), i.e.,

$$e_{\max} = -\frac{K_1(R/\lambda)}{K_1'(R/\lambda)} E\lambda \quad (108)$$

Therefore, the depolarization level depends on the size of the obstacle and the strength of the field. The smaller size needs a stronger stimulation to reach the same depolarization. When e_{max} exceeds the threshold voltage for excitation, action potentials occur and can propagate in tissue. The threshold electrical filed strength E_{th} is then estimated as

$$E_{th} = -\frac{e_{th}}{\lambda} \frac{K_1'(R/\lambda)}{K_1(R/\lambda)} \quad (109)$$

where $e_{th} = V_{th} - V_{rest}$. For a small heterogeneity of radius *R*, the electrical field needed is

$$E_{th} \propto 1/R \quad (110)$$

and therefore, as *E* increases, excitations occur at smaller obstacles (Fig.73a).

Second, in the real heart, there are different kinds and sizes of obstacles. For example, the coronary arteries form a scale-free structure, which provides many obstacles with different sizes (Figs.74 a and b). Luther et al [568] showed that during a field stimulation, multiple depolarization sites occur (Fig.74c). Based on the scale-free distribution of obstacle size, Luther et al showed that the activation time (τ) of the whole tissue also follows a power-law with respect to *E*, i.e., $\tau \propto E^{\beta}$, which was demonstrated in their experiments (Fig.74d) [568].

Third, to control a spatiotemporal chaotic systems, many control sites are needed, as shown in studies by Hu and Qu [539]. It is technically not feasible to apply control at many sites using electrodes in real hearts. However, excitations around the obstacles by a field stimulus make it possible to have multiple control sites in the heart to control arrhythmias.

Termination of arrhythmias by low-energy field stimuli based on the above theory was first demonstrated in computer simulations by Pumir et al (Fig.73 b and c) [566], and later in animal experiments by Luther et al and Fenton et al [568, 569].

10. Conclusions and perspective

SCD due to VF is a leading killer in the developed countries [1, 2]. VF and other cardiac arrhythmias have been studied for more than a century, and clinical, experimental, and computational modeling studies have led to important insights into the mechanisms. However, current anti-arrhythmic drugs have limited efficacy at preventing arrhythmias and impacting SCD, and not uncommonly make some arrhythmias worse rather than better. The most reliable therapy is still based on the simple idea of using a large electrical stimulation to destroy all the waves by eliminating the excitable gaps or using radiofrequency catheter ablation to block the reentrant pathway [570].

The difficulty of treating this disease lies in the fact that the heart is a complex system that is regulated by many biological factors at different scales, and the abnormal electrical activities are emergent phenomena arising from dynamical instabilities. Besides many of the dynamics reviewed in this article, there are several general features of arrhythmias that are closely related to complex dynamical systems, such that these features can only be fully understood in the context of nonlinear and stochastic dynamics:

1. Unlike many other human diseases, the transition from normal sinus rhythm to arrhythmias, particularly atrial and ventricular arrhythmias, is a change in the dynamical state of the same heart which does not necessarily require a change in the properties of the heart itself. For example, in every normal healthy heart, VF can be induced by large enough properly-timed electrical stimulation (commonly known as the VF threshold). On the other hand, if the induced arrhythmias are promptly defibrillated, the heart will return back to its normal state and work properly. Therefore, in a simple dynamical view, one can consider this transition as a change of topology of the electrical wave dynamics, or a transition between two states with different basins of attraction (Fig.75). In other words, sinus rhythm is one solution of the heart and VF is another solution. In the normal heart, there is a high threshold to across from the sinus rhythm basin to the VF basin, but in the diseased hearts, the thresholds are much lower. Based on this simple dynamical view, therapeutics must target the transition (by increasing the threshold) rather than trying to remove the VF basin completely, since VF is also a solution of the normal heart. However, arrhythmia solutions differing from that of the normal heart also occur in diseased hearts, which can be also therapeutic targets.

2. Lethal ventricular arrhythmias, such as VF, are “*rare*” and random events. Compared to the number of heart beats during a lifetime, or even the number of PVCs that are often very frequent, especially in diseased hearts, lethal ventricular arrhythmic events are very rare. For example, if a patient has one PVC per minute, he/she will have a half million PVCs in a year, but sustained arrhythmias often occur on a time scale of months, years or even decades. For arrhythmias triggered by a PVC, the odds are very low (less than one in several million PVCs). Moreover, once an arrhythmia is successfully terminated, the patient may not have another event for years or decades. The question, then, is what is special about the PVC that triggers the lethal event? This remains one of the most interesting questions in cardiac electrophysiology and is central to efforts to develop effective therapeutics, identifying individuals at risk who should be treated, and predicting when or under what conditions the arrhythmias will occur. A famous query posed by a leading cardiologist, Dr. Douglas Zipes, epitomizes this issue: “*Why did my patient die on Tuesday and not on Monday?*” [571]. A different way of asking this question is: why do cardiac arrhythmias occur so randomly and unpredictably? If one can identify the patients at high risk for life-threatening arrhythmic events, this alone would greatly improve selection of patients for ICD therapy, since currently only 1 of 5 ICDs implanted actually delivers a life-saving shock [18, 19].

There are many challenges still facing experimental and computational modeling studies. Even though modern technologies allow experimental measurements at many scales, ranging from genetics, to subcellular, cellular and tissue scale mappings, experiments are usually carried out under specific conditions in specific animal models, which capture only some aspects relevant to human patients. In addition, arrhythmias in the human heart are typically rare events, occurring at a time scale of months or years. How to identify the factors that are responsible in triggering arrhythmias in human heart is difficult to assess from animal experiments.

Theoretical and computational modeling studies have generated important insights into the mechanisms of the dynamics that are important for arrhythmias that will help to surmount these challenges. Due to the accurate experimental measurement of electrical properties and structures, and the modeling approach pioneered by Hodgkin and Huxley, the heart may be the most quantitatively modeled system in biology. However, computer simulation itself faces many challenges. Because of the limitations in computational power, it is impossible to include all the molecular and structural information in a computer model of cardiac tissue (or the whole-heart), mandating a multi-scale modeling approach. The approach of "*coarse graining*" is the major means to represent a high-dimensional lower ("finer") scale system using a low-dimensional model at a higher ("coarser") scale, e.g., a myocyte's action potential and Ca^{2+} cycling are described by several dozen ordinary differential equations. These low-dimensional action potential and Ca^{2+} cycling models have been critical in tissue and organ scale studies. However, there are many gaps in the coarse graining process, and how to close these gaps is challenging, not only in cardiac modeling but also in biological modeling in general [146]. One such gaps is the transition from single cell modeling to tissue modeling. Ideally, one would like to use a cell model with detailed spatiotemporal intracellular Ca^{2+} cycling dynamics in tissue- and organ scale simulations so that the effect of the spatiotemporal Ca^{2+} cycling dynamics (such as Ca^{2+} waves and sub-cellular discordant Ca^{2+} alternans) on tissue-scale excitation dynamics can be investigated. However, this is computationally impractical, and no such simulation has been carried out so far. It is only possible to simulate a very small piece of tissue (e.g., several hundred cells) using current advanced computational technology (e.g., GPU computation). Alternatively, one can omit the spatial information at the sub-cellular level and represent it by a low-dimensional system. Most of the existing action potential models are low-dimensional cell models. Such models are largely valid under normal excitation-contraction coupling conditions where local control is dominant. However, once spontaneous Ca^{2+} release and Ca^{2+} waves occur in a myocyte, representing these dynamics in a low-dimensional model becomes nontrivial. Based on a recent study by Nivala et al [111], the cell is in criticality at the spark-to-wave transition, which cannot be captured by a low-dimensional cell model, or even represent it correctly and accurately by a low-dimensional system. Therefore, overcoming this bottleneck in modeling is essential for developing multi-scale modeling approaches to understand the mechanisms of cardiac arrhythmias.

Even if computational power were not limiting, high-dimensional cardiac models are too complex to systematically analyze the dynamics arising from the complex nonlinear interactions. Nonlinear dynamics and statistical physics are the two sciences dealing with complex systems that can provide proper analytical techniques for this purpose, especially when used interactively with high-dimensional models to relate dynamical principles to biological entities.

How to properly integrate diversified experimental data with computer modeling and determine the model parameters is another challenge. A close combination of modeling with experiments is necessary for the systems biology approaches, but is not straightforward. The data available for model parameters: 1) are limited and 2) vary from lab to lab and from experiment to experiment, sometimes by several-fold. In addition, based on recent simulation and experimental studies [572–574], very different combinations of channel conductance can give rise to the same or similar action potentials, indicating that the traditional way of using the averaged data may not be appropriate. Alternative modeling approaches are required.

Moreover, biological systems tend to rely on multiple redundant parallel mechanisms, which can work synergistically or competitively to promote or suppress a phenomenon. For example, in the heart, both voltage and Ca^{2+} cycling systems can generate instabilities resulting in alternans. How to infer the origins of mechanisms from experimental measurements is an important but challenging issue. Computer modeling may provide tell-tale signatures to differentiate the origins. For example, simulation studies have shown that the properties of spatially discordant APD and Ca^{2+} alternans exhibit different signatures when the instabilities originate from voltage versus Ca^{2+}, which can be used to infer the mechanistic origins of alternans [298].

Finally, the ultimate goal of understanding the underlying mechanisms of arrhythmias is to use them for arrhythmia risk stratification and development of effective therapeutics, which is the most challenging problem in the research of cardiac arrhythmias. There is no doubt that the mechanistic insights gained from the nonlinear dynamics and mathematical modeling will be of great importance for prediction of arrhythmia risk and finding proper therapeutic targets, not only for drug therapies but also for device therapies, such as ICD and catheter ablation. Similar to defibrillation, catheter ablation is another widely used therapy for treating arrhythmias [575, 576], which is largely based on anatomical reentrant circuit in tissue and has limited efficacy. Future mathematical and computational studies are needed to gain better mechanistic insights and to improve the efficacy of these device therapies. A very important future direction in computational cardiology is to design *in silico* drug therapies using systematic approaches to identify robust therapeutic strategies. An effective and robust therapy should at least be able to suppress one type or one cause but not to promote other causes of arrhythmias, or ideally, suppress all causes. The failure of the current anti-arrhythmic drugs is because they suppress one cause but promote other causes of arrhythmias, ending up increasing mortality [16, 17]. Considering the complexity of the problem, it will be difficult to identify the risk factors as well as develop robust anti-arrhythmic therapeutics based on experimental and clinical studies alone, computer simulations combined with multi-scale modeling and nonlinear dynamics will also play a fundamental role in achieving this ultimate goal.

In conclusion, cardiac arrhythmias can only be fully understood using a systems approach which integrates clinical, experimental, and computational studies. Complex system theories from statistical physics and nonlinear dynamics have been essential tools to unravel the underlying mechanisms and in helping to design novel therapeutic approaches. On the other hand, the nonlinear dynamics itself will also be enriched via this interdisciplinary research. As P.W. Anderson, a Noble laureate in physics, once said [577]: "…, *we should recognize that such roads [between the sciences], while the quickest shortcut to another part of our own science, are not visible from the viewpoint of one science alone*."

Acknowledgments

We are indebted to those whose work relates to the topics reviewed in this article, whether cited or not. We are grateful for grant support from National Institutes of Health and the American Heart Association (to A.G., J.W., and Z.Q.), National Natural Science Foundation of China (to G.H.), and Laubisch and Kawata Endowments (to J.W.).

Abbreviations

1D	one-dimensional
2D	two-dimensional
3D	three-dimensional
APD	action potential duration
AVN	atrial-ventricular node
Ca^{2+}	calcium ion
CICR	calcium-induced calcium release
CV	conduction velocity
CRU	calcium release unit
DAD	delayed aferdepolarization
DI	diastolic interval
EAD	early afterdepolarization
ECG	electrocardiogram
FHN	FitzHugh-Nagumo
HH	Hodgkin-Huxley
HRV	heart rate variability
ICD	implantable cardioverter-defibrillator
$I_{Ca,L}$	L-type calcium current
I_K	time-dependent potassium current
I_{Na}	sodium current
I_{NCX}	Na^+-Ca^{2+} exchange current
I_{to}	transient outward current

K^+	potassium ion
LCC	L-type calcium channel
LR1	phase I of Luo-Rudy
Na^+	sodium ion
NCX	Na^+-Ca^{2+} exchanger
PCL	pacing cycle length
PVC	premature ventricular contraction
RyR	ryanodine receptor
SAN	sino-atrial node
SCD	sudden cardiac death
SERCA	sarcoplasmic/endoplasmic reticulum calcium ATPase
SR	sarcoplasmic reticulum
TWA	T-wave alternans
VF	ventricular fibrillation
VT	ventricular tachycardia

References

1. Zipes DP, Wellens HJ. Sudden cardiac death. Circulation. 1998; 98:2334–2351. [PubMed: 9826323]
2. Rubart M, Zipes DP. Mechanisms of sudden cardiac death. J. Clin. Invest. 2005; 115:2305–2315. [PubMed: 16138184]
3. Winfree AT. Sudden cardiac death: a problem in topology. Sci. Am. 1983; 248:144–149. 152–147, 160–141. [PubMed: 6857229]
4. Glass L. Dynamics of cardiac arrhythmias. Physics Today. 1996:40–45.
5. Karma A, Gilmour RF. Nonlinear dynamics of heart rhythm disorders. Physics Today. 2007; 60:51–57.
6. Qu Z. Chaos in the genesis and maintenance of cardiac arrhythmias. Prog. Biophys. Mol. Biol. 2011; 105:247–257. [PubMed: 21078337]
7. Karma A. Physics of Cardiac Arrhythmogenesis. Annual Review of Condensed Matter Physics. 2013; 4:313–337.
8. Krogh-Madsen T, Christini DJ. Nonlinear dynamics in cardiology. Annu Rev Biomed Eng. 2012; 14:179–203. [PubMed: 22524390]
9. Durrer D, van Dam RT, Freud GE, Janse MJ, Meijler FL, Arzbaecher RC. Total excitation of the isolated human heart. Circulation. 1970; 41:899–912. [PubMed: 5482907]
10. Campbell SE, Gerdes AM, Smith TD. Comparison of regional differences in cardiac myocyte dimensions in rats, hamsters, and guinea pigs. Anat. Rec. 1987; 219:53–59. [PubMed: 3688461]
11. Satoh H, Delbridge LM, Blatter LA, Bers DM. Surface:volume relationship in cardiac myocytes studied with confocal microscopy and membrane capacitance measurements: speciesdependence and developmental effects. Biophys. J. 1996; 70:1494–1504. [PubMed: 8785306]
12. Bers DM. Cardiac excitation-contraction coupling. Nature. 2002; 415:198–205. [PubMed: 11805843]
13. Go AS, Hylek EM, Phillips KA, Chang Y, Henault LE, Selby JV, Singer DE. Prevalence of Diagnosed Atrial Fibrillation in Adults: National Implications for Rhythm Management and

Stroke Prevention: the AnTicoagulation and Risk Factors In Atrial Fibrillation (ATRIA) Study. JAMA. 2001; 285:2370–2375. [PubMed: 11343485]

14. Valderrama AL, Dunbar SB, Mensah GA. Atrial Fibrillation: Public Health Implications. Am. J. Prev. Med. 2005; 29:75–80. [PubMed: 16389130]
15. Chen PS, Wu TJ, Ting CT, Karagueuzian HS, Garfinkel A, Lin SF, Weiss JN. A tale of two fibrillations. Circulation. 2003; 108:2298–2303. [PubMed: 14609997]
16. CAST I. Effect of encainide and flecainide on mortality in a random trial of arrhythmia suppression after myocardial infarction. N. Engl. J. Med. 1989; 321:406–412. [PubMed: 2473403]
17. Waldo AL, Camm AJ, deRuyter H, Friedman PL, Macneil DJ, Pauls JF, Pitt B, Pratt CM, Schwartz PJ, Veltri EP. Effect of d-sotalol on mortality in patients with left ventricular dysfunction after recent and remote myocardial infarction. Lancet. 1996; 348:7–12. [PubMed: 8691967]
18. Tung R, Zimetbaum P, Josephson ME. A Critical Appraisal of Implantable Cardioverter-Defibrillator Therapy for the Prevention of Sudden Cardiac Death. J. Am. Coll. Cardiol. 2008; 52:1111–1121. [PubMed: 18804736]
19. Bardy GH, Lee KL, Mark DB, Poole JE, Packer DL, Boineau R, Domanski M, Troutman C, Anderson J, Johnson G, McNulty SE, Clapp-Channing N, Davidson-Ray LD, Fraulo ES, Fishbein DP, Luceri RM, Ip JH. Amiodarone or an Implantable Cardioverter-Defibrillator for Congestive Heart Failure. N. Engl. J. Med. 2005; 352:225–237. [PubMed: 15659722]
20. Cheng H, Lederer WJ, Cannell MB. Calcium sparks: elementary events underlying excitation-contraction coupling in heart muscle. Science. 1993; 262:740–744. [PubMed: 8235594]
21. Cheng H, Lederer WJ. Calcium Sparks. Physiol. Rev. 2008; 88:1491–1545. [PubMed: 18923188]
22. van der Pol B. A theory of the amplitude of free and forced triode vibrations. Radio review. 1920; 1:701–710. 754–762.
23. van der Pol B, van der Mark J. The heartbeat considered as a relaxation oscillation and an electrical model of the heart. Philosophical Magazine Series 7. 1928; 6:763–775.
24. Lakatta EG, Maltsev VA, Vinogradova TM. A coupled system of intracellular Ca2+ clocks and surface membrane voltage clocks controls the timekeeping mechanism of the heart's pacemaker. Circ. Res. 2010; 106:659–673. [PubMed: 20203315]
25. Guevara MR, Jongsma HJ. Three ways of abolishing automaticity in sinoatrial node: ionic modeling and nonlinear dynamics. Am. J. Physiol. 1992; 262:1268–1286.
26. Kurata Y, Hisatome I, Imanishi S, Shibamoto T. Roles of L-type Ca2+ and delayed-rectifier K+ currents in sinoatrial node pacemaking: insights from stability and bifurcation analyses of a mathematical model. Am J Physiol Heart Circ Physiol. 2003; 285:H2804–2819. [PubMed: 12919936]
27. Kurata Y, Matsuda H, Hisatome I, Shibamoto T. Regional difference in dynamical property of sinoatrial node pacemaking: role of na+ channel current. Biophys. J. 2008; 95:951–977. [PubMed: 18390617]
28. Kurata Y, Hisatome I, Shibamoto T. Roles of sarcoplasmic reticulum Ca2+ cycling and Na+/Ca2+ exchanger in sinoatrial node pacemaking: insights from bifurcation analysis of mathematical models. Am J Physiol Heart Circ Physiol. 2012; 302:H2285–2300. [PubMed: 22447940]
29. Guevara MR, Glass L, Shrier A. Phase locking, period-doubling bifurcations, and irregular dynamics in periodically stimulated cardiac cells. Science. 1981; 214:1350–1353. [PubMed: 7313693]
30. Guevara MR, Glass L. Phase locking, period doubling bifurcations and chaos in a mathematical model of a periodically driven oscillator: a theory for the entrainment of biological oscillators and the generation of cardiac dysrhythmias. J. Math. Biol. 1982; 14:1–23. [PubMed: 7077182]
31. Glass L, Guevara MR, Shrier A, Perez R. Bifurcation and chaos in a periodically stimulated cardiac oscillator. Physica D: Nonlinear Phenomena. 1983; 7:89–101.
32. Glass L, Guevara MR, Belair J, Shrier A. Global bifurcations of a periodically forced biological oscillator. Physical Review A. 1984; 29:1348–1357.
33. Clay JR, Guevara MR, Shrier A. Phase resetting of the rhythmic activity of embryonic heart cell aggregates. Experiment and theory. Biophys. J. 1984; 45:699–714. [PubMed: 6722263]
34. Glass L, Josephson ME. Resetting and annihilation of reentrant abnormally rapid heartbeat. Phys. Rev. Lett. 1995; 75:2059–2062. [PubMed: 10059198]

35. Guevara MR, Shrier A. Phase resetting in a model of cardiac Purkinje fiber. Biophys. J. 1987; 52:165–175. [PubMed: 3663827]
36. Kunysz AM, Munk AA, Shrier A. Phase resetting and dynamics in isolated atrioventricular nodal cell clusters. Chaos. 1995; 5:184–192. [PubMed: 12780172]
37. Michaels DC, Chialvo DR, Matyas EP, Jalife J. Chaotic activity in a mathematical model of the vagally driven sinoatrial node. Circ. Res. 1989; 65:1350–1360. [PubMed: 2805248]
38. Anumonwo JM, Delmar M, Vinet A, Michaels DC, Jalife J. Phase resetting and entrainment of pacemaker activity in single sinus nodal cells. Circ. Res. 1991; 68:1138–1153. [PubMed: 2009613]
39. Huang X, Mi Y, Qian Y, Hu G. Phase-locking behaviors in an ionic model of sinoatrial node cell and tissue. Phys Rev E Stat Nonlin Soft Matter Phys. 2011; 83:061917. [PubMed: 21797413]
40. Peng CK, Havlin S, Stanley HE, Goldberger AL. Quantification of scaling exponents and crossover phenomena in nonstationary heartbeat time series. Chaos. 1995; 5:82–87. [PubMed: 11538314]
41. Ivanov PC, Rosenblum MG, Peng CK, Mietus J, Havlin S, Stanley HE, Goldberger AL. Scaling behaviour of heartbeat intervals obtained by wavelet-based time series analysis. Nature. 1996; 383:323–327. [PubMed: 8848043]
42. Goldberger AL, Amaral LAN, Hausdorff JM, Ivanov PC, Peng C-K, Stanley HE. Fractal dynamics in physiology: Alterations with disease and aging. Proc. Natl. Acad. Sci. USA. 2002; 99:2466–2472. [PubMed: 11875196]
43. Tapanainen JM, Thomsen PE, Kober L, Torp-Pedersen C, Makikallio TH, Still AM, Lindgren KS, Huikuri HV. Fractal analysis of heart rate variability and mortality after an acute myocardial infarction. Am. J. Cardiol. 2002; 90:347–352. [PubMed: 12161220]
44. Perkiomaki JS, Jokinen V, Tapanainen J, Airaksinen KE, Huikuri HV. Autonomic markers as predictors of nonfatal acute coronary events after myocardial infarction. Ann Noninvasive Electrocardiol. 2008; 13:120–129. [PubMed: 18426437]
45. Glass L. Introduction to controversial topics in nonlinear science: is the normal heart rate chaotic? Chaos. 2009; 19:028501. [PubMed: 19566276]
46. Traube L. Ein fall von pulsus bigeminus nebst bemerkungen tiber die lebershwellungen bei klappenfehlern und uber acute leberatrophic. Ber. Klin. Wschr. 1872; 9:185.
47. Hering HE. Das Wesen des Herzalternans. Muenchener Med Wochenschr. 1908; 4:1414–1421.
48. Lewis T. Notes upon alternation of the heart. Quart. J. Med. 1910; 4:141–144.
49. Kalter HH, Schwartz ML. Electrical alternans. New York state journal of medicine. 1948; 48:1164–1166. [PubMed: 18858860]
50. Rosenbaum DS, Jackson LE, Smith JM, Garan H, Ruskin JN, Cohen RJ. Electrical alternans and vulnerability to ventricular arrhythmias. N. Engl. J. Med. 1994; 330:235–241. [PubMed: 8272084]
51. Verrier RL, Klingenheben T, Malik M, El-Sherif N, Exner DV, Hohnloser SH, Ikeda T, Martinez JP, Narayan SM, Nieminen T, Rosenbaum DS. Microvolt T-wave alternans physiological basis, methods of measurement, and clinical utility--consensus guideline by International Society for Holter and Noninvasive Electrocardiology. J. Am. Coll. Cardiol. 2011; 58:1309–1324. [PubMed: 21920259]
52. Nolasco JB, Dahlen RW. A graphic method for the study of alternation in cardiac action potentials. J. Appl. Physiol. 1968; 25:191–196. [PubMed: 5666097]
53. Guevara MR, Ward G, Shrier A, Glass L. Electrical alternans and period doubling bifurcations. IEEE Comp. Cardiol. 1984; 562:167–170.
54. Chialvo DR, Jalife J. Non-linear dynamics of cardiac excitation and impulse propagation. Nature. 1987; 330:749–752. [PubMed: 3696239]
55. Glass L, Guevara MR, Shrier A. Universal bifurcations and the classification of cardiac arrhythmias. Ann. N. Y. Acad. Sci. 1987; 504:168–178. [PubMed: 3477114]
56. Lewis TJ, Guevara MR. Chaotic dynamics in an ionic model of the propagated cardiac action potential. J. Theor. Biol. 1990; 146:407–432. [PubMed: 2259213]
57. Vinet A, Chialvo DR, Michaels DC, Jalife J. Nonlinear dynamics of rate-dependent activation in models of single cardiac cells. Circ. Res. 1990; 67:1510–1524. [PubMed: 2245510]

58. Chialvo DR, Gilmour RF, Jalife J. Low dimensional chaos in cardiac tissue. Nature. 1990; 343:653–657. [PubMed: 2304537]
59. Chialvo DR, Michaels DC, Jalife J. Supernomal excitability as a mechanism of chaotic dynamics of activation in cardiac Purkinje fibers. Circ. Res. 1990; 66:525–545. [PubMed: 2297816]
60. Karagueuzian HS, Khan SS, Hong K, Kobayashi Y, Denton T, Mandel WJ, Diamond GA. Action potential alternans and irregular dynamics in quinidine-intoxicated ventricular muscle cells. Implications for ventricular proarrhythmia. Circulation. 1993; 87:1661–1672. [PubMed: 8491022]
61. Watanabe M, Otani NF, Gilmour RF. Biphasic restitution of action potential duration and complex dynamics in ventricular myocardium. Circ. Res. 1995; 76:915–921. [PubMed: 7729010]
62. Hastings HM, Fenton FH, Evans SJ, Hotomaroglu O, Geetha J, Gittelson K, Nilson J, Garfinkel A. Alternans and the onset of ventricular fibrillation. Phys Rev E Stat Phys Plasmas Fluids Relat Interdiscip Topics. 2000; 62:4043–4048. [PubMed: 11088928]
63. Fox JJ, Bodenschatz E, Gilmour RF. Period-doubling instability and memory in cardiac tissue. Phys. Rev. Lett. 2002; 89:138101. [PubMed: 12225067]
64. Pastore JM, Girouard SD, Laurita KR, Akar FG, Rosenbaum DS. Mechanism linking T-wave alternans to the genesis of cardiac fibrillation. Circulation. 1999; 99:1385–1394. [PubMed: 10077525]
65. Qu Z, Garfinkel A, Chen PS, Weiss JN. Mechanisms of discordant alternans and induction of reentry in simulated cardiac tissue. Circulation. 2000; 102:1664–1670. [PubMed: 11015345]
66. McWilliam JA. Fibrillar contraction of the heart. J Physiol-London. 1887; 8:296–310.
67. Mines GR. On dynamic equilibrium of the heart. J Physiol-London. 1913; 46:349–482. [PubMed: 16993210]
68. Mines GR. On circulating excitation on heart muscles and their possible relation to tachycardia and fibrillation. Trans.R.Soc.Can. 1914; 4:43–52.
69. Wiener N, Rosenbluth A. The mathematical formulation of the problem of conduction of impulses in a network of connected excitable elements, specifically in cardiac muscle. Arch. Inst. Cardiol. México. 1946; 16:205–265. [PubMed: 20245817]
70. Winfree AT. Spiral waves of chemical activity. Science. 1972; 175:634–636. [PubMed: 17808803]
71. Suzuki, R.; Sato, S.; Nagumo, J. Notes of Professional Group on Nonlinear THeory of IECE (Japan), Feb. 26, 1963. 1963. Electrochemcial Active Netwrok.
72. Zhabotinsky AM, Zaikin AN. Autowave processes in a distributed chemical system. J. Theor. Biol. 1973; 40:45–61. [PubMed: 4723554]
73. Winfree, AT. When Time Breaks Down. Princeton, NJ: Princeton University Press; 1987.
74. Winfree AT. Electrical instability in cardiac muscle: phase singularities and rotors. J. Theor. Biol. 1989; 138:353–405. [PubMed: 2593680]
75. Tyson JJ, Glass L. Arthur T. Winfree (1942-2002). J. Theor. Biol. 2004; 230:433–439. [PubMed: 15363665]
76. Gray RA, Pertsov AM, Jalife J. Spatial and temporal organization during cardiac fibrillation. Nature (London). 1998; 392:75–78. [PubMed: 9510249]
77. Valderrabano M, Chen PS, Lin SF. Spatial distribution of phase singularities in ventricular fibrillation. Circulation. 2003; 108:354–359. [PubMed: 12835210]
78. Bray MA, Lin SF, Wikswo J. Three-dimensional visualization of phase singularities on the isolated rabbit heart. J. Cardiovasc. Electrophysiol. 2002; 13:1311. [PubMed: 12521354]
79. Allessie MA, Bonke FIM, Schopman FJC. Circus movement in rabbit atrial muscle as a mechanism of tachycardia. III. The "leading circle" concept: A new model of circus movement in cardiac tissue without the invoement of an anatomical obstacle. Circ. Res. 1977; 41:9–41. [PubMed: 862147]
80. Chen P-S, Wolf PD, Dixon EG, Danieley ND, Frazier DW, Smith WM, Ideker RE. Mechanism of ventricular vulnerability to single premature stimuli in open chest dogs. Circ. Res. 1988; 62:1191–1209. [PubMed: 2454762]
81. Frazier DW, Wolf PD, Wharton JM, Tang AS, Smith WM, Ideker RE. Stimulus-induced critical point. Mechanism for electrical initiation of reentry in normal canine myocardium. J. Clin. Invest. 1989; 83:1039–1052. [PubMed: 2921316]

82. Davidenko JM, Pertsov AM, Salomonsz R, Baxter W, Jalife J. Stationary and drifting spiral waves of excitation in isolated cardiac muscle. Nature. 1992; 355:349–351. [PubMed: 1731248]

83. Davidenko JM, Kent PF, Chialvo DR, Michaels DC, Jalife J. Sustained vortex-like waves in normal isolated ventricular muscle. Proc Natl Acad Sci U S A. 1990; 87:8785–8789. [PubMed: 2247448]

84. Pertsov AM, Davidenko JM, Salomonsz R, Baxter WT, Jalife J. Spiral waves of excitation underlie reentrant activity in isolated cardiac muscle. Circ. Res. 1993; 72:631–650. [PubMed: 8431989]

85. Ishiguro YS, Honjo H, Opthof T, Okuno Y, Nakagawa H, Yamazaki M, Harada M, Takanari H, Suzuki T, Morishima M, Sakuma I, Kamiya K, Kodama I. Early termination of spiral wave reentry by combined blockade of Na+ and L-type Ca2+ currents in a perfused two-dimensional epicardial layer of rabbit ventricular myocardium. Heart Rhythm. 2009; 6:684–692. [PubMed: 19303369]

86. Winfree AT. Persistent tangled vortex rings in generic excitable media. Nature. 1994; 371:233–236. [PubMed: 8078583]

87. Winfree AT, Strogatz SH. Organizing centers for three-dimensional chemical waves. Nature. 1984; 311:611–615. [PubMed: 6548297]

88. Zykov, VS. Simulation of wave process in excitable media. Manchester and New York: Manchester University Press; 1982.

89. Keener JP, Tyson J. The dynamics of scroll waves in excitable media. SIAM Rev. 1992; 34:1–39.

90. Keener JP, Tyson JJ. Spiral waves in the Belousov-Zhabotinskii reaction. Physica D. 1986; 21:307–324.

91. Panfilov AV, Aliev RR, Mushinsky AV. An integral invariant for scroll rings in a reaction-diffusion system. Physica D. 1989; 36:181–188.

92. Karma A. Meandering transition in two-dimensional excitable media. Phys. Rev. Lett. 1990; 65:2824–2827. [PubMed: 10042704]

93. Barkley D. Linear stability analysis of rotating spiral waves in excitable media. Phys. Rev. Lett. 1992; 68:2090–2093. [PubMed: 10045301]

94. Winfree AT. Varieties of spiral wave behavior: An experimentalist's approach to the theory of excitable media. Chaos. 1991; 1:303–334. [PubMed: 12779929]

95. Bar M, Eiswirth M. Turbulence due to spiral breakup in a continuous excitable medium. Phys.Rev.E. 1993; 48:R1635–R1637.

96. Panfilov AV, Hogeweg P. Spiral breakup in a modified FitzHugh-Nagumo model. Phys.Lett.A. 1993; 176:295–299.

97. Panfilov AV, Hogeweg P. Scroll breakup in a three-dimensional excitable medium. Phys.Rev.E. 1996; 53:1740–1743.

98. Karma A. Spiral breakup in model equations of action potential propagation in cardiac tissue. Phys. Rev. Lett. 1993; 71:1103–1106. [PubMed: 10055449]

99. Karma A. Electrical alternans and spiral wave breakup in cardiac tissue. Chaos. 1994; 4:461–472. [PubMed: 12780121]

100. Courtemanche M. Complex spiral wave dynamics in a spatially distributed ionic model of cardiac electrical activity. Chaos. 1996; 6:579–600. [PubMed: 12780289]

101. Qu Z, Weiss JN, Garfinkel A. Cardiac electrical restitution properties and the stability of reentrant spiral waves: A simulation study. Am. J. Physiol. 1999; 276:H269–H283. [PubMed: 9887041]

102. Qu Z, Xie F, Garfinkel A, Weiss JN. Origins of spiral wave meander and breakup in a two-dimensional cardiac tissue model. Ann. Biomed. Eng. 2000; 28:755–771. [PubMed: 11016413]

103. Fenton F, Karma A. Vortex dynamics in three-dimensional continuous myocardium with fiber rotation: Filament instability and fibrillation. Chaos. 1998; 8:20–47. [PubMed: 12779708]

104. Qu Z, Kil J, Xie F, Garfinkel A, Weiss JN. Scroll wave dynamics in a threedimensional cardiac tissue model: roles of restitution, thickness, and fiber rotation. Biophys. J. 2000; 78:2761–2775. [PubMed: 10827961]

105. Gray RA, Jalife J, Panfilov AV, Baxter WT, Cabo C, Davidenko JM, Pertsov AM. Nonstationary vortexlike reentrant activity as a mechanism of polymorphic ventricular tachycardia in the isolated rabbit heart. Circulation. 1995; 91:2454–2469. [PubMed: 7729033]

106. Weiss JN, Qu Z, Chen PS, Lin SF, Karagueuzian HS, Hayashi H, Garfinkel A, Karma A. The dynamics of cardiac fibrillation. Circulation. 2005; 112:1232–1240. [PubMed: 16116073]

107. Qu, Z.; Garfinkel, A. Nonlinear dynamics of excitation and propagation in cardiac muscle. In: Zipes, DP.; Jalife, J., editors. Cardiac Electrophysiology: From Cell to Bedside. Philadelphia: Saunders; 2004. p. 327-335.

108. Zhao Z, Wen H, Fefelova N, Allen C, Baba A, Matsuda T, Xie LH. Revisiting the ionic mechanisms of early afterdepolarizations in cardiomyocytes: predominant by Ca waves or Ca currents? Am J Physiol Heart Circ Physiol. 2012; 302:H1636–1644. [PubMed: 22307670]

109. Bootman MD, Berridge MJ, Lipp P. Cooking with calcium: the recipes for composing global signals from elementary events. Cell. 1997; 91:367–373. [PubMed: 9363945]

110. Falcke M. Reading the patterns in living cells —the physics of ca2+ signaling. Advances in Physics. 2004; 53:255–440.

111. Nivala M, Ko CY, Nivala M, Weiss JN, Qu Z. Criticality in intracellular calcium signaling in cardiac myocytes. Biophys. J. 2012; 102:2433–2442. [PubMed: 22713558]

112. Aon MA, Cortassa S, O'Rourke B. Percolation and criticality in a mitochondrial network. Proc Natl Acad Sci U S A. 2004; 101:4447–4452. [PubMed: 15070738]

113. Nivala M, Korge P, Nivala M, Weiss JN, Qu Z. Linking flickering to waves and whole-cell oscillations in a mitochondrial network model. Biophys. J. 2011; 101:2102–2111. [PubMed: 22067147]

114. Cao Z, Li P, Zhang H, Xie F, Hu G. Turbulence control with local pacing and its implication in cardiac defibrillation, Chaos. An Interdisciplinary Journal of Nonlinear Science. 2007; 17:015107–015109.

115. Xie F, Qu Z, Weiss JN, Garfinkel A. Coexistence of multiple spiral waves with independent frequencies in a heterogeneous excitable medium. Phys. Rev. E. 2001; 63:031905.

116. Sweeney MO. Antitachycardia Pacing for Ventricular Tachycardia Using Implantable Cardioverter Defibrillators. Pacing Clin. Electrophysiol. 2004; 27:1292–1305. [PubMed: 15461721]

117. Qu Z. Critical mass hypothesis revisited: Role of dynamical wave stability in spontaneous termination of cardiac fibrillation. Am J Physiol Heart Circ Physiol. 2006; 290:H255–263. [PubMed: 16113075]

118. Hodgkin AL, Huxley AF. A Quantitative Description of Membrane Current and Its Application to Conduction and Excitation in Nerve. Journal of Physiology-London. 1952; 117:500–544.

119. Catterall WA, Raman IM, Robinson HPC, Sejnowski TJ, Paulsen O. The Hodgkin-Huxley Heritage: From Channels to Circuits. The Journal of Neuroscience. 2012; 32:14064–14073. [PubMed: 23055474]

120. Schwiening CJ. A brief historical perspective: Hodgkin and Huxley. The Journal of Physiology. 2012; 590:2571–2575. [PubMed: 22787170]

121. Izhikevich EM, Fitzhugh R. FitzHugh-Nagumo model. Scholarpedia. 2006; 1:1349.

122. Fitzhugh R. Impulses and Physiological States in Theoretical Models of Nerve Membrane. Biophys. J. 1961; 1:445–466. [PubMed: 19431309]

123. Nagumo J, Arimoto S, Yoshizawa S. An Active Pulse Transmission Line Simulating Nerve Axon. Proceedings of the IRE. 1962; 50:2061–2070.

124. Keener, JP.; Sneyd, J. Mathematical Physiology. Springer; New York: 1998.

125. Weiss, JN. Ion channels in cardiac muscle. In: Langer, GA., editor. The Mammalian Myocardium. San Diego: Academic Press; 1997.

126. Zeng J, Laurita KR, Rosenbaum DS, Rudy Y. Two components of the delayed rectifier K+ current in ventricular myocytes of the guinea pig type. Theoretical formulation and their role in repolarization. Circ. Res. 1995; 77:140–152. [PubMed: 7788872]

127. Noble D. A modification of the Hodgkin-Huxley equations applicable to Purkinje fibre action and pace-maker potentials. J. Physiol. 1962; 160:317–352. [PubMed: 14480151]

128. Irisawa, H.; Noma, A. Pacemaker mechanisms of rabbit sinoatrial node cells. In: Bouman, LN.; Jonsma, HJ., editors. Cardiac rate and rhythm: Physiological, morphological, adn developmental aspects. London: Martinus Nijhoff; 1982. p. 35-51.

129. Courtemanche M, Ramirez RJ, Nattel S. Ionic mechanisms underlying human atrial action potential properties: insights from a mathematical model. Am. J. Physiol. 1998; 275:H301–321. [PubMed: 9688927]

130. Beeler GW, Reuter H. Reconstruction of the action potential of ventricular myocardial fibres. J. Physiol. (Lond). 1977; 268:177–210. [PubMed: 874889]

131. Bondarenko VE, Szigeti GP, Bett GCL, Kim S-J, Rasmusson RL. Computer model of action potential of mouse ventricular myocytes. Am J Physiol Heart Circ Physiol. 2004; 287:H1378–1403. [PubMed: 15142845]

132. Pandit SV, Clark RB, Giles WR, Demir SS. A mathematical model of action potential heterogeneity in adult rat left ventricular myocytes. Biophys. J. 2001; 81:3029–3051. [PubMed: 11720973]

133. Luo CH, Rudy Y. A model of the ventricular cardiac action potential: depolarization, repolarization, and their interaction. Circ. Res. 1991; 68:1501–1526. [PubMed: 1709839]

134. Puglisi JL, Bers DM. LabHEART: an interactive computer model of rabbit ventricular myocyte ion channels and Ca transport. Am J Physiol Cell Physiol. 2001; 281:C2049–2060. [PubMed: 11698264]

135. Winslow RL, Rice J, Jafri S, Marbán E, O'Rourke B. Mechanisms of altered excitation-contraction coupling in canine tachycardia-induced heart failure, II: model studies. Circ. Res. 1999; 84:571–586. [PubMed: 10082479]

136. ten Tusscher KH, Noble D, Noble PJ, Panfilov AV. A model for human ventricular tissue. Am J Physiol Heart Circ Physiol. 2004; 286:H1573–1589. [PubMed: 14656705]

137. Noble D, Garny A, Noble PJ. How the Hodgkin–Huxley equations inspired the Cardiac Physiome Project. The Journal of Physiology. 2012; 590:2613–2628. [PubMed: 22473779]

138. Luo CH, Rudy Y. A dynamical model of the cardiac ventricular action potential: I. simulations of ionic currents and concentration changes. Circ. Res. 1994; 74:1071–1096. [PubMed: 7514509]

139. Hilgemann DW, Noble D. Excitation-contraction coupling and extracellular calcium transients in rabbit atrium: reconstruction of basic cellular mechanisms. Proc. R. Soc. Lond. B. Biol. Sci. 1987; 230:163–205. [PubMed: 2884668]

140. Clancy CE, Rudy Y. Linking a genetic defect to its cellular phenotype in a cardiac arrhythmia. Nature. 1999; 400:566–569. [PubMed: 10448858]

141. Saucerman JJ, Brunton LL, Michailova AP, McCulloch AD. Modeling beta-adrenergic control of cardiac myocyte contractility in silico. J. Biol. Chem. 2003; 278:47997–48003. [PubMed: 12972422]

142. Hund TJ, Rudy Y. Rate dependence and regulation of action potential and calcium transient in a canine cardiac ventricular cell model. Circulation. 2004; 110:3168–3174. [PubMed: 15505083]

143. Nivala M, de Lange E, Rovetti R, Qu Z. Computational modeling and numerical methods for spatiotemporal calcium cycling in ventricular myocytes. Front Physiol. 2012; 3:114. [PubMed: 22586402]

144. Greenstein JL, Winslow RL. An integrative model of the cardiac ventricular myocyte incorporating local control of ca(2+) release. Biophys. J. 2002; 83:2918–2945. [PubMed: 12496068]

145. Cooper J, Mirams GR, Niederer SA. High-throughput functional curation of cellular electrophysiology models. Prog. Biophys. Mol. Biol. 2011; 107:11–20. [PubMed: 21704062]

146. Qu Z, Garfinkel A, Weiss JN, Nivala M. Multi-scale modeling in biology: How to bridge the gaps between scales? Prog. Biophys. Mol. Biol. 2011; 107:21–31. [PubMed: 21704063]

147. Yao J-A, Gutstein DE, Liu F, Fishman GI, Wit AL. Cell Coupling Between Ventricular Myocyte Pairs From Connexin43-Deficient Murine Hearts. Circ. Res. 2003; 93:736–743. [PubMed: 14500334]

148. Peters NS, Wit AL. Myocardial architecture and ventricular arrhythmogenesis. Circulation. 1998; 97:1746–1754. [PubMed: 9591770]

149. Hubbard ML, Ying W, Henriquez CS. Effect of gap junction distribution on impulse propagation in a monolayer of myocytes: a model study. Europace. 2007; 9(Suppl 6):vi20–vi28. [PubMed: 17959689]

150. Xie Y, Garfinkel A, Camelliti P, Kohl P, Weiss JN, Qu Z. Effects of fibroblast-myocyte coupling on cardiac conduction and vulnerability to reentry: A computational study. Heart Rhythm. 2009; 6:1641–1649. [PubMed: 19879544]
151. Xie Y, Garfinkel A, Weiss JN, Qu Z. Cardiac alternans induced by fibroblast-myocyte coupling: mechanistic insights from computational models. Am J Physiol Heart Circ Physiol. 2009; 297:H775–784. [PubMed: 19482965]
152. Clerc L. Directional differences of impulse spread in trabecular muscle from mammalian heart. J. Physiol. 1976; 255:335–346. [PubMed: 1255523]
153. Valderrabano M. Influence of anisotropic conduction properties in the propagation of the cardiac action potential. Prog. Biophys. Mol. Biol. 2007; 94:144–168. [PubMed: 17482242]
154. Nielsen PMF, Grice IJL, Smaill BH, Hunter PJ. Mathematical model of geometry and fibrous structure of the heart. Am. J. Physiol. 1991; 260:H1365–H1378. [PubMed: 2012234]
155. Roth BJ. How the anisotropy of the intracellular and extracellular conductivities influences stimulation of cardiac muscle. J. Math. Biol. 1992; 30:633–646. [PubMed: 1640183]
156. Lin SF, Roth BJ, Wikswo JP Jr. Quatrefoil reentry in myocardium: an optical imaging study of the induction mechanism. J. Cardiovasc. Electrophysiol. 1999; 10:574–586. [PubMed: 10355700]
157. Efimov IR, Cheng Y, Van Wagoner DR, Mazgalev T, Tchou PJ. Virtual electrode-induced phase singularity: a basic mechanism of defibrillation failure. Circ. Res. 1998; 82:918–925. [PubMed: 9576111]
158. Wikswo JP Jr, Lin SF, Abbas RA. Virtual electrodes in cardiac tissue: a common mechanism for anodal and cathodal stimulation. Biophys. J. 1995; 69:2195–2210. [PubMed: 8599628]
159. Henriquez CS. Simulating the electrical behavior of cardiac tissue using the bidomain model. Crit. Rev. Biomed. Eng. 1993; 21:1–77. [PubMed: 8365198]
160. Roth BJ. Mechanisms for electrical stimulation of excitable tissue. Crit. Rev. Biomed. Eng. 1994; 22:253–305. [PubMed: 8598130]
161. Hunter PJ, Pullan AJ, Smaill BH. Modeling total heart function. Annu Rev Biomed Eng. 2003; 5:147–177. [PubMed: 14527312]
162. Potse M, Dube xB, Richer J, Vinet A, Gulrajani RM. A Comparison of Monodomain and Bidomain Reaction-Diffusion Models for Action Potential Propagation in the Human Heart. Biomedical Engineering, IEEE Transactions on. 2006; 53:2425–2435.
163. Roth BJ. Frequency locking of meandering spiral waves in cardiac tissue. Physical Review E (Statistical Physics, Plasmas, Fluids, and Related Interdisciplinary Topics). 1998; 57:R3735–3738.
164. Xie F, Qu Z, Yang J, Baher A, Weiss JN, Garfinkel A. A simulation study of the effects of cardiac anatomy in ventricular fibrillation. J. Clin. Invest. 2004; 113:686–693. [PubMed: 14991066]
165. Rodriguez B, Li L, Eason JC, Efimov IR, Trayanova NA. Differences between left and right ventricular chamber geometry affect cardiac vulnerability to electric shocks. Circ. Res. 2005; 97:168–175. [PubMed: 15976315]
166. Sato D, Xie LH, Sovari AA, Tran DX, Morita N, Xie F, Karagueuzian H, Garfinkel A, Weiss JN, Qu Z. Synchronization of chaotic early afterdepolarizations in the genesis of cardiac arrhythmias. Proc Natl Acad Sci U S A. 2009; 106:2983–2988. [PubMed: 19218447]
167. Ten Tusscher KH, Hren R, Panfilov AV. Organization of ventricular fibrillation in the human heart. Circ. Res. 2007; 100:e87–101. [PubMed: 17540975]
168. Trayanova NA. Whole-heart modeling: applications to cardiac electrophysiology and electromechanics. Circ. Res. 2011; 108:113–128. [PubMed: 21212393]
169. Rush S, Larsen H. A practical algorithm for solving dynamic membrane equations. IEEE Trans. Biomed. Eng. 1978; 25:389–392. [PubMed: 689699]
170. Qu Z, Garfinkel A. An advanced numerical algorithm for solving partial differential equation in cardiac conduction. IEEE Trans. Biomed. Eng. 1999; 49:1166–1168. [PubMed: 10493080]
171. Sundnes J, Lines GT, Tveito A. An operator splitting method for solving the bidomain equations coupled to a volume conductor model for the torso. Math. Biosci. 2005; 194:233–248. [PubMed: 15854678]

172. Sato D, Xie Y, Weiss JN, Qu Z, Garfinkel A, Sanderson AR. Acceleration of cardiac tissue simulation with graphic processing units. Med. Biol. Eng. Comput. 2009; 47:1011–1015. [PubMed: 19655187]

173. Plank G, Zhou L, Greenstein JL, Cortassa S, Winslow RL, O'Rourke B, Trayanova NA. From mitochondrial ion channels to arrhythmias in the heart: computational techniques to bridge the spatio-temporal scales. Philosophical transactions. Series A, Mathematical, physical, and engineering sciences. 2008; 366:3381–3409.

174. Gillespie DT. Exact stochastic simulation of coupled chemical reactions. The Journal of Physical Chemistry. 1977; 81:2340–2361.

175. DeFelice, LJ.; Clay, JR. Membrane current and membrane potential from single-channel kinetics. In: Sakmann, B.; Neher, E., editors. Single-Channel Recording. New York & London: Plenum Press; 1985. p. 323-344.

176. Fox RF. Stochastic versions of the Hodgkin-Huxley equations. Biophys. J. 1997; 72:2068–2074. [PubMed: 9129809]

177. Berridge MJ, Lipp P, Bootman MD. The versatility and universality of calcium signalling. Nat Rev Mol Cell Biol. 2000; 1:11–21. [PubMed: 11413485]

178. Fabiato A. Calcium-induced release of calcium from the cardiac sarcoplasmic reticulum. Am. J. Physiol. 1983; 245:C1–14. [PubMed: 6346892]

179. Sneyd J, Girard S, Clapham D. Calcium wave propagation by calcium-induced calcium release: an unusual excitable system. Bull. Math. Biol. 1993; 55:315–344. [PubMed: 8431705]

180. Girard S, Luckhoff A, Lechleiter J, Sneyd J, Clapham D. Two-dimensional model of calcium waves reproduces the patterns observed in Xenopus oocytes. Biophys. J. 1992; 61:509–517. [PubMed: 1547335]

181. Falcke M, Tsimring L, Levine H. Stochastic spreading of intracellular Ca(2+) release. Phys Rev E Stat Phys Plasmas Fluids Relat Interdiscip Topics. 2000; 62:2636–2643. [PubMed: 11088743]

182. Sobie EA, Dilly KW, dos Santos Cruz J, Lederer WJ, Jafri MS. Termination of cardiac Ca(2+) sparks: an investigative mathematical model of calcium-induced calcium release. Biophys. J. 2002; 83:59–78. [PubMed: 12080100]

183. Izu LT, Means SA, Shadid JN, Chen-Izu Y, Balke CW. Interplay of ryanodine receptor distribution and calcium dynamics. Biophys. J. 2006; 91:95–112. [PubMed: 16603499]

184. Hake J, Edwards AG, Yu Z, Kekenes-Huskey PM, Michailova AP, McCammon JA, Holst MJ, Hoshijima M, McCulloch AD. Modeling Cardiac Calcium Sparks in a Three-Dimensional Reconstruction of a Calcium Release Unit. J. Physiol. 2012; 590:4403–4422. [PubMed: 22495592]

185. Restrepo JG, Weiss JN, Karma A. Calsequestrin-mediated mechanism for cellular calcium transient alternans. Biophys. J. 2008; 95:3767–3789. [PubMed: 18676655]

186. Chen W, Wasserstrom JA, Shiferaw Y. Role of coupled gating between cardiac ryanodine receptors in the genesis of triggered arrhythmias. Am J Physiol Heart Circ Physiol. 2009; 297:H171–180. [PubMed: 19429830]

187. Wagner J, Keizer J. Effects of rapid buffers on Ca2+ diffusion and Ca2+ oscillations. Biophys. J. 1994; 67:447–456. [PubMed: 7919018]

188. Hodgkin AL, Huxley AF, Katz B. Measurement of current-voltage relations in the membrane of the giant axon of Loligo. J. Physiol. 1952; 116:424–448. [PubMed: 14946712]

189. Neher E, Sakmann B. Single-channel currents recorded from membrane of denervated frog muscle fibres. Nature. 1976; 260:799–802. [PubMed: 1083489]

190. Hamill OP, Marty A, Neher E, Sakmann B, Sigworth FJ. Improved patch-clamp techniques for high-resolution current recording from cells and cell-free membrane patches. Pflugers Arch. 1981; 391:85–100. [PubMed: 6270629]

191. Efimov IR, Nikolski VP, Salama G. Optical imaging of the heart. Circ. Res. 2004; 95:21–33. [PubMed: 15242982]

192. McGee R, Sansom MSP, Usherwood PNR. Charaterization of a delayed rectifier K(+) channel in NG108-15 neuroblastoma X glioma cells: gating kinetics and the effects of enrichment of membrane phospholipids with arachidonic acid. J.Membrane Biol. 1988; 102:21–34. [PubMed: 2456394]

193. Sansom MS, Ball FG, Kerry CJ, McGee R, Ramsey RL, Usherwood PN. Markov, fractal, diffusion, and related models of ion channel gating. A comparison with experimental data from two ion channels. Biophys. J. 1989; 56:1229–1243. [PubMed: 2482085]

194. Liebovitch, LS. Single channels: from Markovian to fractal models. In: Zipes, DP.; Jalife, J., editors. Cardiac electrophysiology: from cell to bedside. Philadelphia: W.B.Saunders Co.; 1995. p. 293-304.

195. Millhauser GL, Salpeter EE, Oswald RE. Diffusion models of ion-channel gating and the origin of power-law distributions from single-channel recording. Proc Natl Acad Sci U S A. 1988; 85:1503–1507. [PubMed: 2449693]

196. Lowen SB, Liebovitch LS, White JA. Fractal ion-channel behavior generates fractal firing patterns in neuronal models. Phys. Rev. E. 1999; 59:5970–5980.

197. Goychuk I, Hanggi P. Ion channel gating: a first-passage time analysis of the Kramers type. Proc Natl Acad Sci U S A. 2002; 99:3552–3556. [PubMed: 11891285]

198. Platt N, Hammel SM, Heagy JF. Effects of additive noise on on-off intermittency. Phys. Rev. Lett. 1994; 72:3498–3501. [PubMed: 10056215]

199. Hu G, Qu Z, Xie F, Shu S-Q. On-off intermittency in continuous systems. Communications in Theoretical Physics. 1997; 27:311–316.

200. Yu YH, Kwak K, Lim TK. On-off intermittency in an experimental synchronization process. Physics Letters A. 1995; 198:34–38.

201. Berridge MJ, Bootman MD, Lipp P. Calcium--a life and death signal. Nature. 1998; 395:645–648. [PubMed: 9790183]

202. Clapham DE. Calcium signaling. Cell. 2007; 131:1047–1058. [PubMed: 18083096]

203. Stern MD, Cheng H. Putting out the fire: what terminates calcium-induced calcium release in cardiac muscle? Cell Calcium. 2004; 35:591–601. [PubMed: 15110149]

204. Winslow RL, Greenstein JL. Extinguishing the sparks. Biophys. J. 2013; 104:2115–2117. [PubMed: 23708349]

205. Zima AV, Picht E, Bers DM, Blatter LA. Partial inhibition of sarcoplasmic reticulum ca release evokes long-lasting ca release events in ventricular myocytes: role of luminal ca in termination of ca release. Biophys. J. 2008; 94:1867–1879. [PubMed: 18024505]

206. Hinch R. A Mathematical Analysis of the Generation and Termination of Calcium Sparks. Biophys. J. 2004; 86:1293–1307. [PubMed: 14990462]

207. Stern MD, Rios E, Maltsev VA. Life and death of a cardiac calcium spark. J. Gen. Physiol. 2013; 142:257–274. [PubMed: 23980195]

208. Risken, H. The Fokker-Plank Equation. Berlin: Springer; 1989.

209. Lechleiter J, Girard S, Peralta E, Clapham D. Spiral calcium wave propagation and annihilation in Xenopus laevis oocytes. Science. 1991; 252:123–126. [PubMed: 2011747]

210. Newman EA, Zahs KR. Calcium Waves in Retinal Glial Cells. Science. 1997; 275:844–847. [PubMed: 9012354]

211. Dani JW, Chernjavsky A, Smith SJ. Neuronal activity triggers calcium waves in hippocampal astrocyte networks. Neuron. 1992; 8:429–440. [PubMed: 1347996]

212. Marchant J, Callamaras N, Parker I. Initiation of IP(3)-mediated Ca(2+) waves in Xenopus oocytes. EMBO J. 1999; 18:5285–5299. [PubMed: 10508162]

213. Marchant JS, Parker I. Role of elementary Ca(2+) puffs in generating repetitive Ca(2+) oscillations. EMBO J. 2001; 20:65–76. [PubMed: 11226156]

214. Cheng H, Lederer MR, Lederer WJ, Cannell MB. Calcium sparks and [Ca2+]i waves in cardiac myocytes. Am. J. Physiol. 1996; 270:C148–C159. [PubMed: 8772440]

215. Wier WG, ter Keurs HE, Marban E, Gao WD, Balke CW. Ca2+ 'sparks' and waves in intact ventricular muscle resolved by confocal imaging. Circ. Res. 1997; 81:462–469. [PubMed: 9314826]

216. Lipp P, Niggli E. Microscopic spiral waves reveal positive feedback in subcellular calcium signaling. Biophys. J. 1993; 65:2272–2276. [PubMed: 8312468]

217. Wasserstrom JA, Shiferaw Y, Chen W, Ramakrishna S, Patel H, Kelly JE, O'Toole MJ, Pappas A, Chirayil N, Bassi N, Akintilo L, Wu M, Arora R, Aistrup GL. Variability in timing of

spontaneous calcium release in the intact rat heart is determined by the time course of sarcoplasmic reticulum calcium load. Circ. Res. 2010; 107:1117–1126. [PubMed: 20829511]

218. ter Keurs HEDJ, Boyden PA. Calcium and Arrhythmogenesis. Physiol. Rev. 2007; 87:457–506. [PubMed: 17429038]
219. Falcke M. On the role of stochastic channel behavior in intracellular Ca2+ dynamics. Biophys. J. 2003; 84:42–56. [PubMed: 12524264]
220. Skupin A, Kettenmann H, Falcke M. Calcium signals driven by single channel noise. PLoS Comput Biol. 2010; 6
221. Skupin A, Kettenmann H, Winkler U, Wartenberg M, Sauer H, Tovey SC, Taylor CW, Falcke M. How does intracellular Ca2+ oscillate: by chance or by the clock? Biophys. J. 2008; 94:2404–2411. [PubMed: 18065468]
222. Thurley K, Smith IF, Tovey SC, Taylor CW, Parker I, Falcke M. Timescales of IP(3)-evoked Ca(2+) spikes emerge from Ca(2+) puffs only at the cellular level. Biophys. J. 2011; 101:2638–2644. [PubMed: 22261051]
223. Stanley HE. Scaling, universality, and renormalization: Three pillars of modern critical phenomena. Rev. Mod. Phys. 1999; 71:S358–S366.
224. Bak P, Tang C, Wiesenfeld K. Self-organized criticality. Phys Rev A. 1988; 38:364–374. [PubMed: 9900174]
225. Turcotte DL, Rundle JB. Self-organized complexity in the physical, biological, and social sciences. Proc Natl Acad Sci U S A. 2002; 99(Suppl 1):2463–2465. [PubMed: 11875195]
226. Nivala M, Ko CY, Nivala M, Weiss JN, Qu Z. The Emergence of Subcellular Pacemaker Sites for Calcium Waves and Oscillations. J. Physiol. 2013; 591:5305–5320. [PubMed: 24042497]
227. Lorenz CD, Ziff RM. Precise determination of the bond percolation thresholds and finite-size scaling corrections for the sc, fcc, and bcc lattices. Phys. Rev. E. 1998; 57:230–236.
228. Stauffer, D.; Aharony, A. Introduction to Percolation Theory. 2nd ed.. Taylor & Francis; Philadelphia: 1994.
229. Baddeley D, Jayasinghe ID, Lam L, Rossberger S, Cannell MB, Soeller C. Optical single-channel resolution imaging of the ryanodine receptor distribution in rat cardiac myocytes. Proc Natl Acad Sci U S A. 2009; 106:22275–22280. [PubMed: 20018773]
230. Rooney TA, Sass EJ, Thomas AP. Agonist-induced cytosolic calcium oscillations originate from a specific locus in single hepatocytes. J. Biol. Chem. 1990; 265:10792–10796. [PubMed: 2113061]
231. Thorn P, Lawrie AM, Smith PM, Gallacher DV, Petersen OH. Local and global cytosolic Ca2+ oscillations in exocrine cells evoked by agonists and inositol trisphosphate. Cell. 1993; 74:661–668. [PubMed: 8395347]
232. Kasai H, Li YX, Miyashita Y. Subcellular distribution of Ca2+ release channels underlying Ca2+ waves and oscillations in exocrine pancreas. Cell. 1993; 74:669–677. [PubMed: 8395348]
233. Simpson PB, Mehotra S, Lange GD, Russell JT. High Density Distribution of Endoplasmic Reticulum Proteins and Mitochondria at Specialized Ca2+ Release Sites in Oligodendrocyte Processes. J. Biol. Chem. 1997; 272:22654–22661. [PubMed: 9278423]
234. Stanley, HE. Introduction to Phase Transitions and Critical Phenomena. London: Oxford University Press; 1971.
235. Lakatta EG, Maltsev VA, Bogdanov KY, Stern MD, Vinogradova TM. Cyclic variation of intracellular calcium: a critical factor for cardiac pacemaker cell dominance. Circ. Res. 2003; 92:e45–50. [PubMed: 12595348]
236. Ivanov PC, Amaral LA, Goldberger AL, Havlin S, Rosenblum MG, Struzik ZR, Stanley HE. Multifractality in human heartbeat dynamics. Nature. 1999; 399:461–465. [PubMed: 10365957]
237. Ponard JG, Kondratyev AA, Kucera JP. Mechanisms of intrinsic beating variability in cardiac cell cultures and model pacemaker networks. Biophys. J. 2007; 92:3734–3752. [PubMed: 17325022]
238. Franz MR, Schaefer J, Schottler M, Seed WA, Noble MIM. Electrical and mechanical restitution of the human heart at different rates of stimulation. Circ. Res. 1983; 53:815–822. [PubMed: 6640866]

239. Franz MR, Swerdlow CD, Liem LB, Schaefer J. Cycle length dependence of human action potential duration in vivo: Effects of single extrastimuli, sudden sustained rate acceleration and deceleration, and different steady-state frequencies. J. Clin. Invest. 1988; 82:972–979. [PubMed: 3417875]
240. Qu Z, Shiferaw Y, Weiss JN. Nonlinear dynamics of cardiac excitation-contraction coupling: an iterated map study. Phys Rev E. 2007; 75:011927.
241. Qu Z, Weiss JN, Garfinkel A. Spatiotemporal chaos in a simulated ring of cardiac cells. Phys. Rev. Lett. 1997; 78:1387–1390.
242. Xie Y, Hu G, Sato D, Weiss JN, Garfinkel A, Qu Z. Dispersion of refractoriness and induction of reentry due to chaos synchronization in a model of cardiac tissue. Phys. Rev. Lett. 2007; 99:118101. [PubMed: 17930473]
243. Kalb SS, Dobrovolny HM, Tolkacheva EG, Idriss SF, Krassowska W, Gauthier DJ. The restitution portrait: a new method for investigating rate-dependent restitution. J. Cardiovasc. Electrophysiol. 2004; 15:698–709. [PubMed: 15175067]
244. Fenton FH, Evans SJ, Hastings HM. Memory in an excitable medium: A mechanism for spiral wave breakup in the low-excitability limit. Phys. Rev. Lett. 1999; 83:3964–3967.
245. Cherry EM, Fenton FH. Suppression of Alternans and Conduction Blocks Despite Steep APD Restitution: Electrotonic, Memory and Conduction Velocity Restitution Effects. Am. J. Physiol. Heart. Circ. Physiol. 2004; 286:H2332–H2341. [PubMed: 14751863]
246. Tolkacheva EG, Schaeffer DG, Gauthier DJ, Krassowska W. Condition for alternans and stability of the 1: 1 response pattern in a "memory" model of paced cardiac dynamics. Phys Rev E Stat Nonlin Soft Matter Phys. 2003; 67:031904. [PubMed: 12689098]
247. Choi BR, Liu T, Salama G. Adaptation of cardiac action potential durations to stimulation history with random diastolic intervals. J. Cardiovasc. Electrophysiol. 2004; 15:1188–1197. [PubMed: 15485446]
248. Baher A, Qu Z, Hayatdavoudi A, Lamp ST, Yang MJ, Xie F, Turner S, Garfinkel A, Weiss JN. Short-term Cardiac Memory and Mother Rotor Fibrillation. Am J Physiol Heart Circ Physiol. 2007; 292:H180–189. [PubMed: 16891403]
249. Qu Z, Xie Y, Garfinkel A, Weiss JN. T-wave alternans and arrhythmogenesis in cardiac diseases. Front Physiol. 2010; 1:154. [PubMed: 21286254]
250. Hopenfeld B. Mechanism for action potential alternans: the interplay between L-type calcium current and transient outward current. Heart Rhythm. 2006; 3:345–352. [PubMed: 16500310]
251. Maoz A, Krogh-Madsen T, Christini DJ. Instability in action potential morphology underlies phase 2 reentry: a mathematical modeling study. Heart Rhythm. 2009; 6:813–822. [PubMed: 19467510]
252. Lukas A, Antzelevitch C. Differences in the electrophysiological response of canine ventricular epicardium and endocardium to ischemia. Role of the transient outward current. Circulation. 1993; 88:2903–2915. [PubMed: 8252704]
253. Qu Z, Chung D. Mechanisms and determinants of ultralong action potential duration and slow rate-dependence in cardiac myocytes. PLoS One. 2012; 7:e43587. [PubMed: 22952713]
254. Fox JJ, McHarg JL, Gilmour RF. Ionic mechanism of electrical alternans. Am. J. Physiol. Heart Circ. Physiol. 2002; 282:H516–H530. [PubMed: 11788399]
255. Koller ML, Riccio ML, Gilmour RF Jr. Dynamic restitution of action potential duration during electrical alternans and ventricular fibrillation. Am. J. Physiol. 1998; 275:H1635–H1642. [PubMed: 9815071]
256. de Lange E, Kucera JP. The transfer functions of cardiac tissue during stochastic pacing. Biophys. J. 2009; 96:294–311. [PubMed: 19134481]
257. Lemay M, de Lange E, Kucera JP. Uncovering the dynamics of cardiac systems using stochastic pacing and frequency domain analyses. PLoS Comput Biol. 2012; 8:e1002399. [PubMed: 22396631]
258. Yehia AR, Jeandupeux D, Alonso F, Guevara MR. Hysteresis and bistability in the direct transition from 1:1 to 2:1 rhythm in periodically driven single ventricular cells. Chaos: An Interdisciplinary Journal of Nonlinear Science. 1999; 9:916–931.

259. Hall GM, Bahar S, Gauthier DJ. Prevalence of Rate-Dependent Behaviors in Cardiac Muscle. Phys. Rev. Lett. 1999; 82:2995–2998.

260. Walker ML, Wan X, Kirsch GE, Rosenbaum DS. Hysteresis effect implicates calcium cycling as a mechanism of repolarization alternans. Circulation. 2003; 108:2704–2709. [PubMed: 14581412]

261. Berger RD. Electrical restitution hysteresis: good memory or delayed response? Circ. Res. 2004; 94:567–569. [PubMed: 15031267]

262. Vinet A. Memory and bistability in a one-dimensional loop of model cardaic cells. Journal of Biological Systems. 1999; 07:451–473.

263. Huang X, Qian Y, Zhang X, Hu G. Hysteresis and bistability in periodically paced cardiac tissue. Phys Rev E Stat Nonlin Soft Matter Phys. 2010; 81:051903. [PubMed: 20866257]

264. Chudin E, Goldhaber J, Garfinkel A, Weiss J, Kogan B. Intracellular Ca2+ dynamics and the stability of ventricular tachycardia. Biophys. J. 1999; 77:2930–2941. [PubMed: 10585917]

265. Diaz ME, Eisner DA, O'Neill SC. Depressed ryanodine receptor activity increases variability and duration of the systolic Ca2+ transient in rat ventricular myocytes. Circ. Res. 2002; 91:585–593. [PubMed: 12364386]

266. Diaz ME, O'Neill SC, Eisner DA. Sarcoplasmic reticulum calcium content fluctuation is the key to cardiac alternans. Circ. Res. 2004; 94:650–656. [PubMed: 14752033]

267. Kockskamper J, Blatter LA. Subcellular Ca2+ alternans represents a novel mechanism for the generation of arrhythmogenic Ca2+ waves in cat atrial myocytes. J. Physiol. 2002; 545:65–79. [PubMed: 12433950]

268. Xie LH, Weiss JN. Arrhythmogenic consequences of intracellular calcium waves. Am J Physiol Heart Circ Physiol. 2009; 297:H997–H1002. [PubMed: 19561309]

269. Aistrup GL, Shiferaw Y, Kapur S, Kadish AH, Wasserstrom JA. Mechanisms underlying the formation and dynamics of subcellular calcium alternans in the intact rat heart. Circ. Res. 2009; 104:639–649. [PubMed: 19150887]

270. Gaeta SA, Bub G, Abbott GW, Christini DJ. Dynamical mechanism for subcellular alternans in cardiac myocytes. Circ. Res. 2009; 105:335–342. [PubMed: 19628792]

271. Tian Q, Kaestner L, Lipp P. Noise-free visualization of microscopic calcium signaling by pixel-wise fitting. Circ. Res. 2012; 111:17–27. [PubMed: 22619280]

272. Eisner DA, Choi HS, Diaz ME, O'Neill SC, Trafford AW. Integrative analysis of calcium cycling in cardiac muscle. Circ. Res. 2000; 87:1087–1094. [PubMed: 11110764]

273. Shannon TR, Ginsburg KS, Bers DM. Potentiation of Fractional Sarcoplasmic Reticulum Calcium Release by Total and Free Intra-Sarcoplasmic Reticulum Calcium Concentration. Biophys. J. 2000; 78:334–343. [PubMed: 10620297]

274. Shiferaw Y, Watanabe MA, Garfinkel A, Weiss JN, Karma A. Model of intracellular calcium cycling in ventricular myocytes. Biophys. J. 2003; 85:3666–3686. [PubMed: 14645059]

275. Xie LH, Sato D, Garfinkel A, Qu Z, Weiss JN. Intracellular Ca alternans: coordinated regulation by sarcoplasmic reticulum release, uptake, and leak. Biophys. J. 2008; 95:3100–3110. [PubMed: 18539635]

276. Tao T, O'Neill SC, Diaz ME, Li YT, Eisner DA, Zhang H. Alternans of cardiac calcium cycling in a cluster of ryanodine receptors: a simulation study. Am J Physiol Heart Circ Physiol. 2008; 295:H598–609. [PubMed: 18515647]

277. Huertas M, Smith GD, Gyorke S. Analysis of Calcium Alternans in a Cardiac Myocyte Model that Uses Moment Equations to Represent Heterogenous Junctional SR Calcium. Biophys. J. 2009; 96:277a.

278. Mahajan A, Shiferaw Y, Sato D, Baher A, Olcese R, Xie L-H, Yang M-J, Chen P-S, Restrepo JG, Karma A, Garfinkel A, Qu Z, Weiss JN. A rabbit ventricular action potential model replicating cardiac dynamics at rapid heart rates. Biophys. J. 2008; 94:392–410. [PubMed: 18160660]

279. Picht E, DeSantiago J, Blatter LA, Bers DM. Cardiac alternans do not rely on diastolic sarcoplasmic reticulum calcium content fluctuations. Circ. Res. 2006; 99:740–748. [PubMed: 16946134]

280. Huser J, Wang YG, Sheehan KA, Cifuentes F, Lipsius SL, Blatter LA. Functional coupling between glycolysis and excitation-contraction coupling underlies alternans in cat heart cells. J. Physiol. 2000; 524(Pt 3):795–806. [PubMed: 10790159]

281. Shkryl VM, Maxwell JT, Domeier TL, Blatter LA. Refractoriness of sarcoplasmic reticulum Ca release determines Ca alternans in atrial myocytes. American Journal of Physiology - Heart and Circulatory Physiology. 2012; 302:H2310–H2320. [PubMed: 22467301]

282. Cui X, Rovetti RJ, Yang L, Garfinkel A, Weiss JN, Qu Z. Period-Doubling Bifurcation in an Array of Coupled Stochastically Excitable Elements Subjected to Global Periodic Forcing. Phys. Rev. Lett. 2009; 103:044102–044104. [PubMed: 19659359]

283. Rovetti R, Cui X, Garfinkel A, Weiss JN, Qu Z. Spark-Induced Sparks As a Mechanism of Intracellular Calcium Alternans in Cardiac Myocytes. Circ. Res. 2010; 106:1582–1591. [PubMed: 20378857]

284. Qu Z, Nivala M, Weiss JN. Calcium alternans in cardiac myocytes: Order from disorder. J. Mol. Cell. Cardiol. 2013; 58:100–109. [PubMed: 23104004]

285. Izu LT, Banyasz T, Balke CW, Chen-Izu Y. Eavesdropping on the social lives of Ca(2+) sparks. Biophys. J. 2007; 93:3408–3420. [PubMed: 17675349]

286. Sobie EA, Song LS, Lederer WJ. Local recovery of Ca2+ release in rat ventricular myocytes. J. Physiol. 2005; 565:441–447. [PubMed: 15817631]

287. Sobie EA, Song LS, Lederer WJ. Restitution of Ca(2+) release and vulnerability to arrhythmias. J. Cardiovasc. Electrophysiol. 2006; 17(Suppl 1):S64–S70. [PubMed: 16686684]

288. Ramay HR, Liu OZ, Sobie EA. Recovery of cardiac calcium release is controlled by sarcoplasmic reticulum refilling and ryanodine receptor sensitivity. Cardiovasc. Res. 2011; 91:598–605. [PubMed: 21613275]

289. Liu OZ, Lederer WJ, Sobie EA. Does the Goldilocks Principle apply to calcium release restitution in heart cells? J. Mol. Cell. Cardiol. 2012; 52:3–6. [PubMed: 22056316]

290. Li Y, Diaz ME, Eisner DA, O'Neill S. The effects of membrane potential, SR Ca2+ content and RyR responsiveness on systolic Ca2+ alternans in rat ventricular myocytes. J. Physiol. 2009; 587:1283–1292. [PubMed: 19153161]

291. Nivala M, Qu Z. Calcium Alternans in a Couplon Network Model of Ventricular Myocytes: Role of Sarcoplasmic Reticulum Load. Am J Physiol Heart Circ Physiol. 2012; 303:H341–352. [PubMed: 22661509]

292. Weiss JN, Nivala M, Garfinkel A, Qu Z. Alternans and arrhythmias: from cell to heart. Circ. Res. 2011; 108:98–112. [PubMed: 21212392]

293. Shiferaw Y, Sato D, Karma A. Coupled dynamics of voltage and calcium in paced cardiac cells. Phys Rev E Stat Nonlin Soft Matter Phys. 2005; 71:021903. [PubMed: 15783348]

294. Wan X, Cutler M, Song Z, Karma A, Matsuda T, Baba A, Rosenbaum DS. New experimental evidence for mechanism of arrhythmogenic membrane potential alternans based on balance of electrogenic INCX/ICa currents. Heart Rhythm. 2012; 9:1698–1705. [PubMed: 22721857]

295. Gilmour RF, Otani NF, Watanabe MA. Memory and complex dynamics in cardiac Purkinje fibers. Am. J. Physiol. Heart Circ. Physiol. 1997; 41:H1826–H1832.

296. Otani NF, Gilmour RF. Memory models for the electrical properties of local cardiac systems. J. Theor. Biol. 1997; 187:409–436. [PubMed: 9245581]

297. Jordan PN, Christini DJ. Characterizing the contribution of voltage- and calcium-dependent coupling to action potential stability: implications for repolarization alternans. Am J Physiol Heart Circ Physiol. 2007; 293:H2109–2118. [PubMed: 17586611]

298. Sato D, Shiferaw Y, Qu Z, Garfinkel A, Weiss JN, Karma A. Inferring the cellular origin of voltage and calcium alternans from the spatial scales of phase reversal during discordant alternans. Biophys. J. 2007; 92:L33–35. [PubMed: 17172300]

299. Blatter LA, Kockskamper J, Sheehan KA, Zima AV, Huser J, Lipsius SL. Local calcium gradients during excitation-contraction coupling and alternans in atrial myocytes. J. Physiol. 2003; 546:19–31. [PubMed: 12509476]

300. Shiferaw Y, Karma A. Turing instability mediated by voltage and calcium diffusion in paced cardiac cells. Proc Natl Acad Sci U S A. 2006; 103:5670–5675. [PubMed: 16574775]

301. Turing AM. The chemical basis of morphogenesis. Phil. Roy. Soc. Lond. B. 1952; 237:37–72.

302. Echebarria B, Karma A. Instability and spatiotemporal dynamics of alternans in paced cardiac tissue. Phys. Rev. Lett. 2002; 88:208101. [PubMed: 12005608]

303. Echebarria B, Karma A. Amplitude equation approach to spatiotemporal dynamics of cardiac alternans. Phys Rev E Stat Nonlin Soft Matter Phys. 2007; 76:051911. [PubMed: 18233691]

304. Gaeta SA, Krogh-Madsen T, Christini DJ. Feedback-control induced pattern formation in cardiac myocytes: a mathematical modeling study. J. Theor. Biol. 2010; 266:408–418. [PubMed: 20620154]

305. Elf J, Ehrenberg M. Spontaneous separation of bi-stable biochemical systems into spatial domains of opposite phases. Syst Biol (Stevenage). 2004; 1:230–236. [PubMed: 17051695]

306. Qu Z, Xie L-H, Olcese R, Karagueuzian HS, Chen P-S, Garfinkel A, Weiss JN. Early afterdepolarizations in cardiac myocytes: beyond reduced repolarization reserve. Cardiovasc. Res. 2013; 99:6–15. [PubMed: 23619423]

307. Cranefield PF. Action potentials, afterpotentials, and arrhythmias. Circ. Res. 1977; 41:415–423. [PubMed: 409566]

308. Rosen MR, Moak JP, Damiano B. The clinical relevance of afterdepolarizations. Ann. N. Y. Acad. Sci. 1984; 427:84–93. [PubMed: 6378020]

309. Weiss JN, Garfinkel A, Karagueuzian HS, Chen PS, Qu Z. Early afterdepolarizations and cardiac arrhythmias. Heart Rhythm. 2010; 7:1891–1899. [PubMed: 20868774]

310. Keating MT, Sanguinetti MC. Molecular and cellular mechanisms of cardiac arrhythmias. Cell. 2001; 104:569–580. [PubMed: 11239413]

311. Liu GX, Choi BR, Ziv O, Li W, de Lange E, Qu Z, Koren G. Differential conditions for early after-depolarizations and triggered activity in cardiomyocytes derived from transgenic LQT1 and LQT2 rabbits. J. Physiol. 2012; 590:1171–1180. [PubMed: 22183728]

312. Nuss HB, Kaab S, Kass DA, Tomaselli GF, Marban E. Cellular basis of ventricular arrhythmias and abnormal automaticity in heart failure. Am J Physiol Heart Circ Physiol. 1999; 277:H80–H91.

313. Li GR, Lau CP, Ducharme A, Tardif JC, Nattel S. Transmural action potential and ionic current remodeling in ventricles of failing canine hearts. Am J Physiol Heart Circ Physiol. 2002; 283:H1031–1041. [PubMed: 12181133]

314. Hauswirth O, Noble D, Tsien RW. The mechanism of oscillatory activity at low membrane potentials in cardiac Purkinje fibres. J. Physiol. 1969; 200:255–265. [PubMed: 5761950]

315. Rosen MR. A short, biased history of triggered activity. Hellenic J Cardiol. 2009; 50:170–178. [PubMed: 19465357]

316. Koval OM, Guan X, Wu Y, Joiner ML, Gao Z, Chen B, Grumbach IM, Luczak ED, Colbran RJ, Song LS, Hund TJ, Mohler PJ, Anderson ME. CaV1.2 beta-subunit coordinates CaMKII-triggered cardiomyocyte death and afterdepolarizations. Proc Natl Acad Sci U S A. 2010; 107:4996–5000. [PubMed: 20194790]

317. Alseikhan BA, DeMaria CD, Colecraft HM, Yue DT. Engineered calmodulins reveal the unexpected eminence of Ca2+ channel inactivation in controlling heart excitation. Proc Natl Acad Sci U S A. 2002; 99:17185–17190. [PubMed: 12486220]

318. Antzelevitch C. Heterogeneity of cellular repolarization in LQTS: the role of M cells. European Heart Journal Supplements. 2001; 3:K2–K16.

319. Guo D, Zhao X, Wu Y, Liu T, Kowey PR, Yan GX. L-type calcium current reactivation contributes to arrhythmogenesis associated with action potential triangulation. J. Cardiovasc. Electrophysiol. 2007; 18:196–203. [PubMed: 17212595]

320. Yamada M, Ohta K, Niwa A, Tsujino N, Nakada T, Hirose M. Contribution of L-Type Ca2+ Channels to Early Afterdepolarizations Induced by IKr and IKs Channel Suppression in Guinea Pig Ventricular Myocytes. J. Membr. Biol. 2008; 222:151–166. [PubMed: 18566732]

321. Tanskanen AJ, Greenstein JL, O'Rourke B, Winslow RL. The Role of Stochastic and Modal Gating of Cardiac L-Type Ca2+ Channels on Early After-Depolarizations. Biophys. J. 2005; 88:85–95. [PubMed: 15501946]

322. Tran DX, Sato D, Yochelis A, Weiss JN, Garfinkel A, Qu Z. Bifurcation and Chaos in a Model of Cardiac Early Afterdepolarizations. Phys. Rev. Lett. 2009; 102:258103. [PubMed: 19659123]

323. Sato D, Xie LH, Nguyen TP, Weiss JN, Qu Z. Irregularly appearing early afterdepolarizations in cardiac myocytes: random fluctuations or dynamical chaos? Biophys. J. 2010; 99:765–773. [PubMed: 20682253]

324. Chang MG, Chang CY, de Lange E, Xu L, O'Rourke B, Karagueuzian HS, Tung L, Marban E, Garfinkel A, Weiss JN, Qu Z, Abraham MR. Dynamics of Early Afterdepolarization-Mediated Triggered Activity in Cardiac Monolayers. Biophys. J. 2012; 102:2706–2714. [PubMed: 22735520]

325. Izhikevich, EM. Dynamical Systems in Neuroscience. Cambridge: MIT press; 2007.

326. Noble D. Applications of Hodgkin-Huxley equations to excitable tissues. Physiol. Rev. 1966; 46:1–50. [PubMed: 5323501]

327. Volders PG, Vos MA, Szabo B, Sipido KR, de Groot SH, Gorgels AP, Wellens HJ, Lazzara R. Progress in the understanding of cardiac early afterdepolarizations and torsades de pointes: time to revise current concepts. Cardiovasc. Res. 2000; 46:376–392. [PubMed: 10912449]

328. Crutchfield JP, Farmer JD, Huberman BA. Fluctuations and simple chaotic dynamics. Physics Reports. 1982; 92:45–82.

329. Gao JB, Hwang SK, Liu JM. When Can Noise Induce Chaos? Phys. Rev. Lett. 1999; 82:1132.

330. Lai YC, Liu Z, Billings L, Schwartz IB. Noise-induced unstable dimension variability and transition to chaos in random dynamical systems. Phys Rev E Stat Nonlin Soft Matter Phys. 2003; 67:026210. [PubMed: 12636779]

331. Billings L, Schwartz IB. Exciting chaos with noise: unexpected dynamics in epidemic outbreaks. J. Math. Biol. 2002; 44:31–48. [PubMed: 11942524]

332. Yeh YH, Wakili R, Qi XY, Chartier D, Boknik P, Kaab S, Ravens U, Coutu P, Dobrev D, Nattel S. Calcium-handling abnormalities underlying atrial arrhythmogenesis and contractile dysfunction in dogs with congestive heart failure. Circ Arrhythm Electrophysiol. 2008; 1:93–102. [PubMed: 19808399]

333. Xie L-H, Chen F, Karagueuzian HS, Weiss JN. Oxidative Stress-Induced Afterdepolarizations and Calmodulin Kinase II Signaling. Circ. Res. 2009; 104:79–86. [PubMed: 19038865]

334. Keener J. Propagation and Its Failure in Coupled Systems of Discrete Excitable Cells. SIAM Journal on Applied Mathematics. 1987; 47:556–572.

335. Keener JP. The Effects of Discrete Gap Junction Coupling On Propagation in Myocardium. J. Theor. Biol. 1991; 148:49–82. [PubMed: 2016885]

336. Joyner RW. Effects of the discrete pattern of electrical coupling on propagation through an electrical syncytium. Circ. Res. 1982; 50:192–200. [PubMed: 7055854]

337. Jongsma HJ, Wilders R. Gap junctions in cardiovascular disease. Circ. Res. 2000; 86:1193–1197. [PubMed: 10864907]

338. Kleber AG, Rudy Y. Basic mechanisms of cardiac impulse propagation and associated arrhythmias. Physiol. Rev. 2004; 84:431–488. [PubMed: 15044680]

339. Qu Z. Dynamical effects of diffusive cell coupling on cardiac excitation and propagation: a simulation study. Am J Physiol Heart Circ Physiol. 2004; 287:H2803–2812. [PubMed: 15271669]

340. Pertsov AM, Wellner M, Jalife J. Eikonal Relation in Highly Dispersive Excitable Media. Phys. Rev. Lett. 1997; 78:2656–2659.

341. Wellner M, Pertsov AM. Generalized eikonal equation in excitable media. Phys. Rev. E. 1997; 55:7656–7661.

342. Winfree AT. Alternative stable rotors in an excitable medium. Physica D: Nonlinear Phenomena. 1991; 49:125–140.

343. Comtois P, Vinet A. Curvature effects on activation speed and repolarization in an ionic model of cardiac myocytes. Phys. Rev. E. 1999; 60:4619–4628.

344. Cabo C, Pertsov AM, Baxter WT, Davidenko JM, Gray RA, Jalife J. Wave-front curvature as a cause of slow conduction and block in isolated cardiac muscle. Circ. Res. 1994; 75:1014–1028. [PubMed: 7525101]

345. Courtemanche M, Glass L, Keener JP. Instabilities of a propagating pulse in a ring of excitable media. Phys. Rev. Lett. 1993; 70:2182–2185. [PubMed: 10053491]

346. Konta T, Ikeda K, Yamaki M, Nakamura K, Honma K, Kubota I, Yasui S. Significance of discordant ST alternans in ventricular fibrillation. Circulation. 1990; 82:2185–2189. [PubMed: 2242541]
347. Cao JM, Qu Z, Kim YH, Wu TJ, Garfinkel A, Weiss JN, Karagueuzian HS, Chen PS. Spatiotemporal heterogeneity in the induction of ventricular fibrillation by rapid pacing: importance of cardiac restitution properties. Circ. Res. 1999; 84:1318–1331. [PubMed: 10364570]
348. Qian YW, Clusin WT, Lin SF, Han J, Sung RJ. Spatial heterogeneity of calcium transient alternans during the early phase of myocardial ischemia in the blood-perfused rabbit heart. Circulation. 2001; 104:2082–2087. [PubMed: 11673350]
349. Hayashi H, Shiferaw Y, Sato D, Nihei M, Lin SF, Chen PS, Garfinkel A, Weiss JN, Qu Z. Dynamic origin of spatially discordant alternans in cardiac tissue. Biophys. J. 2007; 92:448–460. [PubMed: 17071663]
350. Mironov S, Jalife J, Tolkacheva EG. Role of Conduction Velocity Restitution and Short-Term Memory in the Development of Action Potential Duration Alternans in Isolated Rabbit Hearts. Circulation. 2008; 118:17–25. [PubMed: 18559701]
351. Choi BR, Jang W, Salama G. Spatially discordant voltage alternans cause wavebreaks in ventricular fibrillation. Heart Rhythm. 2007; 4:1057–1068. [PubMed: 17675081]
352. Chinushi M, Kozhevnikov D, Caref EB, Restivo M, El-Sherif N. Mechanism of discordant T wave alternans in the in vivo heart. J. Cardiovasc. Electrophysiol. 2003; 14:632–638. [PubMed: 12875425]
353. Ziv O, Morales E, Song YK, Peng X, Odening KE, Buxton AE, Karma A, Koren G, Choi BR. Origin of complex behaviour of spatially discordant alternans in a transgenic rabbit model of type 2 long QT syndrome. J. Physiol. 2009; 587:4661–4680. [PubMed: 19675070]
354. Gizzi A, Cherry EM, Gilmour RF Jr, Luther S, Filippi S, Fenton FH. Effects of pacing site and stimulation history on alternans dynamics and the development of complex spatiotemporal patterns in cardiac tissue. Front Physiol. 2013; 4:71. [PubMed: 23637684]
355. de Diego C, Pai RK, Dave AS, Lynch A, Thu M, Chen F, Xie LH, Weiss JN, Valderrabano M. Spatially discordant alternans in cardiomyocyte monolayers. Am J Physiol Heart Circ Physiol. 2008; 294:H1417–1425. [PubMed: 18223190]
356. Selvaraj RJ, Picton P, Nanthakumar K, Mak S, Chauhan VS. Endocardial and epicardial repolarization alternans in human cardiomyopathy: evidence for spatiotemporal heterogeneity and correlation with body surface T-wave alternans. J. Am. Coll. Cardiol. 2007; 49:338–346. [PubMed: 17239715]
357. Hiromoto K, Shimizu H, Furukawa Y, Kanemori T, Mine T, Masuyama T, Ohyanagi M. Discordant repolarization alternans-induced atrial fibrillation is suppressed by verapamil. Circ J. 2005; 69:1368–1373. [PubMed: 16247213]
358. Watanabe MA, Fenton FH, Evans SJ, Hastings HM, Karma A. Mechanisms for discordant alternans. J. Cardiovasc. Electrophysiol. 2001; 12:196–206. [PubMed: 11232619]
359. Qu Z, Karagueuzian HS, Garfinkel A, Weiss JN. Effects of Na(+) channel and cell coupling abnormalities on vulnerability to reentry: a simulation study. Am J Physiol Heart Circ Physiol. 2004; 286:H1310–H1321. [PubMed: 14630634]
360. Fox JJ, Riccio ML, Hua F, Bodenschatz E, Gilmour RF. Spatiotemporal transition to conduction block in canine ventricle. Circ. Res. 2002; 90:289–296. [PubMed: 11861417]
361. Fox JJ, Gilmour RF, Bodenschatz E. Conduction block in one-dimensional heart fibers. Phys. Rev. Lett. 2002; 89:198101. [PubMed: 12443153]
362. Qu Z, Garfinkel A, Weiss JN. Vulnerable window for conduction block in a onedimensional cable of cardiac cells, 2: Multiple extrasystoles. Biophys. J. 2006; 91:805–815. [PubMed: 16679366]
363. Wang S, Xie Y, Qu Z. Coupled iterated map models of action potential dynamics in a one-dimensional cable of coupled cardiac cells. New Journal of Physics. 2007; 10:055001.
364. Sato D, Shiferaw Y, Garfinkel A, Weiss JN, Qu Z, Karma A. Spatially Discordant Alternans in Cardiac Tissue. Role of Calcium Cycling. Circ. Res. 2006; 99:520–527. [PubMed: 16902177]

365. Skardal PS, Karma A, Restrepo JG. Unidirectional pinning and hysteresis of spatially discordant alternans in cardiac tissue. Phys. Rev. Lett. 2012; 108:108103. [PubMed: 22463458]

366. Pecora LM, Carroll TL. Synchronization in chaotic systems. Phys. Rev. Lett. 1990; 64:821–824. [PubMed: 10042089]

367. Heagy JF, Carroll TL, Pecora LM. Synchronous chaos in coupled oscillator systems. Phys. Rev. E. 1994; 50:1874–1885.

368. Maron BJ, Link MS, Wang PJ, Estes NA. Clinical profile of commotio cordis: an under appreciated cause of sudden death in the young during sports and other activities. J. Cardiovasc. Electrophysiol. 1999; 10:114–120. [PubMed: 9930916]

369. Kohl P. Recognition and prevention of Commotio cordis. Heart Rhythm. 2005; 2:902. author reply 902-903. [PubMed: 16051135]

370. Shibata N, Chen PS, Dixon EG, Wolf PD, Danieley ND, Smith WM, Ideker RE. Influence of shock strength and timing on induction of ventricular arrhythmias in dogs. Am. J. Physiol. 1988; 255:H891–901. [PubMed: 3177678]

371. Gotoh M, Uchida T, Mandel WJ, Fishbein MC, Chen PS, Karagueuzian HS. Cellular graded responses and ventricular vulnerability to reentry by a premature stimulus in isolated canine ventricle. Circulation. 1997; 95:2141–2154. [PubMed: 9133525]

372. Roth BJ. The pinwheel experiment revisited. J. Theor. Biol. 1998; 190:389–393. [PubMed: 9533873]

373. Yang MJ, Tran DX, Weiss JN, Garfinkel A, Qu Z. The pinwheel experiment revisited: effects of cellular electrophysiological properties on vulnerability to cardiac reentry. Am J Physiol Heart Circ Physiol. 2007; 293:H1781–H1790. [PubMed: 17586622]

374. Qu Z, Weiss JN. Effects of Na(+) and K(+) channel blockade on vulnerability to and termination of fibrillation in simulated normal cardiac tissue. Am J Physiol Heart Circ Physiol. 2005; 289:H1692–H1701. [PubMed: 15937096]

375. Tran DX, Yang MJ, Weiss JN, Garfinkel A, Qu Z. Vulnerability to re-entry in simulated two-dimensional cardiac tissue: effects of electrical restitution and stimulation sequence. Chaos. 2007; 17:043115. [PubMed: 18163779]

376. Trénor B, Romero L, Ferrero J, Sáiz J, Moltó G, Alonso J. Vulnerability to Reentry in a Regionally Ischemic Tissue: A Simulation Study. Ann. Biomed. Eng. 2007; 35:1756–1770. [PubMed: 17616818]

377. Zhang H, Kharche S, Holden AV, Hancox JC. Repolarisation and vulnerability to re-entry in the human heart with short QT syndrome arising from KCNQ1 mutation--A simulation study. Prog. Biophys. Mol. Biol. 2008; 96:112–131. [PubMed: 17905416]

378. Arce H, Xu A, Gonzalez H, Guevara MR. Alternans and higher-order rhythms in an ionic model of a sheet of ischemic ventricular muscle. Chaos. 2000; 10:411–426. [PubMed: 12779397]

379. Clayton R, Taggart P. Regional differences in APD restitution can initiate wavebreak and re-entry in cardiac tissue: A computational study. BioMedical Engineering OnLine. 2005; 4:54. [PubMed: 16174290]

380. Clayton RH, Holden AV. Dispersion of cardiac action potential duration and the initiation of re-entry: a computational study. Biomed Eng Online. 2005; 4:11. [PubMed: 15720712]

381. Qu Z, Garfinkel A, Weiss JN. Vulnerable window for conduction block in a one-dimensional cable of cardiac cells, 1: Single extrasystoles. Biophys. J. 2006; 91:793–804. [PubMed: 16679367]

382. Sampson KJ, Henriquez CS. Simulation and prediction of functional block in the presence of structural and ionic heterogeneity. Am J Physiol Heart Circ Physiol. 2001; 281:H2597–H2603. [PubMed: 11709428]

383. Fox JJ, Riccio ML, Drury P, Werthman A, Gilmour RF Jr. Dynamic mechanism for conduction block in heart tissue. New Journal of Physics. 2003; 5:101.101–101.114.

384. Otani NF. Theory of action potential wave block at-a-distance in the heart. Phys. Rev. E. 2007; 75:021910–021917.

385. Henry H, Rappel WJ. Dynamics of conduction blocks in a model of paced cardiac tissue. Phys Rev E Stat Nonlin Soft Matter Phys. 2005; 71:051911. [PubMed: 16089575]

386. Akar FG, Rosenbaum DS. Transmural electrophysiological heterogeneities underlying arrhythmogenesis in heart failure. Circ. Res. 2003; 93:638–645. [PubMed: 12933704]

387. Restivo M, Gough W, El-Sherif N. Ventricular arrhythmias in the subacute myocardial infarction period. High-resolution activation and refractory patterns of reentrant rhythms. Circ. Res. 1990; 66:1310–1327. [PubMed: 2335029]

388. Gelzer ARM, Koller ML, Otani NF, Fox JJ, Enyeart MW, Hooker GJ, Riccio ML, Bartoli CR, Gilmour RF Jr. Dynamic Mechanism for Initiation of Ventricular Fibrillation In Vivo. Circulation. 2008; 118:1123–1129. [PubMed: 18725487]

389. Laurita KR, Rosenbaum DS. Interdependence of modulated dispersion and tissue structure in the mechanism of unidirectional block. Circ. Res. 2000; 87:922–928. [PubMed: 11073889]

390. Viswanathan PC, Shaw RM, Rudy Y. Effects of IKr and IKs heterogeneity on action potential duration and its rate dependence: a simulation study. Circulation. 1999; 99:2466–2474. [PubMed: 10318671]

391. Yin H, El-Sherif N, Caref EB, Ndrepepa G, Levin R, Isber N, Stergiopolus K, Assadi MA, Gough WB, Restivo M. Actions of lidocaine on reentrant ventricular rhythms in the subacute myocardial infarction period in dogs. Am. J. Physiol. 1997; 272:H299–H309. [PubMed: 9038950]

392. Glass L. Multistable spatiotemporal patterns of cardiac activity. Proc Natl Acad Sci U S A. 2005; 102:10409–10410. [PubMed: 16027355]

393. Lerma C, Lee CF, Glass L, Goldberger AL. The rule of bigeminy revisited: analysis in sudden cardiac death syndrome. J. Electrocardiol. 2007; 40:78–88. [PubMed: 17069837]

394. Laurita KR, Girouard SD, Akar FG, Rosenbaum DS. Modulated dispersion explains changes in arrhythmia vulnerability during premature stimulation of the heart. Circulation. 1998; 98:2774–2780. [PubMed: 9851966]

395. Laurita KR, Girouard SD, Rosenbaum DS. Modulation of ventricular repolarization by a premature stimulus. Role of epicardial dispersion of repolarization kinetics demonstrated by optical mapping of the intact guinea pig heart. Circ. Res. 1996; 79:493–503. [PubMed: 8781482]

396. Restivo M, Caref EB, Kozhevnikov DO, El-Sherif N. Spatial dispersion of repolarization is a key factor in the arrhythmogenicity of long QT syndrome. J. Cardiovasc. Electrophysiol. 2004; 15:323–331. [PubMed: 15030424]

397. El-Sherif N, Gough WB, Restivo M. Reentrant ventricular arrhythmias in the late myocardial infarction period: Mechanism by which a short-long-short cardiac sequence facilitates the induction of reentry. Circulation. 1991; 83:268–278. [PubMed: 1984885]

398. Kay GN, Plumb VJ, Arciniegas JG, Henthorn RW, Waldo AL. Torsade de pointes: the long-short initiating sequence and other clinical features: observations in 32 patients. J. Am. Coll. Cardiol. 1983; 2:806–817. [PubMed: 6630761]

399. Gomes JA, Alexopoulos D, Winters SL, Deshmukh P, Fuster V, Suh K. The role of silent ischemia, the arrhythmic substrate and the short-long sequence in the genesis of sudden cardiac death. J. Am. Coll. Cardiol. 1989; 14:1618–1625. [PubMed: 2584549]

400. Denker S, Lehmann M, Mahmud R, Gilbert C, Akhtar M. Facilitation of ventricular tachycardia induction with abrupt changes in ventricular cycle length. Am. J. Cardiol. 1984; 53:508–515. [PubMed: 6198893]

401. Denker S, Lehmann M, Mahmud R, Gilbert C, Akhtar M. Effects of alternating cycle lengths on refractoriness of the His-Purkinje system. J. Clin. Invest. 1984; 74:559–570. [PubMed: 6746907]

402. Osaka T, Kodama I, Tsuboi N, Toyama J, Yamada K. Effects of activation sequence and anisotropic cellular geometry on the repolarization phase of action potential of dog ventricular muscles. Circulation. 1987; 76:226–236. [PubMed: 3594771]

403. Comtois P, Vinet A, Nattel S. Wave block formation in homogeneous excitable media following premature excitations: dependence on restitution relations. Phys Rev E Stat Nonlin Soft Matter Phys. 2005; 72:031919. [PubMed: 16241494]

404. Garfinkel A, Chen PS, Walter DO, Karagueuzian HS, Kogan B, Evans SJ, Karpoukhin M, Hwang C, Uchida T, Gotoh M, Nwasokwa O, Sager P, Weiss JN. Quasiperiodicity and chaos in cardiac fibrillation. J. Clin. Invest. 1997; 99:305–314. [PubMed: 9005999]

405. Kim YH, Garfinkel A, Ikeda T, Wu TJ, Athill CA, Weiss JN, Karagueuzian HS, Chen PS. Spatiotemporal complexity of ventricular fibrillation revealed by tissue mass reduction in

isolated swine right ventricle. Further evidence for the quasiperiodic route to chaos hypothesis. J. Clin. Invest. 1997; 100:2486–2500. [PubMed: 9366563]

406. Frame LH, Simson MB. Oscillations of conduction, action potential duration, and refractoriness: a mechanism for spontaneous termination of reentrant tachycardias. Circulation. 1988; 78:1277–1287. [PubMed: 3180384]
407. Ito H, Glass L. Theory of reentrant excitation in a ring of cardiac tissue. Physica D. 1992; 56:84–106.
408. Courtemanche M, Keener JP, Glass L. A delay equation representation of pulse circulation on a ring in excitable media. SIAM J. Appl. Math. 1996; 56:119–142.
409. Karma A, Levine H, Zou X. Theory of pulse instability in electrophysiological models of excitable tissues. Physica D. 1994; 73:113–127.
410. Vinet A. Quasiperiodic circus movement in a loop model of cardiac tissue: multistability and low dimensional equivalence. Ann. Biomed. Eng. 2000; 28:704–720. [PubMed: 11016410]
411. Hund TJ, Otani NF, Rudy Y. Dynamics of action potential head-tail interaction during reentry in cardiac tissue: ionic mechanisms. Am J Physiol Heart Circ Physiol. 2000; 279:H1869–1879. [PubMed: 11009475]
412. Comtois P, Vinet A. Stability and bifurcation in an integral-delay model of cardiac reentry including spatial coupling in repolarization. Phys Rev E Stat Nonlin Soft Matter Phys. 2003; 68:051903. [PubMed: 14682816]
413. Comtois P, Vinet A. Multistability of reentrant rhythms in an ionic model of a two-dimensional annulus of cardiac tissue. Phys Rev E Stat Nonlin Soft Matter Phys. 2005; 72:051927. [PubMed: 16383665]
414. Xie F, Qu Z, Garfinkel A. Dynamics of reentry around a circular obstacle in cardiac tissue. Phys. Rev. E. 1998; 58:6355–6358.
415. Barkley D. Euclidean symmetry and the dynamics of rotating spiral waves. Phys. Rev. Lett. 1994; 72:164–167. [PubMed: 10055592]
416. Skinner GS, Swinney HL. Periodic to quasiperiodic transition of chemical spiral rotation. Physica D: Nonlinear Phenomena. 1991; 48:1–16.
417. Li G, Ouyang Q, Petrov V, Swinney HL. Transition from simple rotating chemical spirals to meandering and traveling spirals. Phys. Rev. Lett. 1996; 77:2105–2108. [PubMed: 10061858]
418. Courtemanche M, Winfree AT. Re-entrant rotating waves in a Beeler-Reuter based model of two-dimensional cardiac conduction. Int. J. Bif., Chaos. 1991; 1:431–444.
419. Efimov IR, Krinsky VI, Jalife J. Dynamics of rotating vortices in the Beeler-Reuter model of cardiac tissue. Chaos, Solitons & Fractals. 1995; 5:513–526.
420. Beaumont J, Davidenko N, Davidenko JM, Jalife J. Spiral waves in two-dimensional models of ventricular muscle: Formation of a stationary core. Biophys. J. 1998; 75:1–14. [PubMed: 9649363]
421. Fenton FH, Cherry EM, Hastings HM, Evans SJ. Multiple mechanisms of spiral wave breakup in a model of cardiac electrical activity. Chaos. 2002; 12:852–892. [PubMed: 12779613]
422. Qu Z, Weiss JN, Garfinkel A. From local to global spatiotemporal chaos in a cardiac tissue model. Phys. Rev. E. 2000; 61:727–732.
423. Bernus O, Verschelde H, Panfilov AV. Spiral wave stability in cardiac tissue with biphasic restitution. Phys Rev E Stat Nonlin Soft Matter Phys. 2003; 68:021917. [PubMed: 14525016]
424. Ten Tusscher KH, Panfilov AV. Reentry in heterogeneous cardiac tissue described by the Luo-Rudy ventricular action potential model. Am J Physiol Heart Circ Physiol. 2003; 284:H542–H548. [PubMed: 12388228]
425. Xu L, Qu Z, Di Z. Drifting dynamics of dense and sparse spiral waves in heterogeneous excitable media. Phys Rev E Stat Nonlin Soft Matter Phys. 2009; 79:036212. [PubMed: 19392040]
426. Xie F, Qu Z, Weiss JN, Garfinkel A. Interactions between stable spiral waves with different frequencies in cardiac tissue. Phys. Rev. E. 1999; 59:2203–2205.
427. Xie F, Qu Z, Garfinkel A, Weiss JN. Electrophysiological heterogeneity and stability of reentry in simulated cardiac tissue. Am J Physiol Heart Circ Physiol. 2001; 280:H535–545. [PubMed: 11158949]

428. Winfree AT. Electrical turbulence in three-dimensional heart muscle. Science. 1994; 266:1003–1006. [PubMed: 7973648]

429. Aranson I, Mitkov I. Helicoidal instability of a scroll vortex in three-dimensional reaction-diffusion systems. Physical Review E (Statistical Physics, Plasmas, Fluids, and Related Interdisciplinary Topics). 1998; 58:4556–4559.

430. Nam K, Ott E, Guzdar PN, Gabbay M. Stability of spiral wave vortex filaments with phase twists. Physical Review E (Statistical Physics, Plasmas, Fluids, and Related Interdisciplinary Topics). 1998; 58:2580–2585.

431. Qu Z, Xie F, Garfinkel A. Diffusion-induced 3-dimensional vortex filament instability in excitable media. Phys. Rev. Lett. 1999; 83:2668–2671.

432. Henry H, Hakim V. Linear Stability of Scroll Waves. Phys. Rev. Lett. 2000; 85:5328–5331. [PubMed: 11135988]

433. Henry H, Hakim V. Scroll waves in isotropic excitable media: Linear instabilities, bifurcations, and restabilized states. Phys. Rev. E. 2002; 65:046235.

434. Luengviriya C, Storb U, Lindner G, Müller SC, Bär M, Hauser MJ. Scroll wave instabilities in an excitable chemical medium. Phys. Rev. Lett. 2008; 100:148302. [PubMed: 18518076]

435. Panfilov AV, Keener JP. Reentry in three-dimensional Fitzhugh-Nagumo medium with rotational anisotropy. Physica D. 1995; 84:545–552.

436. Fenton F, Karma A. Fiber-rotation-induced vortex turbulence in thick myocardium. Phys. Rev. Lett. 1998; 81:481–484.

437. Keener JP. The dynamics of three-dimensional scroll waves in excitable media. Physica D: Nonlinear Phenomena. 1988; 31:269–276.

438. Jahnke W, Henze C, Winfree AT. Chemical vortex dynamics in three-dimensional excitable media. Nature. 1988; 336:662–665.

439. Bánsági T Jr, Steinbock O. Nucleation and Collapse of Scroll Rings in Excitable Media. Phys. Rev. Lett. 2006; 97:198301. [PubMed: 17155661]

440. Panfilov AV, Rudenko AN. Two regimes of the scroll ring drift in the three-dimensional active media. Physica D. 1987; 215

441. Biktashev VN, Holden AV, Zhang H. Tension of organizing filaments of scroll waves. Phil. Trans. R. Soc. Lond. A. 1994; 347:611–630.

442. Krinsky VI, Hamm E, Voignier V. Dense and sparse vortices in excitable media drift in opposite directions in electric field. Phys. Rev. Lett. 1996; 70:3854–3857. [PubMed: 10061126]

443. Di Z, Qu Z, Weiss JN, Garfinkel A. A kinematic study of spiral wave drift due to an electric field. Phys. Lett. A. 2003; 308:179–186.

444. Hakim V, Karma A. Theory of spiral wave dynamics in weakly excitable media: Asymptotic reduction to a kinematic model and applications. Physical Review E (Statistical Physics, Plasmas, Fluids, and Related Interdisciplinary Topics). 1999; 60:5073–5105.

445. Steinbock O, Schutze J, Muller C. Electric-field-induced drift and deformation of spiral waves in an excitable medium. Phys. Rev. Lett. 1992; 68:248–251. [PubMed: 10045573]

446. Munuzuri AP, Gomez-Gesteira M, Perez-Munuzuri V, Krinsky VI, Perez-Villar V. Mechanism of the electric-field-induced vortex drift in excitable media. Phys.Rev.E. 1993; 48:R3232–R3235.

447. Alonso S, Panfilov AV. Negative filament tension at high excitability in a model of cardiac tissue. Phys. Rev. Lett. 2008; 100:218101. [PubMed: 18518639]

448. Alonso S, Sagues F, Mikhailov AS. Taming Winfree turbulence of scroll waves in excitable media. Science. 2003; 299:1722–1725. [PubMed: 12560470]

449. Zhang H, Cao Z, Wu NJ, Ying HP, Hu G. Suppress Winfree turbulence by local forcing excitable systems. Phys. Rev. Lett. 2005; 94:188301. [PubMed: 15904413]

450. Alonso S, Bär M, Panfilov A. Negative Tension of Scroll Wave Filaments and Turbulence in Three-Dimensional Excitable Media and Application in Cardiac Dynamics. Bull. Math. Biol. 2013; 75:1351–1376. [PubMed: 22829178]

451. Alonso S, Panfilov AV. Negative filament tension in the Luo-Rudy model of cardiac tissue. Chaos. 2007; 17:015102. [PubMed: 17411259]

452. Hwang S-M, Yea K-H, Lee KJ. Regular and Alternant Spiral Waves of Contractile Motion on Rat Ventricle Cell Cultures. Phys. Rev. Lett. 2004; 92:198103. [PubMed: 15169449]

453. Hwang S-M, Kim TY, Lee KJ. Complex-periodic spiral waves in confluent cardiac cell cultures induced by localized inhomogeneities. PNAS. 2005; 102:10363–10368. [PubMed: 15985555]

454. Kim TY, Woo SJ, Hwang SM, Hong JH, Lee KJ. Cardiac beat-to-beat alternations driven by unusual spiral waves. Proc Natl Acad Sci U S A. 2007; 104:11639–11642. [PubMed: 17606916]

455. Bursac N, Aguel F, Tung L. Multiarm spirals in a two-dimensional cardiac substrate. Proc Natl Acad Sci U S A. 2004; 101:15530–15534. [PubMed: 15492227]

456. Agladze KI, Krinsky VI. Multi-armed vortices in an active chemical medium. Nature. 1982; 296:424–426.

457. Muller SC, Steinbock O. Multi-armed spirals in a light-controlled excitable reation. International Journal of Bifurcation and Chaos. 1993; 03:437–443.

458. Garfinkel, A.; Qu, Z. Nonlinear dynamics of excitation and propagation in cardiac muscle. In: Zipes, DP.; Jalife, J., editors. Cardiac Electrophysiology: From Cell to Bedside. Philadelphia: W.B.Saunders Co.; 1999. p. 315-320.

459. Garfinkel A, Kim YH, Voroshilovsky O, Qu Z, Kil JR, Lee MH, Karagueuzian HS, Weiss JN, Chen PS. Preventing ventricular fibrillation by flattening cardiac restitution. Proc. Natl. Acad. Sci. USA. 2000; 97:6061–6066. [PubMed: 10811880]

460. Riccio ML, Koller ML, Gilmour RF Jr. Electrical restitution and spatiotemporal organization during ventricular fibrillation. Circ. Res. 1999; 84:955–963. [PubMed: 10222343]

461. Wu TJ, Lin SF, Weiss JN, Ting CT, Chen PS. Two types of ventricular fibrillation in isolated rabbit hearts - Importance of excitability and action potential duration restitution. Circulation. 2002; 106:1859–1866. [PubMed: 12356642]

462. Lou Q, Li W, Efimov IR. The role of dynamic instability and wavelength in arrhythmia maintenance as revealed by panoramic imaging with blebbistatin vs. 2,3-butanedione monoxime. Am J Physiol Heart Circ Physiol. 2012; 302:H262–269. [PubMed: 22037192]

463. Samie FH, Berenfeld O, Anumonwo J, Mironov SF, Udassi S, Beaumont J, Taffet S, Pertsov AM, Jalife J. Rectification of the background potassium current - A determinant of rotor dynamics in ventricular fibrillation. Circ. Res. 2001; 89:1216–1223. [PubMed: 11739288]

464. Jalife J, Berenfeld O, Mansour M. Mother rotors and fibrillatory conduction: a mechanism of atrial fibrillation. Cardiovasc. Res. 2002; 54:204–216. [PubMed: 12062327]

465. Wu TJ, Lin SF, Baher A, Qu Z, Garfinkel A, Weiss JN, Ting CT, Chen PS. Mother rotors and the mechanisms of D600-induced type 2 ventricular fibrillation. Circulation. 2004; 110:2110–2118. [PubMed: 15466637]

466. Choi BR, Liu T, Salama G. The distribution of refractory periods influences the dynamics of ventricular fibrillation. Circ. Res. 2001; 88:E49–E58. [PubMed: 11249880]

467. Choi BR, Nho W, Liu T, Salama G. Life span of ventricular fibrillation frequencies. Circ. Res. 2002; 91:339–345. [PubMed: 12193467]

468. Valderrabano M, Yang JZ, Omichi C, Kil J, Lamp ST, Qu Z, Lin SF, Karagueuzian HS, Garfinkel A, Chen PS, Weiss JN. Frequency analysis of ventricular fibrillation in swine ventricles. Circ. Res. 2002; 90:213–222. [PubMed: 11834715]

469. Moe GK, Rheinboldt WC, Abildskov JA. A computer model of atrial fibrillation. Am.Heart J. 1964; 67:200–220. [PubMed: 14118488]

470. Moe GK. On the multiple wavelet hypothesis of atrial fibrillation. Arch. Int. Pharmacodyn. Ther. 1982; 14:183–188.

471. Moore EN, Spear JF, Fisch C. “Supernormal” Conduction and Excitability. J. Cardiovasc. Electrophysiol. 1993; 4:320–337. [PubMed: 8269303]

472. Kwon O, Kim TY, Lee KJ. Period-2 spiral waves supported by nonmonotonic wave dispersion. Phys. Rev. E. 2010; 82:046213.

473. Echebarria B, Röder G, Engel H, Davidsen J, Bär M. Supernormal conduction in cardiac tissue promotes concordant alternans and action potential bunching. Phys. Rev. E. 2011; 83:040902.

474. de Lange E, Kucera JP, Qu Z. Supernormal Excitability Causes Alternans, Block, Wavebreak and Reentry in Cardiac Tissue. Biophys. J. 2011; 100:435.

475. de Lange E, Kucera JP. Alternans resonance and propagation block during supernormal conduction in cardiac tissue with decreased [K(+)](o). Biophys. J. 2010; 98:1129–1138. [PubMed: 20371312]

476. Kim TY, Hong JH, Heo R, Lee KJ. Alternans by non-monotonic conduction velocity restitution, bistability and memory. New Journal of Physics. 2013; 15:013046.

477. Chang MG, Sato D, de Lange E, Lee J-H, Karagueuzian HS, Garfinkel A, Weiss JN, Qu Z. Bi-stable wave propagation and early afterdepolarization-mediated cardiac arrhythmias. Heart rhythm. 2012; 9:115–122. [PubMed: 21855520]

478. Chang MG, de Lange E, Calmettes G, Garfinkel A, Qu Z, Weiss JN. Pro- and antiarrhythmic effects of ATP-sensitive potassium current activation on reentry during early afterdepolarization-mediated arrhythmias. Heart Rhythm. 2013; 10:575–582. [PubMed: 23246594]

479. Xie Y, Sato D, Garfinkel A, Qu Z, Weiss JN. So little source, so much sink: requirements for afterdepolarizations to propagate in tissue. Biophys. J. 2010; 99:1408–1415. [PubMed: 20816052]

480. Tveito A, Lines GT. A condition for setting off ectopic waves in computational models of excitable cells. Math. Biosci. 2008; 213:141–150. [PubMed: 18539188]

481. Camelliti P, Borg TK, Kohl P. Structural and functional characterisation of cardiac fibroblasts. Cardiovasc. Res. 2005; 65:40–51. [PubMed: 15621032]

482. Kohl P, Camelliti P. Cardiac myocyte-nonmyocyte electrotonic coupling: implications for ventricular arrhythmogenesis. Heart Rhythm. 2007; 4:233–235. [PubMed: 17275764]

483. Miragoli M, Salvarani N, Rohr S. Myofibroblasts induce ectopic activity in cardiac tissue. Circ. Res. 2007; 101:755–758. [PubMed: 17872460]

484. Jacquemet V. Pacemaker activity resulting from the coupling with nonexcitable cells. Phys Rev E Stat Nonlin Soft Matter Phys. 2006; 74:011908. [PubMed: 16907128]

485. Kryukov AK, Petrov VS, Averyanova LS, Osipov GV, Chen W, Drugova O, Chan CK. Synchronization phenomena in mixed media of passive, excitable, and oscillatory cells. Chaos. 2008; 18:037129. [PubMed: 19045503]

486. Singh R, Xu J, Garnier NG, Pumir A, Sinha S. Self-organized transition to coherent activity in disordered media. Phys. Rev. Lett. 2012; 108:068102. [PubMed: 22401124]

487. Janse MJ, van Capelle FJ, Morsink H, Kléber AG, Wilms-Schopman F, Cardinal R, d'Alnoncourt CN, Durrer D. Flow of "injury" current and patterns of excitation during early ventricular arrhythmias in acute regional myocardial ischemia in isolated porcine and canine hearts. Evidence for two different arrhythmogenic mechanisms. Circ. Res. 1980; 47:151–165. [PubMed: 7397948]

488. Keener JP. Model for the onset of fibrillation following coronary artery occlusion. J. Cardiovasc. Electrophysiol. 2003; 14:1225–1232. [PubMed: 14678140]

489. Peercy B, Keener J. Coupled Cell Model of Border Zone Arrhythmias. SIAM Journal on Applied Dynamical Systems. 2005; 4:679–710.

490. Yochelis A, Knobloch E, Xie Y, Qu Z, Garfinkel A. Generation of finite wave trains in excitable media. Europhys. Lett. 2008; 83:64005.

491. Asano Y, Davidenko JM, Baxter WT, Gray RA, Jalife J. Optical mapping of druginduced polymorphic arrhythmias and torsade de pointes in the isolated rabbit heart. J. Am. Coll. Cardiol. 1997; 29:831–842. [PubMed: 9091531]

492. Choi BR, Burton F, Salama G. Cytosolic Ca2+ triggers early afterdepolarizations and Torsade de Pointes in rabbit hearts with type 2 long QT syndrome. J Physiol-London. 2002; 543:615–631. [PubMed: 12205194]

493. Boyett MR, Honjo H, Kodama I. The sinoatrial node, a heterogeneous pacemaker structure. Cardiovasc. Res. 2000; 47:658–687. [PubMed: 10974216]

494. Rosen MR, Robinson RB, Brink PR, Cohen IS. The road to biological pacing. Nat Rev Cardiol. 2011; 8:656–666. [PubMed: 21844918]

495. Noble D, Noble SJ. A model of sino-atrial node electrical activity based on a modification of the DiFrancesco-Noble (1984) equations. Proc. R. Soc. Lond. B. Biol. Sci. 1984; 222:295–304. [PubMed: 6149553]

496. Wilders R, Jongsma HJ, van Ginneken AC. Pacemaker activity of the rabbit sinoatrial node. A comparison of mathematical models. Biophys. J. 1991; 60:1202–1216. [PubMed: 1722117]

497. Zhang H, Holden AV, Kodama I, Honjo H, Lei M, Varghese T, Boyett MR. Mathematical models of action potentials in the periphery and center of the rabbit sinoatrial node. Am J Physiol Heart Circ Physiol. 2000; 279:H397–421. [PubMed: 10899081]

498. Kurata Y, Hisatome I, Imanishi S, Shibamoto T. Dynamical description of sinoatrial node pacemaking: improved mathematical model for primary pacemaker cell. Am J Physiol Heart Circ Physiol. 2002; 283:H2074–2101. [PubMed: 12384487]

499. Kohlhardt M, Figulla HR, Tripathi O. The slow membrane channel as the predominant mediator of the excitation process of the sinoatrial pacemaker cell. Basic Res. Cardiol. 1976; 71:17–26. [PubMed: 1259682]

500. Maltsev VA, Lakatta EG. Dynamic interactions of an intracellular Ca2+ clock and membrane ion channel clock underlie robust initiation and regulation of cardiac pacemaker function. Cardiovasc. Res. 2008; 77:274–284. [PubMed: 18006441]

501. Lakatta EG, DiFrancesco D. What keeps us ticking: a funny current, a calcium clock, or both? J. Mol. Cell. Cardiol. 2009; 47:157–170. [PubMed: 19361514]

502. Ju Y-K, Allen DG. Intracellular calcium and Na+-Ca2+ exchange current in isolated toad pacemaker cells. The Journal of Physiology. 1998; 508:153–166. [PubMed: 9490832]

503. Bogdanov KY, Vinogradova TM, Lakatta EG. Sinoatrial Nodal Cell Ryanodine Receptor and Na+-Ca2+ Exchanger : Molecular Partners in Pacemaker Regulation. Circ. Res. 2001; 88:1254–1258. [PubMed: 11420301]

504. Maltsev AV, Maltsev VA, Mikheev M, Maltseva LA, Sirenko SG, Lakatta EG, Stern MD. Synchronization of stochastic Ca(2)(+) release units creates a rhythmic Ca(2)(+) clock in cardiac pacemaker cells. Biophys. J. 2011; 100:271–283. [PubMed: 21244823]

505. Maltsev AV, Yaniv Y, Stern MD, Lakatta EG, Maltsev VA. RyR-NCX-SERCA Local Cross-Talk Ensures Pacemaker Cell Function at Rest and During the Fight-or-Flight Reflex. Circ. Res. 2013; 113:e94–e100. [PubMed: 24158576]

506. Butters TD, Aslanidi OV, Inada S, Boyett MR, Hancox JC, Lei M, Zhang H. Mechanistic links between Na+ channel (SCN5A) mutations and impaired cardiac pacemaking in sick sinus syndrome. Circ. Res. 2010; 107:126–137. [PubMed: 20448214]

507. Fedorov VV, Schuessler RB, Hemphill M, Ambrosi CM, Chang R, Voloshina AS, Brown K, Hucker WJ, Efimov IR. Structural and Functional Evidence for Discrete Exit Pathways That Connect the Canine Sinoatrial Node and Atria. Circ. Res. 2009; 104:915–923. [PubMed: 19246679]

508. Joung B, Tang L, Maruyama M, Han S, Chen Z, Stucky M, Jones LR, Fishbein MC, Weiss JN, Chen PS, Lin SF. Intracellular calcium dynamics and acceleration of sinus rhythm by beta-adrenergic stimulation. Circulation. 2009; 119:788–796. [PubMed: 19188501]

509. Efimov IR, Fedorov VV, Joung B, Lin S-F. Mapping Cardiac Pacemaker Circuits: Methodological Puzzles of the Sinoatrial Node Optical Mapping. Circ. Res. 2010; 106:255–271. [PubMed: 20133911]

510. Peng C-K, Mietus J, hausdorff JM, Havlin S, Stanley HE, Goldberger AL. Long-range anticorrelation and non-gaussian behavior of the heartbeat. Phys. Rev. Lett. 1993; 70:1343–1346. [PubMed: 10054352]

511. Tulppo MP, Kiviniemi AM, Hautala AJ, Kallio M, Seppänen T, Mäkikallio TH, Huikuri HV. Physiological Background of the Loss of Fractal Heart Rate Dynamics. Circulation. 2005; 112:314–319. [PubMed: 16009791]

512. Yamamoto Y, Hughson RL. On the fractal nature of heart rate variability in humans: effects of data length and beta-adrenergic blockade. American Journal of Physiology - Regulatory, Integrative and Comparative Physiology. 1994; 266:R40–R49.

513. Yeragani VK, Srinivasan K, Vempati S, Pohl R, Balon R. Fractal dimension of heart rate time series: an effective measure of autonomic function. J. Appl. Physiol. 1993; 75:2429–2438. [PubMed: 8125861]

514. Lombardi F. Origin of heart rate variability and turbulence: an appraisal of autonomic modulation of cardiovascular function. Frontiers in Physiology. 2011; 2

515. Glass L. Chaos and heart rate variability. J. Cardiovasc. Electrophysiol. 1999; 10:1358–1360. [PubMed: 10515560]

516. Hu J, Gao J, Tung WW. Characterizing heart rate variability by scale-dependent Lyapunov exponent. Chaos. 2009; 19:028506. [PubMed: 19566281]

517. Freitas U, Roulin E, Muir JF, Letellier C. Identifying chaos from heart rate: the right task? Chaos. 2009; 19:028505. [PubMed: 19566280]

518. Kucera JP, Heuschkel MO, Renaud P, Rohr S. Power-Law Behavior of Beat-Rate Variability in Monolayer Cultures of Neonatal Rat Ventricular Myocytes. Circ. Res. 2000; 86:1140–1145. [PubMed: 10850965]

519. Mandel Y, Weissman A, Schick R, Barad L, Novak A, Meiry G, Goldberg S, Lorber A, Rosen MR, Itskovitz-Eldor J, Binah O. Human embryonic and induced pluripotent stem cell-derived cardiomyocytes exhibit beat rate variability and power-law behavior. Circulation. 2012; 125:883–893. [PubMed: 22261196]

520. Perkiömäki J. Heart Rate Variability and Nonlinear Dynamics in Risk Stratification. Frontiers in Physiology. 2011; 2

521. Bub G, Shrier A, Glass L. Global organization of dynamics in oscillatory heterogeneous excitable media. Phys. Rev. Lett. 2005; 94:028105. [PubMed: 15698236]

522. Jung P, Cornell-Bell A, Madden KS, Moss F. Noise-induced spiral waves in astrocyte syncytia show evidence of self-organized criticality. J. Neurophysiol. 1998; 79:1098–1101. [PubMed: 9463465]

523. Chialvo DR. Emergent complex neural dynamics. Nat Phys. 2010; 6:744–750.

524. Garfinkel A, Spano ML, Ditto WL, Weiss JN. Controlling cardiac chaos. Science. 1992; 257:1230–1235. [PubMed: 1519060]

525. Ott E, Grebogi C, Yorke JA. Controlling chaos. Phys. Rev. Lett. 1990; 64:1196–1199. [PubMed: 10041332]

526. Ditto WL, Rauseo SN, Spano ML. Experimental Control of Chaos. Phys. Rev. Lett. 1990; 65:3211–3214. [PubMed: 10042811]

527. Christini DJ, Collins JJ. Using chaos control and tracking to suppress a pathological nonchaotic rhythm in a cardiac model. Phys.Rev.E. 1996; 53:R49–R52.

528. Hall K, Christini DJ, Tremblay M, Collins JJ, Glass L, Billette J. Dynamic control of cardiac alternans. Phys. Rev. Lett. 1997; 78:4518–4521.

529. Christini DJ, Stein KM, Markowitz SM, Mittal S, Slotwiner DJ, Scheiner MA, Iwai S, Lerman BB. Nonlinear-dynamical arrhythmia control in humans. Proc Natl Acad Sci U S A. 2001; 98:5827–5832. [PubMed: 11320216]

530. Hall GM, Gauthier DJ. Experimental control of cardiac muscle alternans. Phys. Rev. Lett. 2002; 88:198102. [PubMed: 12005667]

531. Kanu UB, Iravanian S, Gilmour RF Jr, Christini DJ. Control of action potential duration alternans in canine cardiac ventricular tissue. IEEE Trans. Biomed. Eng. 2011; 58:894–904. [PubMed: 21041155]

532. Krogh-Madsen T, Karma A, Riccio ML, Jordan PN, Christini DJ, Gilmour RF Jr. Off-site control of repolarization alternans in cardiac fibers. Phys Rev E Stat Nonlin Soft Matter Phys. 2010; 81:011915. [PubMed: 20365407]

533. Jordan PN, Christini DJ. Adaptive diastolic interval control of cardiac action potential duration alternans. J. Cardiovasc. Electrophysiol. 2004; 15:1177–1185. [PubMed: 15485444]

534. Echebarria B, Karma A. Spatiotemporal control of cardiac alternans. Chaos. 2002; 12:923–930. [PubMed: 12779616]

535. Christini DJ, Riccio ML, Culianu CA, Fox JJ, Karma A, Gilmour RF Jr. Control of electrical alternans in canine cardiac purkinje fibers. Phys. Rev. Lett. 2006; 96:104101. [PubMed: 16605736]

536. Garzon A, Grigoriev RO, Fenton FH. Model-based control of cardiac alternans in Purkinje fibers. Phys Rev E Stat Nonlin Soft Matter Phys. 2011; 84:041927. [PubMed: 22181195]

537. Tolkacheva EG, Romeo MM, Guerraty M, Gauthier DJ. Condition for alternans and its control in a two-dimensional mapping model of paced cardiac dynamics. Phys Rev E Stat Nonlin Soft Matter Phys. 2004; 69:031904. [PubMed: 15089319]

538. Qu Z. Controlling cardiac alternans. Heart Rhythm. 2013; 10:573–574. [PubMed: 23274370]

539. Hu G, Qu Z. Controlling spatiotemporal chaos in coupled map lattice systems. Phys. Rev. Lett. 1994; 72:68–71. [PubMed: 10055568]

540. El-Sherif N, Turitto G. Torsade de pointes. Curr. Opin. Cardiol. 2003; 18:6–13. [PubMed: 12496496]

541. Krikler DM, Curry PV. Torsade De Pointes, an atypical ventricular tachycardia. Br Heart J. 1976; 38:117–120. [PubMed: 1259825]

542. Manoach M, Varon D, Neuman M, Netz H. Spontaneous termination and initiation of ventricular fibrillation as a function of heart size, age, autonomic autoregulation, and drugs: a comparative study on different species of different age. Heart Vessels Suppl. 1987; 2:56–68. [PubMed: 3329649]

543. Clayton RH, Murray A, Higham PD, Campbell RW. Self-terminating ventricular tachyarrhythmias--a diagnostic dilemma? Lancet. 1993; 341:93–95. [PubMed: 8093413]

544. Reisin L, Blayer Y, Manoach M. Spontaneous ventricular defibrillation. Br Heart J. 1993; 70:590–591. [PubMed: 8280535]

545. Calabro MP, Luzza F, Carerj S, Oreto G. Spontaneous termination of ventricular fibrillation. Heart. 2004; 90:133. [PubMed: 14729773]

546. Garrey W. The nature of fibrillatory contraction of the heart: its relation to tissue mass and form. Am. J. Physiol. 1914; 33:397–414.

547. Wijffels M, Kirchhof C, Dorland R, Allessie MA. Atrial Fibrillation Begets Atrial Fibrillation - a Study in Awake Chronically Instrumented Goats. Circulation. 1995; 92:1954–1968. [PubMed: 7671380]

548. Ikeda T, Uchida T, Hough D, Lee JJ, Fishbein MC, Mandel WJ, Chen PS, Karagueuzian HS. Mechanism of spontaneous termination of functional reentry in isolated canine right atrium. Evidence for the presence of an excitable but nonexcited core. Circulation. 1996; 94:1962–1973. [PubMed: 8873675]

549. Strain MC, Greenside HS. Size-dependent transition to high-dimensional chaotic dynamics in a two-dimensional excitable medium. Phys. Rev. Lett. 1998; 80:2306–2309.

550. Naccarelli GV, Wolbrette DL, Khan M, Bhatta L, Hynes J, Samii S, Luck J. Old and new antiarrhythmic drugs for converting and maintaining sinus rhythm in atrial fibrillation: comparative efficacy and results of trials. Am. J. Cardiol. 2003; 91:15D–26D.

551. Nattel S, Kneller J, Zou R, Leon LJ. Mechanisms of termination of atrial fibrillation by Class I antiarrhythmic drugs: evidence from clinical, experimental, and mathematical modeling studies. J. Cardiovasc. Electrophysiol. 2003; 14:S133–139. [PubMed: 14760915]

552. Goy JJ, Maendly R, Grbic M, Finci L, Sigwart U. Cardioversion with flecainide in patients with atrial fibrillation of recent onset. Eur. J. Clin. Pharmacol. 1985; 27:737–738. [PubMed: 3987780]

553. Wijffels M, Dorland R, Mast F, Allessie MA. Widening of the excitable gap during pharmacological cardioversion of atrial fibrillation in the goat - Effects of cibenzoline, hydroquinidine, flecainide, and d-sotalol. Circulation. 2000; 102:260–267. [PubMed: 10889140]

554. Amino M, Yamazaki M, Nakagawa H, Honjo H, Okuno Y, Yoshioka K, Tanabe T, Yasui K, Lee JK, Horiba M, Kamiya K, Kodama I. Combined effects of nifekalant and lidocaine on the spiral-type re-entry in a perfused 2-dimensional layer of rabbit ventricular myocardium. Circ J. 2005; 69:576–584. [PubMed: 15849445]

555. Yamazaki M, Honjo H, Nakagawa H, Ishiguro YS, Okuno Y, Amino M, Sakuma I, Kamiya K, Kodama I. Mechanisms of destabilization and early termination of spiral wave reentry in the ventricle by a class III antiarrhythmic agent, nifekalant. Am J Physiol Heart Circ Physiol. 2007; 292:H539–548. [PubMed: 16936005]

556. Banville I, Gray RA. Effect of action potential duration and conduction velocity restitution and their spatial dispersion on alternans and the stability of arrhythmias. J. Cardiovasc. Electrophysiol. 2002; 13:1141–1149. [PubMed: 12475106]

557. Hardage, M.; Sweeney, M. Anti-Tachycardia Pacing and Cardioversion. In: Kroll, M.; Lehmann l, M., editors. Implantable Cardioverter Defibrillator Therapy: The Engineering-Clinical Interface. US: Springer; 1996. p. 325-342.

558. Zhang H, Hu B, Hu G, Ouyang Q, Kurths J. Turbulence control by developing a spiral wave with a periodic signal injection in the complex Ginzburg-Landau equation. Phys Rev E Stat Nonlin Soft Matter Phys. 2002; 66:046303. [PubMed: 12443318]

559. Zhang H, Hu B, Hu G. Suppression of spiral waves and spatiotemporal chaos by generating target waves in excitable media. Phys. Rev. E. 2003; 68:026134.

560. Tang G, Deng M, Hu B, Hu G. Active and passive control of spiral turbulence in excitable media. Phys Rev E Stat Nonlin Soft Matter Phys. 2008; 77:046217. [PubMed: 18517720]

561. Wathen MS, DeGroot PJ, Sweeney MO, Stark AJ, Otterness MF, Adkisson WO, Canby RC, Khalighi K, Machado C, Rubenstein DS, Volosin KJ. f.t.P.R.I. Investigators, Prospective Randomized Multicenter Trial of Empirical Antitachycardia Pacing Versus Shocks for Spontaneous Rapid Ventricular Tachycardia in Patients With Implantable Cardioverter-Defibrillators: Pacing Fast Ventricular Tachycardia Reduces Shock Therapies (PainFREE Rx II) Trial Results. Circulation. 2004; 110:2591–2596. [PubMed: 15492306]

562. Babbs CF, Tacker WA, VanVleet JF, Bourland JD, Geddes LA. Therapeutic indices for transchest defibrillator shocks: effective, damaging, and lethal electrical doses. Am. Heart J. 1980; 99:734–738. [PubMed: 7377095]

563. Hwang C, Swerdlow CD, Kass RM, Gang ES, Mandel WJ, Peter CT, Chen PS. Upper limit of vulnerability reliably predicts the defibrillation threshold in humans. Circulation. 1994; 90:2308–2314. [PubMed: 7955188]

564. Takagi S, Pumir A, Pazo D, Efimov I, Nikolski V, Krinsky V. Unpinning and removal of a rotating wave in cardiac muscle. Phys. Rev. Lett. 2004; 93:058101. [PubMed: 15323732]

565. Ripplinger CM, Krinsky VI, Nikolski VP, Efimov IR. Mechanisms of unpinning and termination of ventricular tachycardia. Am J Physiol Heart Circ Physiol. 2006; 291:H184–192. [PubMed: 16501014]

566. Pumir A, Nikolski V, Hörning M, Isomura A, Agladze K, Yoshikawa K, Gilmour R, Bodenschatz E, Krinsky V. Wave Emission from Heterogeneities Opens a Way to Controlling Chaos in the Heart. Phys. Rev. Lett. 2007; 99:208101. [PubMed: 18233188]

567. Pumir A, Krinsky V. Unpinning of a rotating wave in cardiac muscle by an electric field. J. Theor. Biol. 1999; 199:311–319. [PubMed: 10433895]

568. Luther S, Fenton FH, Kornreich BG, Squires A, Bittihn P, Hornung D, Zabel M, Flanders J, Gladuli A, Campoy L, Cherry EM, Luther G, Hasenfuss G, Krinsky VI, Pumir A, Gilmour RF Jr, Bodenschatz E. Low-energy control of electrical turbulence in the heart. Nature. 2011; 475:235–239. [PubMed: 21753855]

569. Fenton FH, Luther S, Cherry EM, Otani NF, Krinsky V, Pumir A, Bodenschatz E, Gilmour RF Jr. Termination of atrial fibrillation using pulsed low-energy far-field stimulation. Circulation. 2009; 120:467–476. [PubMed: 19635972]

570. John RM, Tedrow UB, Koplan BA, Albert CM, Epstein LM, Sweeney MO, Miller AL, Michaud GF, Stevenson WG. Ventricular arrhythmias and sudden cardiac death. The Lancet. 380:1520–1529.

571. Zipes DP, Rubart M. Neural modulation of cardiac arrhythmias and sudden cardiac death. Heart Rhythm. 2006; 3:108–113. [PubMed: 16399065]

572. Marder E. Variability, compensation, and modulation in neurons and circuits. Proceedings of the National Academy of Sciences. 2011; 108:15542–15548.

573. Sarkar AX, Sobie EA. Quantification of repolarization reserve to understand interpatient variability in the response to proarrhythmic drugs: a computational analysis. Heart Rhythm. 2011; 8:1749–1755. [PubMed: 21699863]

574. Banyasz T, Horvath B, Jian Z, Izu LT, Chen-Izu Y. Sequential dissection of multiple ionic currents in single cardiac myocytes under action potential-clamp. J. Mol. Cell. Cardiol. 2011; 50:578–581. [PubMed: 21215755]

575. John R, Stevenson W. Catheter-based Ablation for Ventricular Arrhythmias. Current Cardiology Reports. 2011; 13:399–406. [PubMed: 21744156]

576. Woods CE, Olgin J. Atrial Fibrillation Therapy Now and in the Future: Drugs, Biologicals, and Ablation. Circ. Res. 2014; 114:1532–1546. [PubMed: 24763469]

577. Anderson PW. More Is Different - Broken Symmetry and Nature of Hierarchical Structure of Science. Science. 1972; 177:393–396. [PubMed: 17796623]

578. Bovo E, Lipsius SL, Zima AV. Reactive Oxygen Species Contribute to the Development of Arrhythmogenic Ca2+ Waves during β-Adrenergic Receptor Stimulation in Rabbit Cardiomyocytes. The Journal of Physiology. 2012; 590:3291–3304. [PubMed: 22586224]

579. Jiang Y, Lee A, Chen J, Ruta V, Cadene M, Chait BT, MacKinnon R. X-ray structure of a voltage-dependent K+ channel. Nature. 2003; 423:33–41. [PubMed: 12721618]

580. Bridge JH, Ershler PR, Cannell MB. Properties of Ca2+ sparks evoked by action potentials in mouse ventricular myocytes. J. Physiol. 1999; 518:469–478. [PubMed: 10381593]

581. Goldhaber JI, Xie LH, Duong T, Motter C, Khuu K, Weiss JN. Action potential duration restitution and alternans in rabbit ventricular myocytes: the key role of intracellular calcium cycling. Circ. Res. 2005; 96:459–466. [PubMed: 15662034]

582. Storb U, Rodrigues Neto C, Bar M, Muller SC. A tomographic study of desynchronization and complex dynamics of scroll waves in an excitable chemical reaction with a gradient. Physical Chemistry Chemical Physics. 2003; 5:2344–2353.

583. Luengviriya C, Müller SC, Hauser MJB. Reorientation of scroll rings in an advective field. Phys. Rev. E. 2008; 77:015201.

584. Maltsev VA, Vinogradova TM, Bogdanov KY, Lakatta EG, Stern MD. Diastolic calcium release controls the beating rate of rabbit sinoatrial node cells: numerical modeling of the coupling process. Biophys. J. 2004; 86:2596–2605. [PubMed: 15041695]

585. Vinogradova TM, Brochet DX, Sirenko S, Li Y, Spurgeon H, Lakatta EG. Sarcoplasmic reticulum Ca2+ pumping kinetics regulates timing of local Ca2+ releases and spontaneous beating rate of rabbit sinoatrial node pacemaker cells. Circ. Res. 2010; 107:767–775. [PubMed: 20651285]

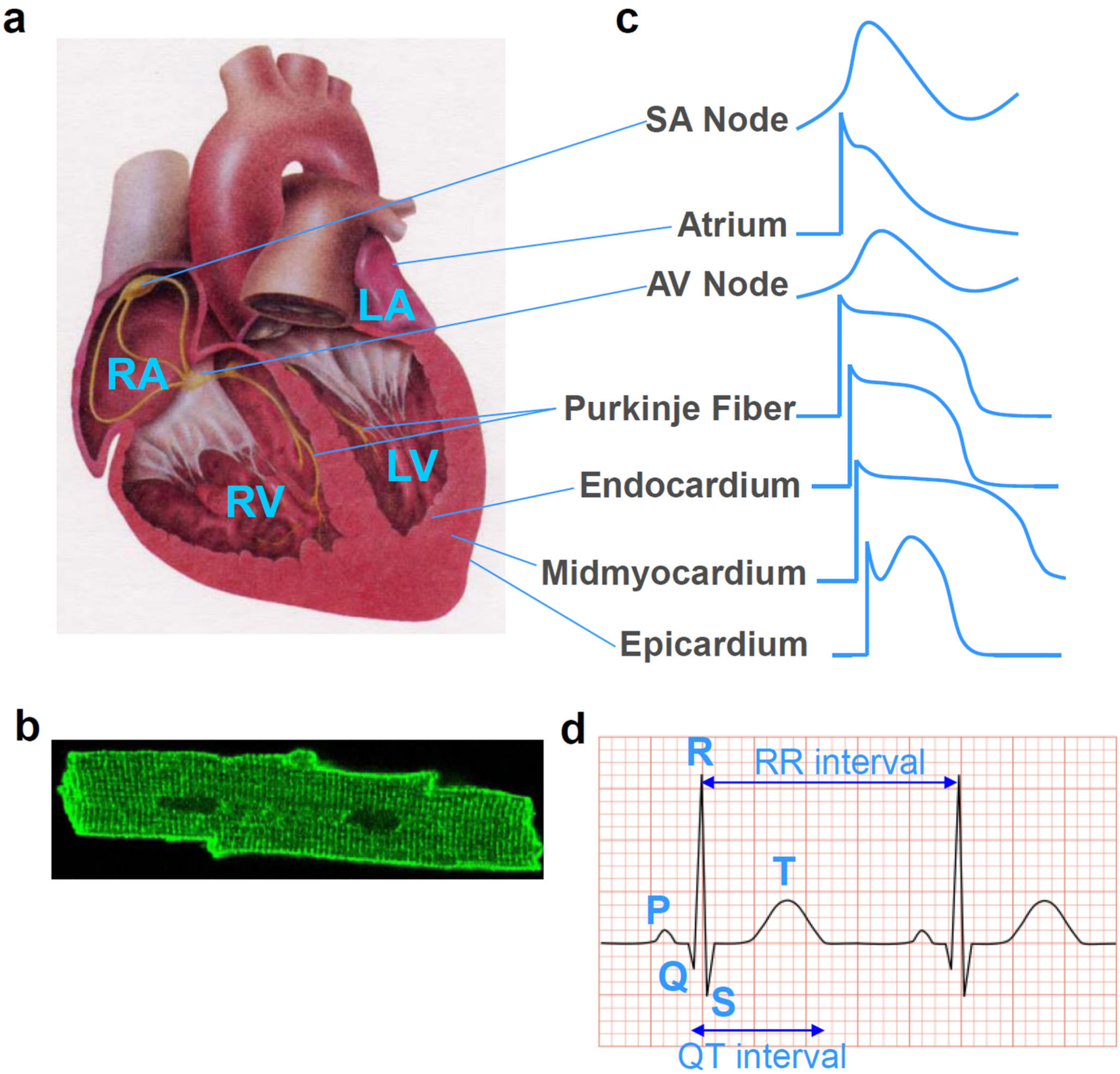

Figure 1. The normal heart structure and function

a. SAN—sino-atrial node; RA—right atrium; LA—left atrium; AVN—atrial-ventricular node; RV—right ventricle; LV—left ventricle. **b**. An image of a ventricular myocyte. **c**. Action potential morphologies in different regions of the heart. **d**. Schematic plot of a normal ECG illustrating the P-wave, the QRS complex, the T-wave, RR interval, and QT interval.

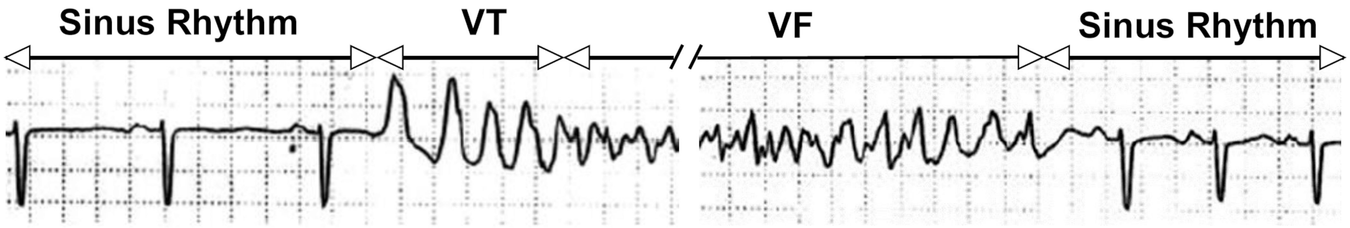

Figure 2. Transitions in cardiac arrhythmias

An ECG from a patient [15] showing the transitions from sinus rhythm to VT, from VT to VF, and from VF back to sinus rhythm.

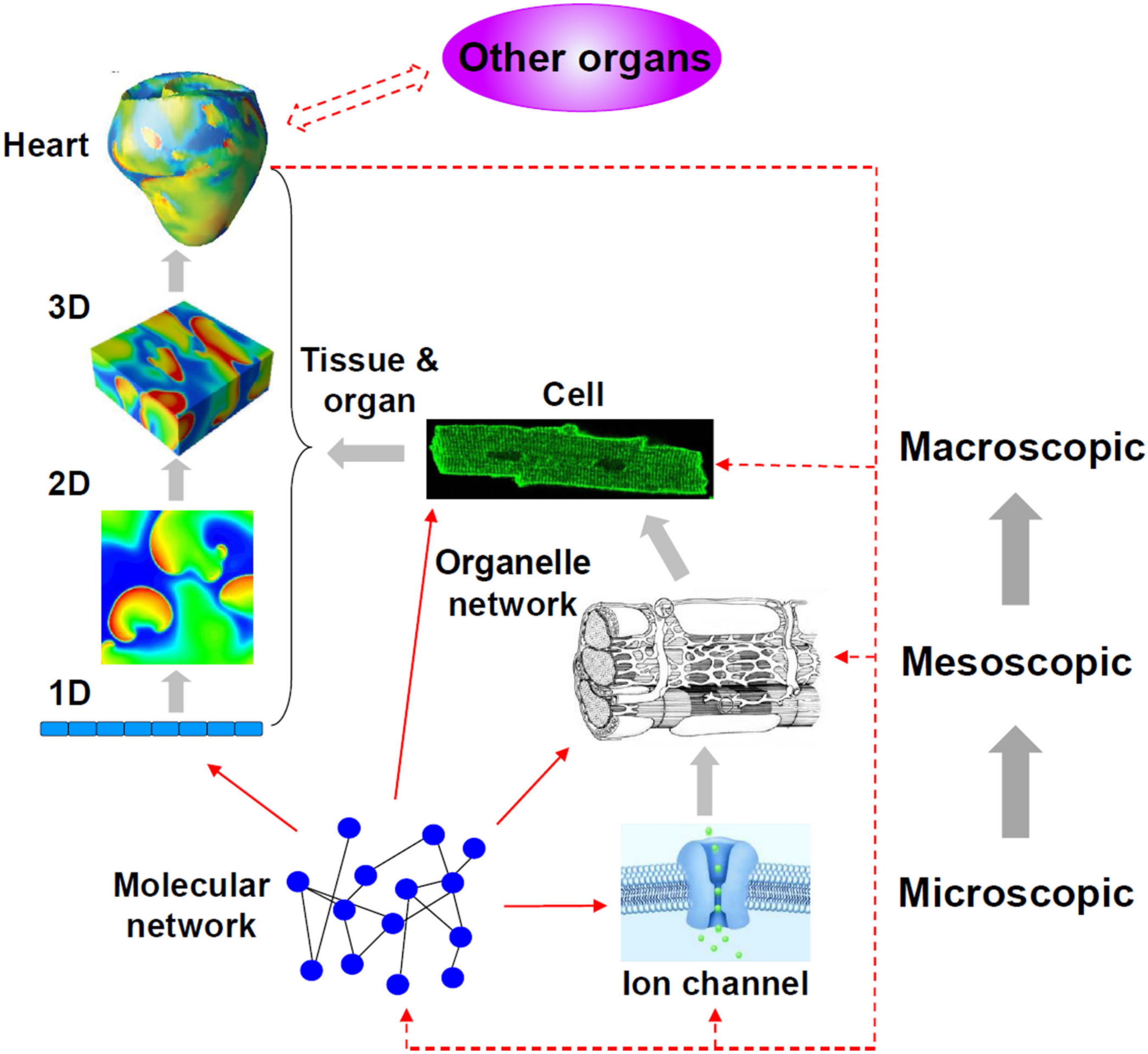

Figure 3. Multi-scale regulation of heart rhythms

A schematic plot of gene and protein network, ion channel, organelle network, cell, and tissue and organ, and their interactions in the heart. Thick gray arrows mark the scale change. Solid red arrows indicate the molecular regulations at different scales. Dashed red arrows indicate feedback regulations.

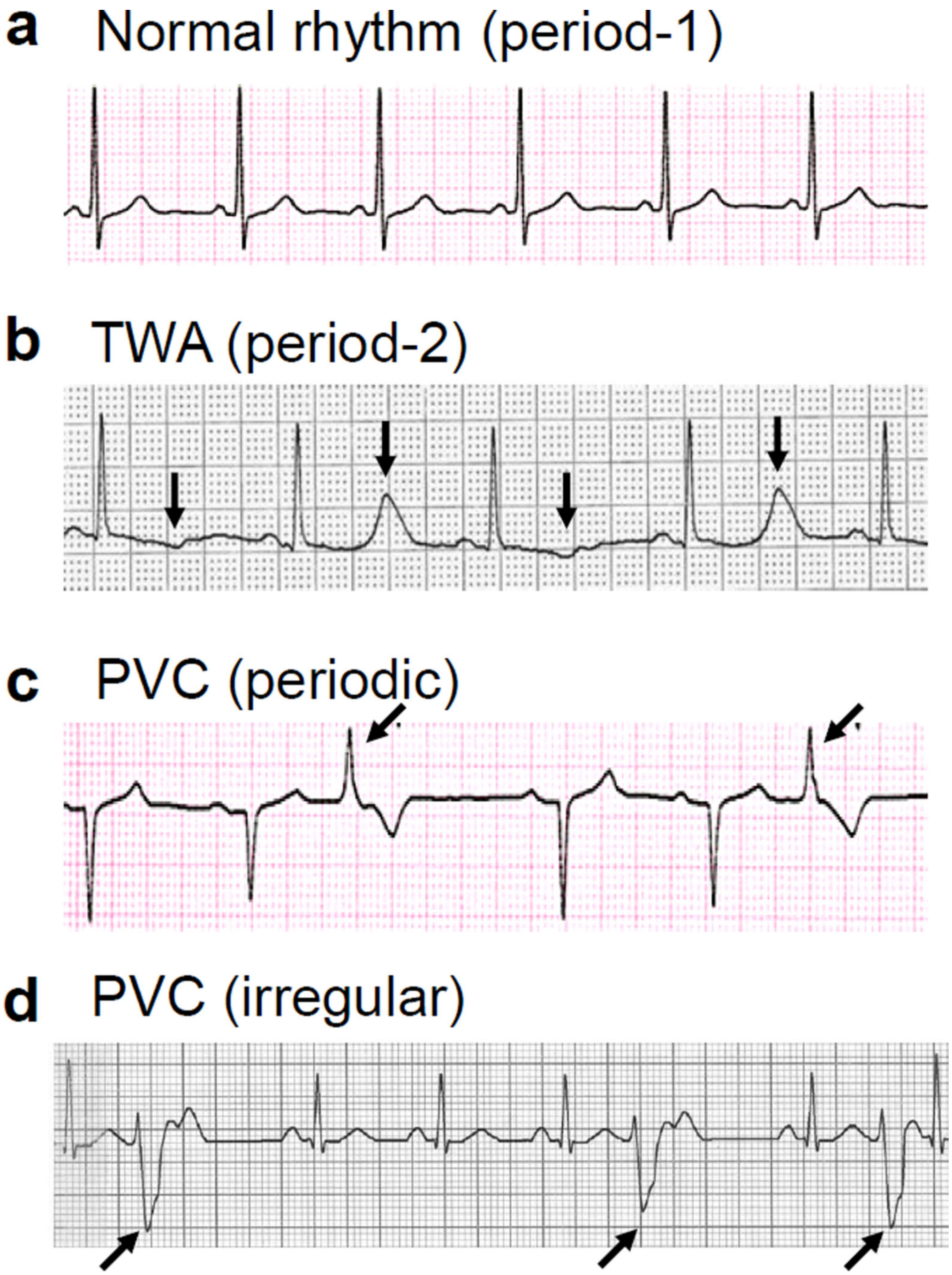

Figure 4. Complex ECG dynamics during sinus rhythm

a. Normal sinus rhythm in which the ECG is regular, exhibiting a period-1 behavior. **b**. TWA in which the T-wave (arrows) exhibits a *large, small, large, small*, …, pattern, resulting in a period-2 behavior. **c**. PVCs (arrows) occur every two beats (trigeminy), resulting in a periodic behavior. **d**. Irregularly occurring PVCs (arrows).

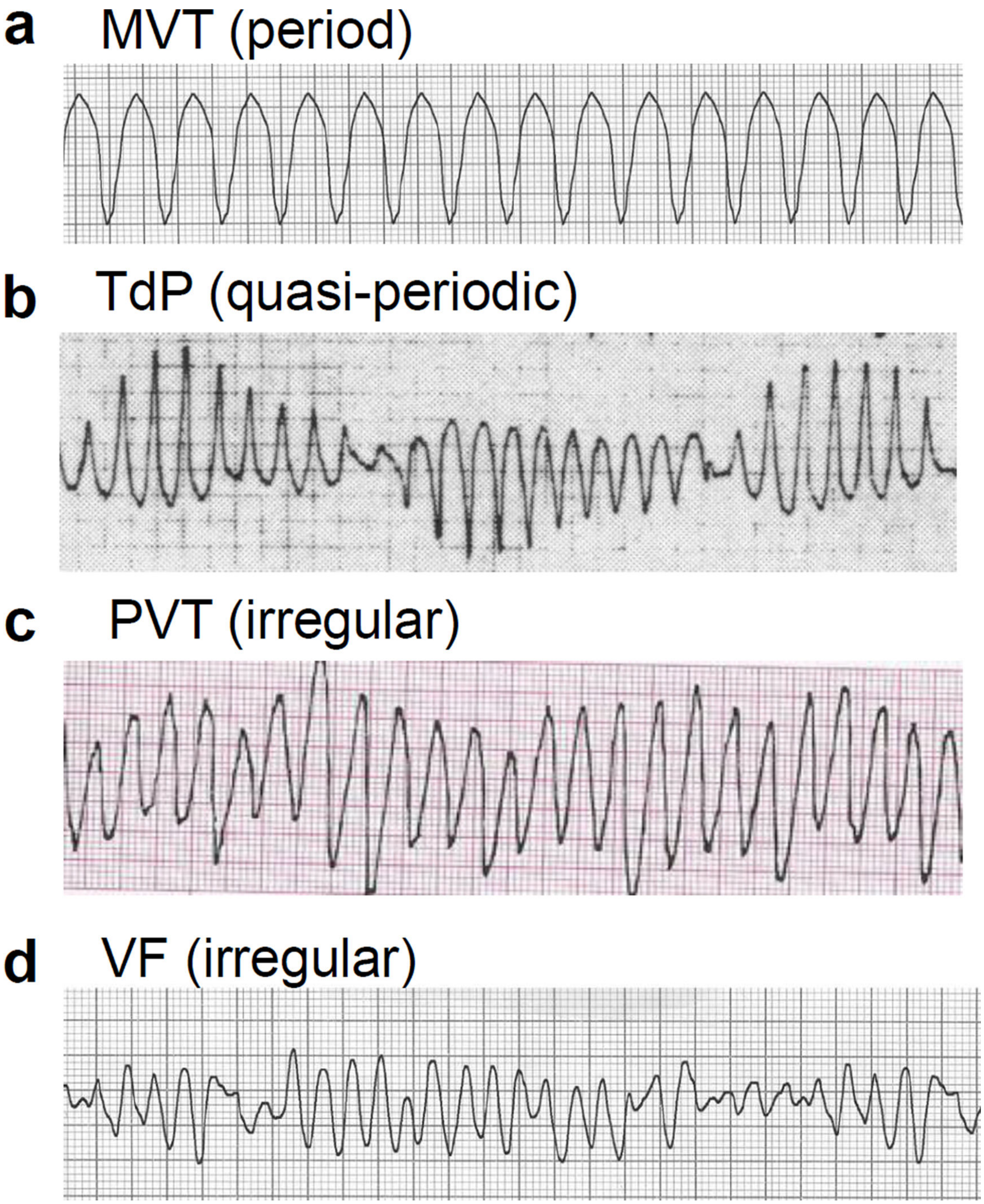

Figure 5. Complex ECG dynamics during ventricular arrhythmias

a. Monomorphic VT (MVT) in which the ECG signal exhibits a period-1 behavior with a rate much faster than sinus rhythm. **b**. Torsade de Pointes (TdP) in which the ECG signal is modulated by another frequency, exhibiting a quasi-periodic behavior. **c**. Polymorphic VT (PVT) in which the ECG exhibits a chaotic or irregular behavior. **d**. VF in which the ECG signal is attenuated and exhibits a chaotic or irregular behavior.

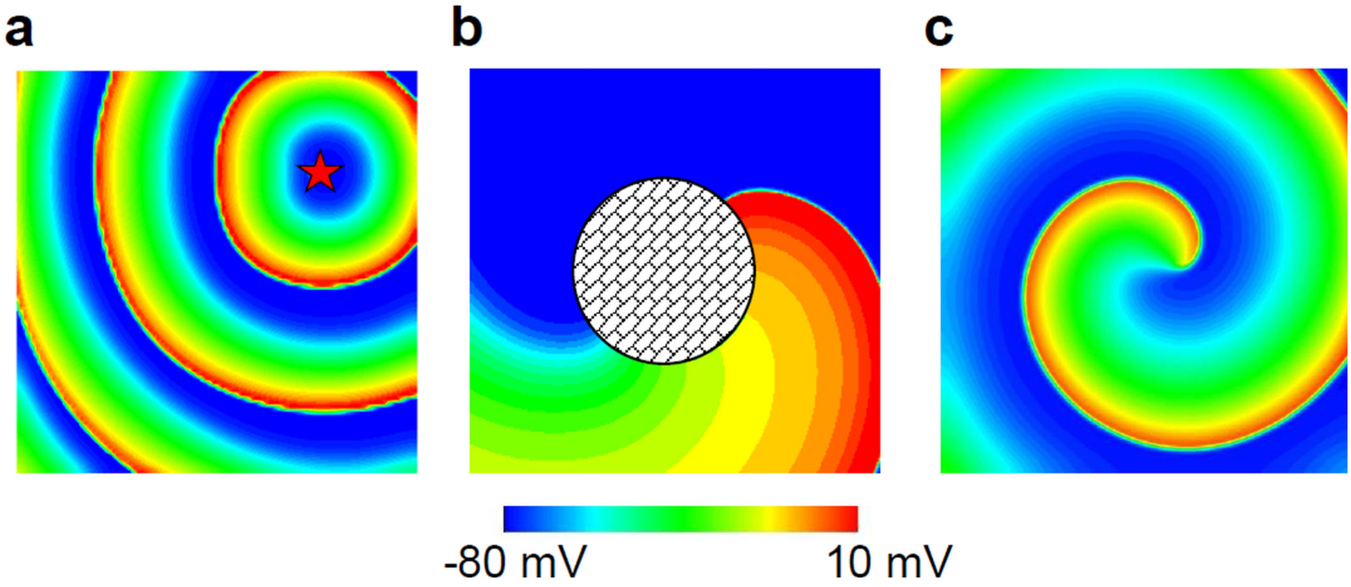

Figure 6. Electrical wave dynamics in arrhythmias

a. Target waves. The star indicates the focal source. **b**. Reentry around an obstacle. **c**. Spiral wave.

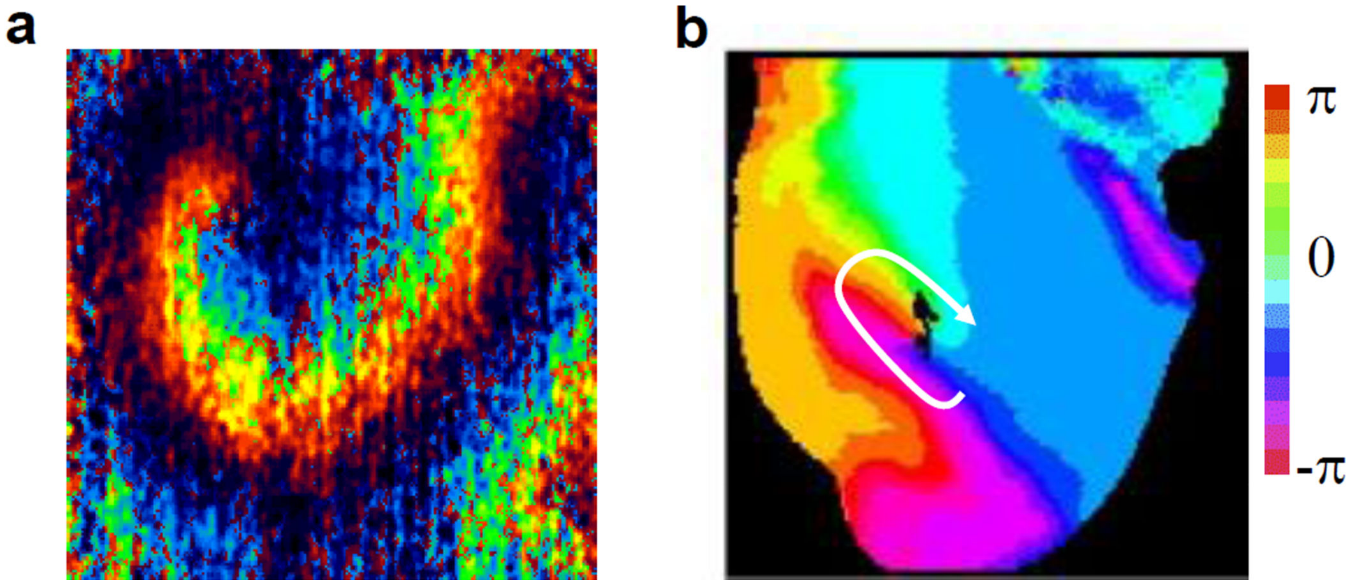

Figure 7. Spiral waves in cardiac tissue

a. A spiral wave recorded from a cultured rat neonatal ventricular myocyte monolayer imaged by Ca^{2+} concentration (courtesy of Miguel Valderrabano). A cultured monolayer is a tissue grown in a dish which is a one-cell thick cardiac tissue suitable for studying cardiac spiral wave dynamics and many other basic dynamical properties in a true 2D setting. **b**. A spiral wave on the epicardium of a rabbit heart shown as a phase map of voltage [85]. Arrow indicates the rotation direction, and the black color in the center is the phase singularity. The spiral wave in the monolayer is more circular than the one from the epicardial surface. This is because the monolayer is more homogeneous while the heart is heterogeneous with fiber orientation causing an elongated spiral core.

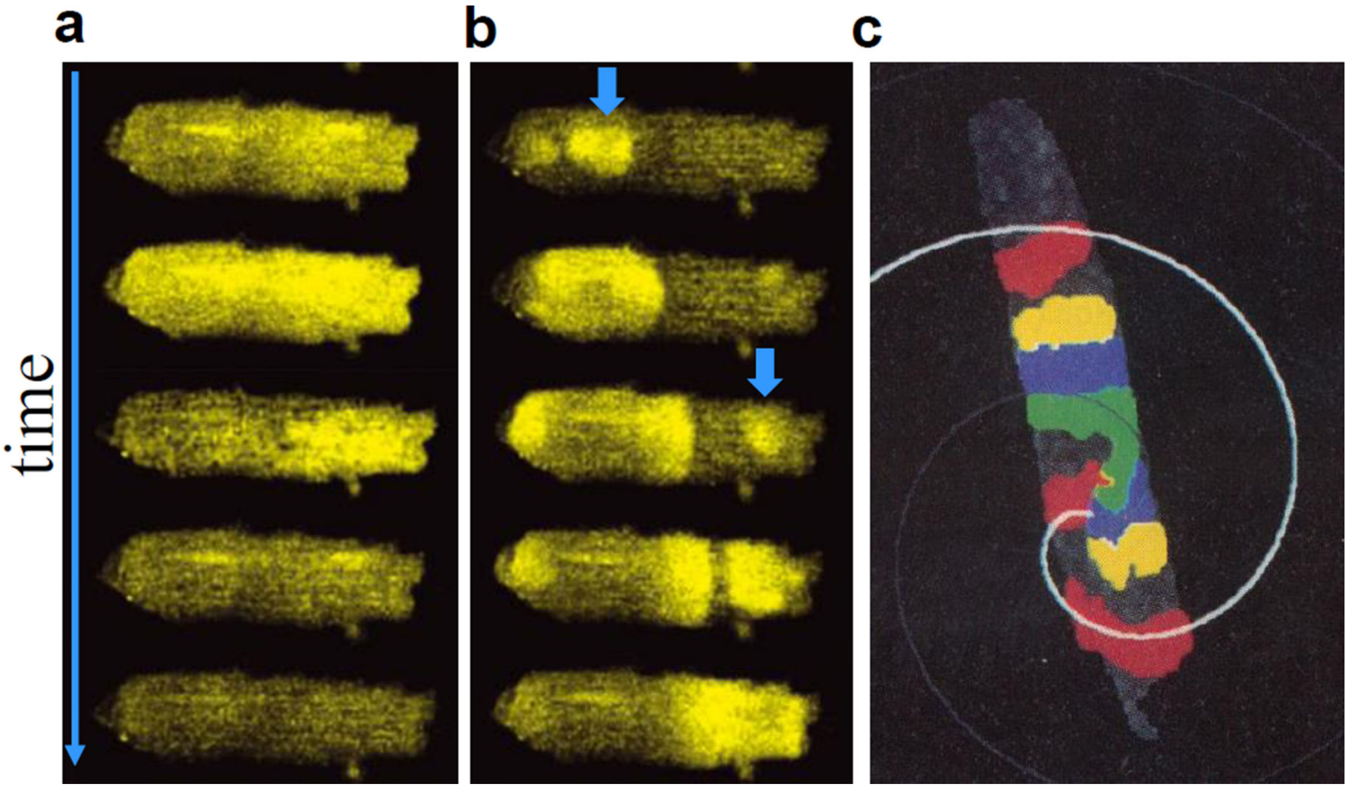

Figure 8. Intracellular Ca^{2+} cycling dynamics in ventricular myocytes

a. Ca^{2+} cycling in a normal action potential, in which Ca^{2+} elevates and decays synchronously in the whole cell. **b**. A spontaneous Ca^{2+} waves, in which Ca^{2+} elevates first in one location and then propagates in the cell as a wave. The origins of the waves are indicated by arrows. Panels a and b are from a cover image of J. Physiol. provided by Bovo et al [578]. **c**. A Ca^{2+} spiral wave observed in a ventricular myocyte by Lipp and Niggli [216].

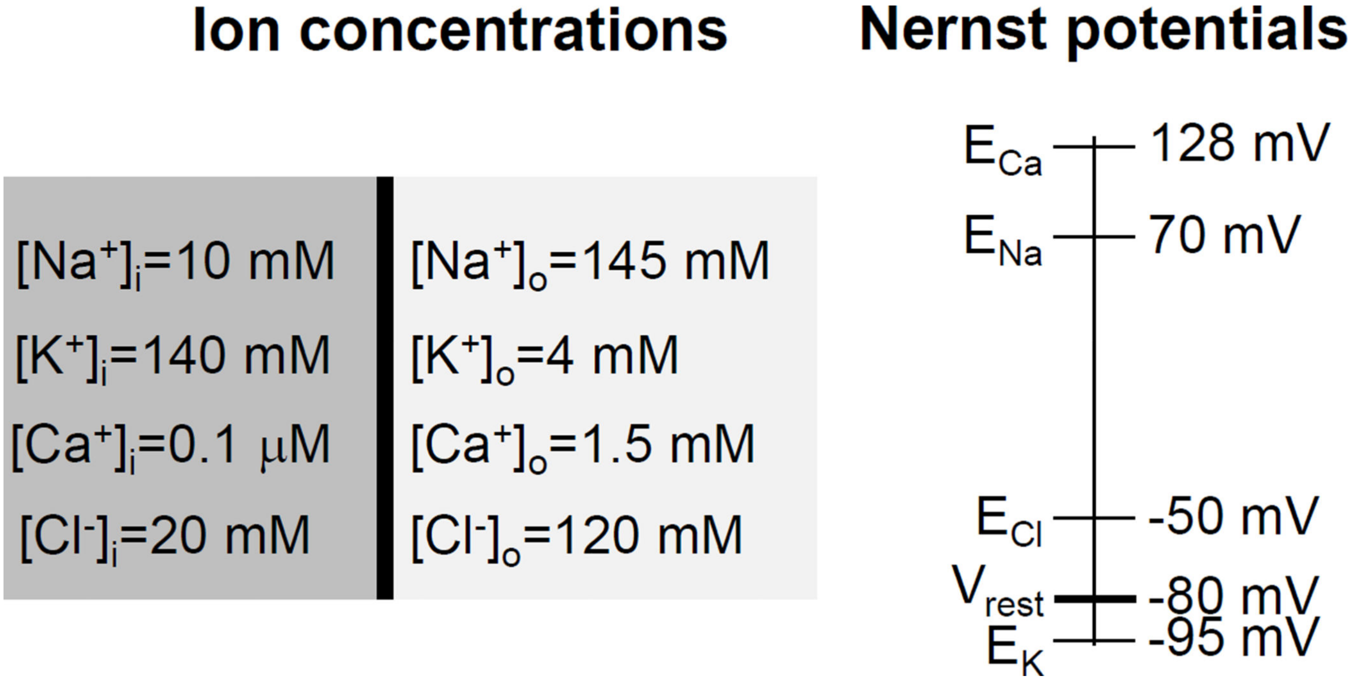

Figure 9. Ionic concentrations and Nernst potentials in the heart

Left panel: ion concentrations inside and outside a cardiac myocyte. Right panel: the Nernst potentials for different ion species. V_{rest} is the resting potential of a myocyte.

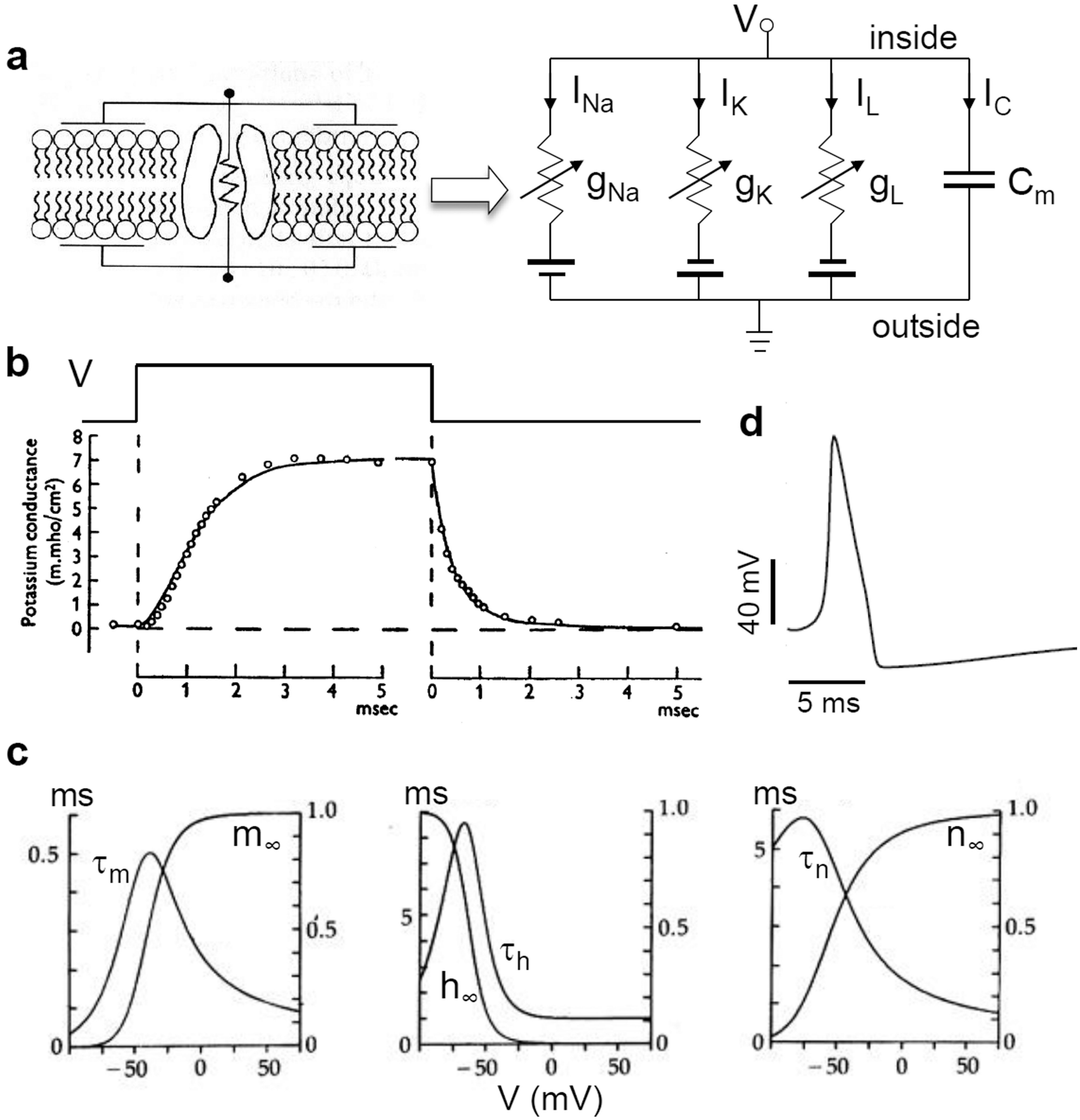

Figure 10. The HH model

a. Left panel: Schematic plot representing the cell membrane as a capacitor and the ion channel as a conductor. Right panel: The electrical circuit of the HH model of the giant axon. **b**. K^+ channel conductance (g_K) in squid giant axon when voltage was depolarized 25 mV from the resting potential, and then repolarized back to the resting potential after a certain time period. Upper trace is the clamped voltage trace. Circles are data from experiments, and the solid lines are fit using the model [118]. **c**. m_∞, h_∞, n_∞, τ_m, τ_h, and τ_n versus V of the HH model. **d**. An action potential of the HH model.

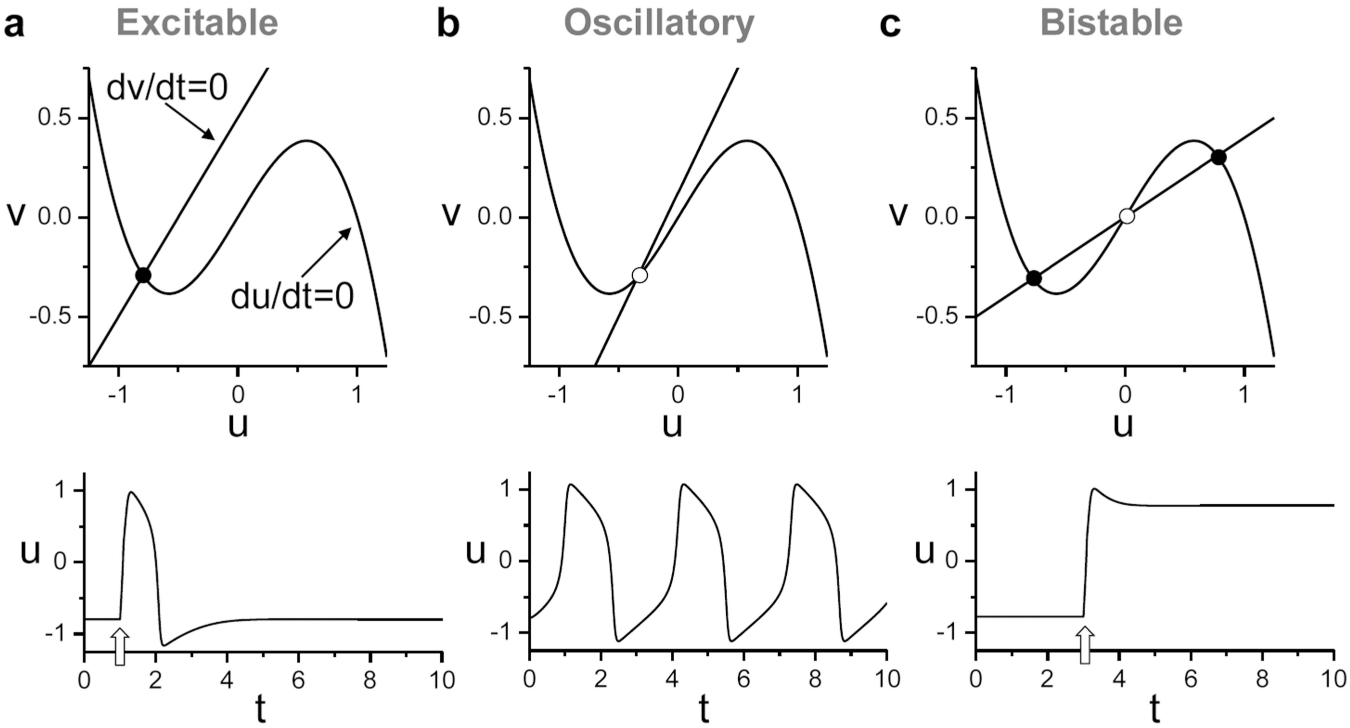

Figure 11. Dynamical behaviors of the FHN model

Upper panels: Nullclines and fixed points. Lower panels: u versus time from simulations. Open arrows in a and c indicate the times when a stimulation pulse is applied to elicit an action potential. **a**. One stable fixed point, the system is excitable. **b**. One unstable fixed point, the system is oscillatory. **c**. Three fixed points, the systems is bistable.

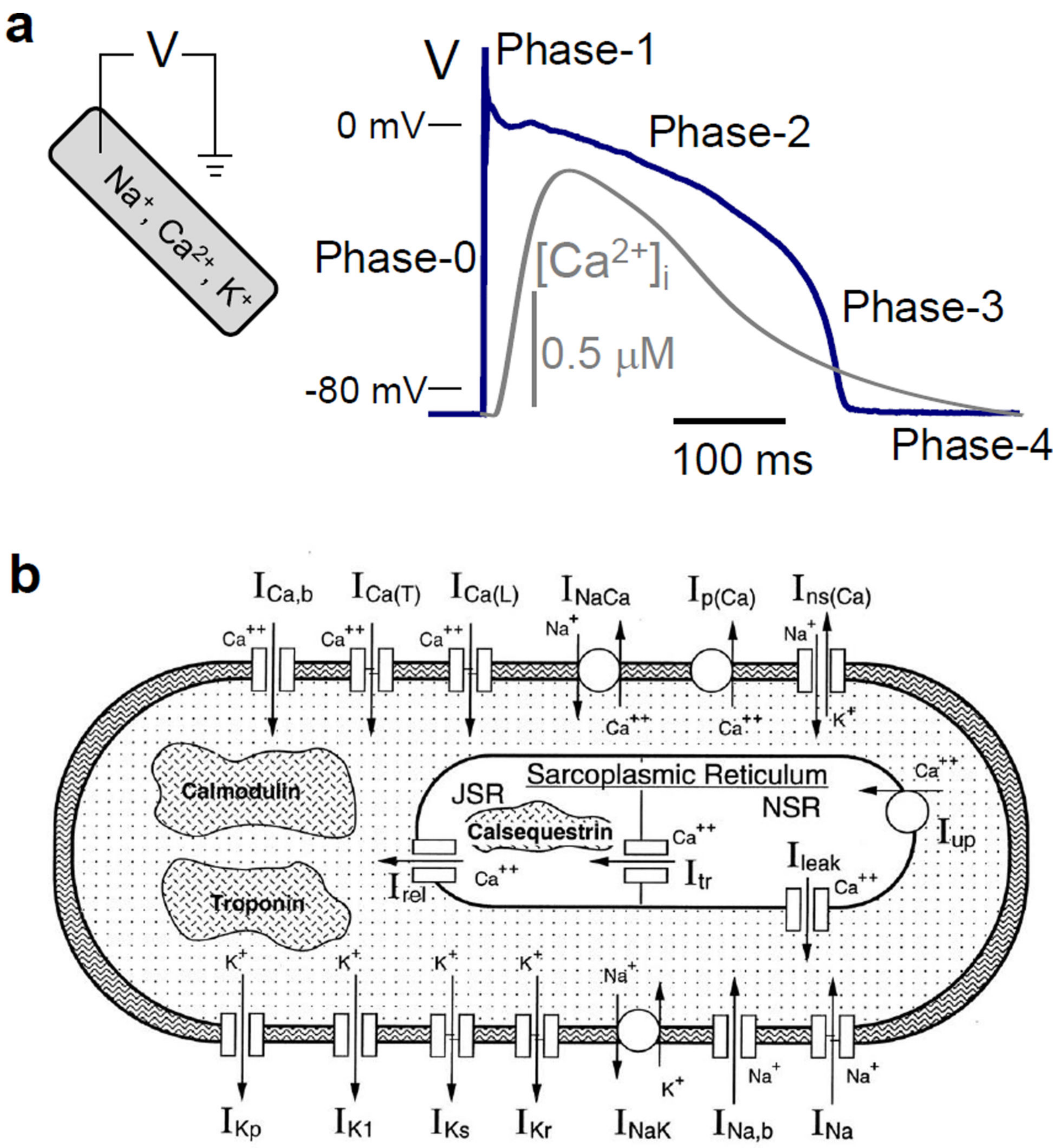

Figure 12. Cardiac action potential

a. A voltage trace showing an action potential of a ventricular myocyte and the corresponding trace of the whole-cell Ca^{2+} concentration. **b**. A schematic diagram of the ventricular myocyte action potential model developed by Zeng et al [126].

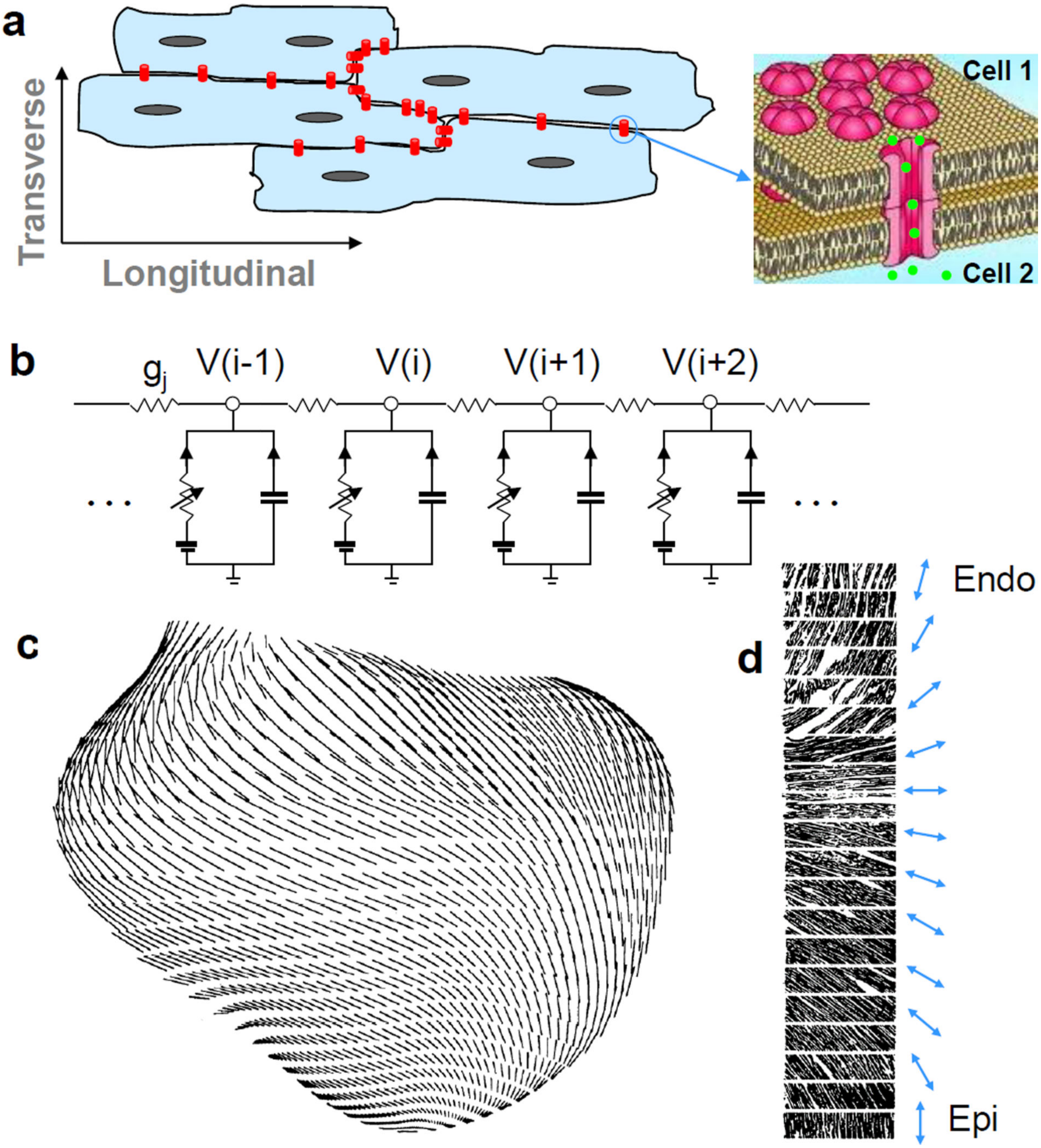

Figure 13. Myocyte coupling and tissue model

a. Left: Schematic plot of coupled myocytes via gap junctions. Right: a schematic plot of a gap junction. **b**. A 1D chain of resistively coupled cardiac cells represented by electrical circuits. **c**. Fiber orientations on the epicardial surface of a dog heart, reproduced from [154]; **d**. Transmural fiber orientation from epicardium to endocardium; the arrows mark the fiber directions.

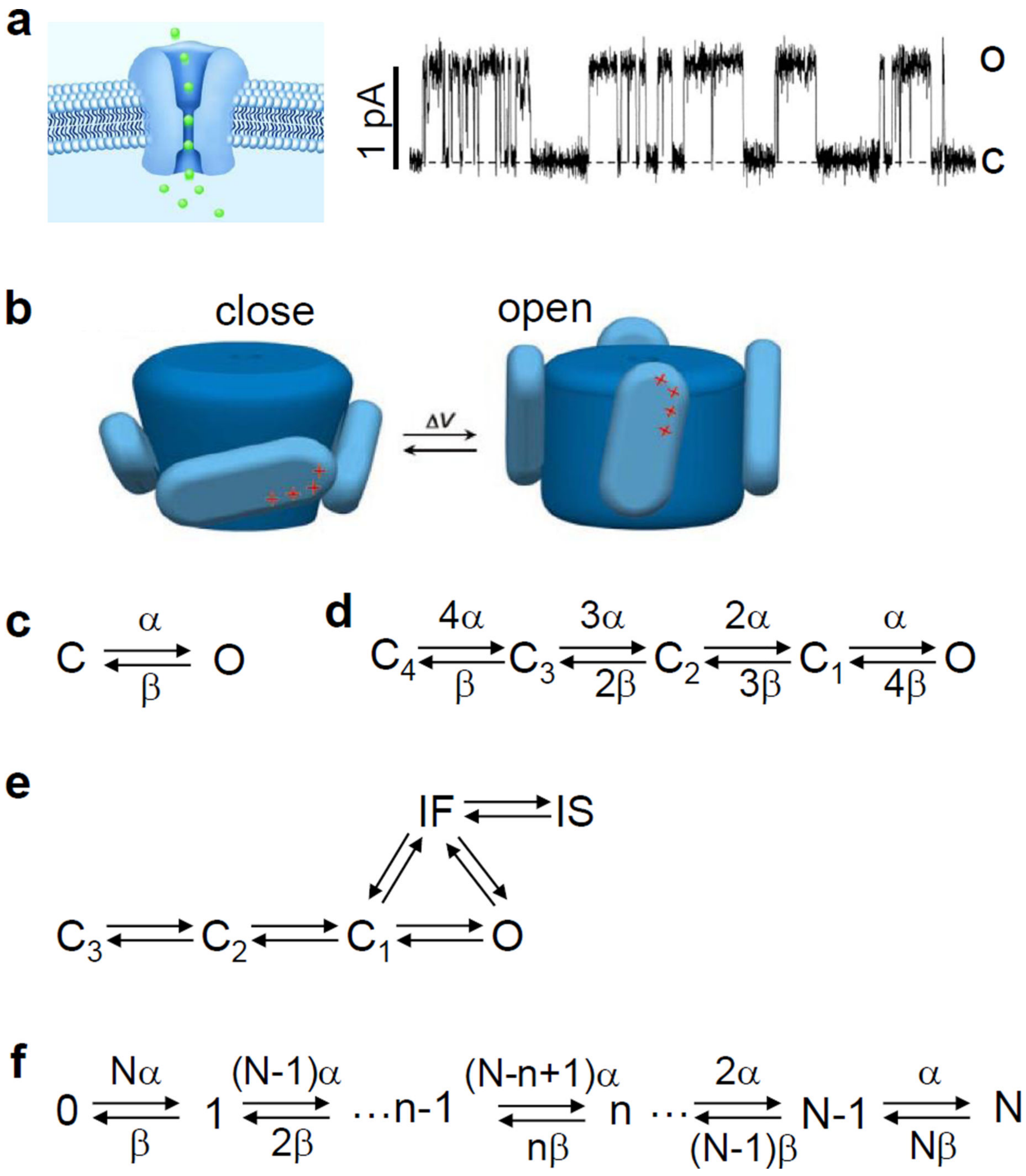

Figure 14. Ion channel and stochastic modeling

a. Left: A schematic plot of an ion channel. Right: An experimental recording of a single channel current. “O” indicates open and “C” indicates closed. **b**. A schematic plot of a model of K^+ channel’s open and closed states, reproduced from Jiang et al [579]. The channel is closed when one or more of the 4 voltage sensors are positioned as on the left and the channel is open when all 4 sensors are positioned as on the right. **c**. A simple two-state model. **d**. A five-state model for the K^+ channel. **e**. A Markov model for Na^+ channel [140]. **f**. A Markov chain model for an ensemble of *N* channels described by the two-state model.

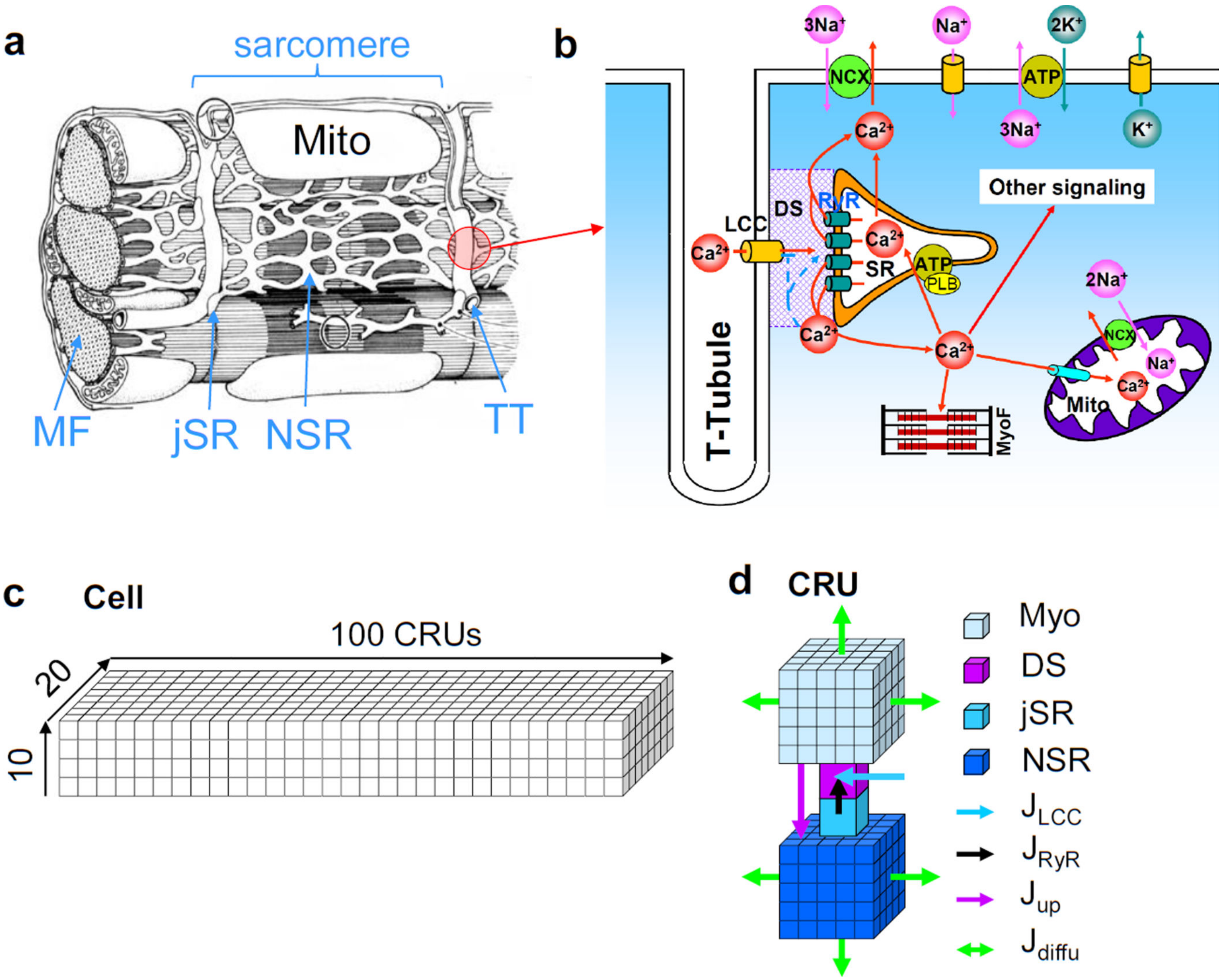

Figure 15. Sub-cellular structure and modeling

a. A schematic plot of ultrastructure of a portion in a ventricular myocyte. TT—Transverse tubule; MF—myofibril; Mito—mitochondrion; SR—sarcoplasmic reticulum. **b**. A schematic plot of intracellular Ca^{2+} signaling regulation and its coupling to voltage. **c**. A coupled CRU network representing a ventricular myocyte. **d**. A schematic plot of a computational CRU with the corresponding spaces and Ca^{2+} fluxes. Myo—myoplasm; DS—dyadic space (as indicated by the patched area in b); jSR—junctional SR; NSR—network SR; J_{LCC}—Ca^{2+} flux from the LCC cluster; J_{RyR}—Ca^{2+} flux from the RyR cluster; J_{up}—Ca^{2+} uptake flux; and J_{diffu}—Ca^{2+} diffusion flux.

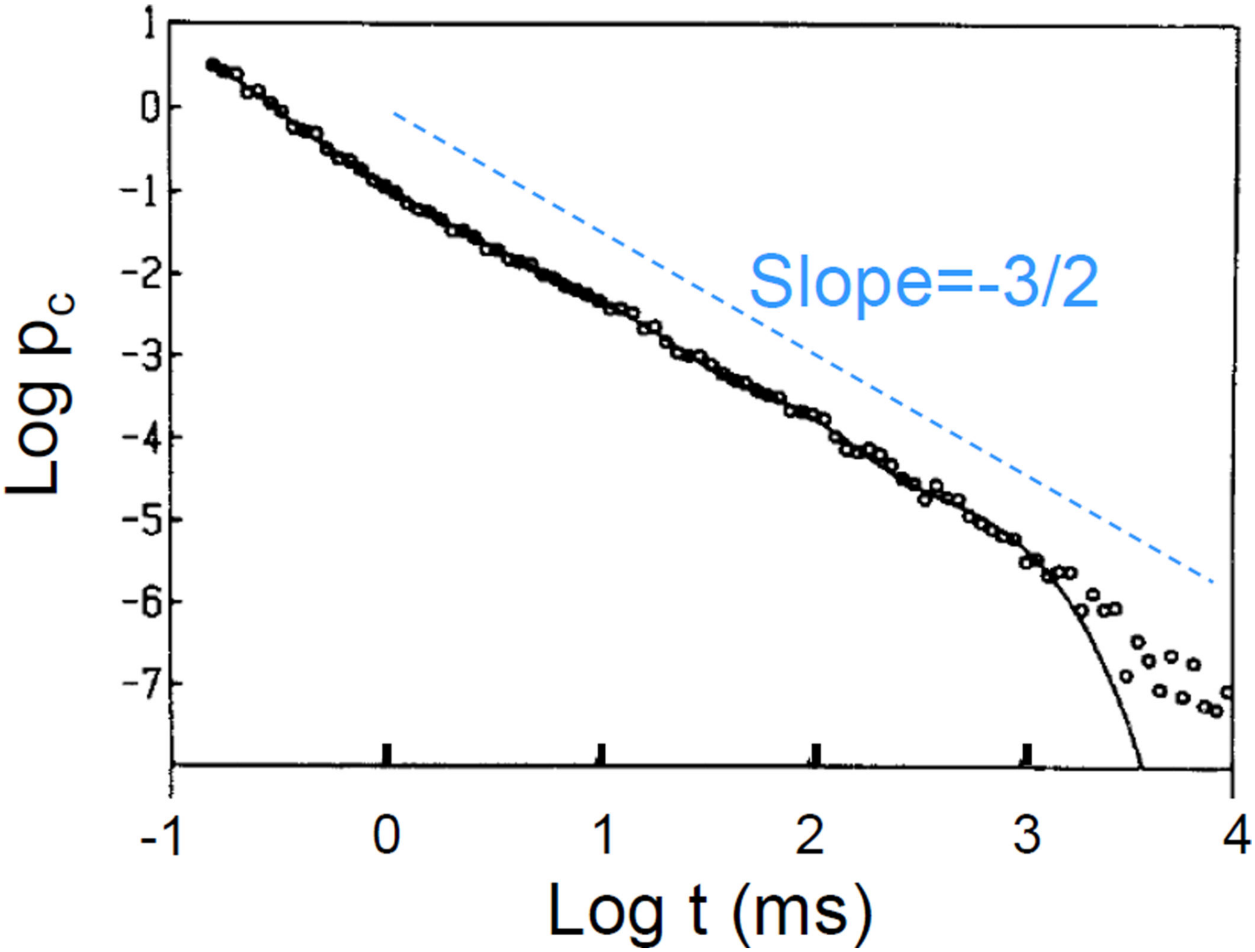

Figure 16. Single channel dynamics

Closed time distribution of an ion channel in a log-log plot showing a power-law distribution with a −3/2 exponent, reproduced from McGee et al [192].

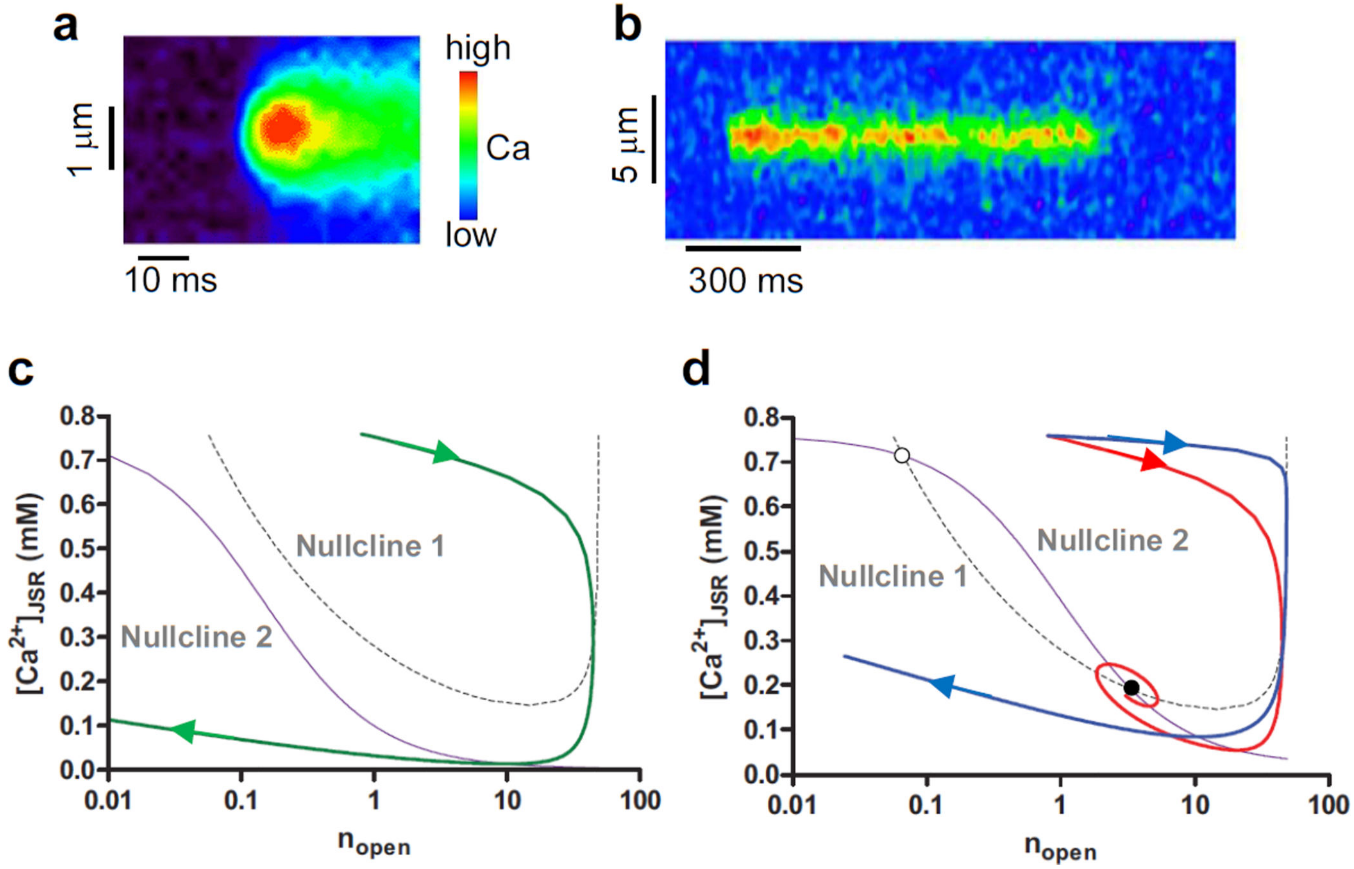

Figure 17. Ca^{2+} sparks and dynamics

a. A normal Ca^{2+} spark, reproduced from Bridge et al [580]; **b**. An ultralong Ca^{2+} spark, reproduced from Zima et al [205]. Panels a and b are spacetime plots with the vertical axis being space and the horizontal axis being time. Note the difference in time and space scales between a and b. **c** and **d**. Nullclines and fixed points of a Ca^{2+} spark model, reproduced and modified from Stern et al [207]. In both cases, n_{open}=0 is also a nullcline (not plotted in the panels). In c, the nullcline n_{open}=0 intersects with nullcline 2 to form the only stable fixed point (at $[Ca^{2+}]_{JSR}$~0.7 mM and n_{open}=0), and nullcline 1 and nullcline 2 have no intersection. The system is monostable and excitable. Green trance is a trajectory of a spark. In d, the nullclines have three intersections with two being stable (one at $[Ca^{2+}]_{JSR}$~0.75 mM and n_{open}=0, and the other labeled by the solid circle) and one unstable (labeled by the open circle). The system is bistable. The red and blue traces are two trajectories under two conditions with the red one trapped by the stable fixed point and the blue one escaped.

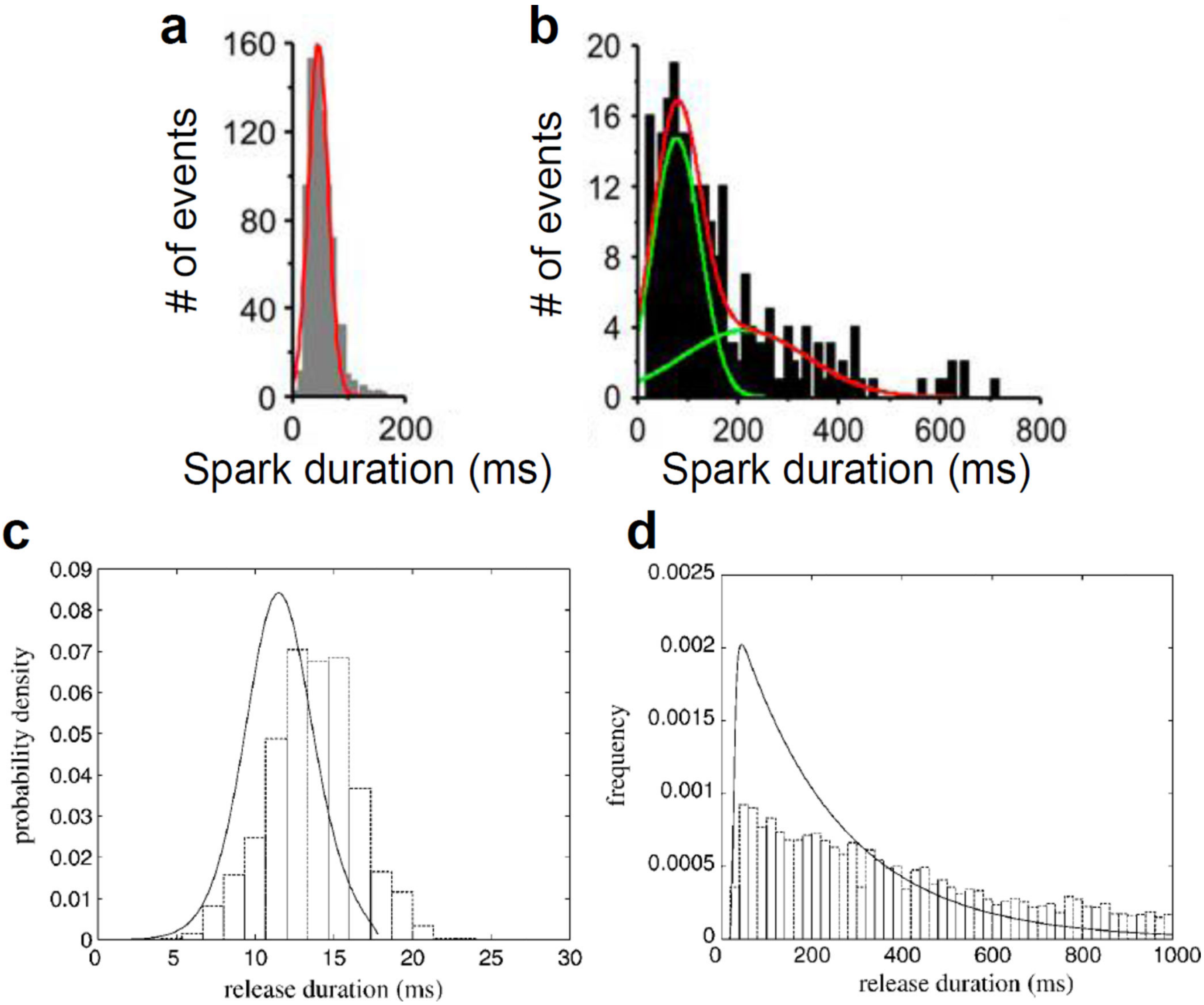

Figure 18. Spark duration distribution

a and **b**. Spark duration distribution measured from an experiment, reproduced from Zima et al [205]. **c** and **d**. Spark duration distribution from computer simulations (bar) and theoretical predictions (line), reproduced from Hinch [206].

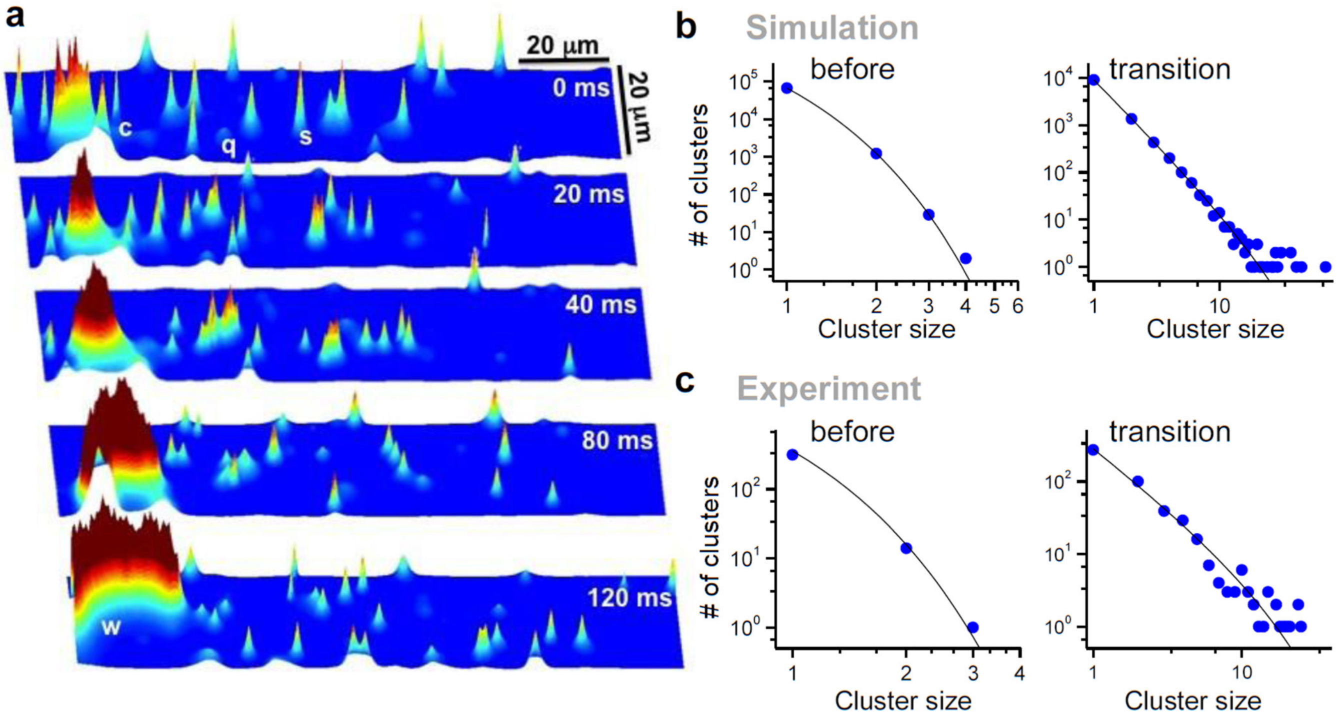

Figure 19. Phase transition and criticality in Ca^{2+} signaling

a. Snapshots of Ca^{2+} concentration from a layer of a myocyte model [143]. The simulation was done by holding voltage at −80 mV and a higher than normal extracellular Ca^{2+} concentration. q—quark; s—spark; c—cluster; w—wave. **b**. Cluster size distributions from a computer simulation for a low and a high extracellular Ca^{2+} concentration. **c**. Same as b but from experiments in a mouse ventricular myocyte [111].

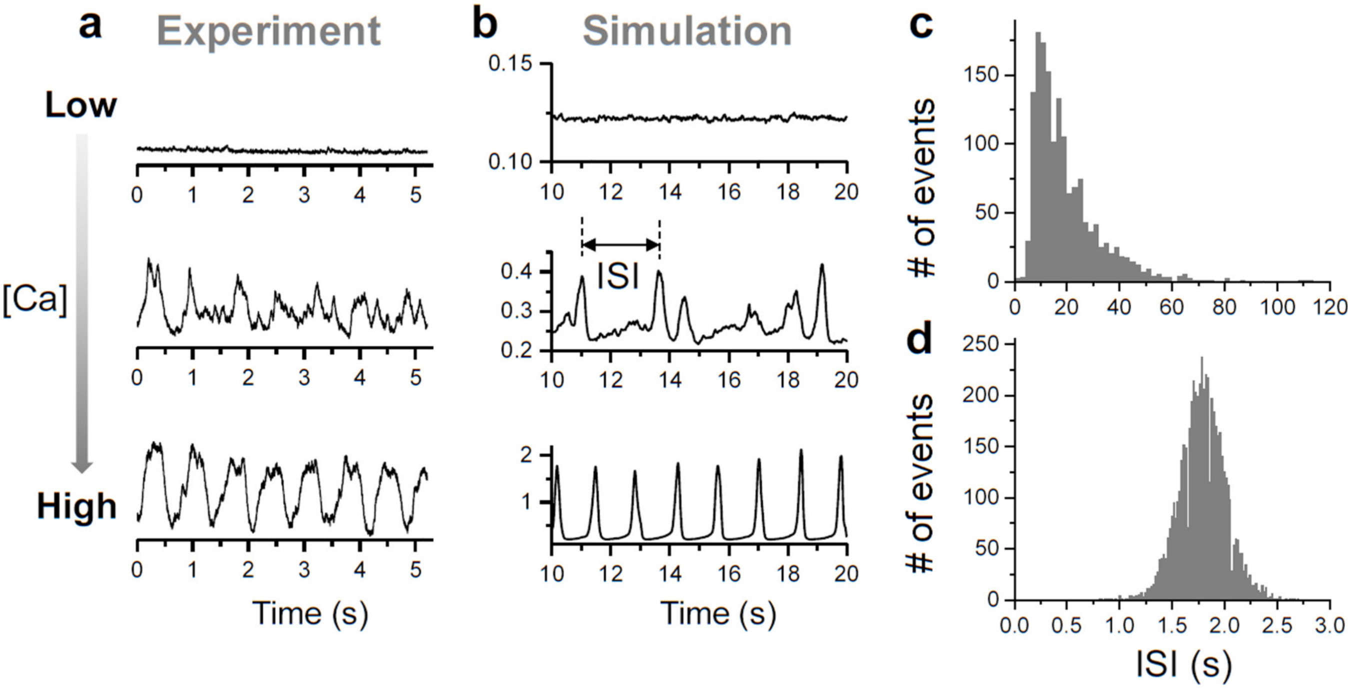

Figure 20. Transition to whole-cell Ca^{2+} oscillations

a. Whole-cell Ca^{2+} concentration versus time for different Ca^{2+} levels recorded from a mouse ventricular myocyte [111]. **b**. Whole-cell Ca^{2+} concentration for different Ca^{2+} levels from a computer model. **c**. Histogram of inter-pulse interval (ISI, defined in panel b) when the system is near the criticality, showing a fat-tail distribution. **d**. Histogram of inter-pulse interval when the Ca^{2+} level is high, showing a Gaussian distribution [226].

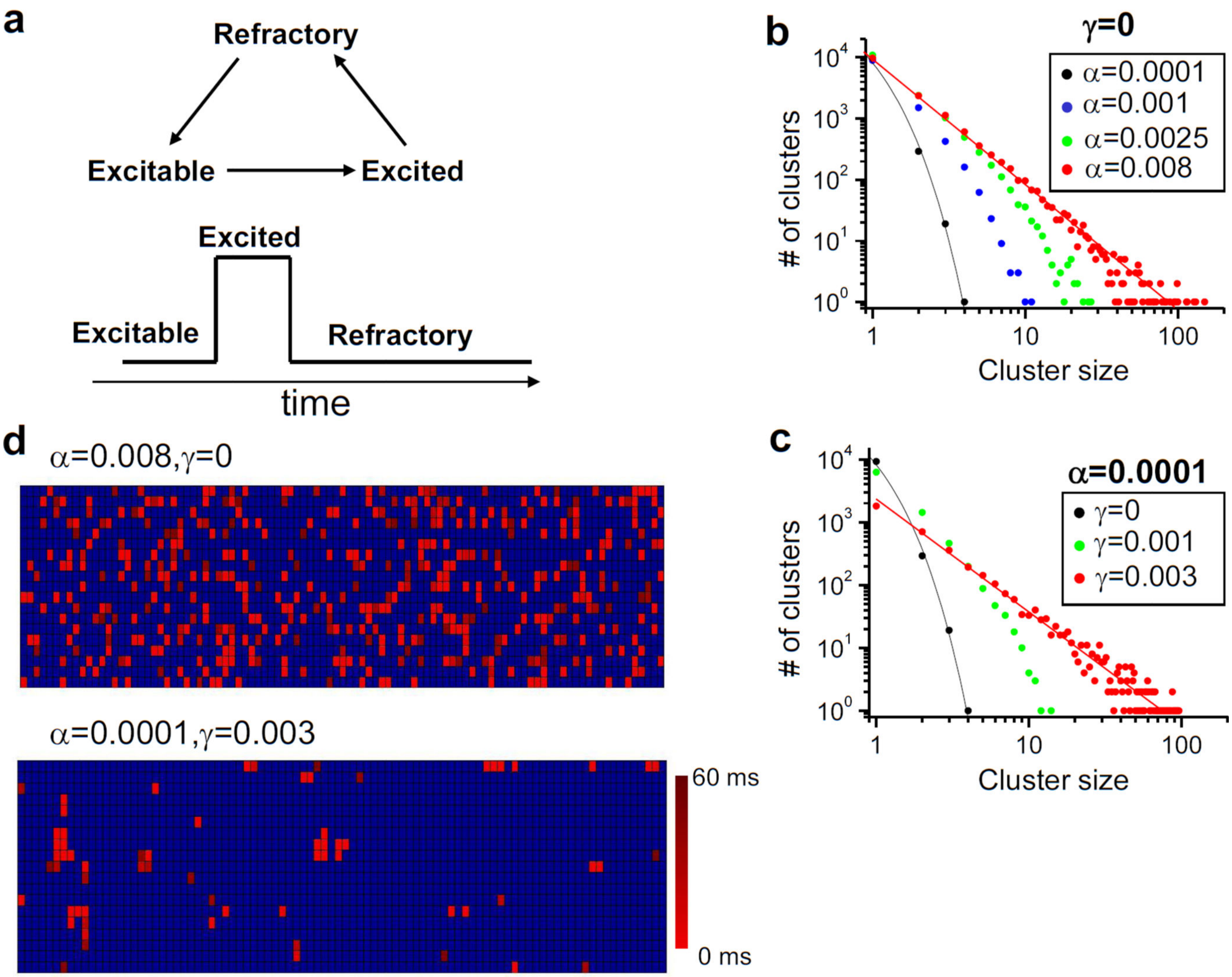

Figure 21. Power-law clustering in an agent-based model

a. Schematics of the three-state model of a CRU. **b**. Cluster-size distributions for different α when the CRUs are uncoupled. **c**. Cluster-size distribution for different γ-values with a small α. **d**. Time-lapse images of 2D slices of the state spaces for the uncoupled (top) and coupled (bottom) systems over a time period equal to the spark duration, both at criticality. The color scale gives the initial time of the spark.

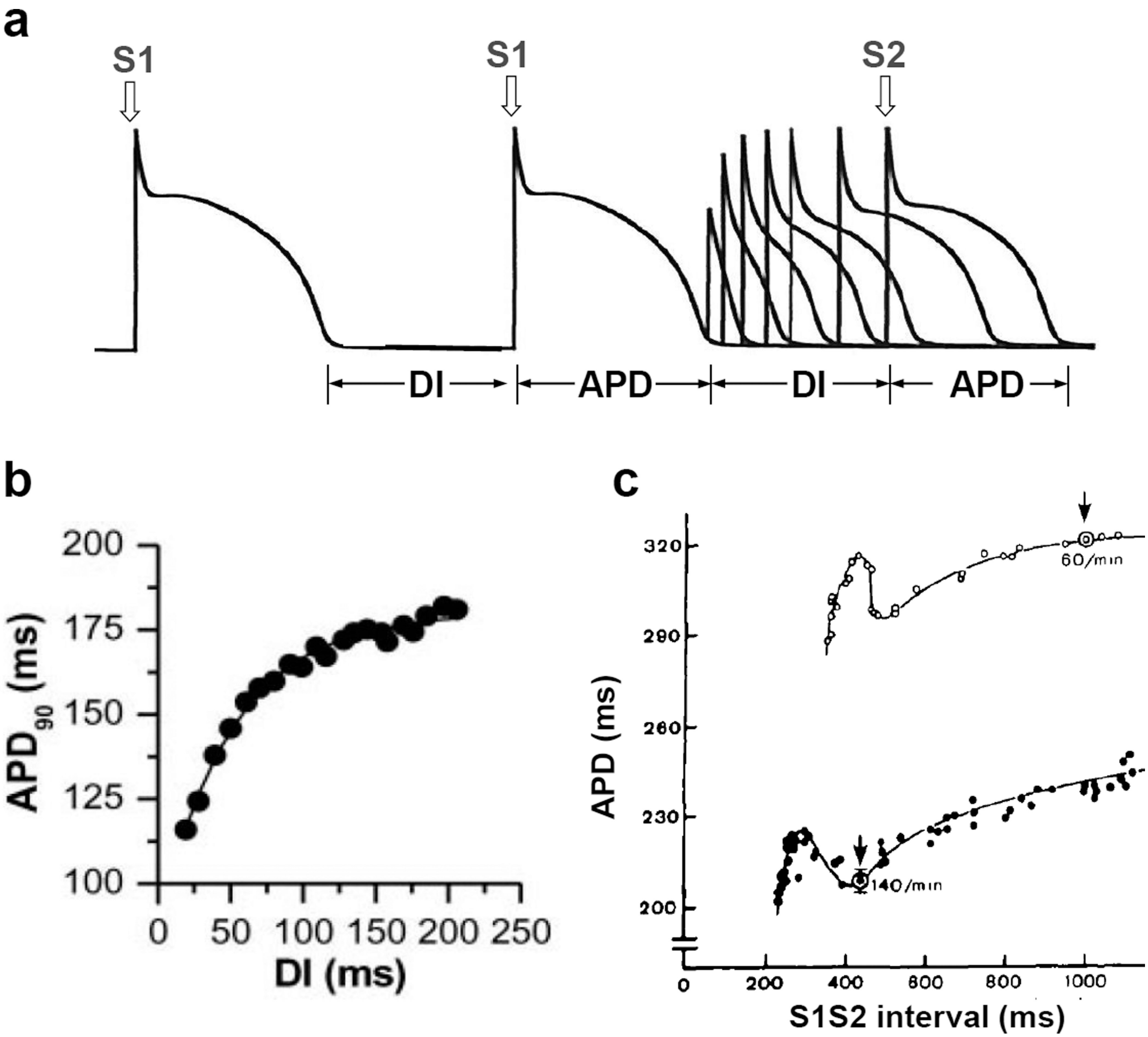

Figure 22. APD restitution

a. The S1S2 protocol: the cell is paced (S1) with a period *T* to a steady state, and then a single stimulus (S2) with a certain S1S2 interval is applied. An S1S2 APD restitution curve is obtained by varying the S1S2 interval and plot the APD of the S2 beat against its preceding DI. **b**. Monotonic APD restitution curve: APD versus DI measured from a rabbit ventricular myocyte [581]. **c**. Non-monotonic APD restitution curve: APD versus S1S2 interval measured from a human heart at two different S1 PCLs, reproduced from Franz et al [238].

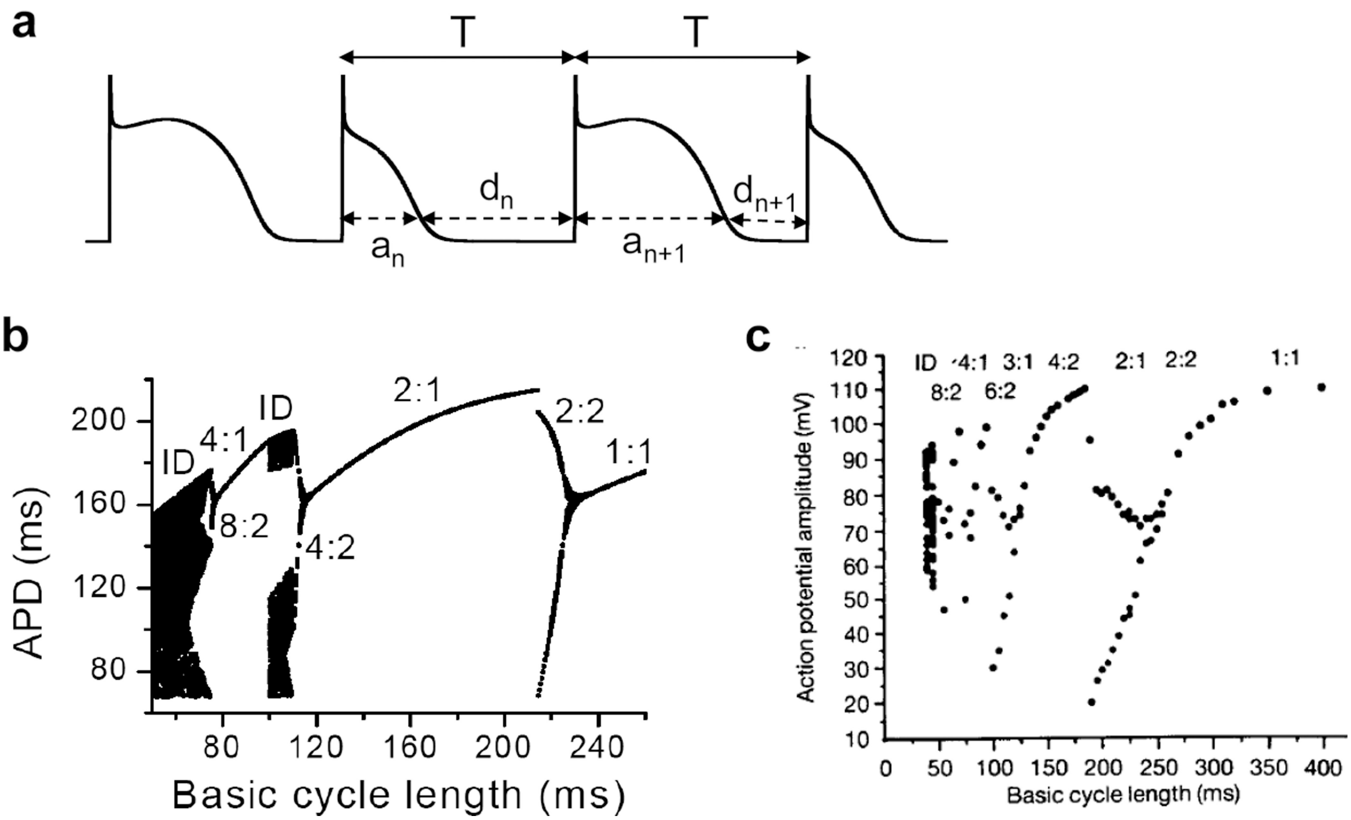

Figure 23. APD alternans and chaos due to steep APD restitution

a. Relationship between APD, DI, and period T under during periodic pacing, i.e., $a_n + d_n = T$. **b**. A bifurcation diagram showing APD versus T (basic cycle length) obtained using Eq. 49 with the APD restitution function: $a_{n+1} = f(d_n) = 220-180e^{-d_n/60}$. The bifurcation sequence shows: 1:1 → 2:2 → 2:1 → 4:2 → ID → 4:1 → 8:2 → ID. "ID" stands for irregular dynamics or dynamical chaos. For each PCL, the first 40 APDs are discarded and the next 100 APDs are plotted. In the alternans (2:2) regime, there are only two APD values though 100 APDs are plotted, however, in the chaotic regime, the values of the 100 APDs are all different, resulting in scattered plots. Stimulation failure was assumed when DI<10 ms. **c**. A bifurcation diagram showing the relationship between the basic cycle length of pacing and beat-to-beat action potential amplitudes in a sheep cardiac Purkinje fiber, reproduced from Chialvo et al [58]. The observed bifurcation sequence is: 1:1 → 2:2 → 2:1 → 4:2 → 3:1 → 6:2 → 4:1 → 8:2 → ID.

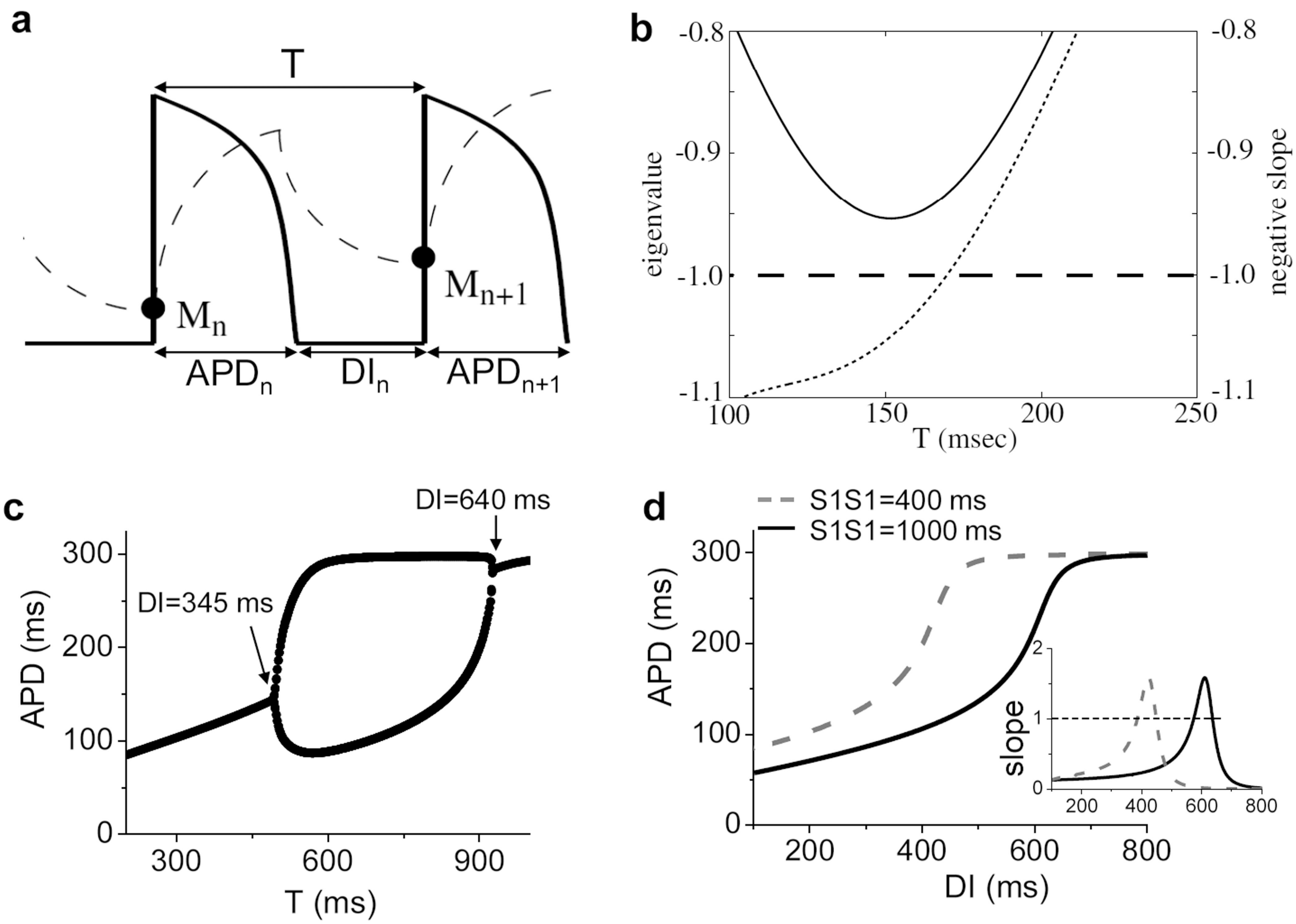

Figure 24. Effects of cardiac memory on APD alternans

a. Schematic plot showing the relation between APD, DI, and the memory variable M. **b**. The eigenvalue of the return map model (solid) and the negative slope of the APD restitution curve (dotted) at the fixed point versus T. Dashed line marks -1. **c**. APD versus PCL (*T*) from model in the presence of I_{to}. **d**. APD restitution curves of two different S1 PCLs from the same model as in c. Inset are the slopes of the two restitution curves. Panels a and b were reproduced from Fox et al [63], and panels c and d from Qu et al [249].

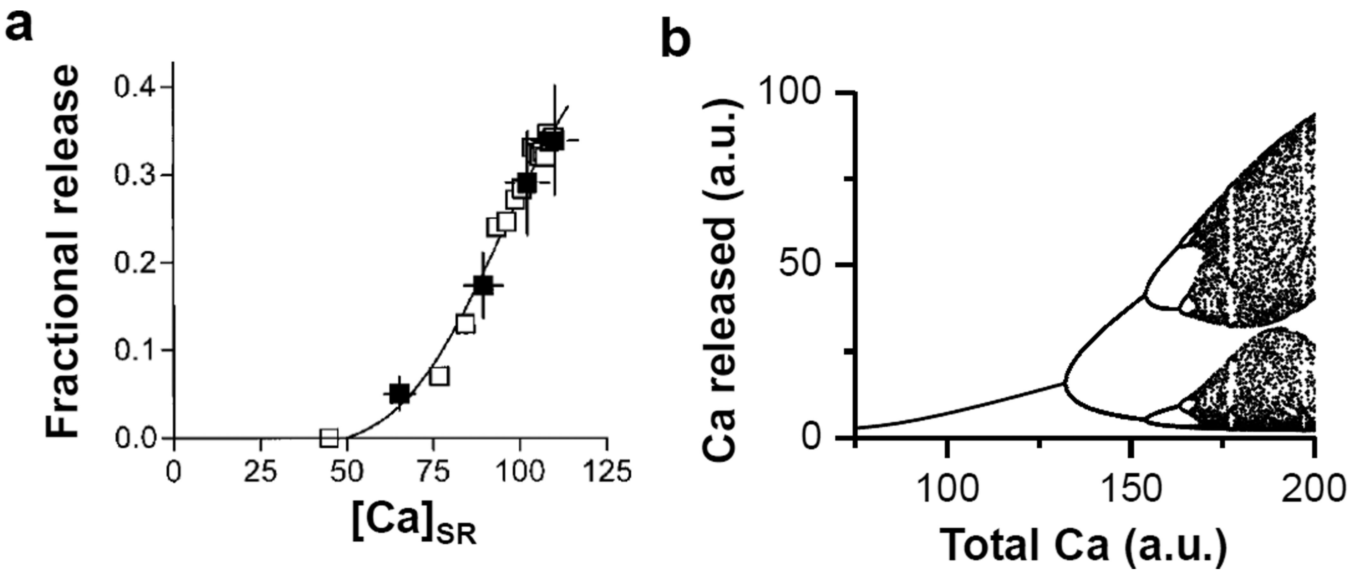

Figure 25. Steep fractional SR Ca^{2+} release and Ca^{2+} alternans

a. A fractional SR Ca^{2+} release curve measured from experiments, reproduced from Shannon et al [273]. The *x*-axis is the Ca^{2+} content in the SR and the *y*-axis the amount of Ca^{2+} released from the SR. **b**. Bifurcation showing Ca^{2+} released from the SR versus total Ca^{2+} in the cell using the iterated model Eq.53.

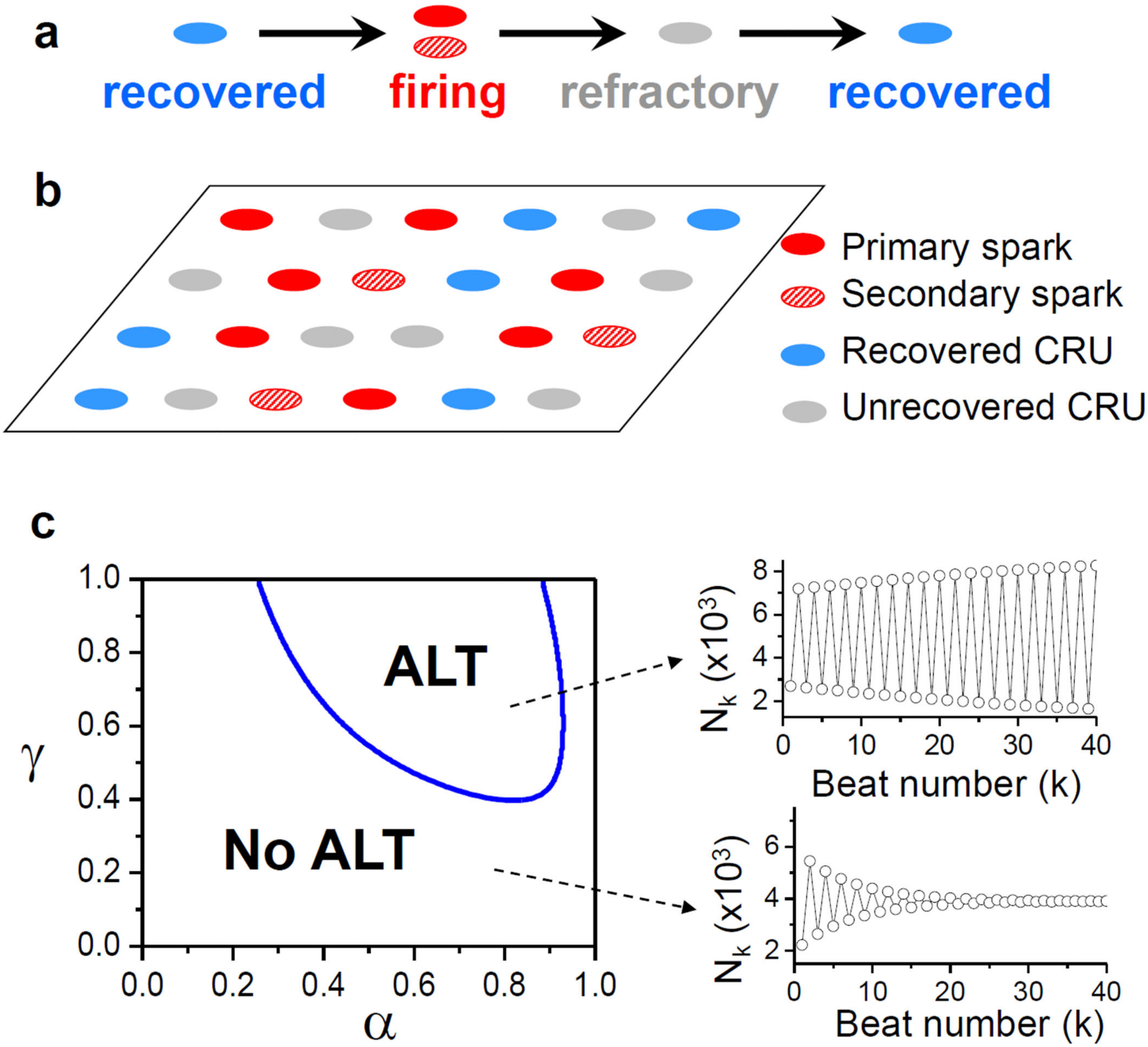

Figure 26. The mean-field theory of alternans

a. The transition between three CRU states: recovered, firing, and refractory. **b**. Schematic plot of a spatial distribution of CRUs in different states. **c**. Left: phase diagram showing alternans (ALT) region and no alternans (NO ALT) region in the α-γ parameter space with β=0.98 obtained from the iterated map model (Eq.57). Upper right: number of sparks versus beat number for a set of parameters in the alternans region. Lower right: number of sparks versus beat number for a set of parameters in the no alternans region.

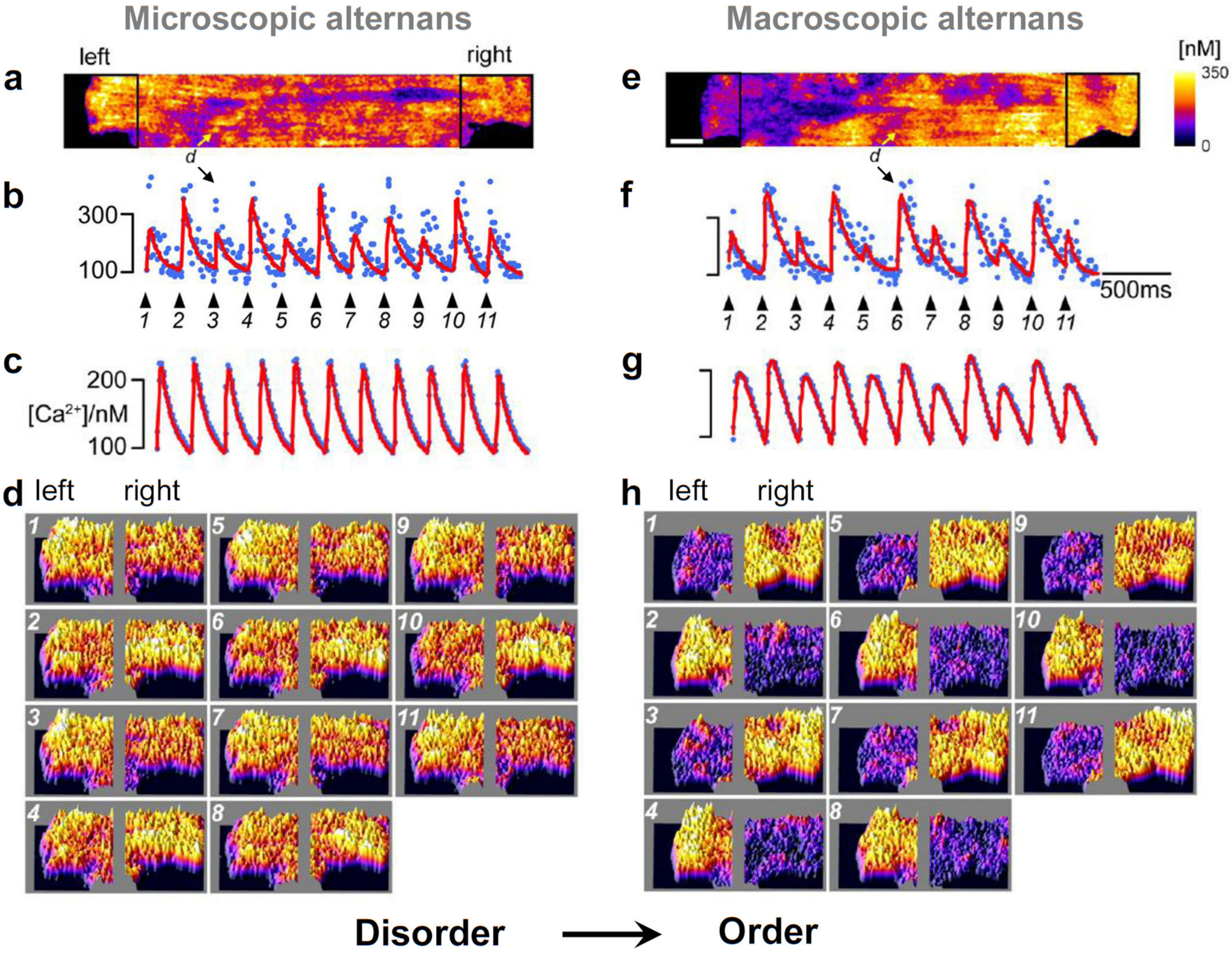

Figure 27. From microscopic to macroscopic alternans (from disorder to order)

a–d. Microscopic alternans without macroscopic alternans at a slower pacing rate. **a**. A snapshot of Ca^{2+} in a ventricular myocyte. **b**. Ca^{2+} recorded from one location (marked as "d') in the cell. **c**. Whole-cell Ca^{2+}. **d**. Snapshots of Ca^{2+} from the left and right ends of the cell. **e–h**. Microscopic alternans leads to macroscopic alternant at a faster pacing rate. The panels are the same as a–d. Panels were modified from Tian et al [271].

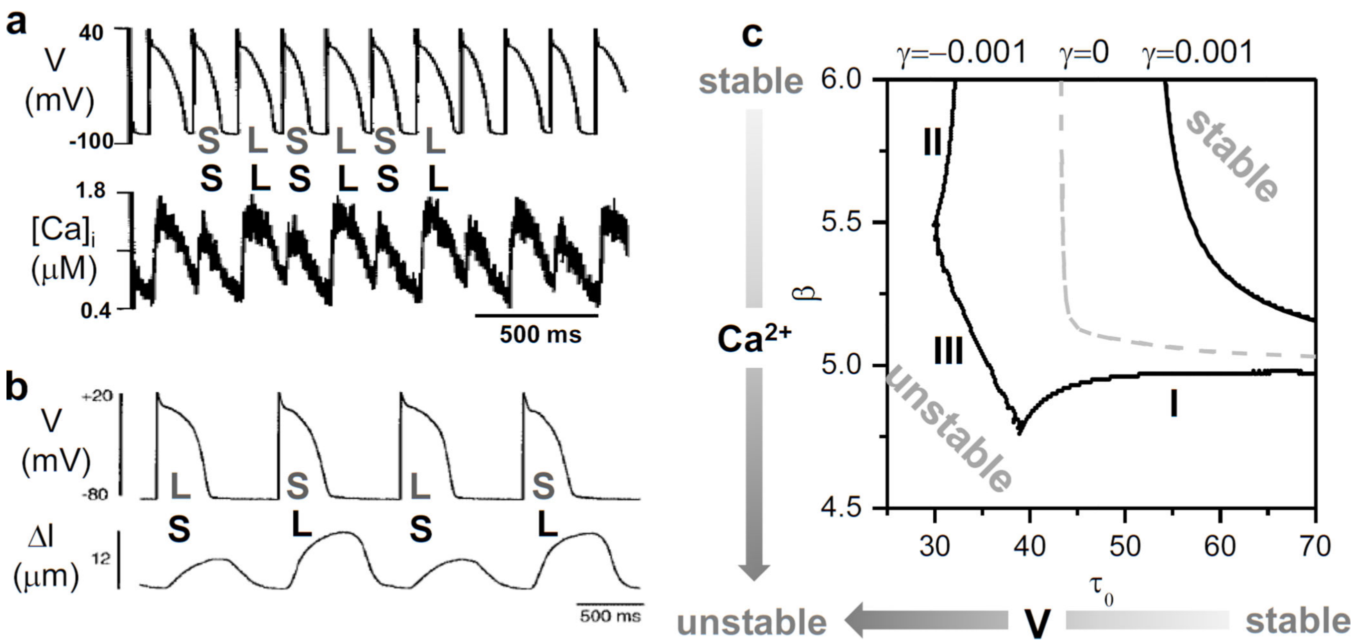

Figure 28. Alternans dynamics due to voltage and Ca^{2+} coupling

a. Voltage and Ca^{2+} versus time from a paced rabbit ventricular myocyte showing concordant APD and Ca^{2+} alternans in which a long ("L") APD associates with a large ("L") Ca^{2+} and a short ("S") APD associates with a small ("S") Ca^{2+} (modified from Chudin et al [264]). **b**. Voltage and cell length change of a cat ventricular myocyte showing discordant APD and contraction alternans in which a long APD associates with a small contraction and a short APD associates with a large contraction (modified from Huser et al [280]). **c**. Phase diagram obtained from the iterated map (Eq.59) for Ca^{2+}-to-APD uncoupled (γ=0), positive Ca^{2+}-to-APD coupling (γ>0), and negative Ca^{2+}-to-APD coupling (γ<0). The stabilities of the Ca^{2+} system and the voltage system decrease along the arrows.

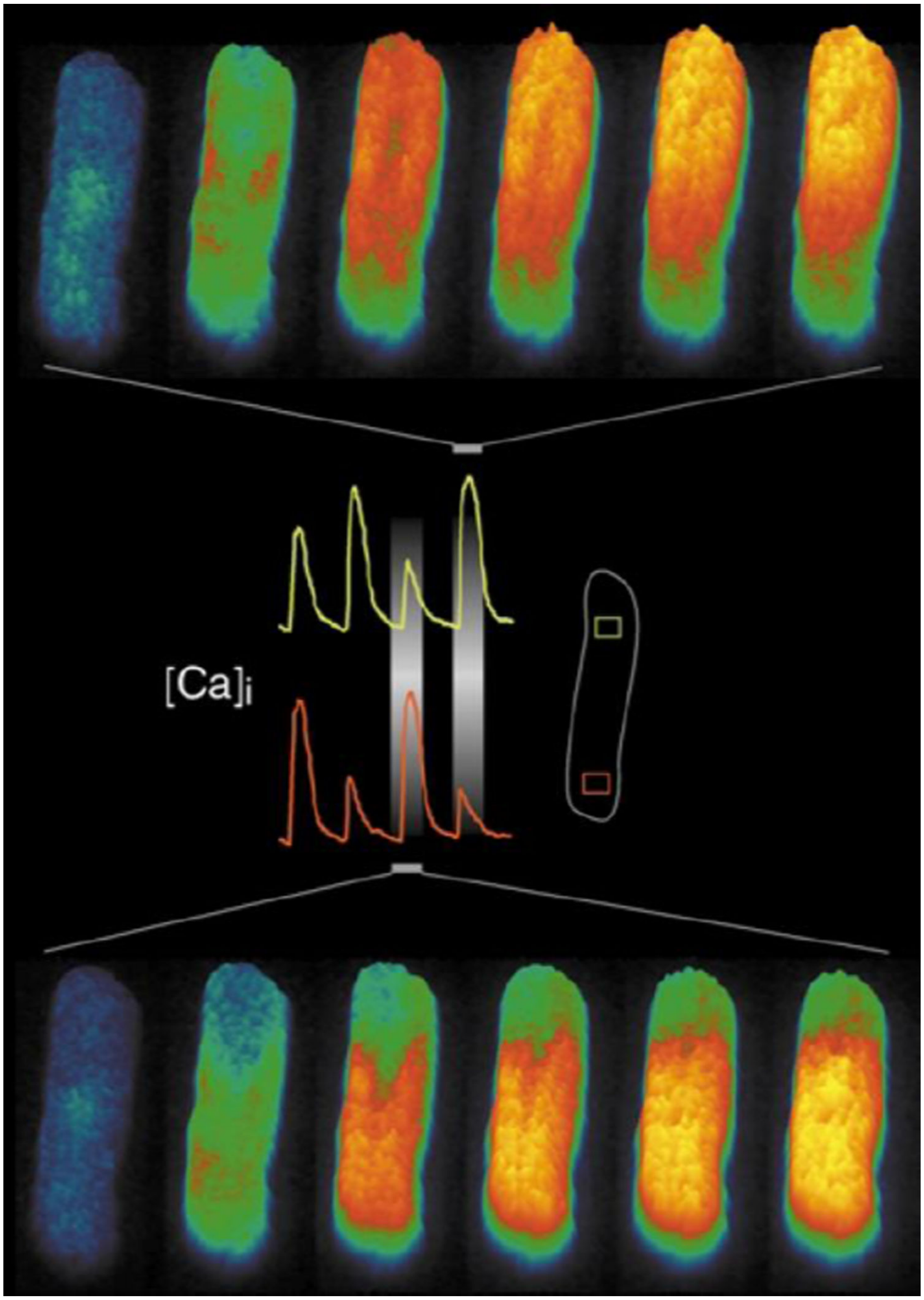

Figure 29. Sub-cellular Ca^{2+} alternans

Snapshots (33 ms apart) of Ca^{2+} in a cat atrial myocyte for two consecutive beats as marked. The Ca^{2+} alternans in the top and bottom regions of the cell are out-of-phase, forming spatially discordant Ca^{2+} alternans (reproduced from Blatter et al [299]).

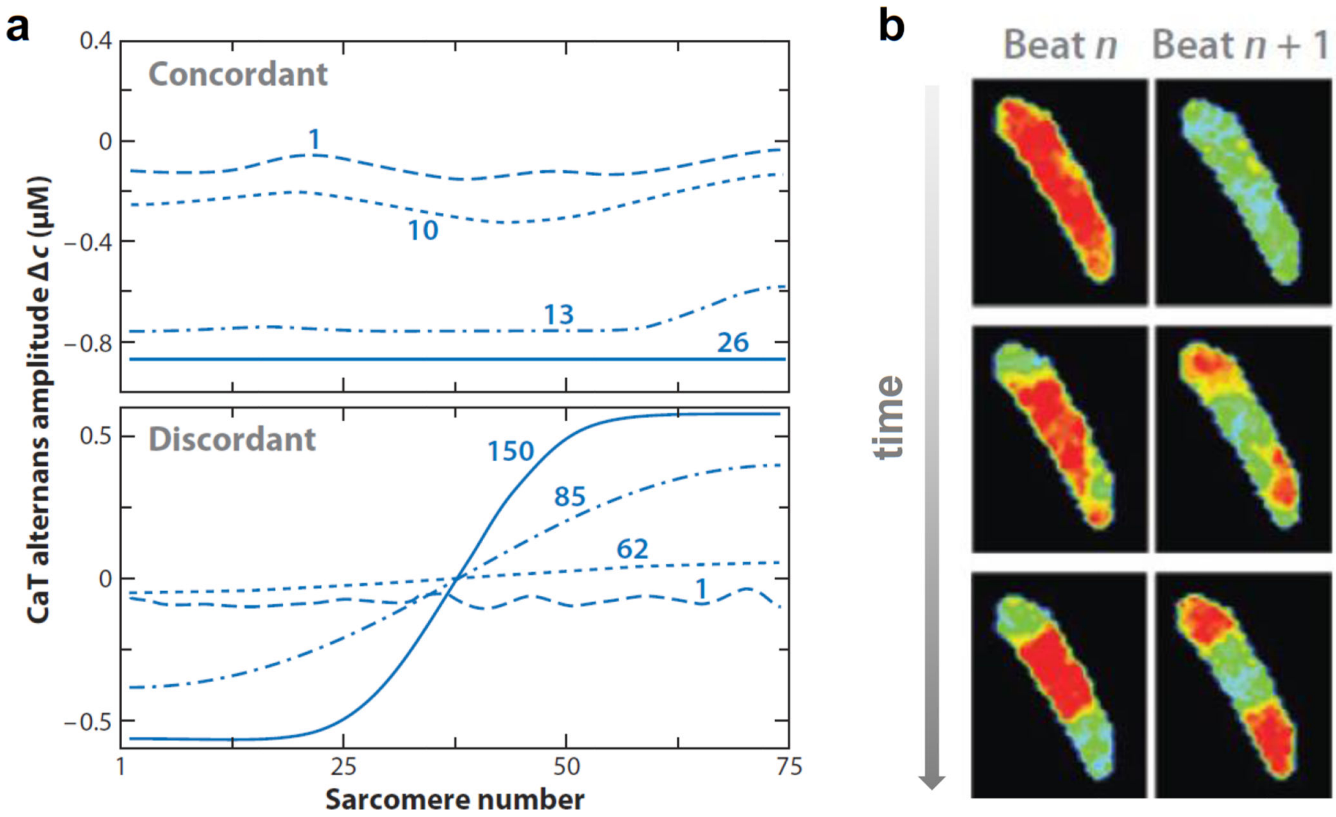

Figure 30. Turing instability induced sub-cellular discordant Ca^{2+} alternans (modified from Karma [7])

a. Computer simulations showing concordant Ca^{2+} alternans develops when the Ca^{2+}-to-APD coupling is positive (upper) but discordant Ca^{2+} alternans develops when the Ca^{2+}-to-APD coupling is negative [300]. **b**. Optical images from two consecutive beats in a guinea pig ventricular myocyte showing a transition from concordant to discordant Ca^{2+} alternans after a feedback control algorithm was turned on to change the APD-to-Ca^{2+} coupling from positive to negative [270].

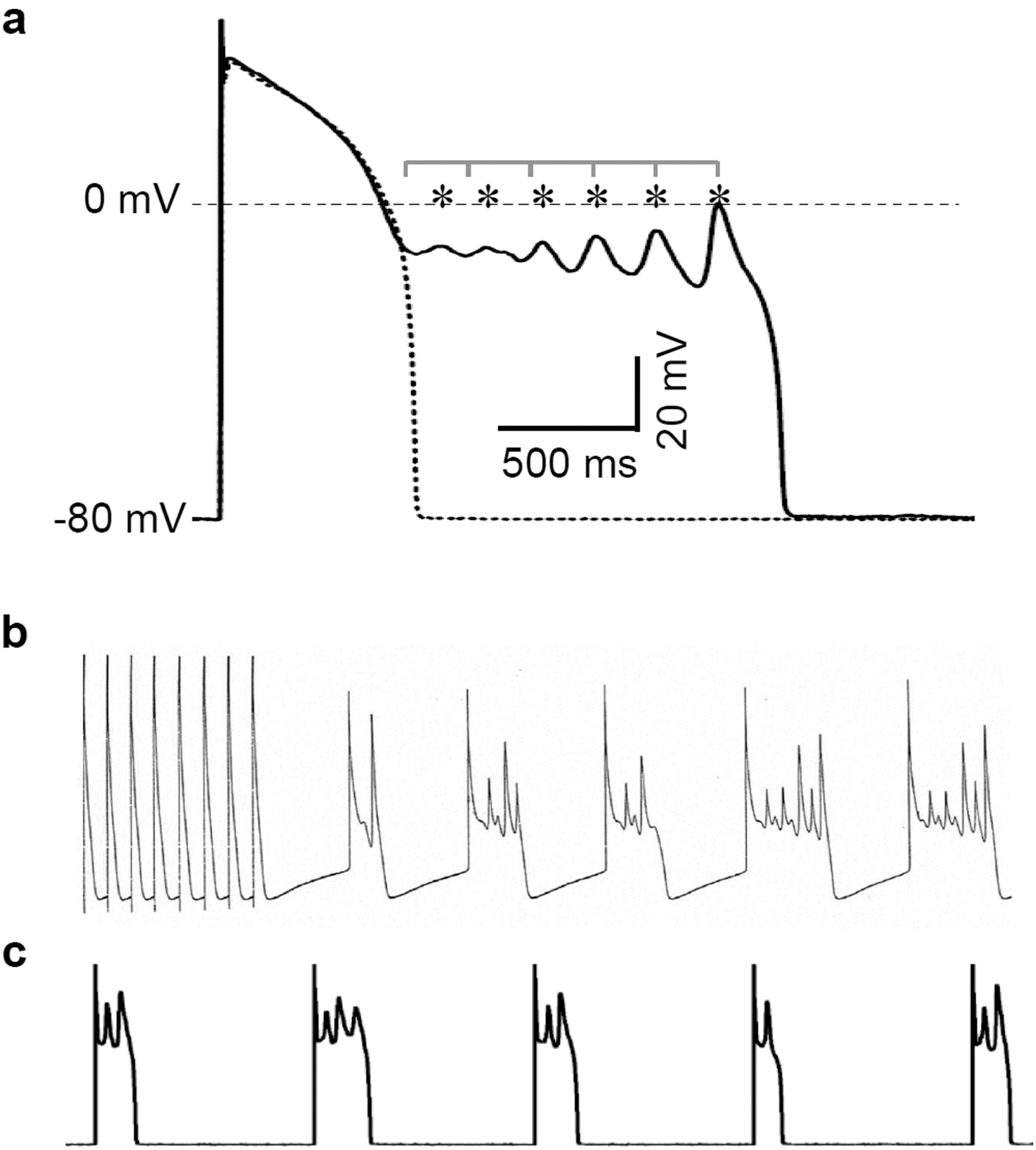

Figure 31. EADs and their irregular dynamics

a. Action potentials recorded from a ventricular myocyte of transgenic long QT rabbit heart before (dashed) and after (solid) isoproterenol [311]. **b**. EADs recorded from a dog Purkinje fiber (Courtesy of Robert Gilmour). **c.** EADs recorded from an isolated rabbit ventricular myocyte [323].

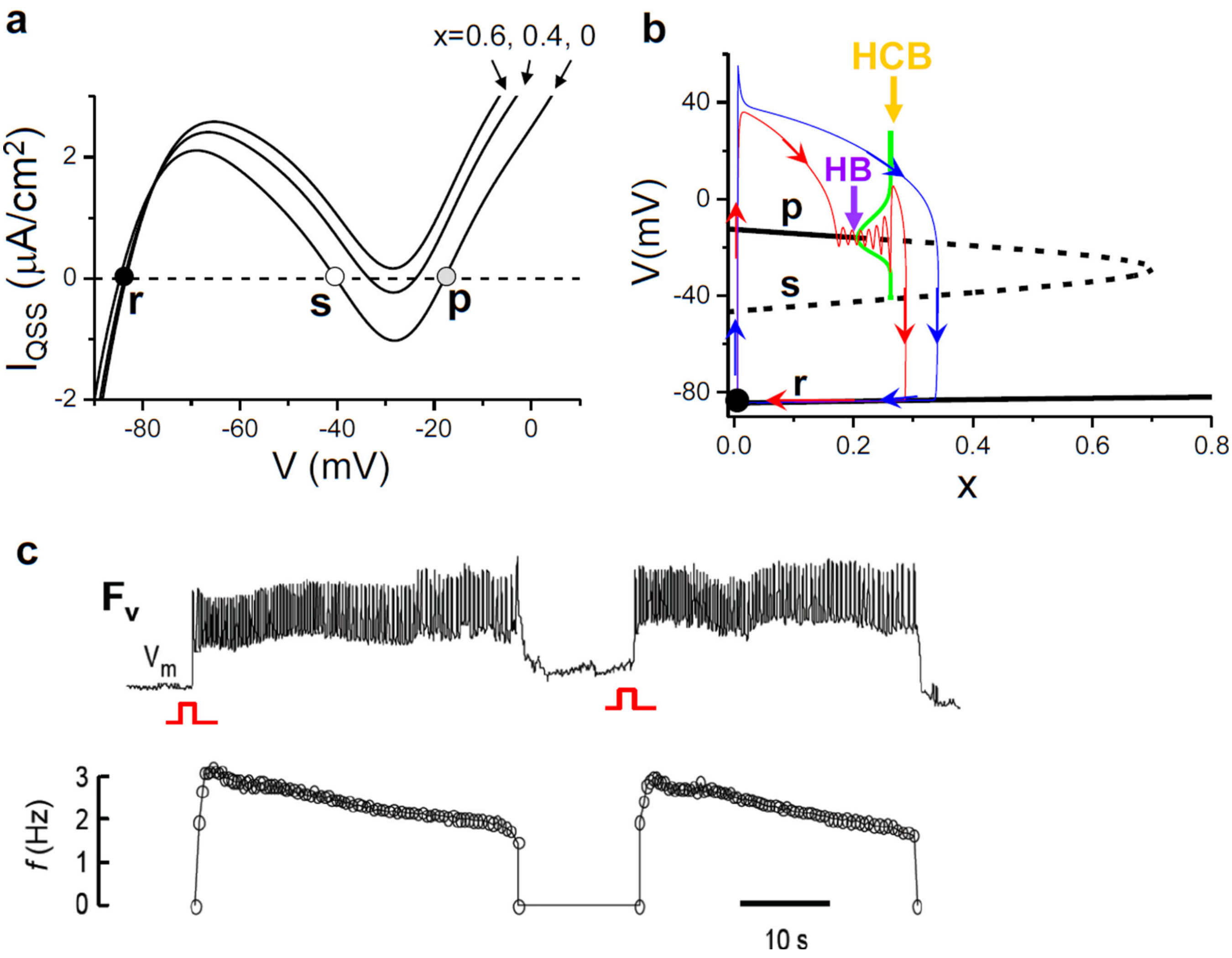

Figure 32. Dynamical mechanisms of EADs

a. Quasi-steady state I–V curves for different *x* values using Eq.63. r, s and p are the three quasi-steady states. **b**. The stability of the r, s and pstates and the Hopf (HB) and homoclinic (HCB) bifurcations versus *x* [322]. The green line is the oscillation amplitude. The blue and the red lines are two action potentials from the original model with different activation time constants of *x*. Arrows along these lines indicate the directions of time. **c**. Experimental recording shown frequency reduction during EAD bursting [324].

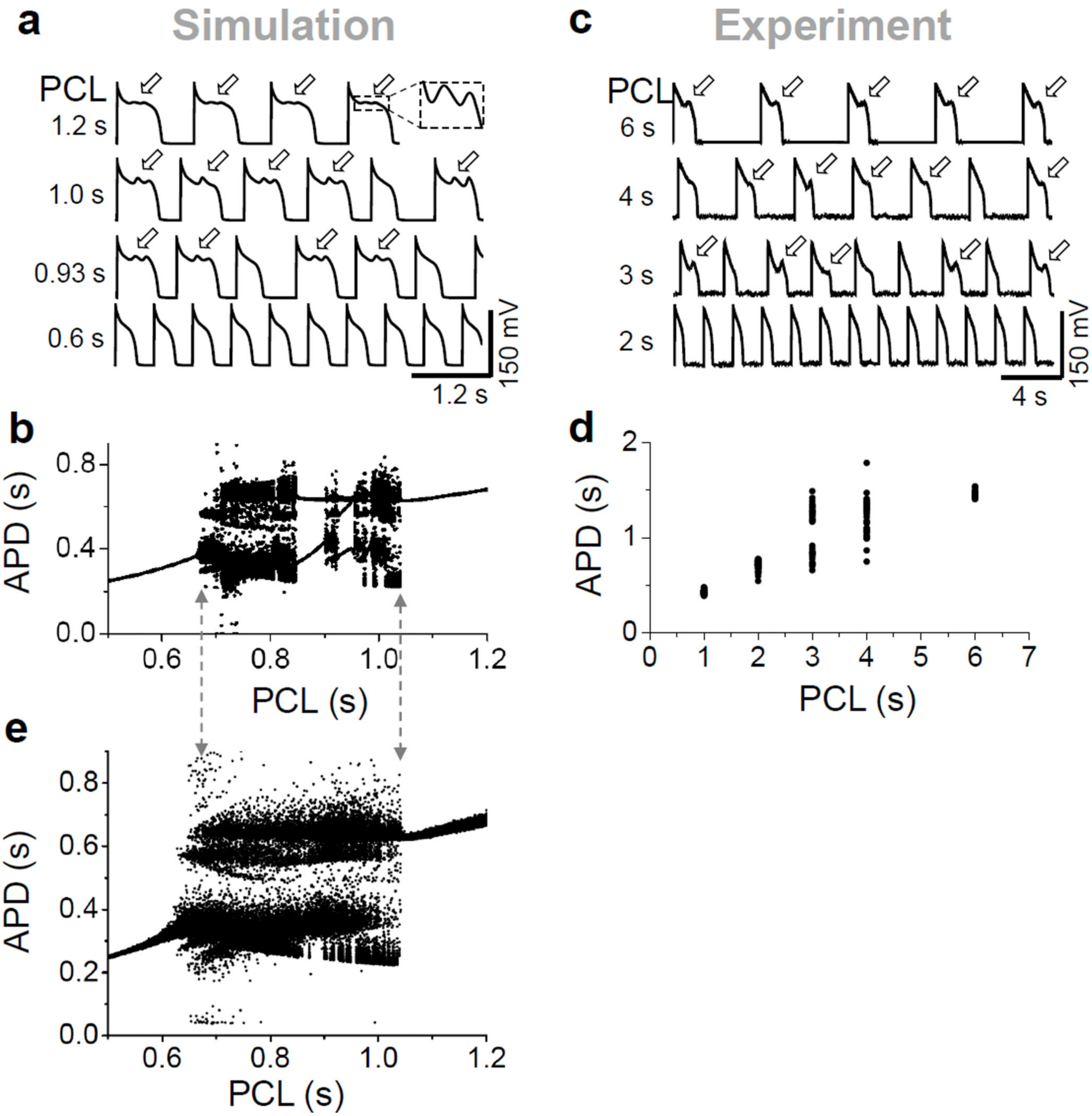

Figure 33. Chaotic dynamics of EADs

a and **b**. Action potentials at different PCL and the bifurcation diagram from a computer model. **c** and **d**. Action potentials at different PCL and the bifurcation diagram from a real myocyte under H_2O_2 stress. Open arrows in a and c indicate EADs in the action potentials. **e**. Same as b but in the presence of channel noise.

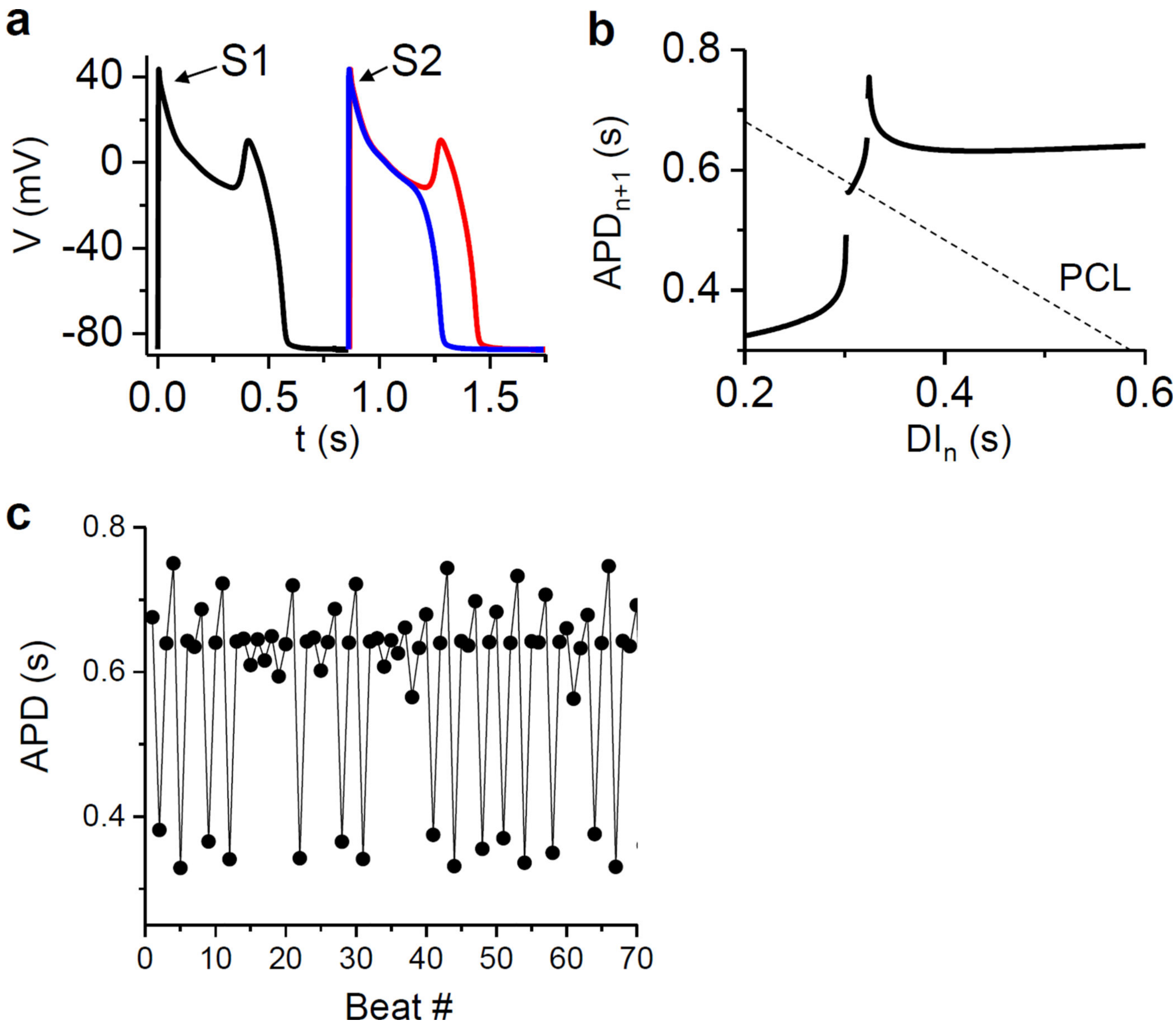

Figure 34. Mechanisms of EAD chaos

a. Action potentials during S1S2 pacing. A 1 ms difference in DI results in two different action potentials, demonstrating the sensitivity of APD on DI. **b**. APD versus DI. **c**. APD versus iteration number showing chaos.

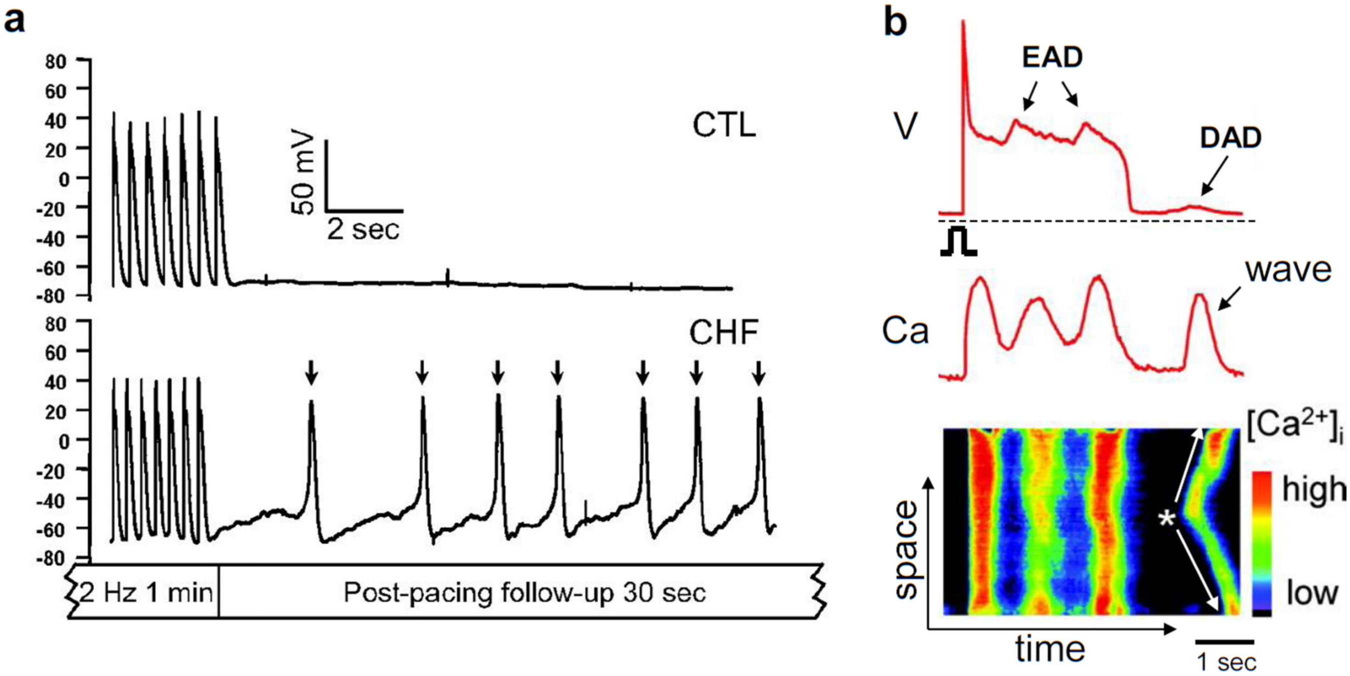

Figure 35. Ca^{2+} waves and DADs in cardiac cells

a. Voltage traces showing pacing induced DADs in HF (indicated by arrows), but not in the normal cell, reproduced from Yeh et al [332]. **b**. A Ca^{2+} wave-induced DAD in a ventricular myocyte, shown by voltage (upper), whole-cell Ca^{2+} concentration (middle), and line scan of Ca^{2+} (bottom). Asterisk and the while arrows indicate the origin and propagation of the Ca^{2+} wave. Reproduced from Xie et al [333].

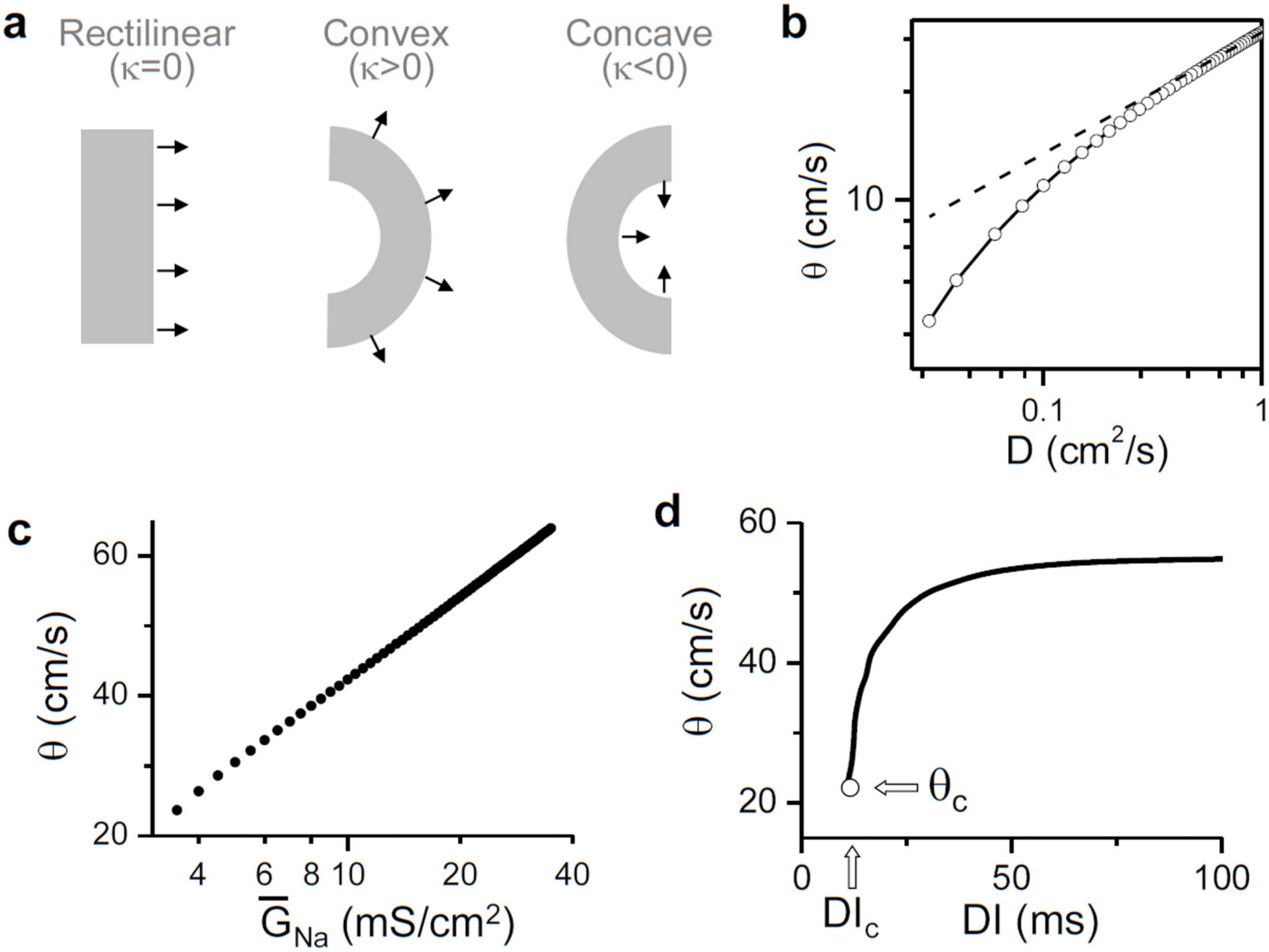

Figure 36. Conduction in cardiac tissue

a. Schematic plot of a rectilinear wave, a convex wave, and concave wave. **b**. CV versus diffusion constant for a discretized system (Δx=125μ m). Dashed line is the continuous limit that $\theta \propto \sqrt{D}$ which is a straight line in a log-log plot. **c**. CV versus the maximum conductance ($\overline{G_{Na}}$) of the Na^+ current. **d**. A CV restitution curve. θ_c is the minimum CV and DI_c is the corresponding DI.

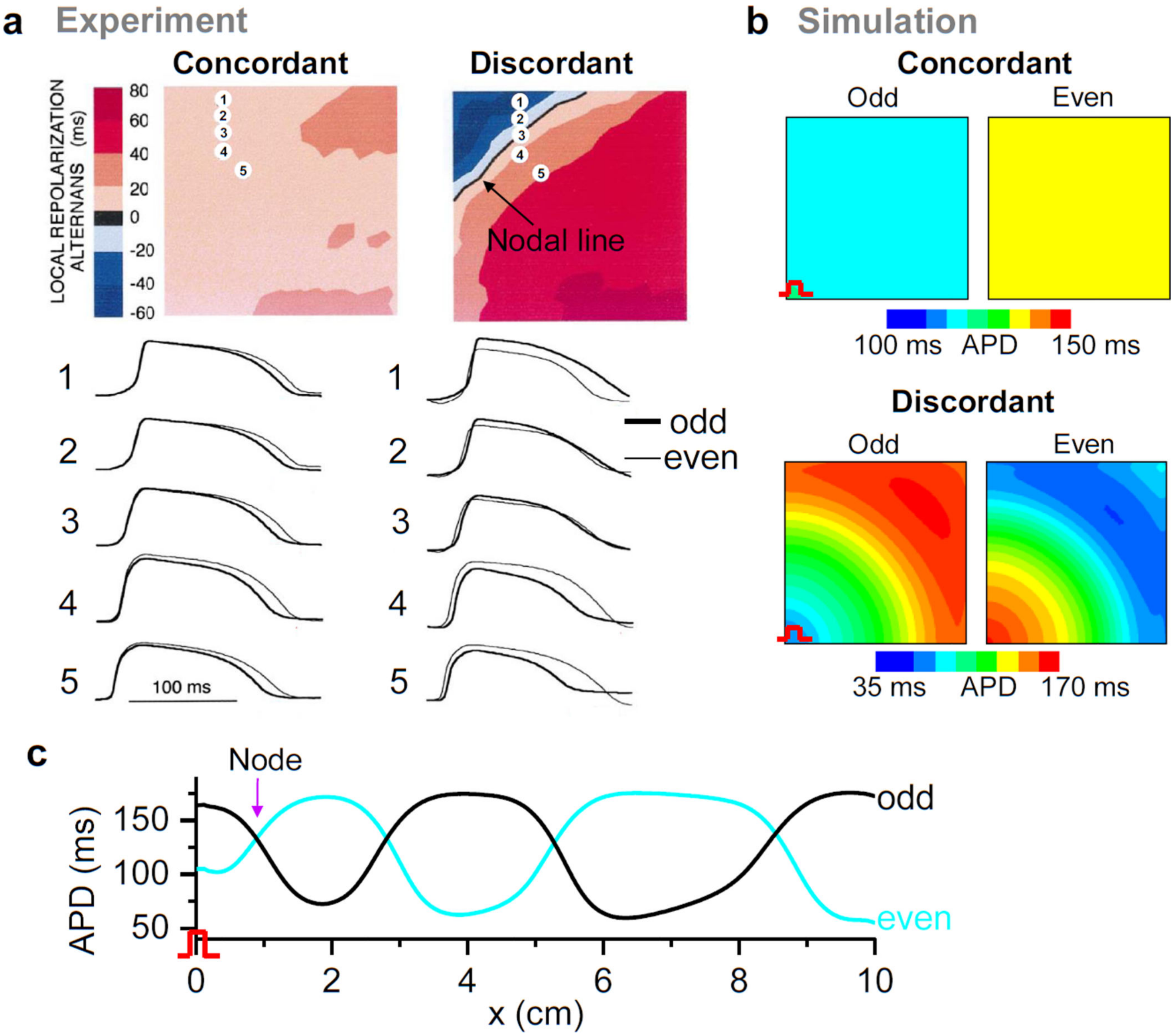

Figure 37. Spatially concordant and discordant APD alternans

a. Spatially concordant and discordant APD alternans in a guinea pig heart, reproduced from Pastore et al [64]. Upper: Alternans magnitude ($\Delta a=a_{n+1}-a_n$) distribution in space; Lower: sample action potential recordings for two consecutive beats from the sites marked on the upper panel. For concordant APD alternans, the color is uniform in space (Δa is positive everywhere in one beat and negative in the following beat). For discordant APD alternans, the color is no longer uniform in space, but changes from one to the other (Δa changes from negative to positive as the color changes from blue to red in space; the color map reverse in the following beat). **b**. Spatially concordant (upper) and discordant (lower) alternans from computer simulations [65]. Shown are APD distributions in space for two consecutive beats. The tissue was periodically paced at the left-lower corner. **c**. Discordant APD alternans from a simulation of a 10 cm 1D cable.

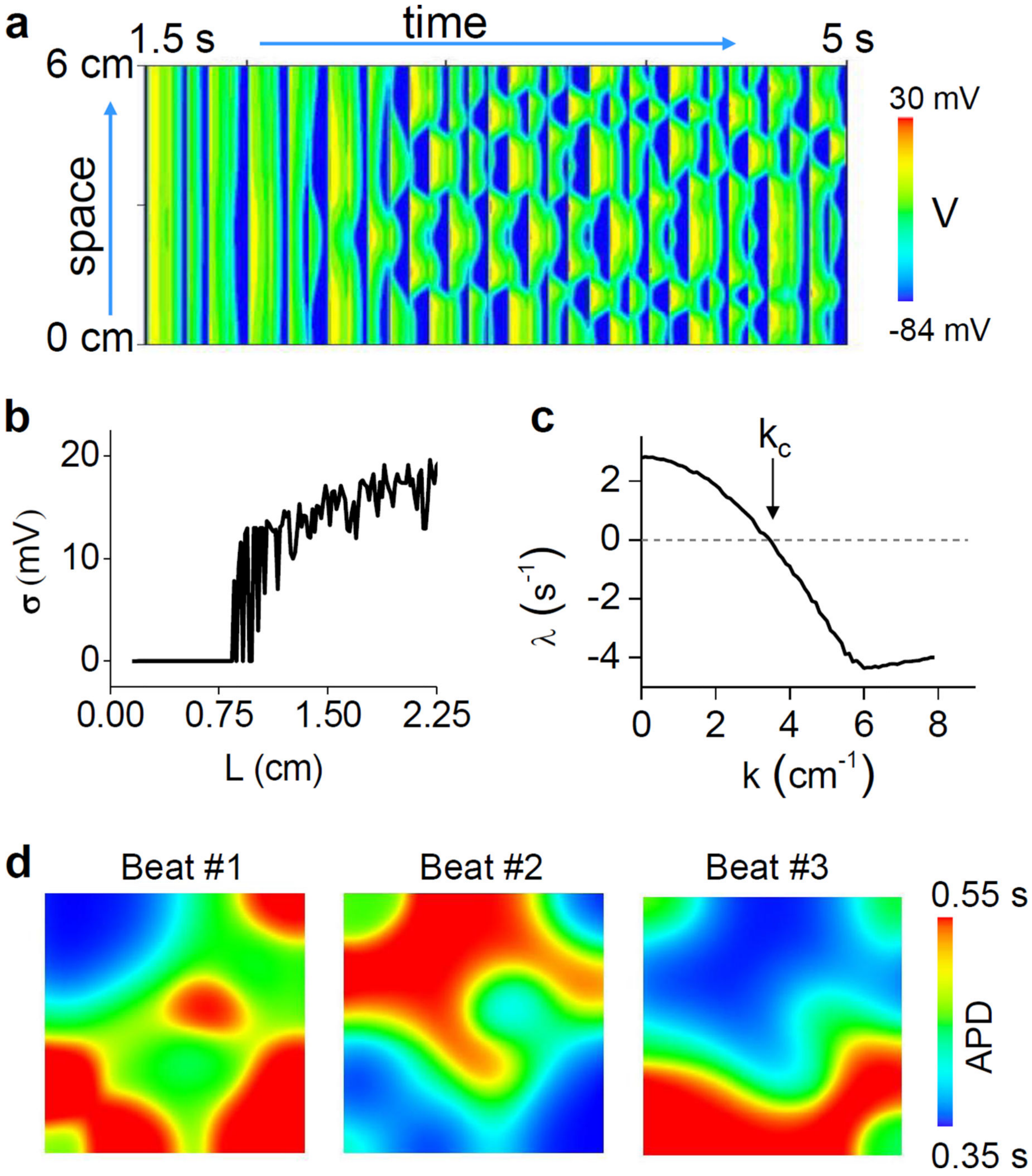

Figure 38. Chaos synchronization in cardiac tissue

a–c. Chaos synchronization in a tissue model with fast pacing-induced chaos. **a**. Time-space plot of voltage of a 1D homogeneous cable (L=6 cm) of coupled myocytes under periodic pacing. All myocytes were identically paced with T=100 ms and started with roughly the same initial condition at t=0. The myocytes were modeled by the Beeler-Reuter model [130] with modifications [242]. **b**. Average standard deviation (<σ>) of voltage versus the cable length L. <σ> was defined as: $<\sigma>=\lim_{D\to\infty}\frac{1}{D-T_0}\int_{T_0}^{D}dt\sqrt{\int_0^L[V(x,t)-\overline{V}(t)]^2dx/L}$, where V^-

(t) is average voltage over the whole cable at time t, T_0 is a time after the transient, and L is the length of the cable. Synchronization therefore occurs when <σ> approaches zero. **c**. The maximum Lyapunov exponent (λ) versus wave number k calculated using the single cell model, which can well predict the critical cable length at which chaos desynchronization occurs. **d**. Chaos synchronization in a tissue model with the presence of EADs. APD distributions for three consecutive beats in a homogeneous 2D tissue (4.5 cm × 4.5 cm) with stimuli applied uniformly at the left edge of the tissue. Islands of long APD (with EADs) surrounded by regions with short APD (without EADs) develop as a result of the spatial instabilities via chaos desynchronization due to chaotic EAD dynamics [166].

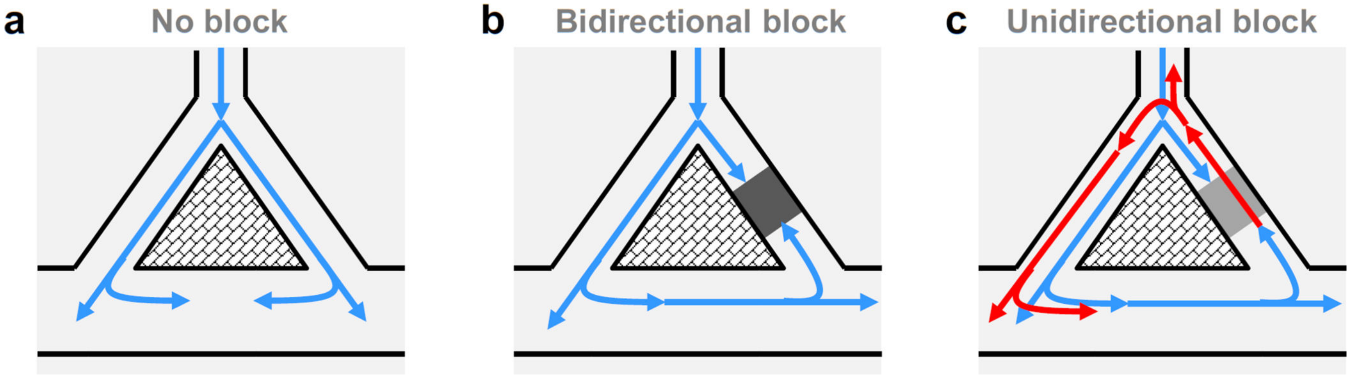

Figure 39. Induction of reentry around an obstacle

a. A PVC successfully propagates through both sides of the obstacle with no conduction block. **b**. A PVC is blocked in the right pathway and the one from the left is also blocked in the right pathway. **c**. A PVC is blocked in the right pathway but the one from the left successfully propagates through the right pathway, forming a reentry around the obstacle.

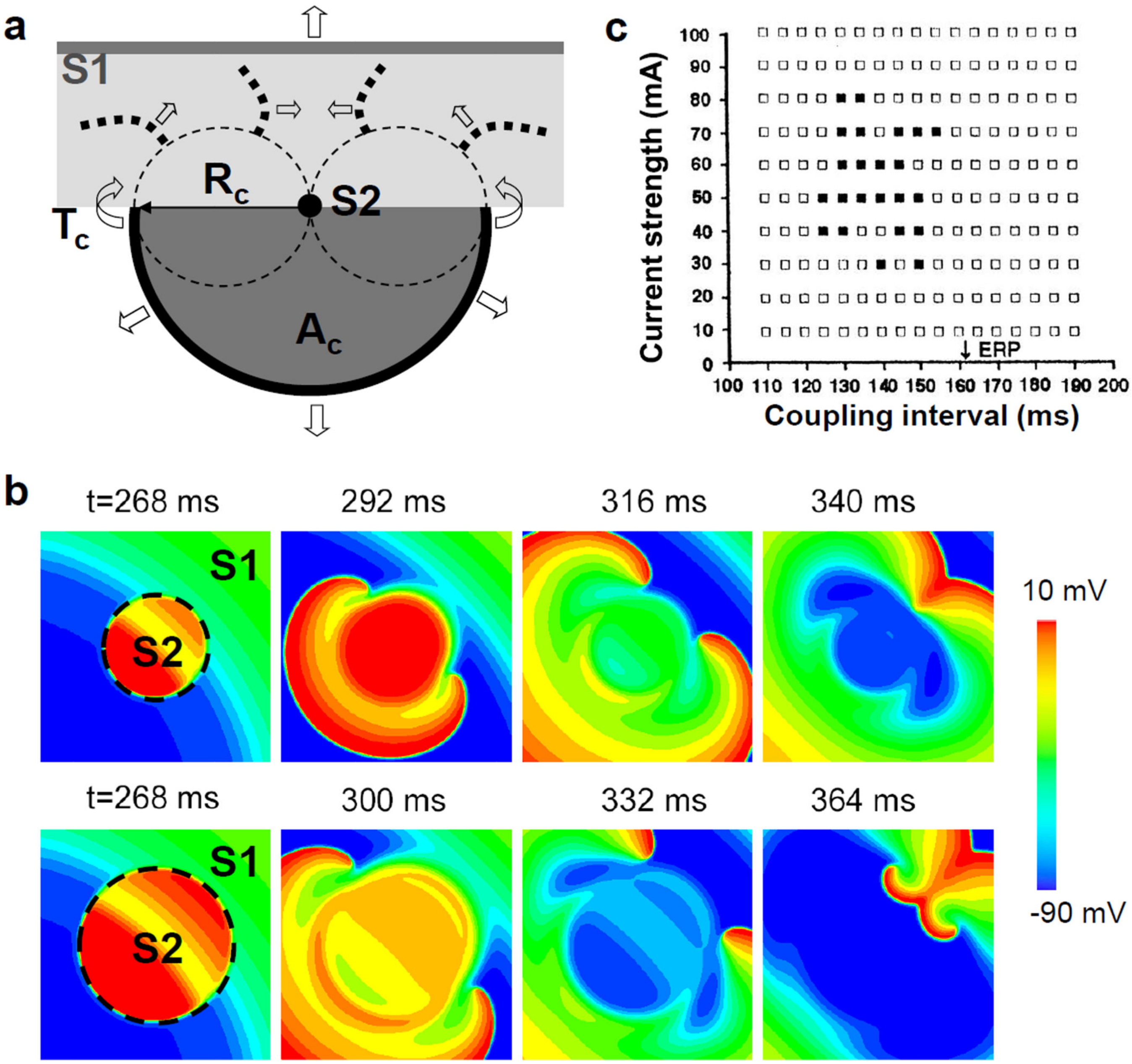

Figure 40. Induction of reentry by a strong stimulus

a. Winfree's pinwheel experiment where S1 is a planar wave propagating upward and S2 is delivered at a critical time (T_c) from a point electrode which depolarizes a critical circular domain (A_c) with a critical radius (R_c). Two singularities are generated at the intersection of the circle's edge with the waveback of S1, which turn inwards to form two spiral waves and figure-of-eight reentry. **b**. Computer simulations showing that an S2 with a smaller area of depolarization results in two phase singularities but no reentry, but an S2 with a larger area of depolarization successfully induces figure-of-eight reentry. **c**. Vulnerable widow (black squares) versus stimulus strength and S1S2 interval, obtained from experiments (reproduced from Gotoh et al [371]).

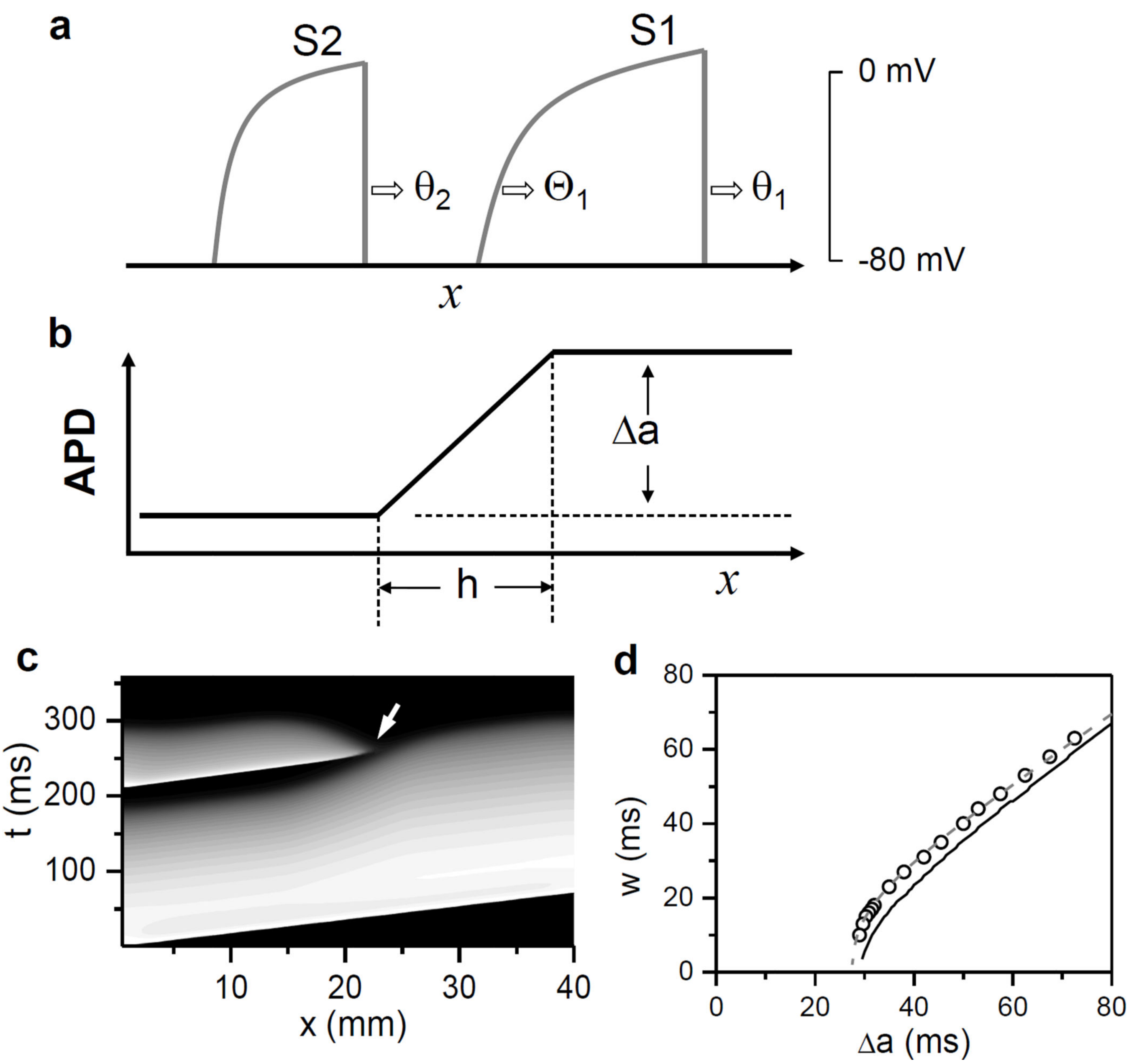

Figure 41. Unidirectional conduction block in heterogeneous tissue

a. A schematic plot showing an S1 wave followed by an S2 wave in a 1D cable. **b**. A schematic plot of an APD gradient in space. **c**. Space-time plot of voltage (in a gray scale) showing S2 block in 1D heterogeneous cable. Pacing stimuli are applied at x=0. Arrow indicates the location at which the S2 wave blocked. **d**. Vulnerable window (w) versus Δa from computer simulations (symbols) and from the theory (Eq.88).

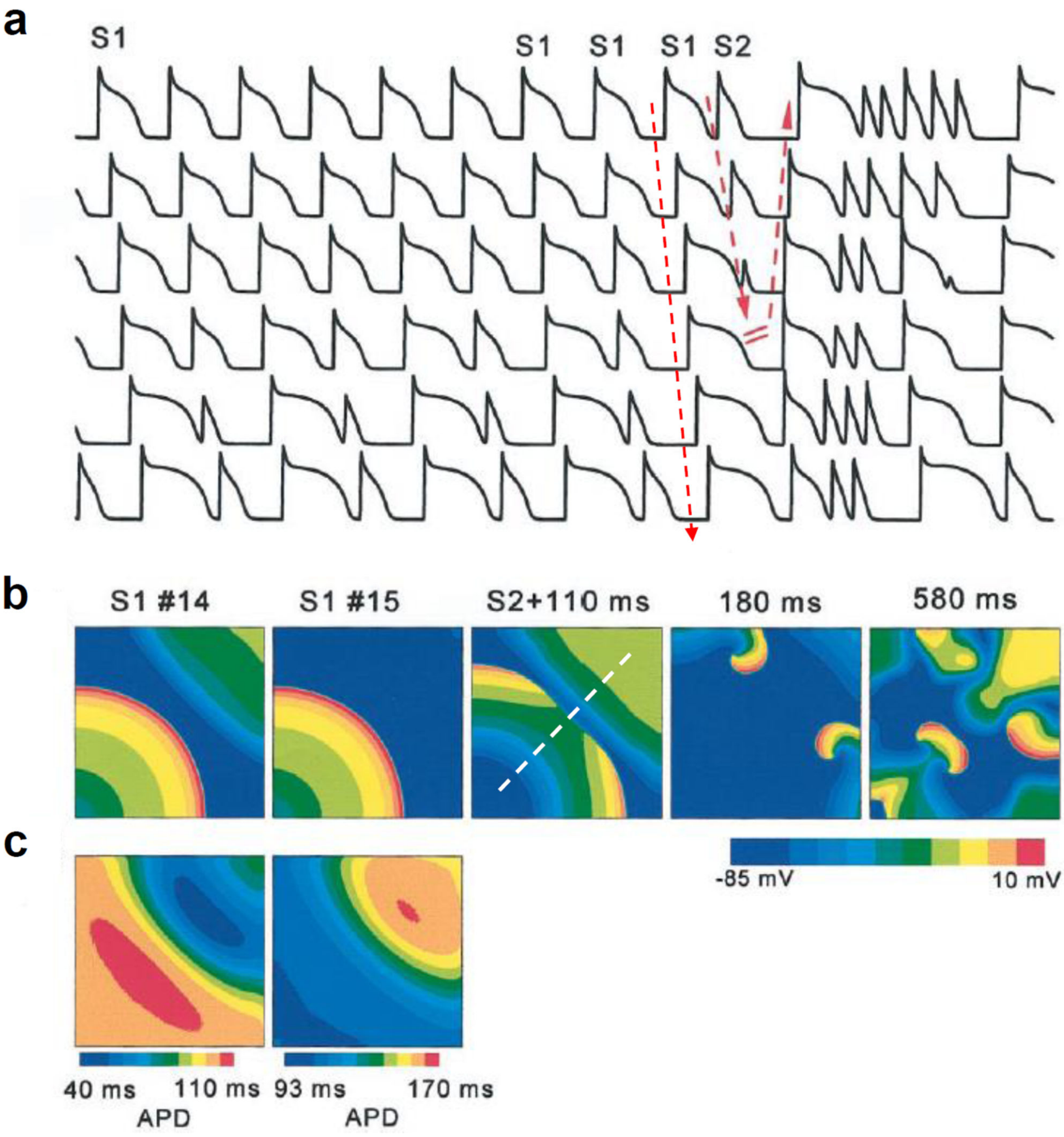

Figure 42. Induction of reentry due to discordant alternans

S1 (15 beats at PCL=170 ms) and S2 (S1S2=120 ms) were delivered at the same site. **a**. Membrane potential at different sites in tissue (along the dashed line indicated in the middle panel in b), with conduction block initiating reentry indicated by arrows. **b**. Snapshots of membrane voltage during last 2 S1 beats (beats 14 and 15) and at various times after S2 was delivered, showing initiation of figure-eight reentry leading to fibrillation. **c**. Spatial APD distribution for the S1 beats 14 and 15, showing discordant APD alternans.

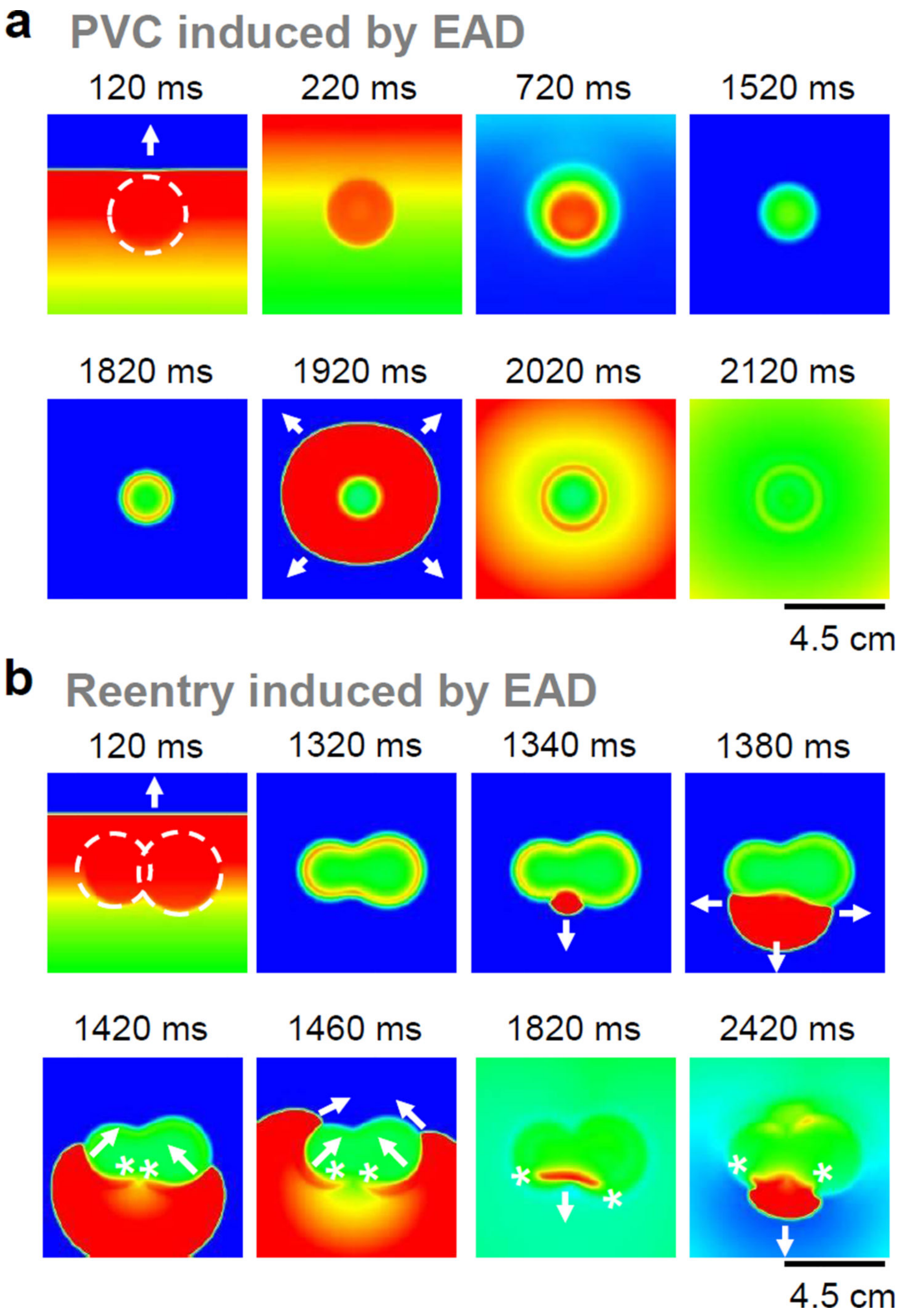

Figure 43. Induction of PVC and reentry by EADs in a 2D heterogeneous tissue

a. A PVC resulted from an EAD in a 2D tissue with a heterogeneous region composed of a circular area in which EADs occur. A PVC is formed by the fourth EAD (around 1820 ms) propagating to the normal tissue in all directions. A single S1 stimulus was applied at the bottom edge of the tissue at *t*=0 to cause a planar wave to propagate from bottom to top. The time of each voltage snapshot is above each panel. **b**. Reentry induced by an EAD in a 2D tissue with a heterogeneous region composed of two circles (dashed) in which EADs occur. Reentry occurs spontaneously due to the EAD successfully propagating in one direction but failing in the other direction, forming figure-of-eight reentry. Asterisks indicate the tips of the spiral wave reentry, while arrows indicate directions of propagation. Panels are modified from a supplemental figure in Chang et al [477].

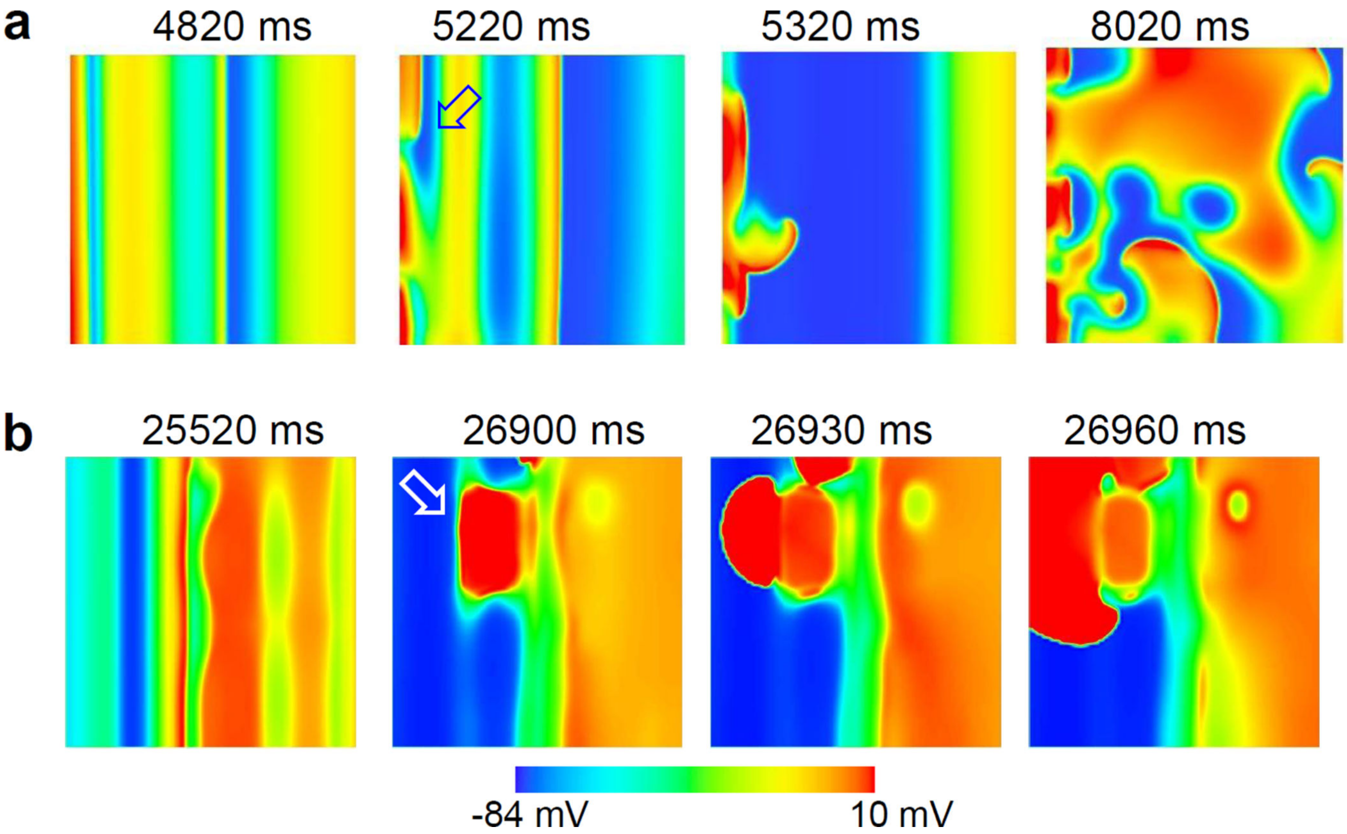

Figure 44. Reentry initiation via spatiotemporal chaotic dynamics

a. Rapid pacing-induced spatiotemporal chaos and wavebreaks in a homogeneous 2D tissue [242]. The stimulation is applied to the cells at the left edge of the tissue, which generates planar waves propagating from left to right. At the beginning, the waves are synchronized in the vertical direction, but as time elapses, this synchronization is lost and voltage gradients develop in the vertical direction which causes localized conduction block (marked by the arrow in the second panel), leading to reentry and complex electrical turbulence. **b**. Pacing-induced spatiotemporal chaos and induction of reentry in a homogeneous tissue in the presence of EADs [166]. The stimulation is applied to the left edge with a slow PCL to allow EADs to occur. Due to chaos, EAD islands form (indicated by the arrow in the second panel), and the EAD propagates in one direction and induces reentry.

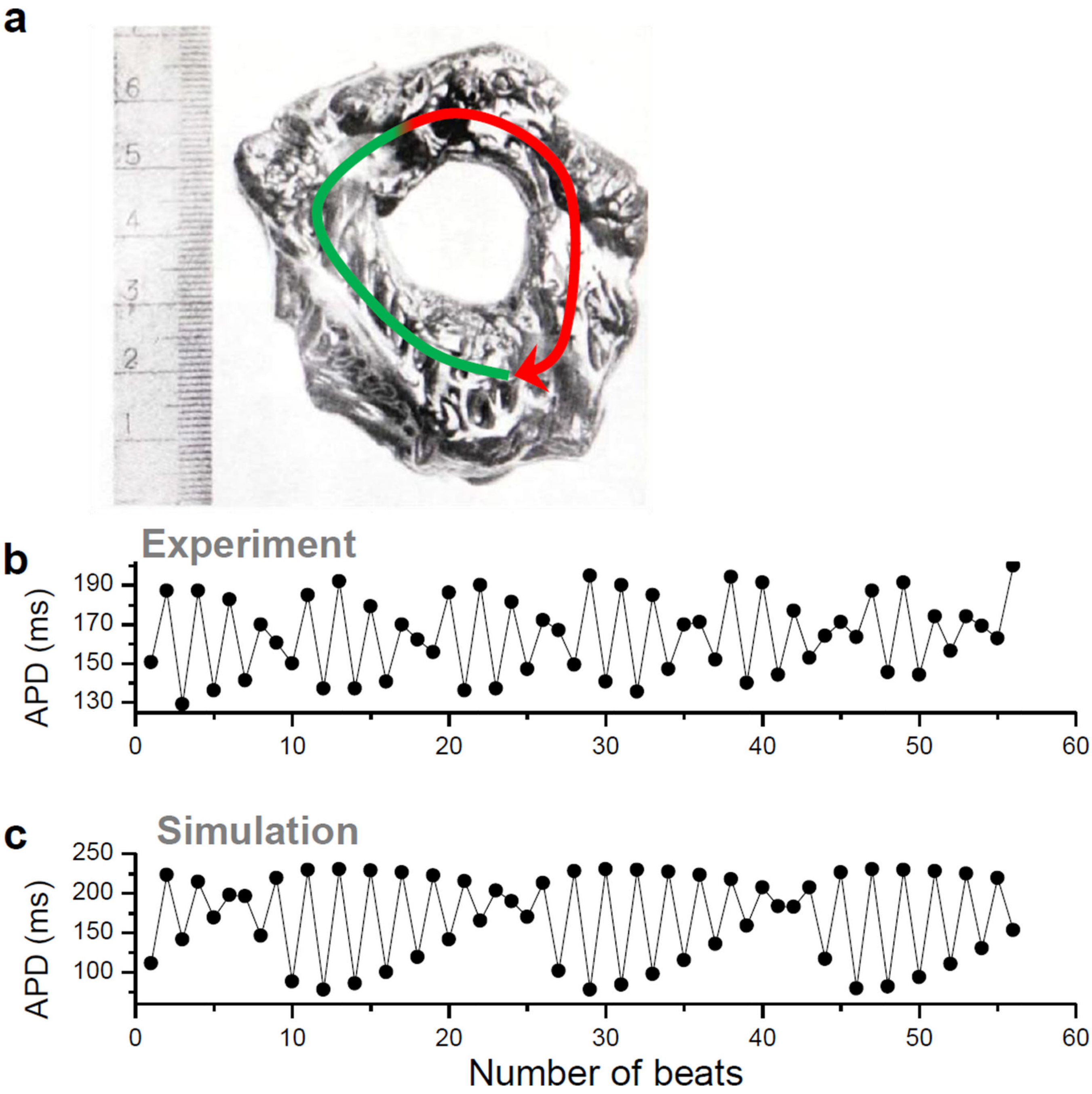

Figure 45. Quasi-periodicity in a ring of cardiac tissue

a. An annulus of tissue cut from a dog ventricle in Mines' experiment (adopted from Glass [4]). The line with an arrow indicates a circulating wave, red indicates that the tissue is refractory, and green means the tissue is recovered. **b**. APD recorded in an experiment from a circulating wave in an annulus of tissue from a dog heart, reproduced from Frame and Simpson [406]. **c**. APD recorded from a computer simulation of a ring of coupled cells.

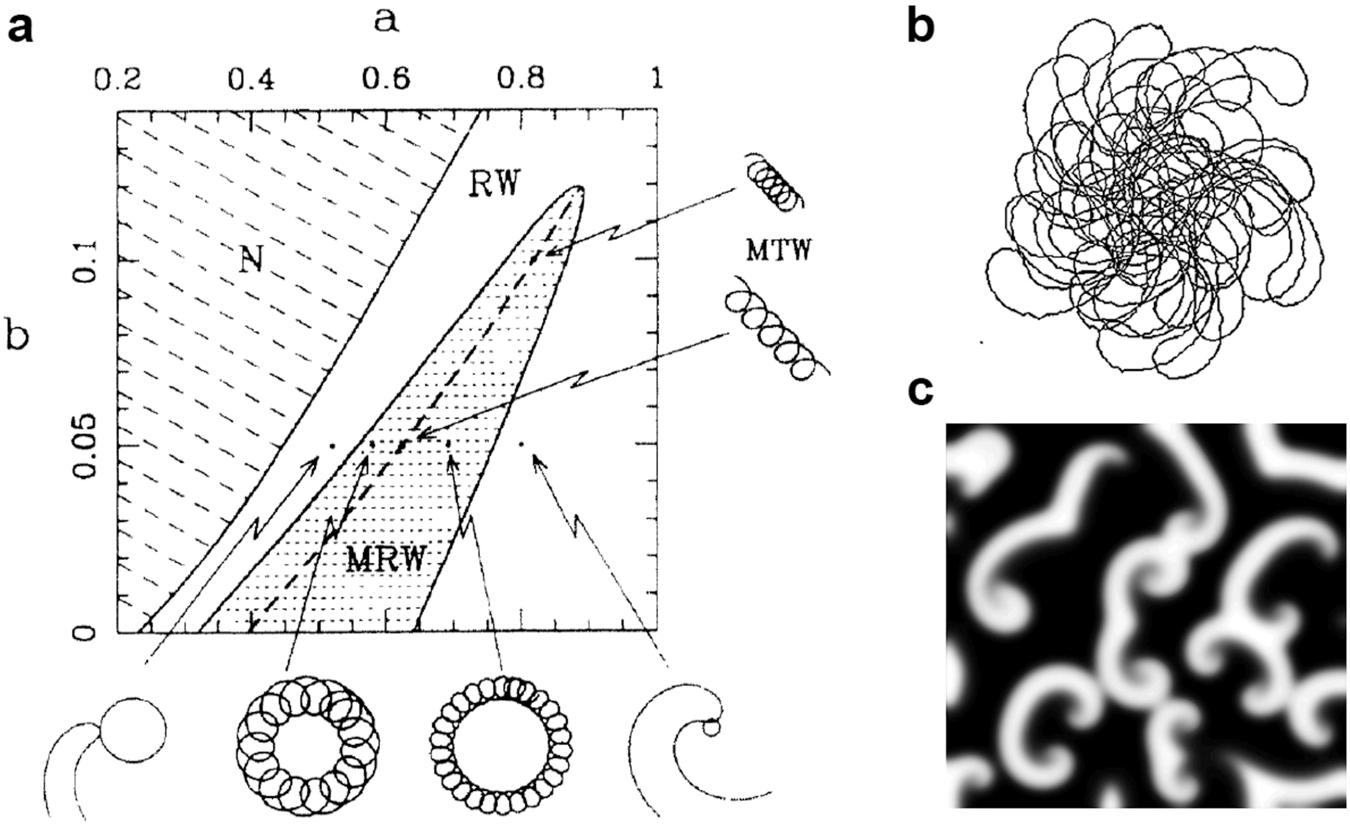

Figure 46. Spiral wave dynamics in generic excitable medium

a. Spiral wave behaviors in a two-parameter space from a two-variable model by Barkley [415]. **b**. Tip trajectory of a spiral wave for a FHN model simulation by Winfree [94]. **c**. Spiral wave breakup in a 2D medium generated using the model by Bar et al [95].

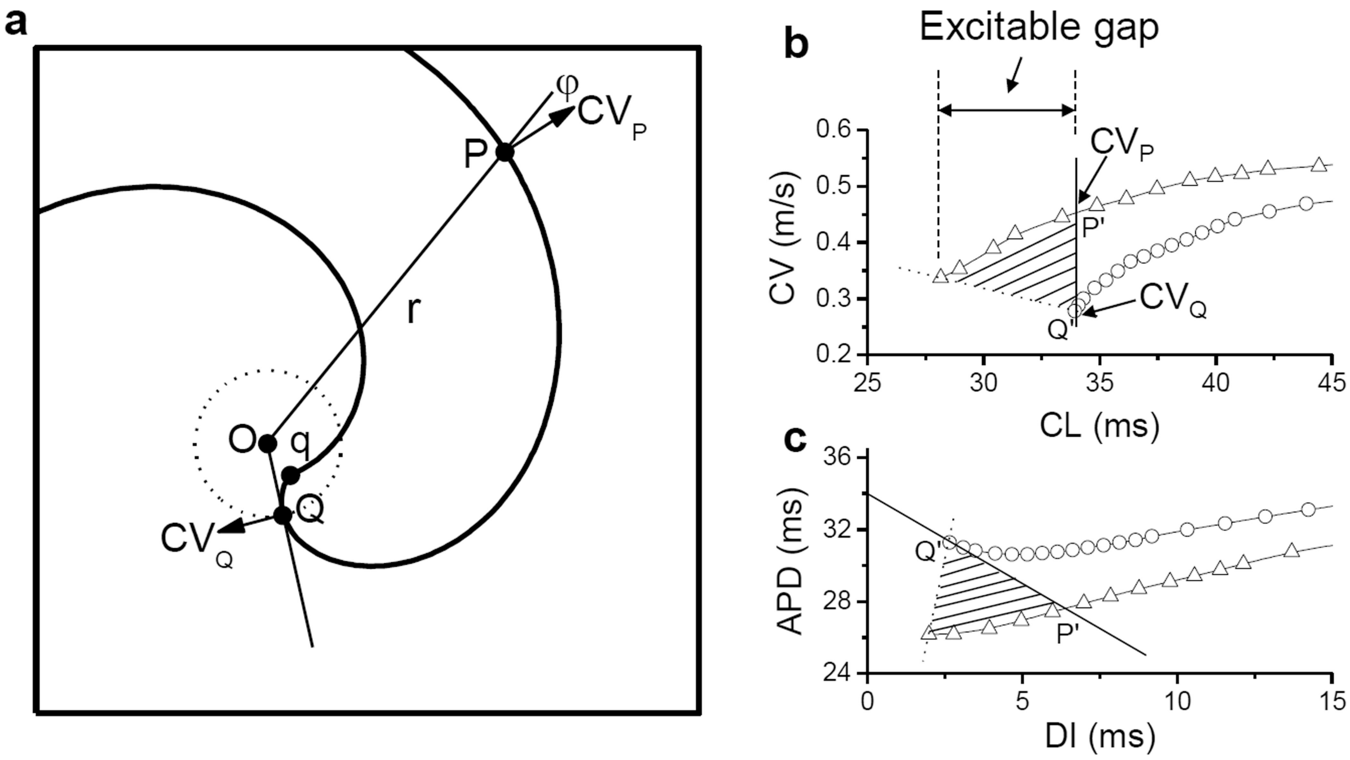

Figure 47. Characteristics of a stable spiral wave in cardiac tissue

a. Schematic plot of characteristic points in a stable spiral wave. “O” is the rotation center. “q” is the joint of the wavefront and waveback. “Q” is the point where decremental conduction meets regenerative conduction. At the Q point, the direction of conduction is normal to its radial direction, which is the only point in a stable spiral has this property. “P” is an arbitrary point in the spiral arm. **b**. CV versus T for two different curvatures. **c**. APD versus DI for two different curvatures. Modified from Qu et al [102].

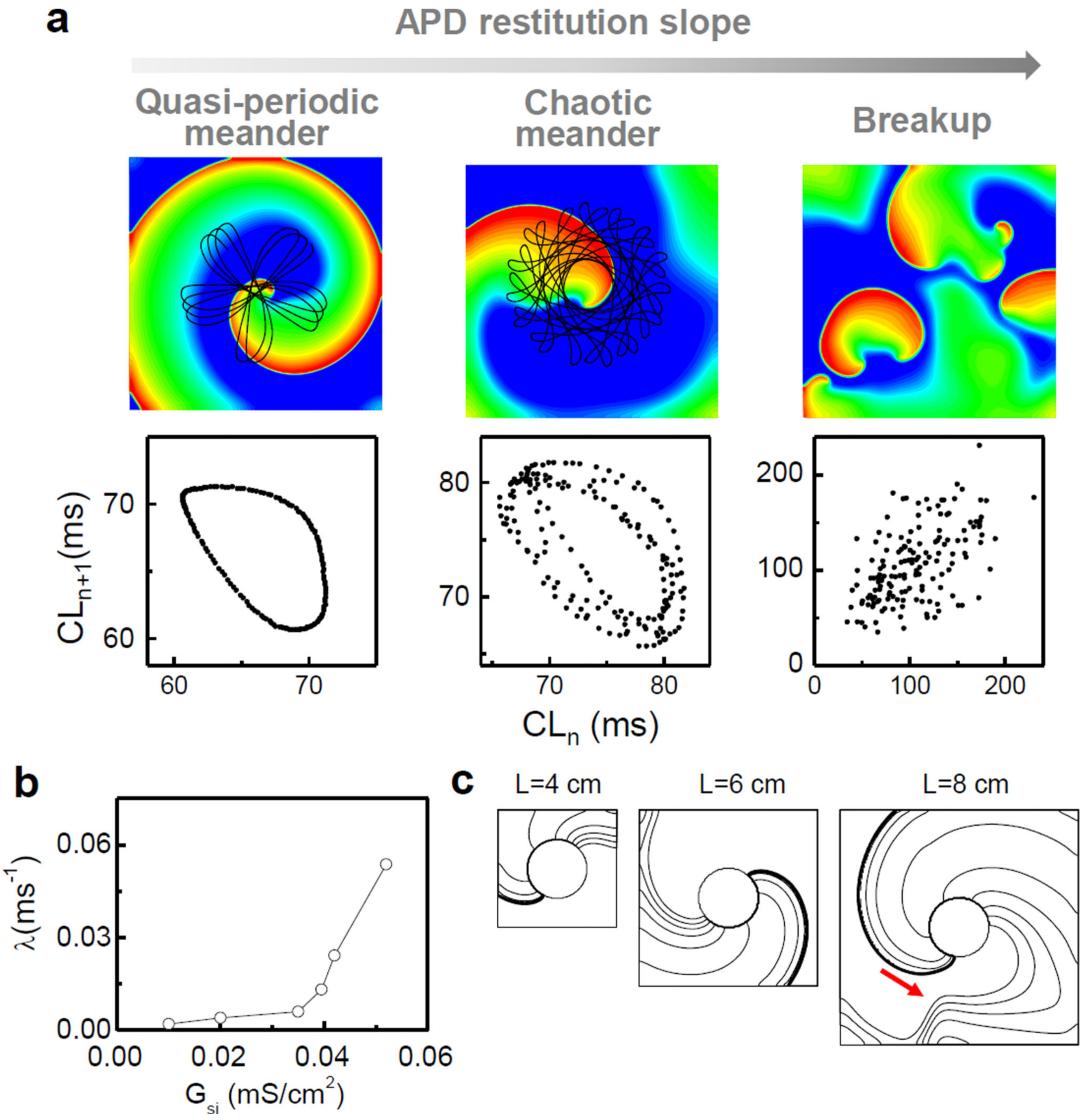

Figure 48. Spiral wave dynamics in a homogeneous 2D tissue model

a. Quasi-periodic and chaotic spiral wave meander and spiral wave breakup in a homogeneous 2D tissue. The spiral wave behaviors were resulted by altering the maximum conductance of the Ca^{2+} current, $\bar{G}_{si}$, in the LR1 model. Upper panels: snapshots of voltage and tip trajectories. Lower panels: return maps of cycle length (CL, recorded from a certain location in the tissue) showing CL$_{n+1}$ versus CL$_n$ for the corresponding cases in the upper panels. **b**. Maximum Lyapunov exponent versus *si G* obtained via numerical simulation. **c**. Development of spatial mode instability as tissue size increases for a reentry around a fixed circular obstacle. A “speed bump” develops (marked by the arrow) in the waveback due to this instability in a large tissue but not in the smaller ones. Panels are modified from Qu et al [102].

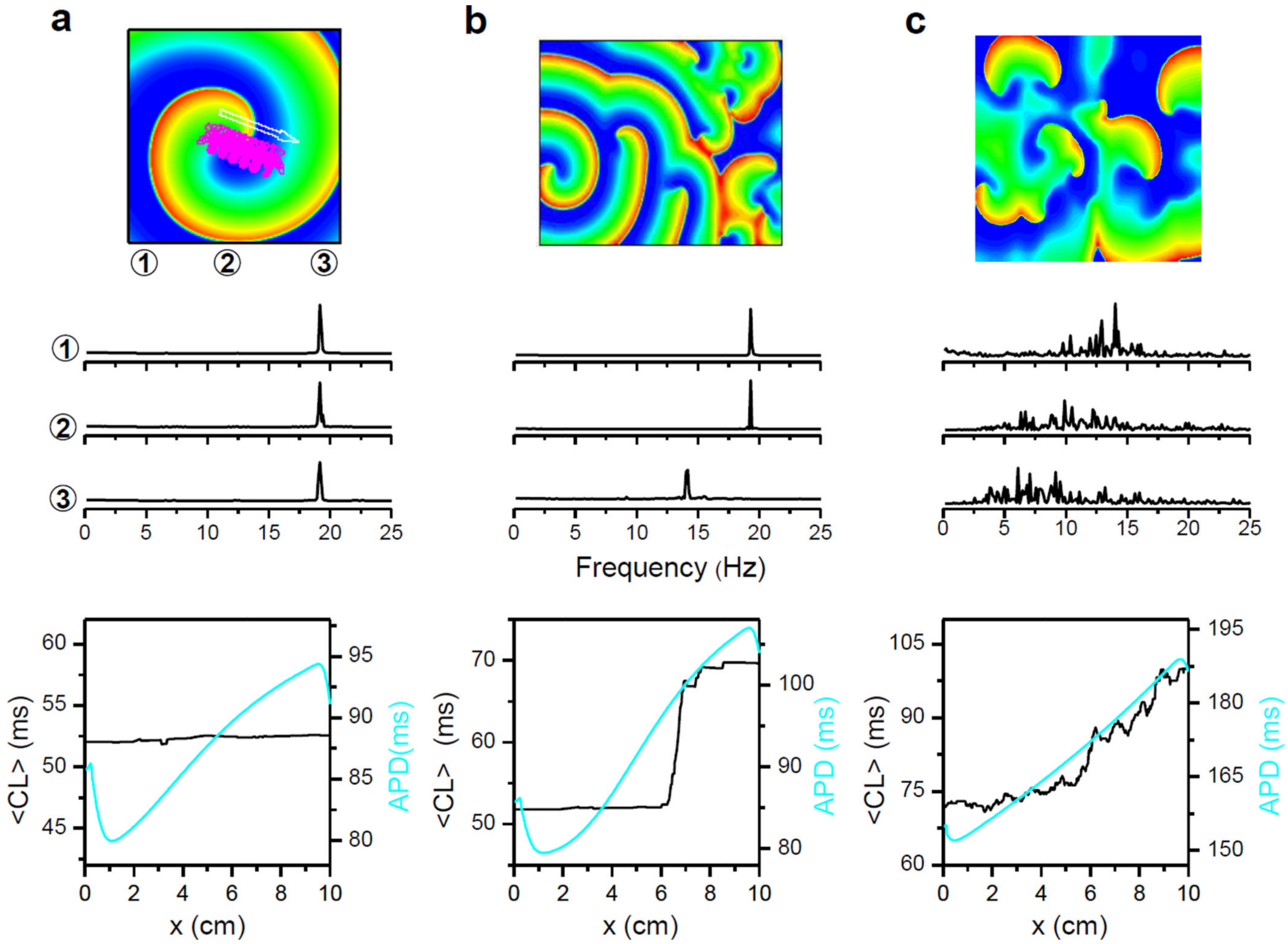

Figure 49. Spiral wave drift and dynamics in heterogeneous 2D tissue models

a. Spiral wave drift in a mildly heterogeneous tissue. Red line is the tip trajectory and arrow indicates the direction of drift. **b**. Wavebreaks and co-existence of multiple spiral waves with different frequencies due to a severe heterogeneity. **c**. Spiral wave breakup via dynamical instabilities in a heterogeneous tissue. Upper panels: snapshot of voltage; Middle panels: FFT spectra for voltage recordings from three different locations of the tissue; Lower panels: averaged cycle length (<*CL*>) versus position recorded during the spiral wave activities and APD versus position recorded during a planar wave propagating from left to right in the same tissue.

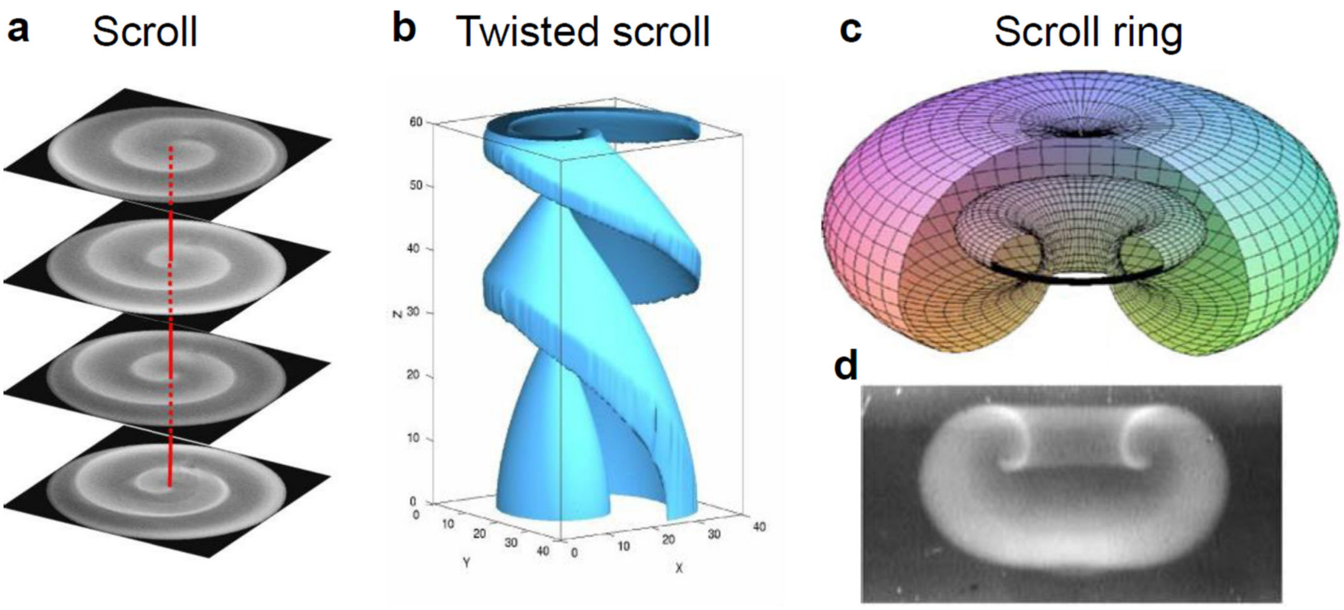

Figure 50. Different types of scroll waves

a. A straight scroll wave [582]. The line linking the spiral tips is called filament of the scroll wave, which is a straight line in this case. **b**. A twisted scroll wave [582]. **c**. A schematic plot of a scroll ring [451]. **d**. An experimentally measured scroll ring in a chemical reaction [583].

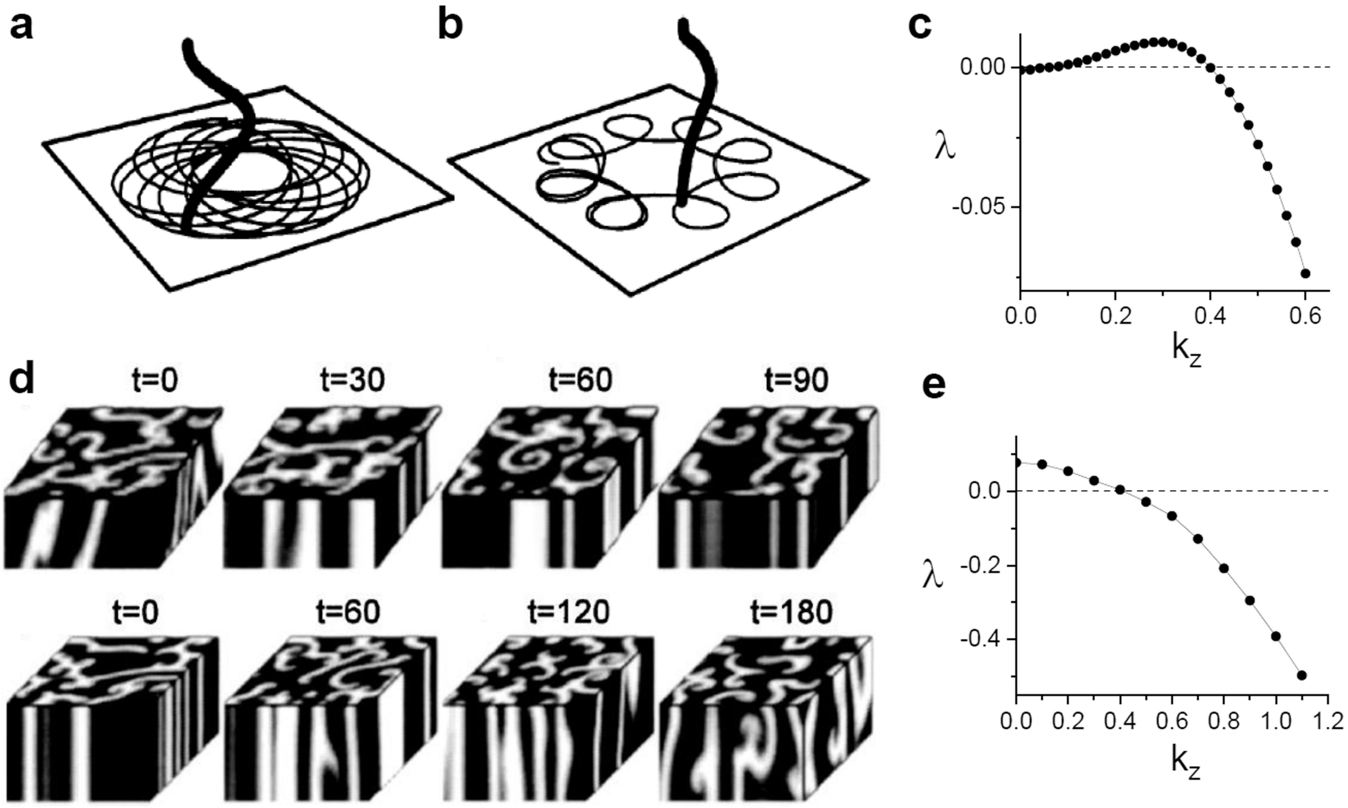

Figure 51. Effects of tissue thickness on scroll wave stability

a. Filament and its trajectory on the bottom surface of a 3D medium for an inward petal of tip trajectory. **b**. Same as a but for an outward petal in tip trajectory. **c**. Maximum Lyapunov exponent versus wave number *k* for the case in b. **d**. Spiral turbulence synchronizes in the z-direction in a thin tissue but desynchronizes in a thick tissue, resulting in 3D turbulence. **e**. Maximum Lyapunov exponent versus wave number k for d. Simulations were done using the Bar model, and panels are modified from Qu et al [431].

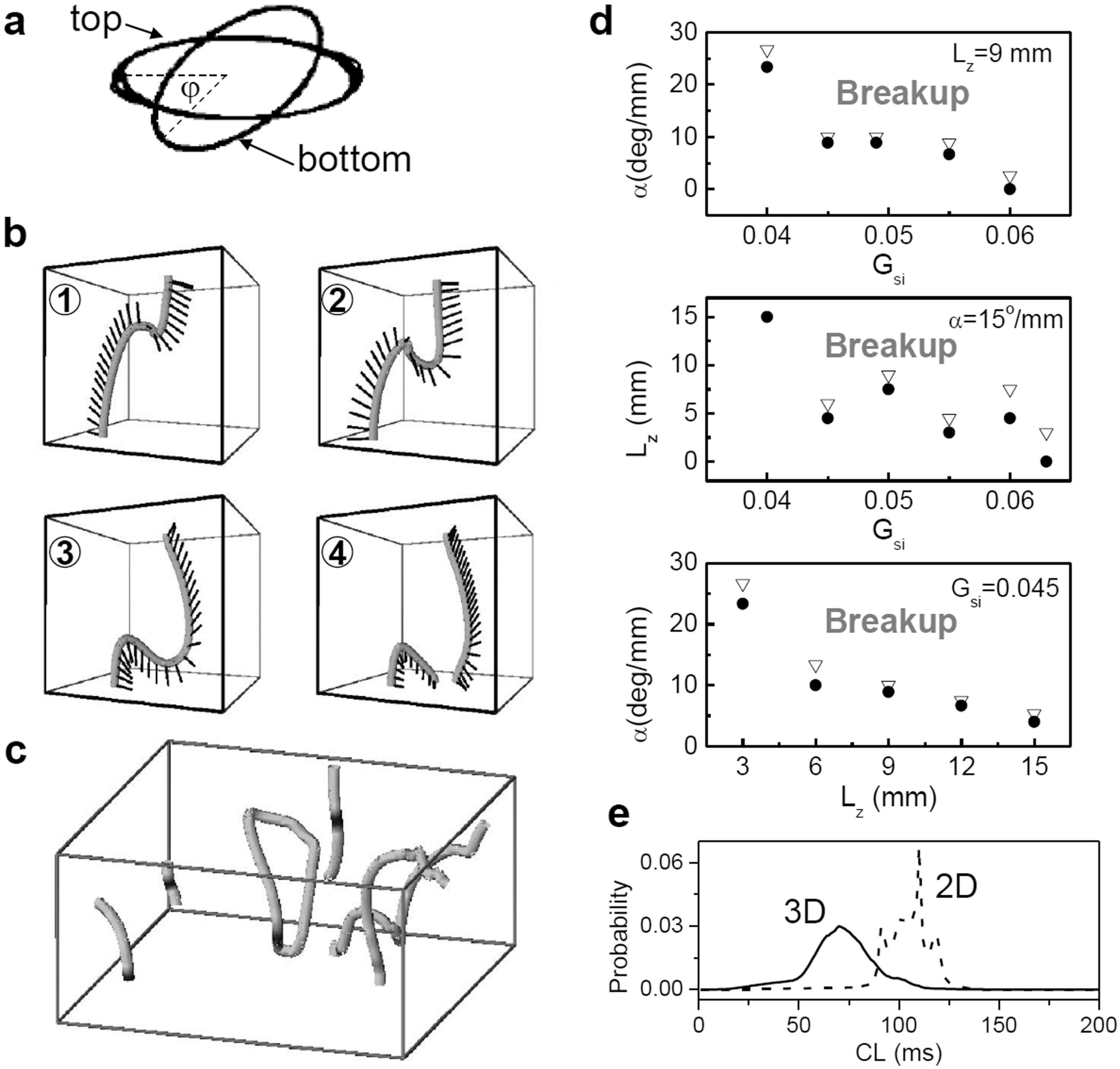

Figure 52. Fiber rotation induced scroll wave twist and breakup

a. Tip trajectories from the top and bottom surfaces of a 3D tissue with fiber rotation. The corresponding 2D spiral wave is stable. Fiber rotation causes spiral wave on the top to rotate out-of-phase with the one at the bottom, forming a twisted filament. **b**. Fiber rotation induced filament twist and bending, and filament break at the bottom surface, when the corresponding 2D spiral wave is in the hypermeandering regime. Time increases from panel 1 to panel 4. **c**. Filament bending and breaks leading to complex filament dynamics. **d**. Relationships between 3D scroll behavior and *si G* (controlling APD restitution steepness), fiber rotation rate α, and tissue thickness L_z. Due to the large-scale computational needs, the boundary of no scroll wave breakup and breakup cannot be determined with high accuracy.

The black circles are the simulations that no breakup occurs while the triangles are the ones that breakup is observed. We connected the full circles by dotted lines to distinguish the no-breakup and breakup regions; i.e., below the line is the nobreakup region, while above is the breakup region. **e**. Cycle length histogram from 2D spiral wave and 3D turbulence of the same action potential model, showing speedup of frequency in 3D due to filament bending and reentry in the third dimension. Panels a, d, and e are modified from Qu et al [104] and b and c from Fenton and Karma [103].

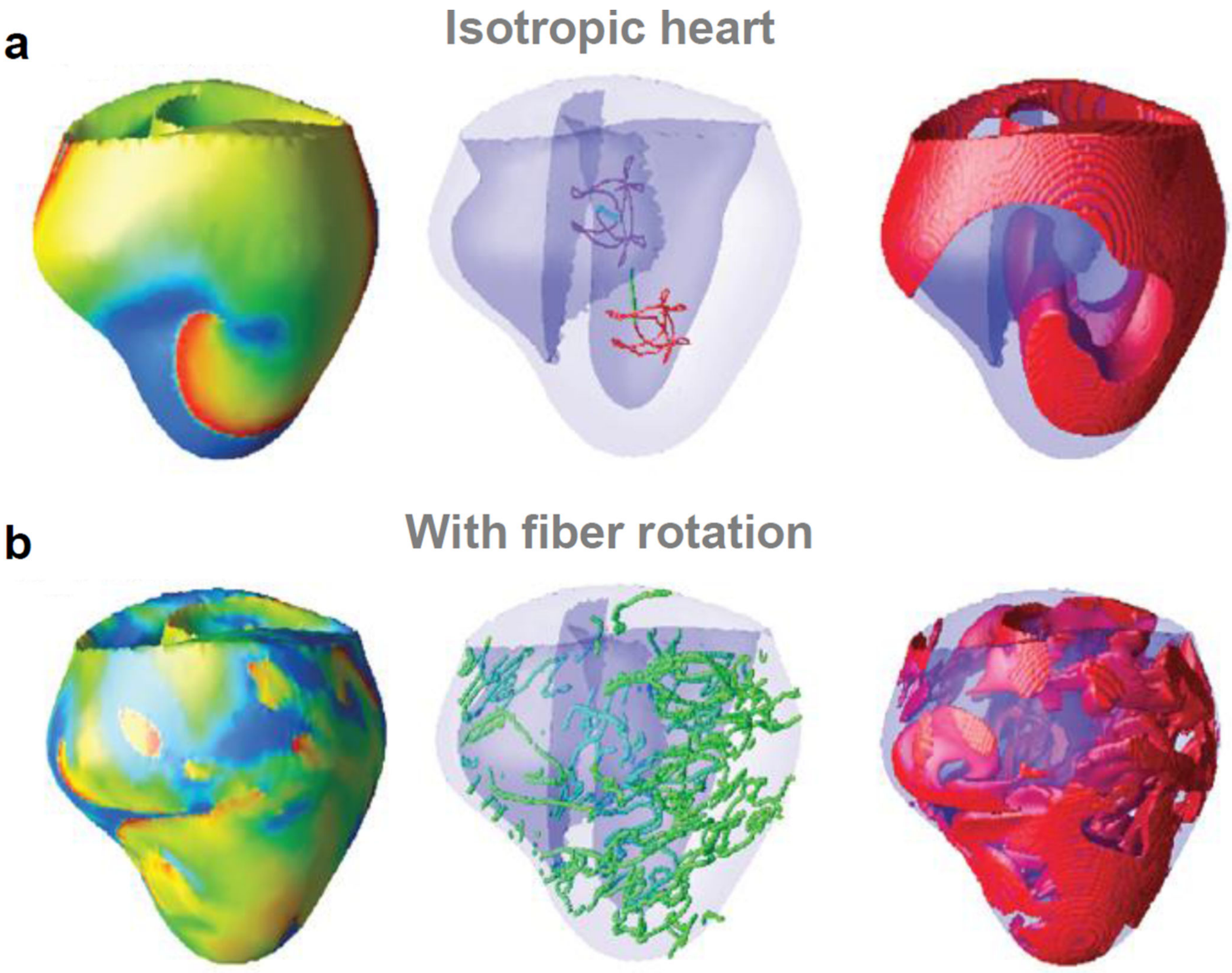

Figure 53. Computer simulation of scroll wave dynamics in a dog heart [164

a. Scroll wave dynamics in computer simulation of a dog ventricle with no fiber structure (homogeneous ventricle). Left: voltage snapshot on the epicardial surface. Middle: filaments (green) in the heart and tip trajectories (red) on the epicardial surfaces. Right: Wavefronts in the heart. **b**. Same as a, but with realistic fiber orientations. The scroll wave remains intact in homogeneous heart in panel a, but breaks up in the presence of realistic fiber structure in panel b, leading to a very complex spatiotemporal scroll pattern.

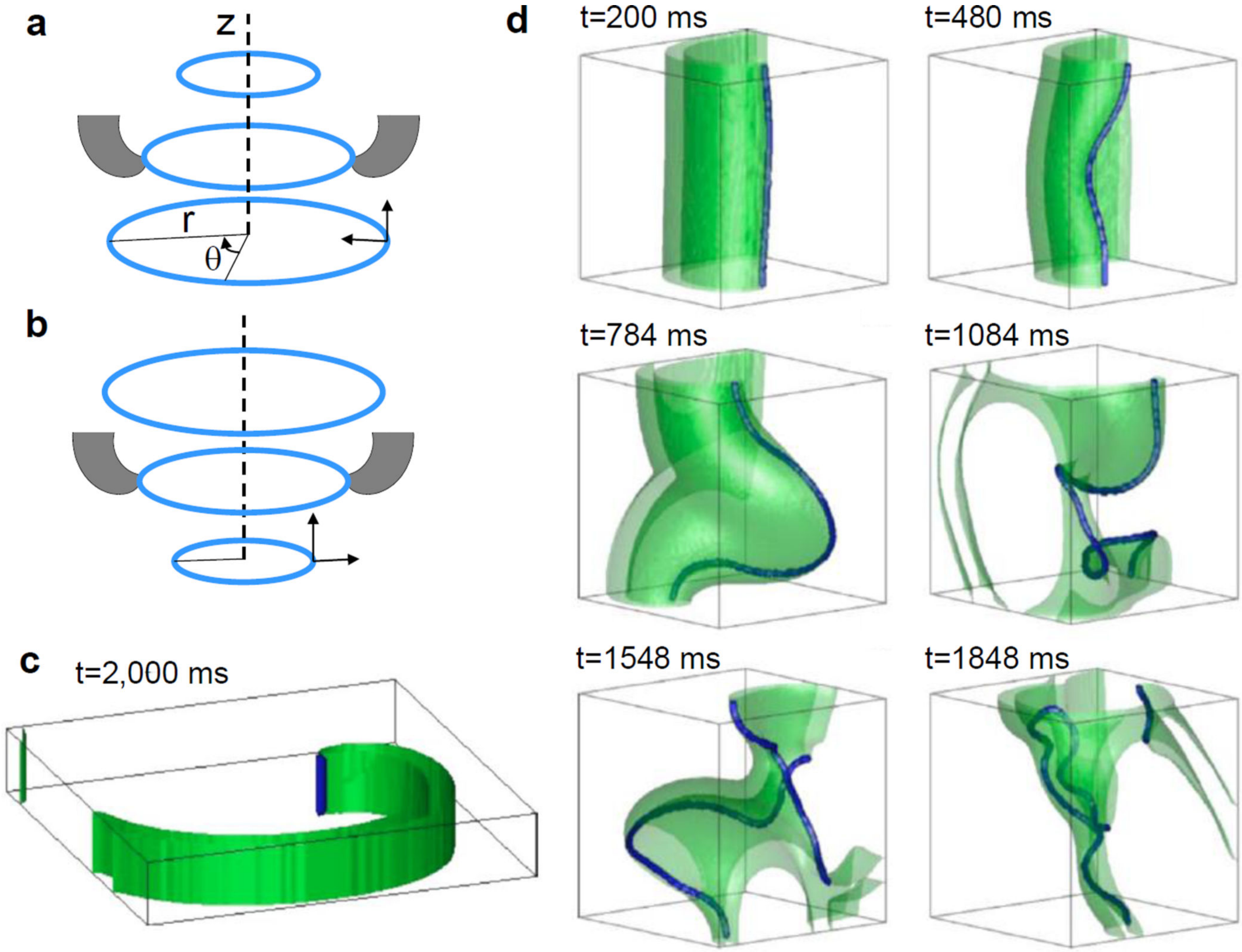

Figure 54. Negative filament tension

a. A normal shrinking scroll ring. The vertical arrow is the drifting direction of the ring and the horizontal arrow is the direction in which the ring shrinks. **b**. Same as a but for an expanding ring. **c**. A straight scroll wave in a thin 3D tissue (z=0.8 cm) with the LR1 model and greatly reduced Na^+ channel conductance to simulate low excitability. **d**. A straight scroll wave decay into a complex spatiotemporal scroll pattern using the same model as in c but a much thicker tissue.

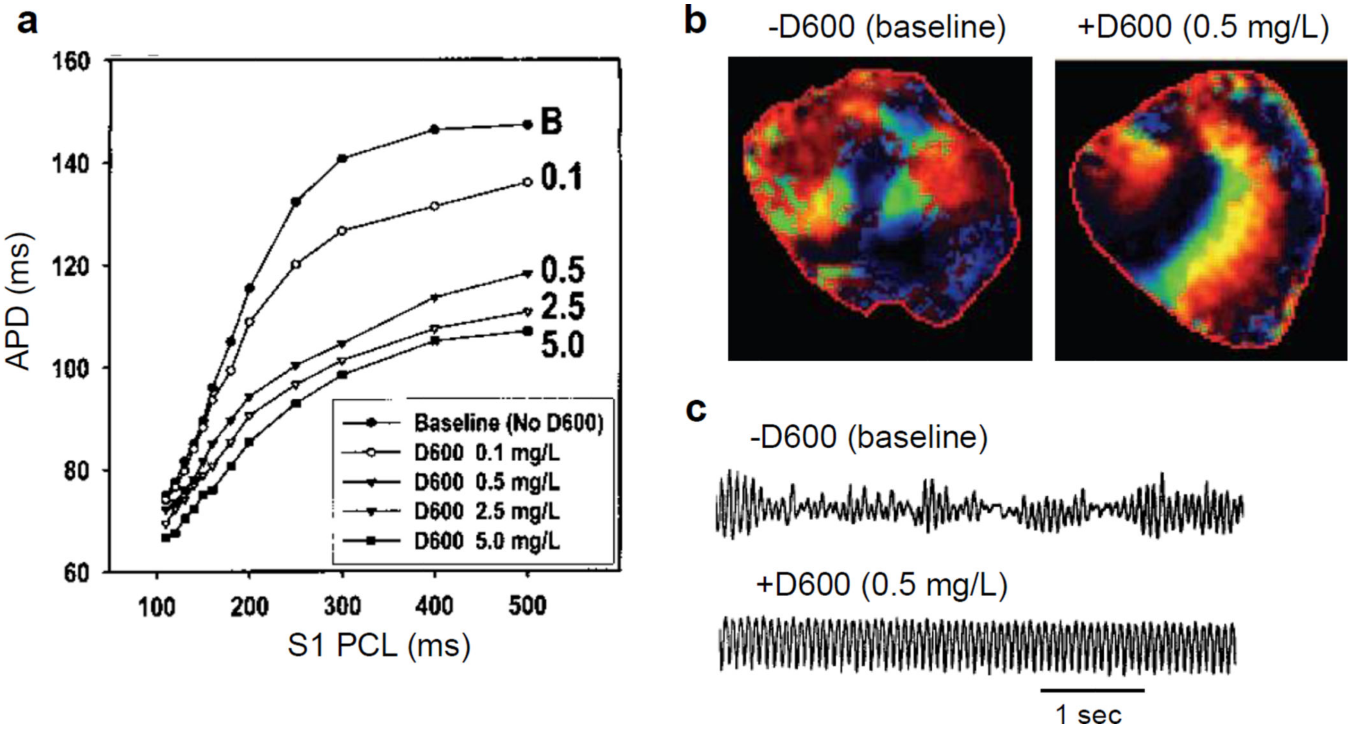

Figure 55. Effect of APD restitution on spiral wave stability in a rabbit heart

a. APD versus PCL for different doses of D600, a Ca^{2+} channel blocker. **b**. Optical images of voltage before and after D600. **c**. Pseudo-ECG before and after D600. Reproduced from Wu et al [461].

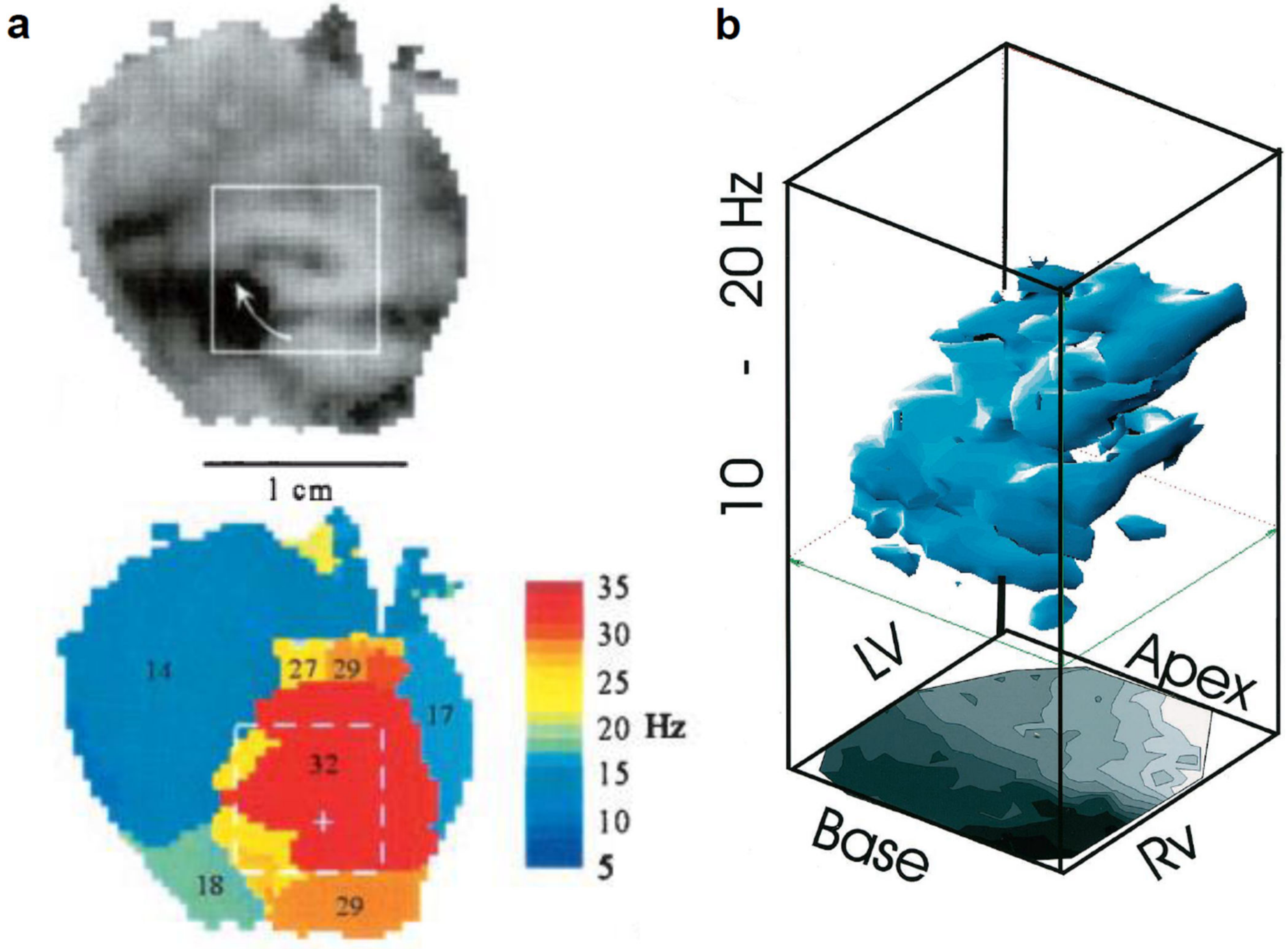

Figure 56. Frequency distribution during fibrillation in real hearts

a. Voltage map (upper panel) and dominant frequency distribution (lower) during fibrillation from a mouse heart, reproduced from Samie et al [463]. **b**. Frequency distribution during fibrillation in a guinea pig heart. z-axis plots the frequency (10–20 Hz) distribution while the x-axis and y-axis are the spatial coordinates from base to apex, and from right to left ventricles, respectively. A map of APDs measured from the same hearts during a basic beat (CL=300 ms) was superimposed at the bottom of the 3D plot to visually correlate APDs in the paced heart to frequency distributions in VF. Note that frequency distributions had the inverse relationship to the APD distribution, decreasing systematically from apex to base (color changes from white to black). Reproduced from Choi et al [466].

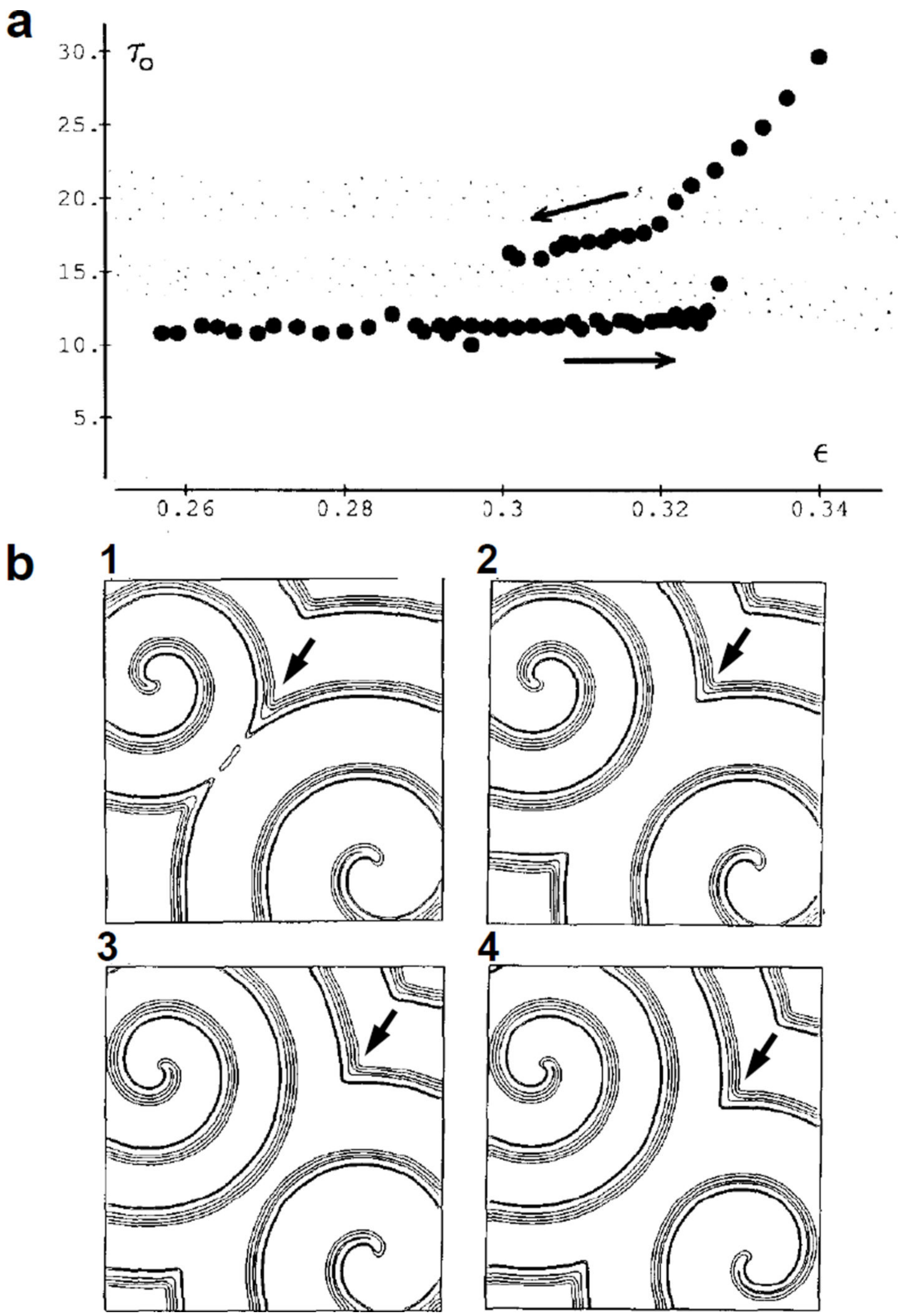

Figure 57. Bistable spiral wave conduction in the FHN model

a. Rotation period of spiral wave versus ε, a parameter in the FHN model that affects excitability. Arrows indicate that as ε changes from small to large, and then from large to small, a hysteresis in rotation period is seen. **b**. Co-existence and competition of the two types of spiral wave in a homogeneous medium. The period of the fast spiral wave is 11.2 and the period of the slow one 16.5. The time interval between panels 1 and 2 is 34, in which the fast one executes three revolutions and the slow one does two revolutions. The time interval between panels 2 to 3 is 16.5, in which the slow one executes one revolution.

The time interval between panels 3 and 4 is 11.2 in which the fast one executes one revolution. Arrows indicate the interface of the two types of conduction wavefronts, which moves southeast. Reproduced from Winfree [342].

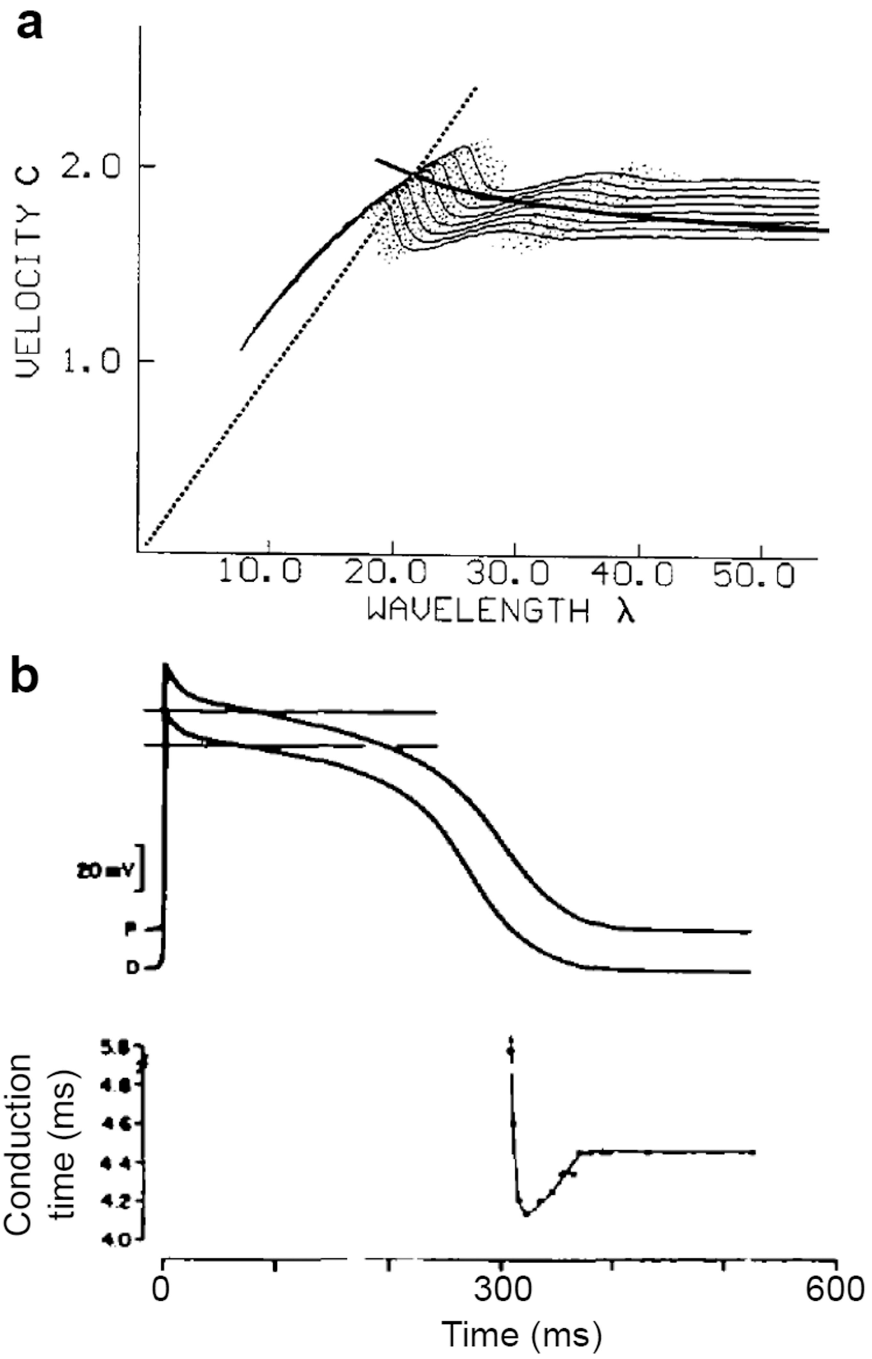

Figure 58. Non-monotonic dispersion relation and supernormal excitability

a. Non-monotonic dispersion relation curves from the FHN model with different ε, reproduced from Winfree [342]. **b**. Supernormal conduction in cardiac Purkinje fiber, reproduced from Moore et al [471]. Upper panel are action potentials from two locations of the fiber with a shift. Lower panel is the conduction time between the two locations for stimulus delivered at different times following the action potential, showing a biphasic conduction time.

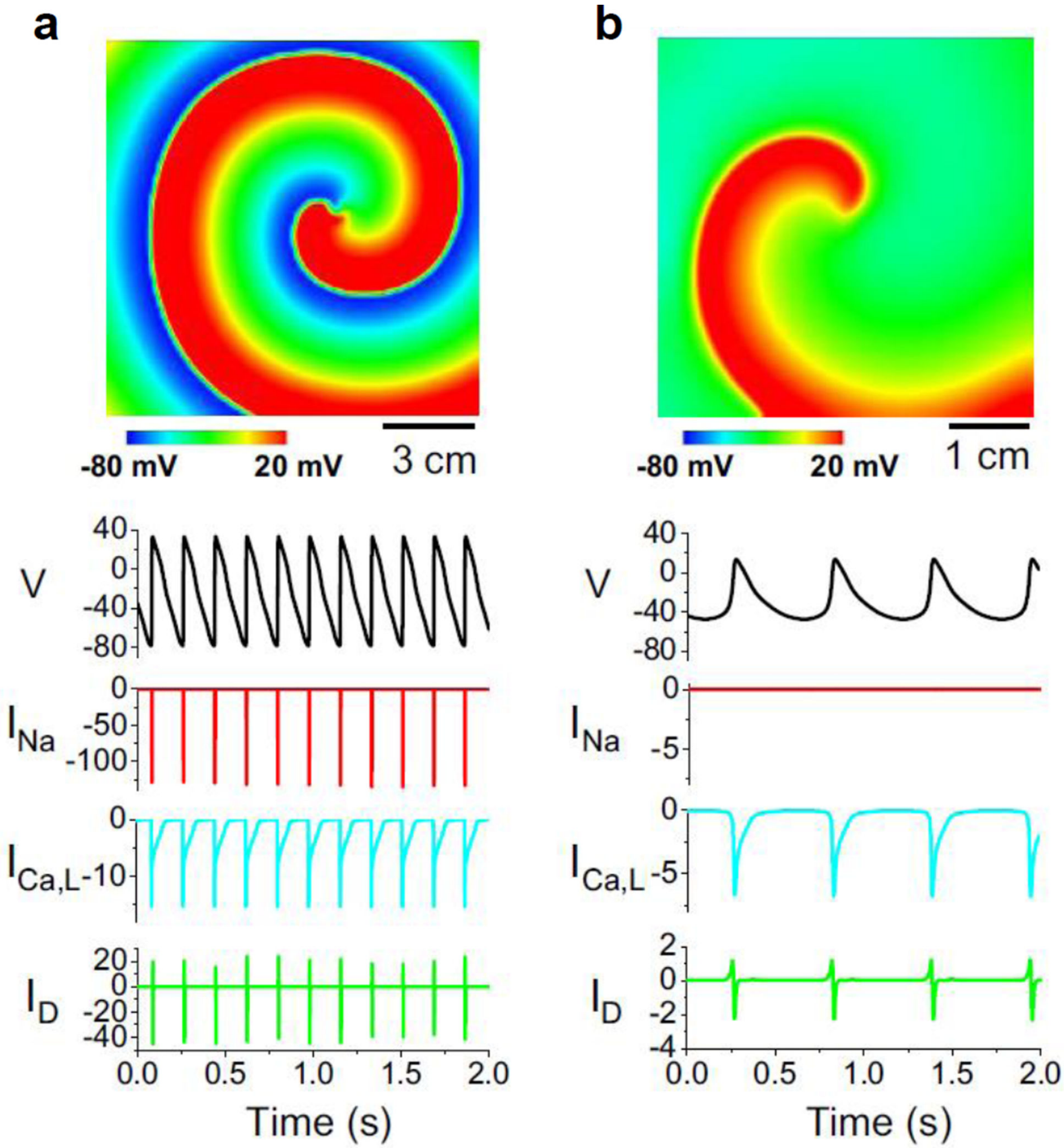

Figure 59. Bi-excitability

a. An I_{Na}-mediated spiral wave in a homogeneous 2D tissue induced by cross-field stimulations, with traces of voltage, I_{Na}, $I_{Ca,L}$, and the diffusion current (I_D) versus time at a representative location. **b**. An $I_{Ca,L}$-mediated spiral wave induced by a different crossfield stimulation pattern in the same tissue, with traces of voltage, I_{Na}, $I_{Ca,L}$, and I_D versus time from the same site as in a.

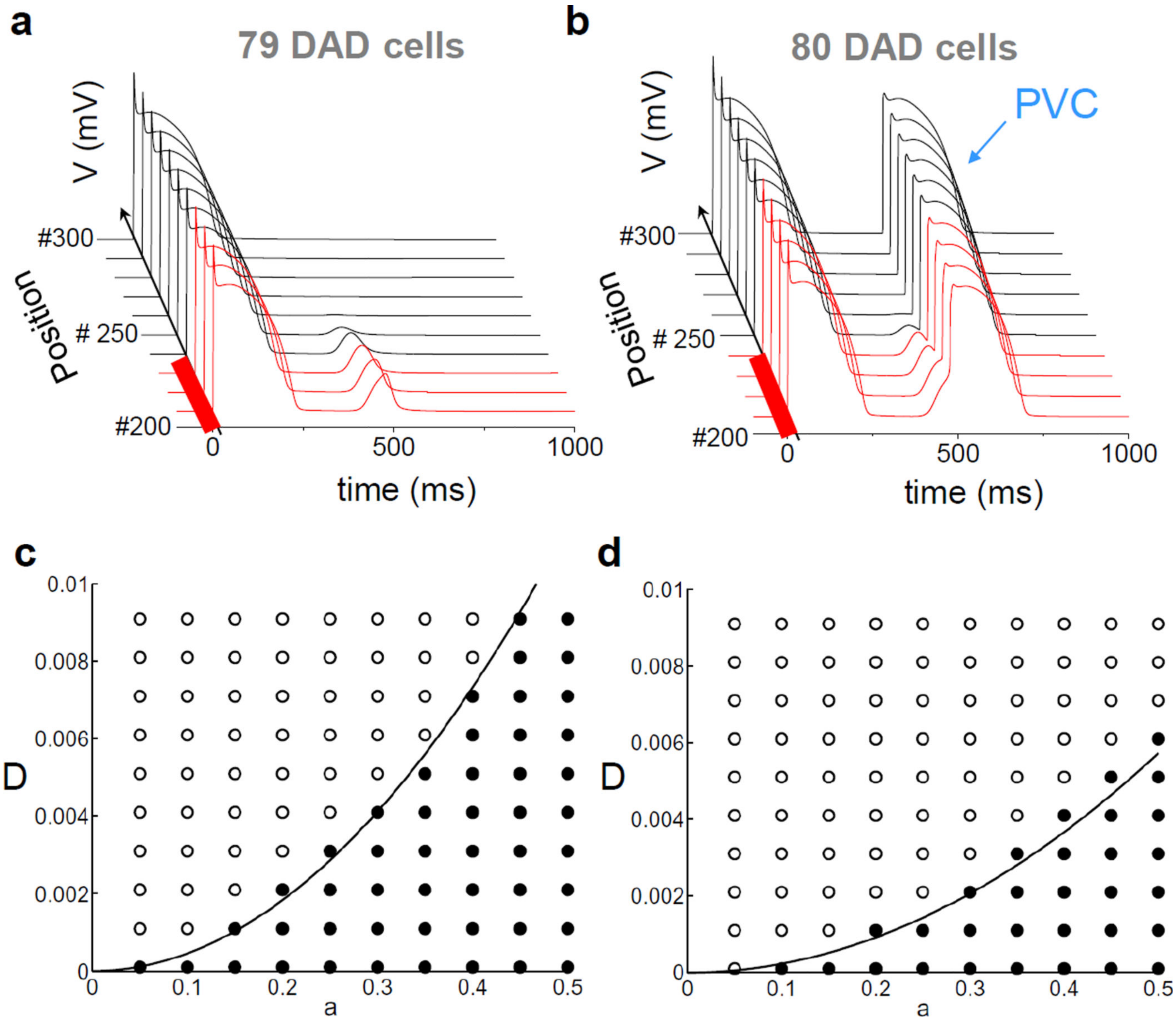

Figure 60. PVC formation in tissue with DAD cells

a. 79 DADs cells in the center of a 400-cell cable results in no PVC. **b**. 80 DADs cells in the center of the same cable result in a PVC, reproduced from Xie et al [479]. **c** and **d**. Stability boundary for PVC to form in a 1D cable and in 2D tissue. Symbols are numerical simulations and lines are the analytical predictions (Eq.103). PVC forms in region of black circles. Reproduced from Tveito and Lines [480].

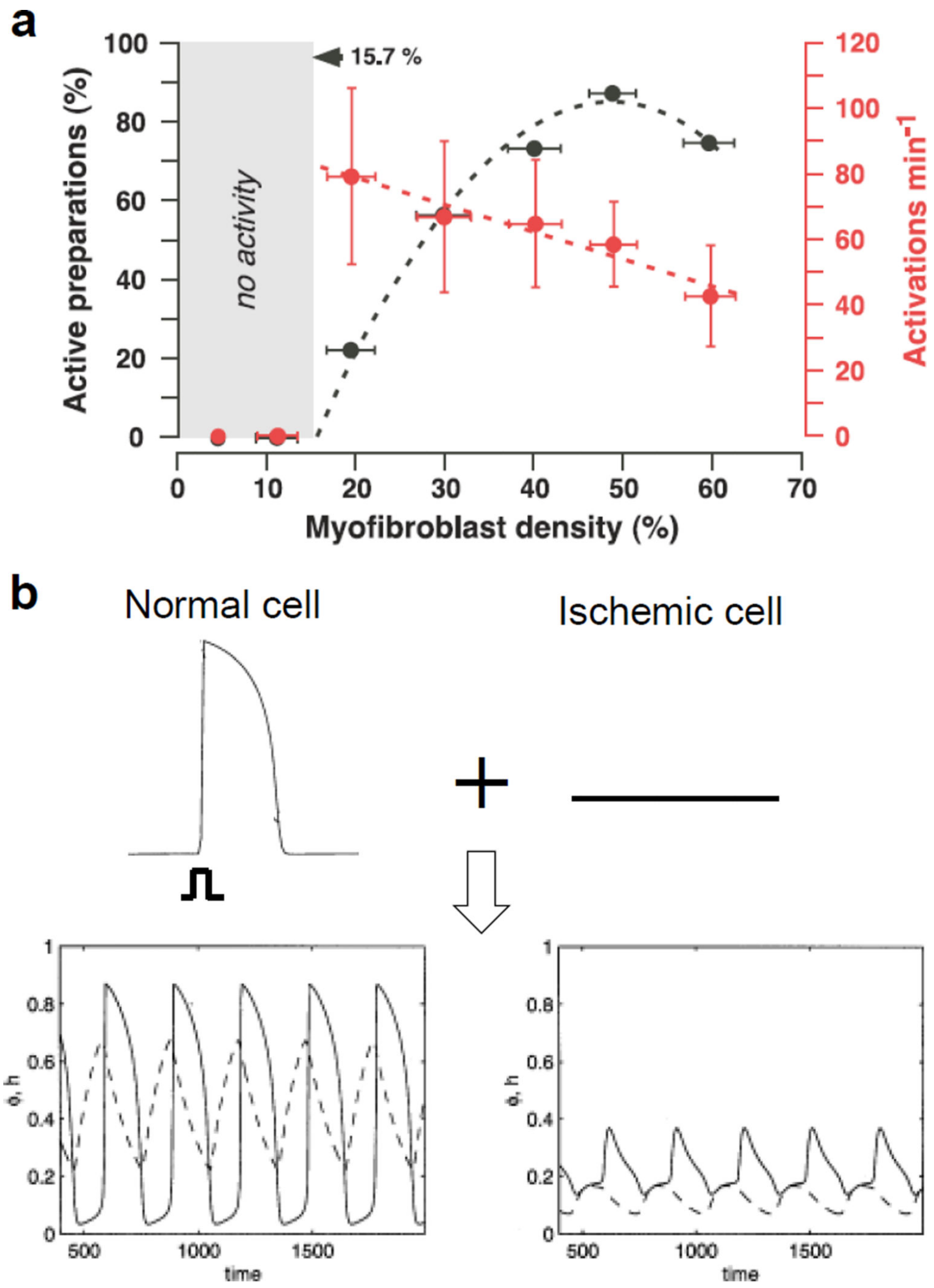

Figure 61. Oscillations induced via coupling of normal excitable cells and non-excitable cells

a. Percentage of monolayers exhibiting oscillations and the average oscillation frequency (number of activations per minute) versus myofibroblast density obtained in cultured rat neonatal ventricular myocyte monolayers, reproduced from Miragoli et al [483]. **b**. A normal ventricular cell coupled with ischemic ventricular cell results in oscillatory behavior from a computer model, modified from Keener [488]. φ is the membrane potential and h is a gating variable. Upper panels indicate that the normal cell is excitable while the ischemic cell is inexcitable with a high resting potential. Lower panels show limit cycle oscillation in both types of cells after they are coupled.

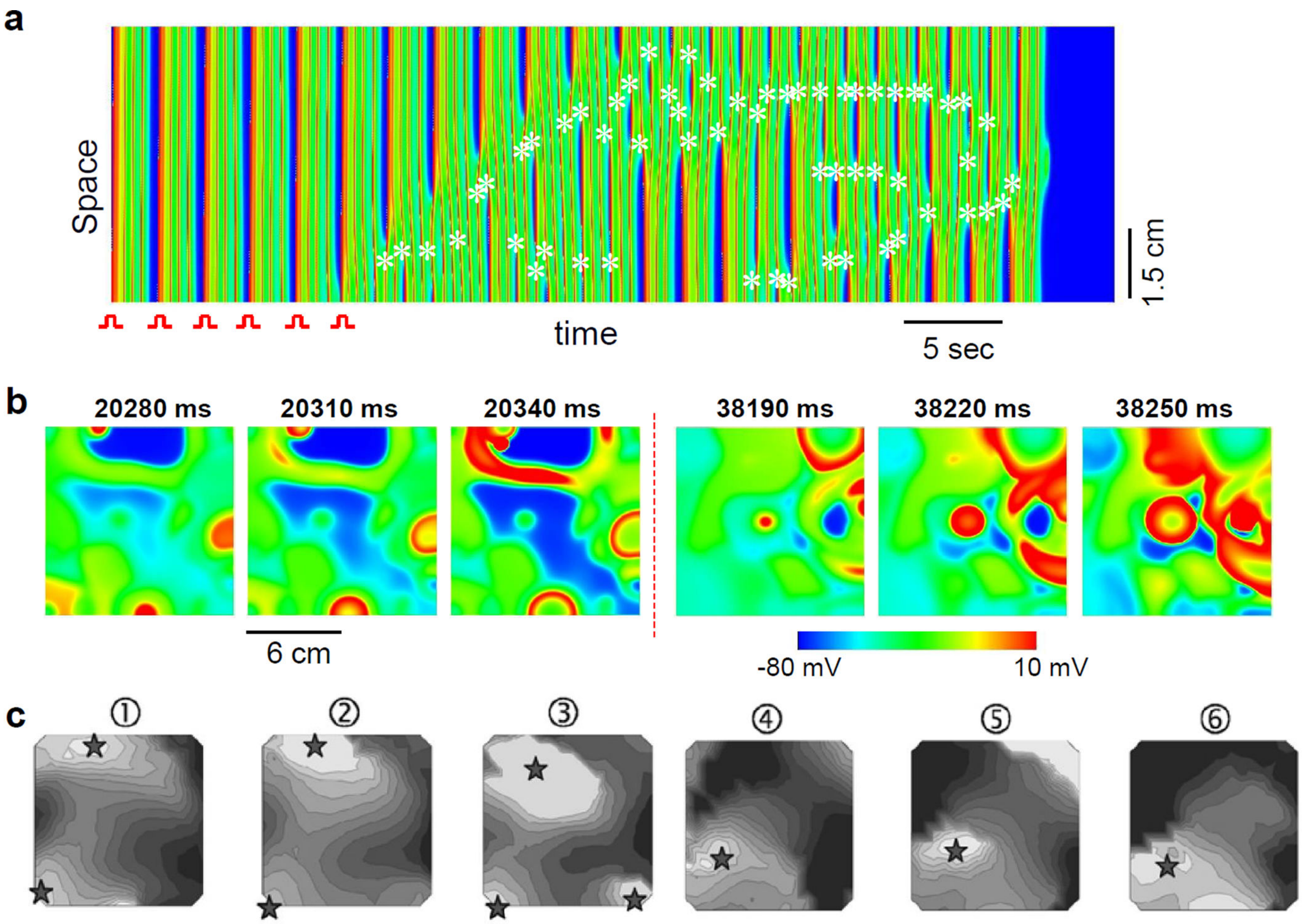

Figure 62. Chaos synchronization induced focal excitations

a. Focal excitations (indicate by "*" in the space-time plot of voltage) form in a homogeneous 1D cable. Six pacing beats were given at one end of the cable as marked. Focal excitations formed after the pacing was stopped, which exhibit an irregular firing pattern and eventually terminate. **b**. Focal excitations (voltage snapshots) form in a homogeneous 2D tissue using the same cell model as in a. Reproduced from Sato et al [166]. **c**. Focal excitations recorded from the epicardial surface in a rabbit heart with optical mapping. Stars mark the origin of the foci and grid lines are isochrones. Reproduced from Choi et al [492].

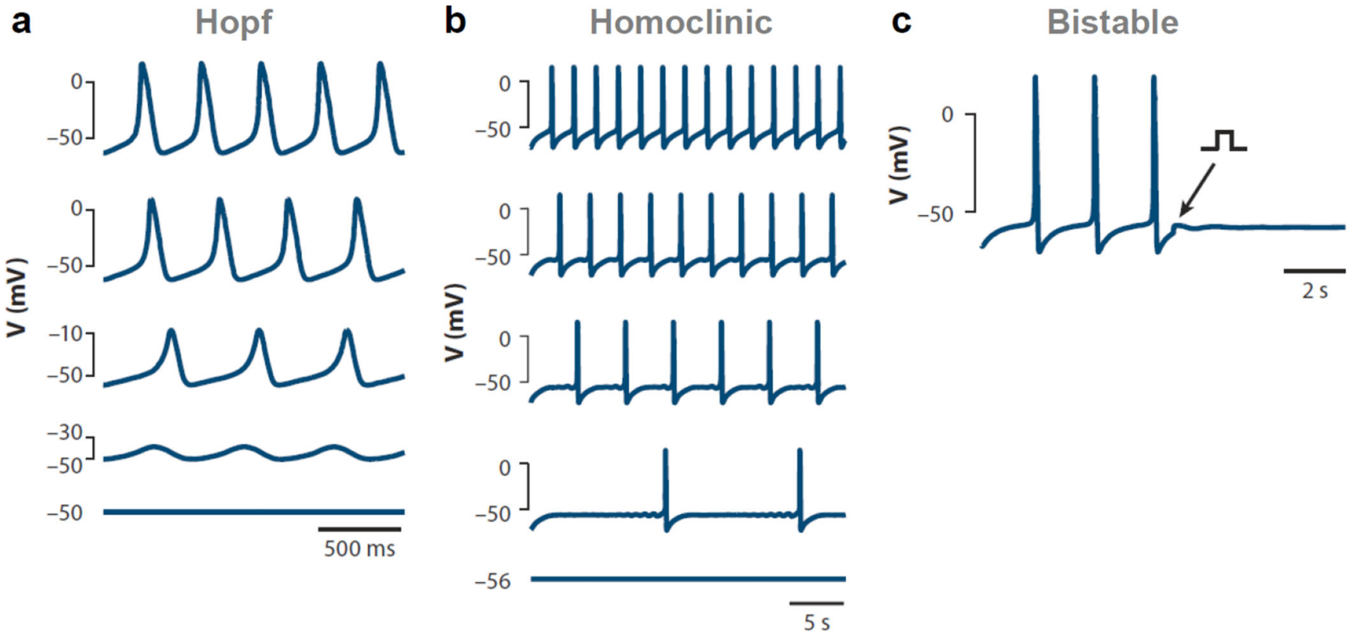

Figure 63. SAN oscillations and abolishment

Simulations of the Irisawa-Noma model of a rabbit SAN node cell illustrating three ways in which limit cycle oscillations can stop, reproduced from Krogh-Madsen et al [8]. **a**. Gradual decline in amplitude due to a supercritical Hopf bifurcation for decreasing Ca^{2+} current conductance. **b**. Skipped beats and increased period due to a homoclinic bifurcation occurring with increasing positive bias current injection. **c**. Termination of oscillation by injection of a brief stimulus current (arrow) due to bistability between a stable limit cycle and a stable fixed point.

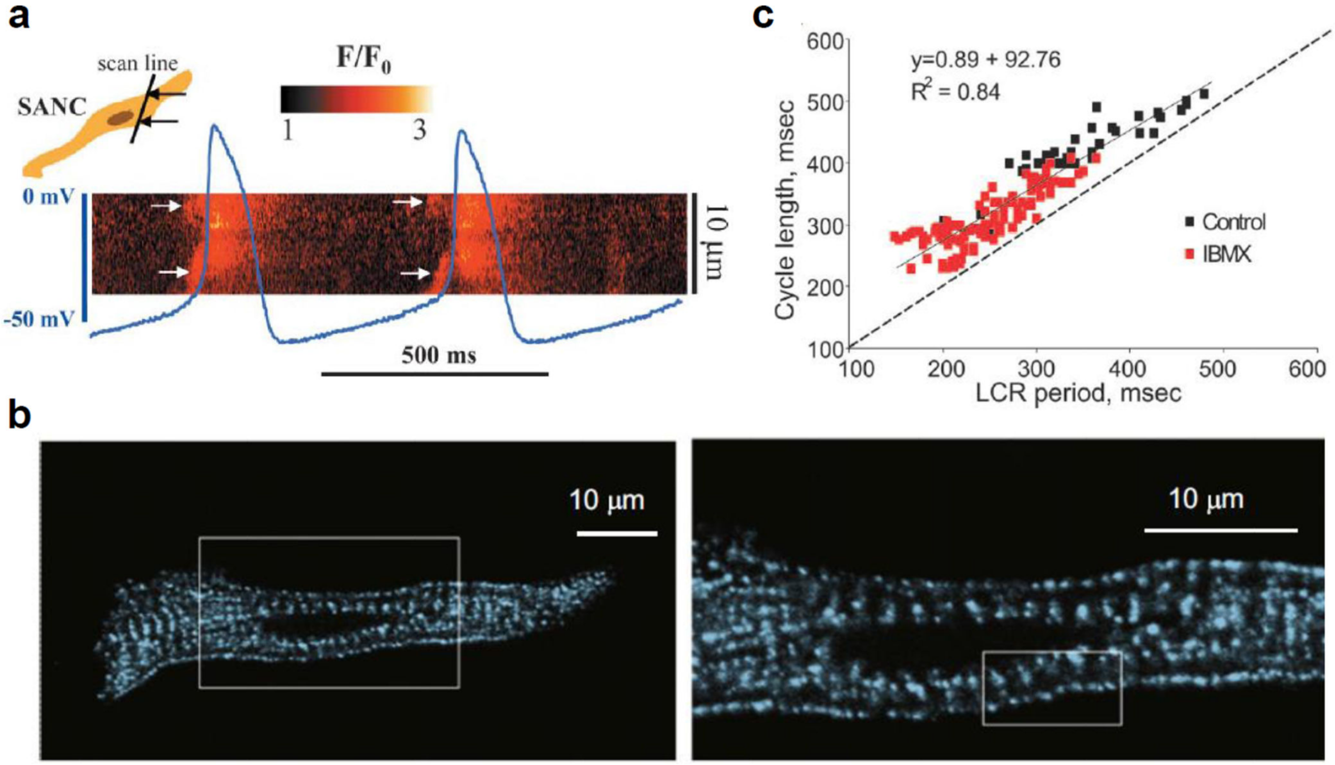

Figure 64. Voltage and Ca^{2+} oscillation in SAN cells

a. Simultaneous recordings of voltage and Ca^{2+} in a rabbit SAN cell. The Ca^{2+} image is a line scan from a line as illustrated in the inset. Reproduced from Maltsev et al [584]. **b**. An optical image of CRUs in a SAN cell. Reproduced from Maltsev et al [504]. **c**. Cycle length versus local Ca^{2+} release (LCR) period from a SAN cell. Reproduced from Vinogradova et al [585].

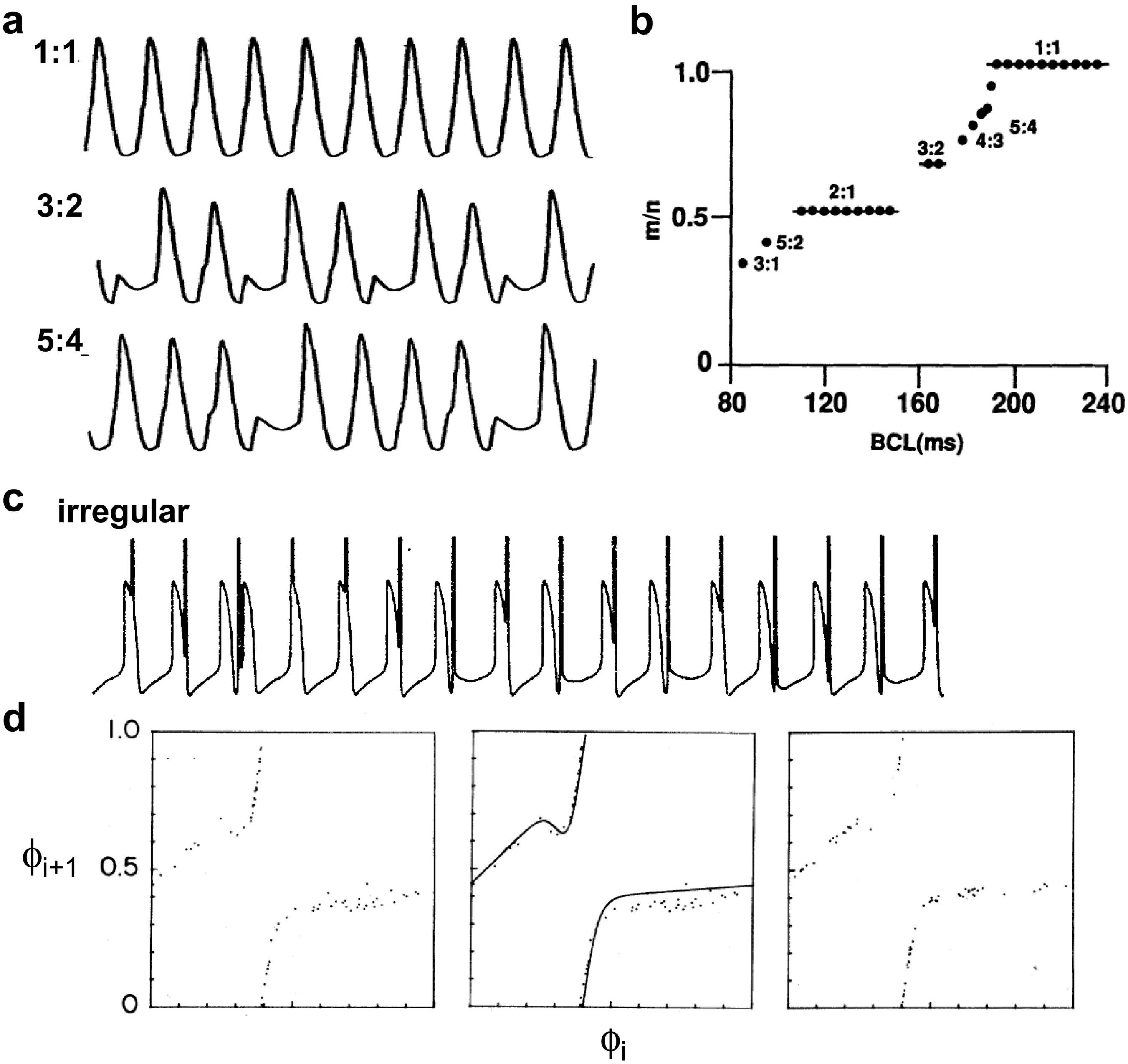

Figure 65. Phase locking and chaos in periodically paced pacemaker cells

a. Voltage recordings from a rabbit SAN cell showing different phase locking ratios. **b**. Summary data of phase locking ratio versus PCL showing “devil’s staircase”. **c**. Voltage recording from a spontaneous beating chick heart cell aggregates showing an irregular response. **d**. Circle map under three conditions. Left: φ_{i+1} versus φ_i obtained from experimental data. Middle: Fitting of the experimental data to a function to obtain a circle map. Right: simulation results using the constructed circle map with noise. Panels a and b are modified from [38]. Panels c and d are modified from [32].

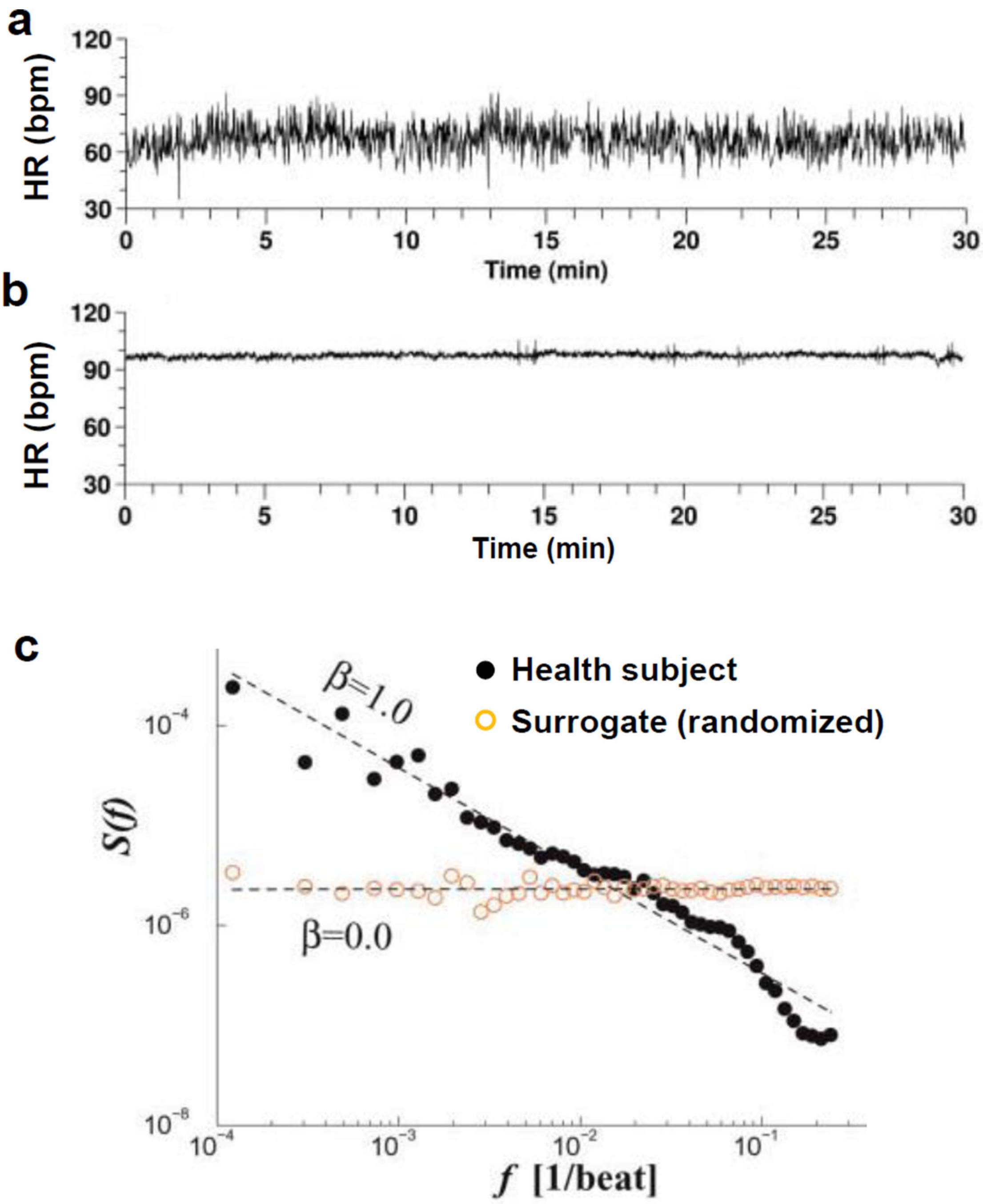

Figure 66. Heart rate variability

a. Heart rate (beats per minute) versus time recorded from a normal human heart. **b**. Heart rate versus time recorded from a diseased heart. **c**. Power spectrum of the heart rate of the normal heart. Reproduced from [42].

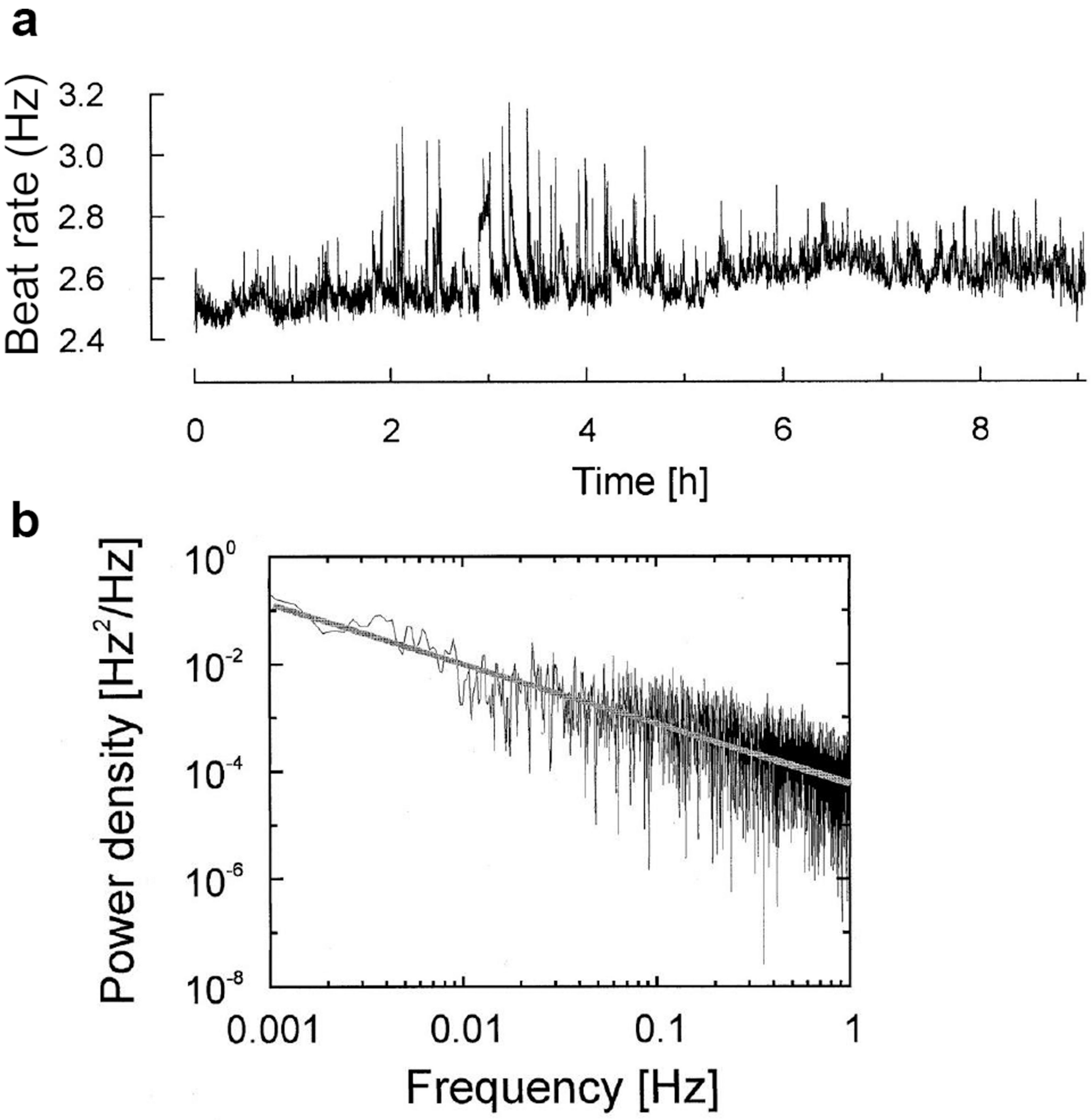

Figure 67. Heart rate variability in cultured monolayers

a. Heart rate versus time. **b**. Power spectrum. Reproduced from [237

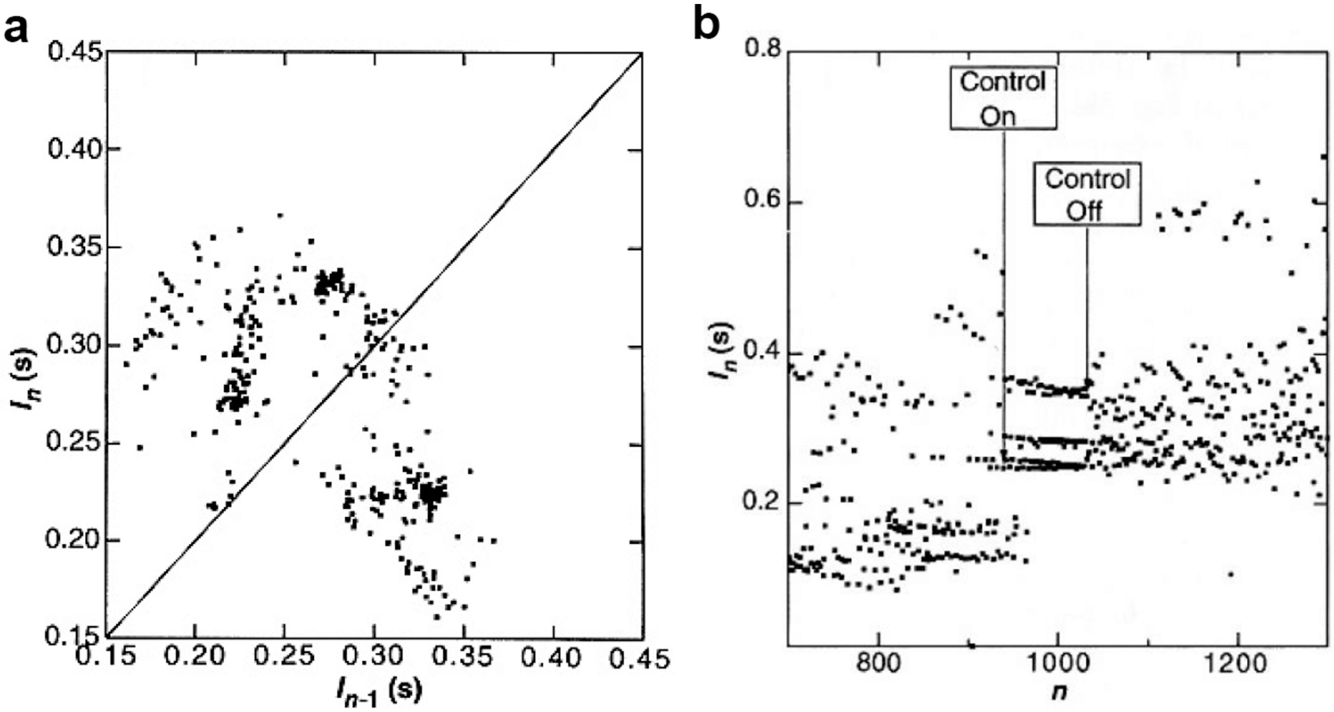

Figure 68. Controlling cardiac chaos

a. Return map of inter-beat interval showing chaos induced by a drug in the septum of a rabbit heart. **b**. The induced chaotic rhythm is converted to periodic rhythm using a chaos control algorithm. Reproduced from Garfinkel et al [524].

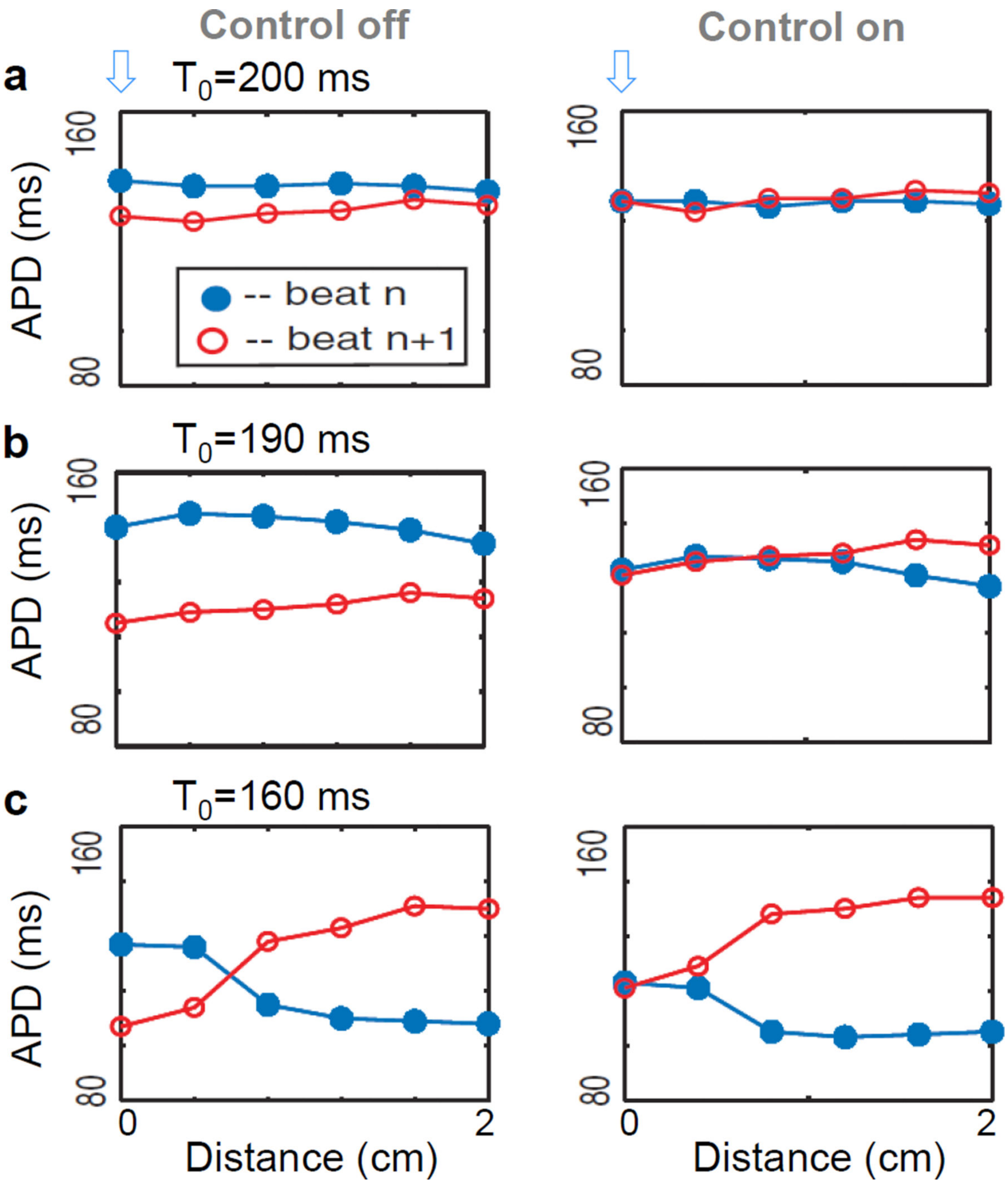

Figure 69. Controlling APD alternans

APD of two consecutive beats recorded from six sites in a Purkinje fiber at different PCL, with and without alternans control. Arrows indicate the pacing and control site. **a**. *T*=200 ms, alternans is concordant and is controlled. **b**. *T*=190 ms. Alternans is concordant and is controlled close to the pacing site but not the entire fiber. **c**. *T*=160 ms, alternans is discordant and control fails. Modified from Christini et al [535].

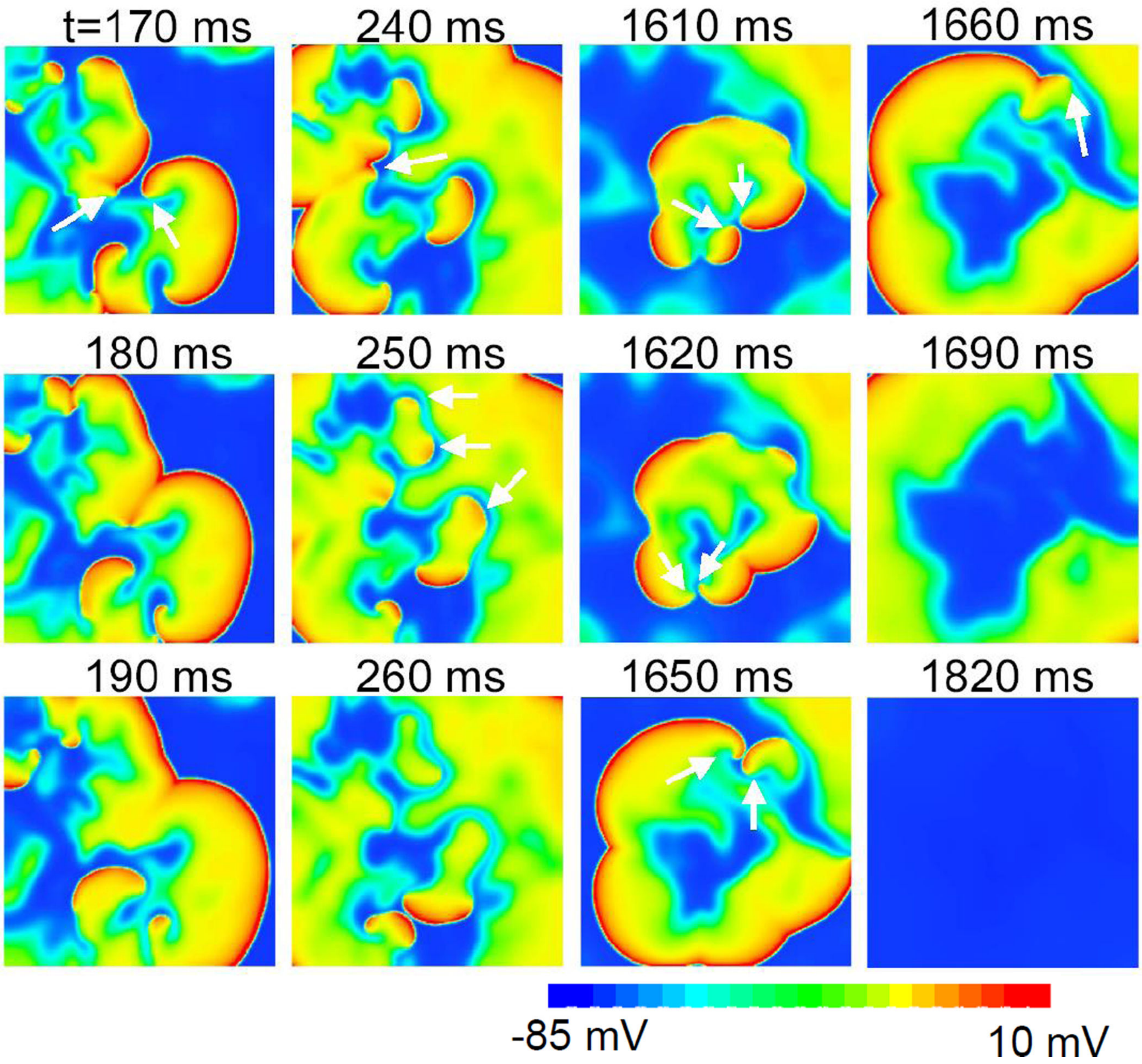

Figure 70. Spontaneous termination of spiral turbulence

Computer simulation showing an episode of spontaneous termination of electrical turbulence in a 2D homogeneous tissue. Arrows indicate the three forms of wave disappearance: spiral tip colliding, waves run into refractory tissue, and drift off the tissue border. Reproduced from Qu [117].

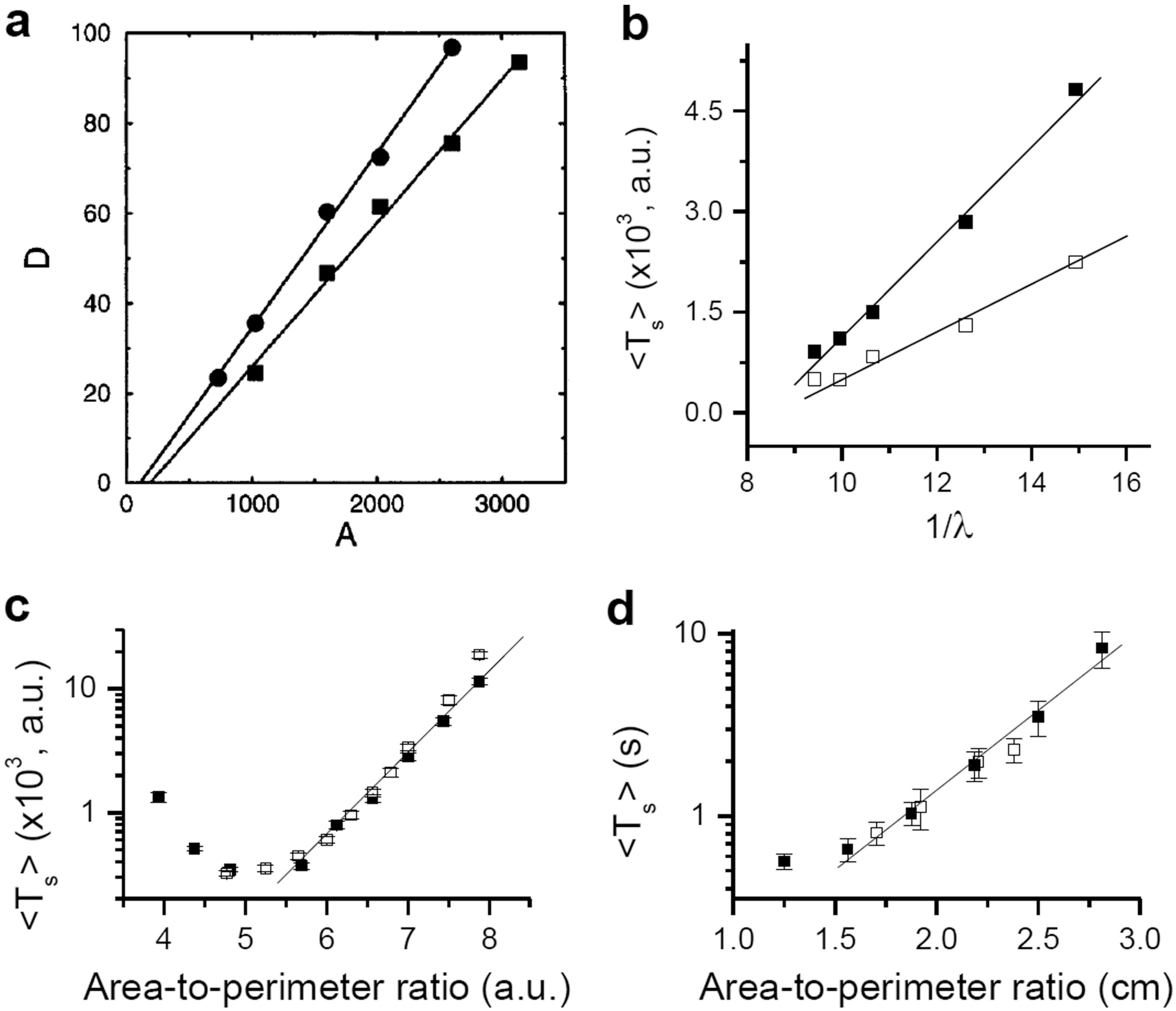

Figure 71. Fibrillation duration versus tissue size and stability

a. Lyapunov dimension versus area, determined from 2D medium. **b**. Average duration of turbulence versus the reciprocal of the maximum Lyapunov exponent. **c**. Average duration of turbulence versus the area-to-perimeter ratio in a 2D medium using the Bar et al model. Simulations were done in square (black) and rectangular (open) tissue. **d**. Same as c but a cardiac tissue model using the LR1 cell model. Reproduced from Qu [117].

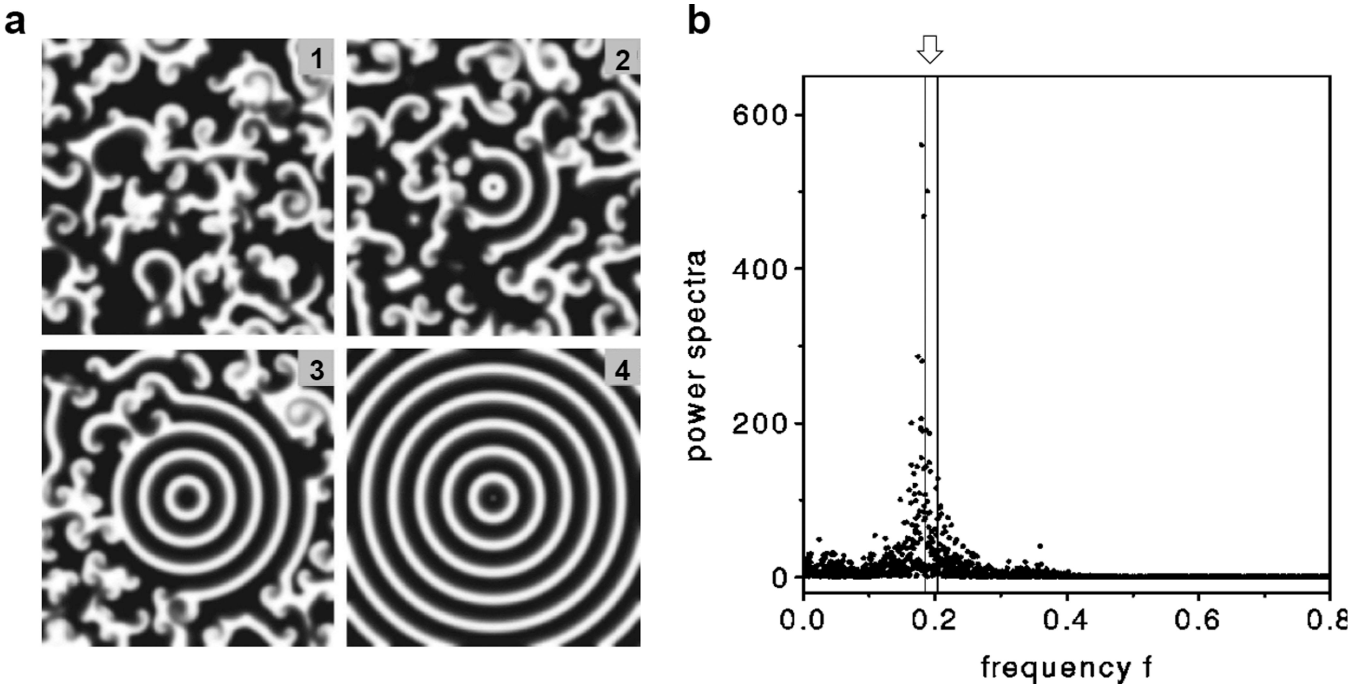

Figure 72. Turbulence control by rapid pacing

a. Turbulence is driven out of the medium by the target waves induced by fast pacing applied in the center. **b**. The power spectrum of the turbulence. The region between the two vertical lines are the pacing frequencies that can successfully control the turbulence. Reproduced from Zhang et al [559].

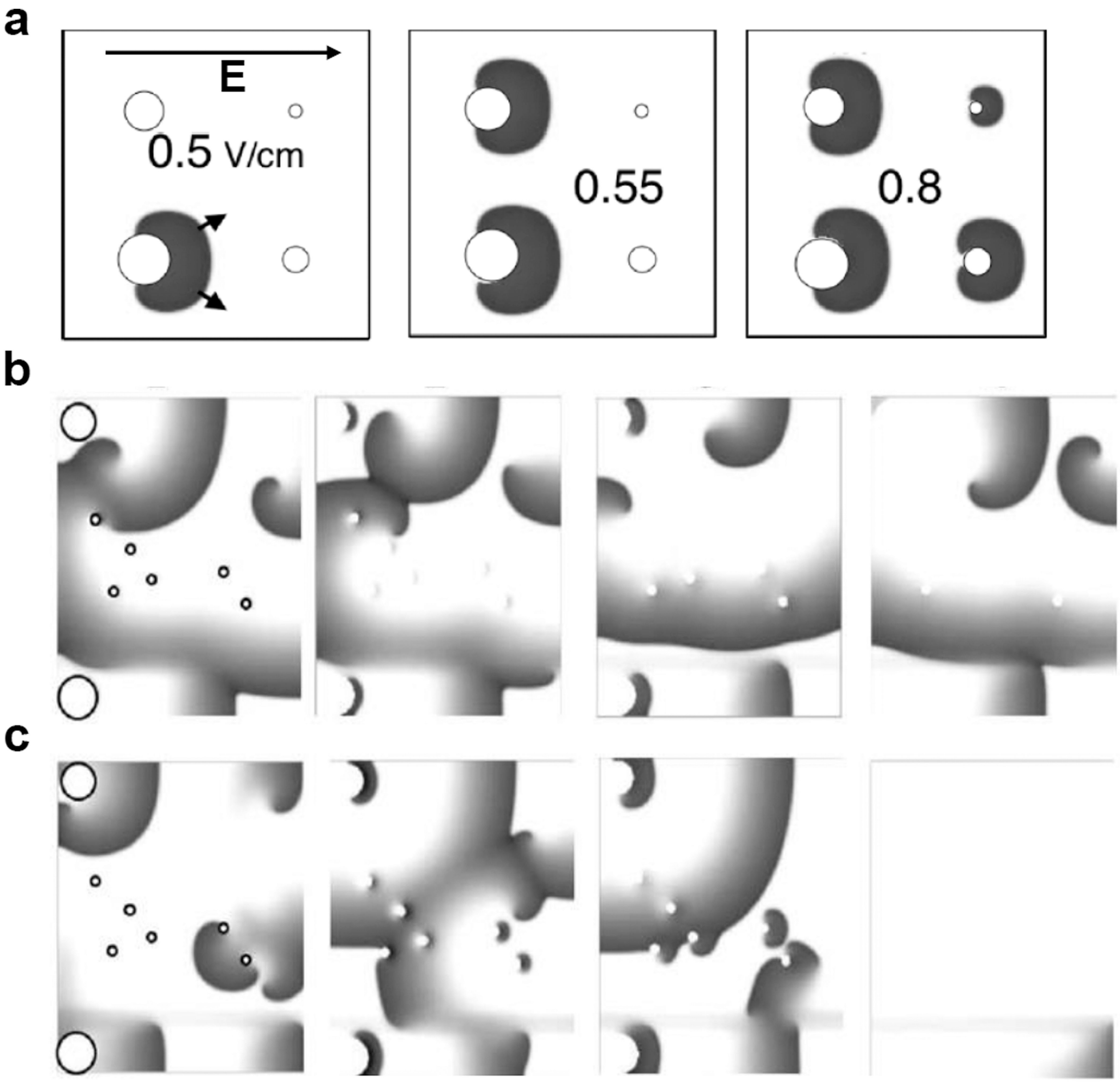

Figure 73. Low energy defibrillation in a computer model

a. Electrical field stimulation induced excitation versus obstacle size and field strength. At low electrical field strength, excitations only occur at the large obstacles, but as the field strength increases, excitations also occur at small obstacles. **b**. Voltage snapshots showing unsuccessful control by field stimulation pacing (T=98 ms) with E=0.6 V/cm. **c**. Voltage snapshots showing unsuccessful control with E=1.1 V/cm in which the electrical waves were terminated. Reproduced from Pumir et al [566].

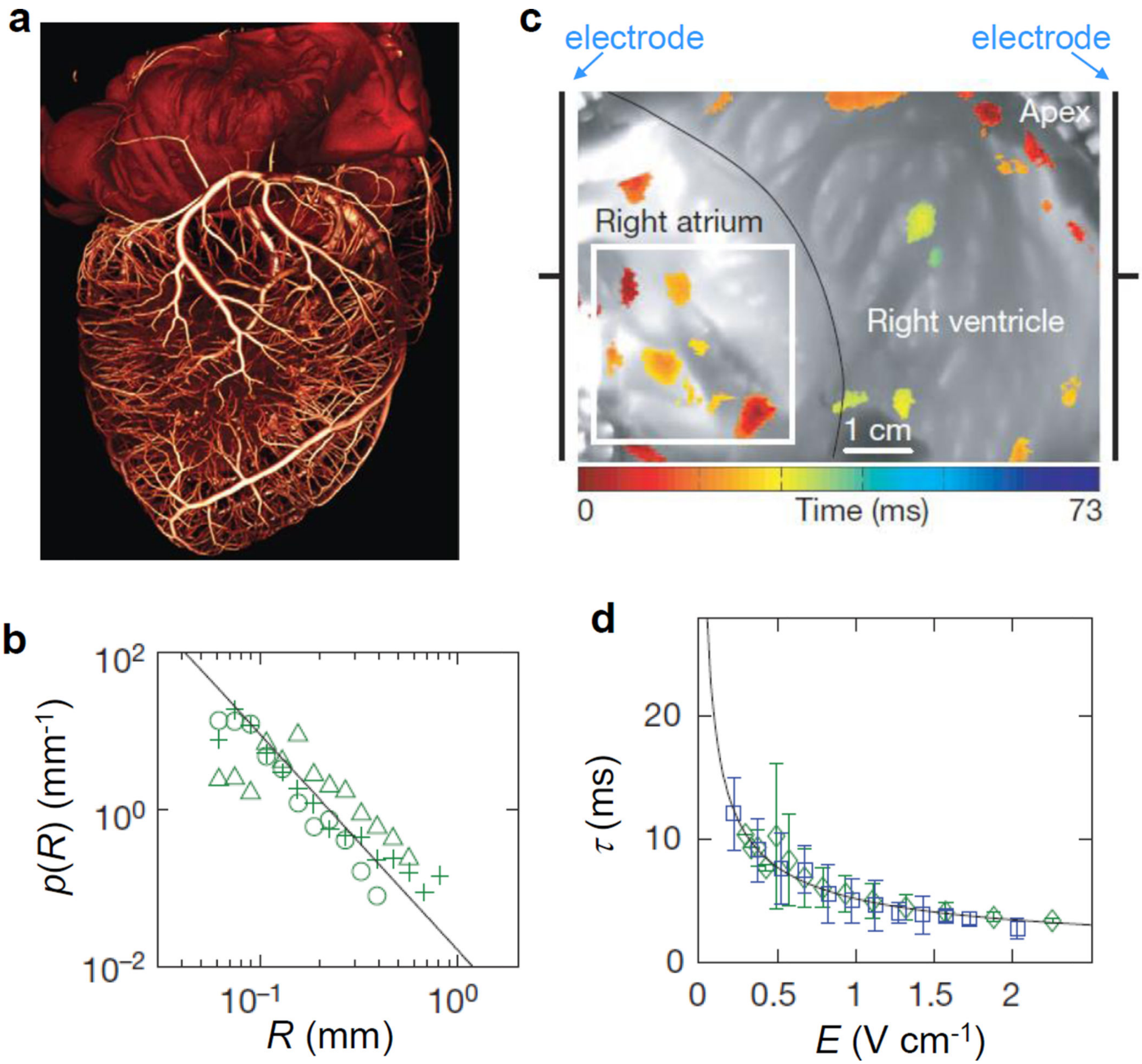

Figure 74. Low energy defibrillation in the real heart

a. Image of coronary arteries in the heart, showing a fractal tree structure. **b**. Probability distribution $p(R)$ of coronary artery radii for ventricular tissue. Different symbols for different hearts. The black line indicates the power law. **c**. Activation sites in cardiac tissue observed in an experiment with a field stimulation (E=0.34 V/cm). Color indicates the time of activation after the stimulus. **d**. Ventricular activation-time measurements (blue squares) and prediction of activation times (green diamonds) based on $p(R)$. The black line indicates the power law. Panel a was reproduced from Karma [7], and panels b–e were reproduced from Luther et al [568].

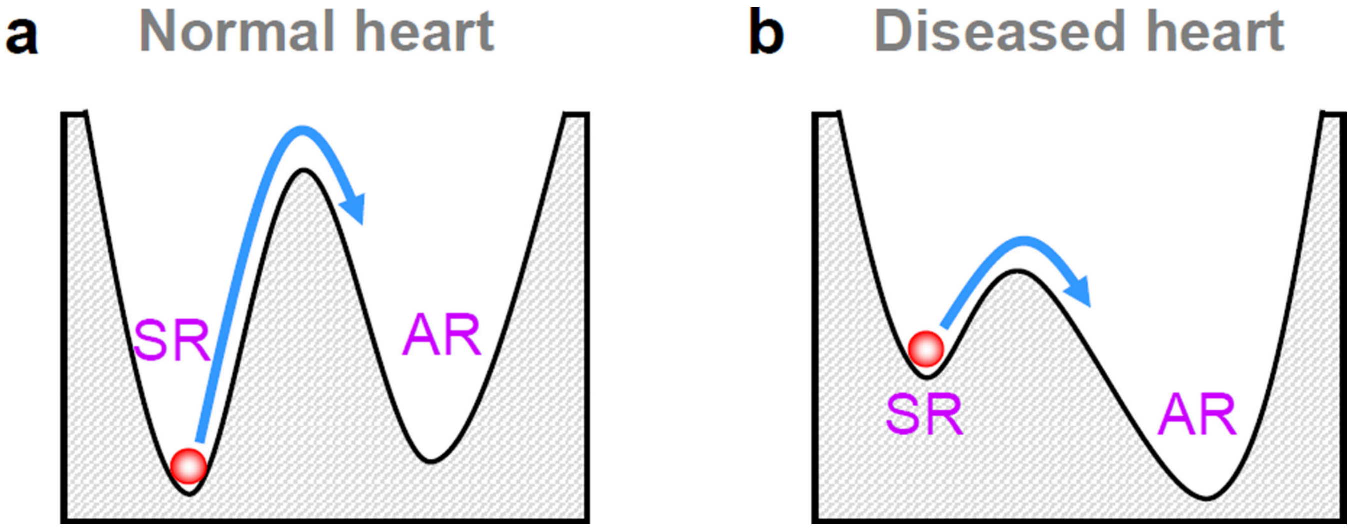

Figure 75. Schematic plots showing basins of attraction of normal sinus rhythm (SR) and arrhythmias (AR)

a. Normal hearts. **b**. Diseased hearts.